UNIVERSITÀ DEGLI STUDI DI BARI
FACOLTÀ DI SCIENZE MATEMATICHE FISICHE E NATURALI
DIPARTIMENTO INTERATENEO DI FISICA "M. MERLIN"
DOTTORATO DI RICERCA IN FISICA
CICLO XX
SETTORE SCIENTIFICO DISCIPLINARE FIS/01

DETECTION OF LOW MOMENTUM PROTONS WITH THE NEW HERMES RECOIL DETECTOR

Dottorando:
VILARDI IGNAZIO

ANNO ACCADEMICO 2006/2007

UNIVERSITÀ DEGLI STUDI DI BARI
FACOLTÀ DI SCIENZE MATEMATICHE FISICHE E NATURALI
DIPARTIMENTO INTERATENEO DI FISICA "M. MERLIN"
DOTTORATO DI RICERCA IN FISICA
CICLO XX
SETTORE SCIENTIFICO DISCIPLINARE FIS/01

DETECTION OF LOW MOMENTUM PROTONS WITH THE NEW HERMES RECOIL DETECTOR

Tutore:
Ch.mo Prof. DE LEO RAFFAELE

Coordinatore:
Ch.mo Prof. MUCIACCIA MARIA TERESA

Dottorando:
VILARDI IGNAZIO

ANNO ACCADEMICO 2006/2007

“*Physics is like sex:*
sure, it may give
some practical results,
but that’s not
why we do it.”

Richard P. Feymann

A mio
nonno
Ignazio

To my
grandfather
Ignazio

Contents

List of Figures

List of Tables

Introduction

Most of our knowledge about the structure of matter has been gained by scattering experiments. After Rutherford discovered the existence of nuclei in atoms more than 90 years ago, it was shown 50 years ago that nuclei are composed of protons and neutrons [Hof57]. Over the past few decades, the research on the structure of matter has made enormous strides. In the late sixties, deep inelastic electron nucleon scattering at SLAC (Stanford Linear Accelerator Center) [Alg76] showed that protons are composed of point-like objects called partons. In the Quark-Parton Model partons are identified with quarks carrying spin and a charge of multiples of one third of the elementary charge e. Further experiments showed that the nucleon consists not only of quarks but also of gluons, which are the mediating particles of the strong interaction.

The results of subsequent polarized Deep Inelastic Scattering (DIS) experiments such as EMC (European Muon Collaboration) at CERN [Ash88, Ash89] in the 1980's led to the startling revelation that the quarks carried much less than half of the spin of the nucleon. In sharp contrast to the quark spin contribution expected from the Quark-Parton Model ($\Delta\Sigma = 0.57$), the EMC experiment measures this contribution to be $\Delta\Sigma = 0.126 \pm 0.010(\text{stat.}) \pm 0.015(\text{syst.})$ [Ash89]. This observation lead to the so-called *spin crisis.* The remainder of the nucleon spin could be attributed to contributions from the quark and gluon angular momenta with the expression

$$\frac{1}{2} = \frac{1}{2}\Delta\Sigma + L_q + \Delta G + L_g \quad , \tag{1}$$

where $\Delta\Sigma = \Delta u + \Delta d + \Delta s$ refers to the sum of the contributions from sea and valence quarks, ΔG is the contribution from gluon spin, and L_q and L_g are the contributions from the orbital angular momenta of quarks and gluons, respectively.

The HERMES (HERa MEasurement of Spin) experiment [Her93] was designed to study the spin structure of the nucleon by measuring scattering interactions between a polarized lepton beam (provided by the HERA lepton proton collider at DESY, Hamburg, Germany) and a longitudinally or transversely polarized targets internal to the storage ring. HERMES was fully approved in July 1993 after the final funding of all components was secured. The original detector and its infrastructure was constructed within about 1.5 years and was commissioned in early Summer 1995. Scattered leptons and particles produced in the deep inelastic lepton-nucleon interactions are detected and identified by a forward spectrometer within an angular acceptance of ±170 mrad horizontally and ±(40-140) mrad vertically. The beam line separates the spectrometer in an upper and lower part with independent detector systems and trigger for the top and bottom sections. The particle identification system allows the identification of leptons with an efficiency of 98% or better, with a hadron contamination less than 1% and provides, after the RICH installation in 1998, full separation between charged pions, kaons and protons over essentially the entire momentum range of the experiment.

Detailed information about $\Delta\Sigma$ and its decomposition into the contributions from quarks and antiquarks of different flavors can be obtained from double-spin asymmetries of cross sections in inclusive polarized DIS, where only the scattered lepton is observed, and semi-inclusive DIS where in addition to the scattered lepton one or more hadrons, produced in the reaction, are identified [Air07b]. From the double-spin asymmetries spin structure functions of the proton $g_1^p(x_{Bj}, Q^2)$ and deuteron $g_1^d(x_{Bj}, Q^2)$ are extracted by HERMES over the kinematic range $0.0041 < x_{Bj} < 0.9$ and $0.18\ \text{GeV}^2 < Q^2 < 20\ \text{GeV}^2$ [Air07b]. Important information about the spin structure of the nucleon can be obtained from the first moment of g_1: a value of

$$\Delta\Sigma = 0.330 \pm 0.011(\text{theo.}) \pm 0.025(\text{exp.})$$

is obtained from HERMES deuteron data. Additionally, $\Delta s + \Delta\bar{s} = -0.085 \pm 0.013(\text{theo.}) \pm 0.008(\text{exp.})$ (negative and different from zero by about 4 σ), $\Delta u + \Delta\bar{u} = 0.842 \pm 0.004(\text{theo.}) \pm 0.008(\text{exp.})$ and $\Delta d + \Delta\bar{d} = -0.427 \pm 0.004(\text{theo.}) \pm 0.008(\text{exp.})$ are also obtained [Air07b]. The data therefore suggest that the quark helicities contribute a substantial fraction to the nucleon helicity, but there is still need for a major contribution from gluons and/or orbital angular momenta of more than half of the sum in Expression 1.

The extraction of ΔG can be performed by measuring longitudinal double spin asymmetries as a function of transverse momentum p_T, relative to the direction of the virtual photon, using charged inclusive hadrons from electroproduction off a deuterium target. At $p_T > 1$ GeV, the asymmetries are sensitive to the spin dependent gluon distribution Δg. To extract the gluon polarization ΔG, information on the background asymmetry and the subprocess kinematics are obtained from a Leading Order Monte Carlo model. By integrating over $1.05 < p_T < 2.5$ GeV, a value of

$$\Delta G = 0.071 \pm 0.034(\text{stat}) \pm 0.010(\text{sys-exp}) \pm 0.1(\text{sys-models})$$

is obtained at $\langle x_{Bj} \rangle = 0.22$ from the HERMES experiment [Lie06]. The data favor a very small contribution from gluon spin to the total spin of the nucleon.

The total angular momentum carried by quarks, $J_q = \frac{1}{2}\Delta\Sigma + L_q$, and by gluons, $J_g = \Delta G + L_g$, in the nucleon may be accessed through Generalized Parton Distributions (GPDs) [Mul94, Ji97a]. GPDs are universal quantities involved in the description of hard exclusive processes. GPDs contain a wealth of information about the quark and gluon structure of the nucleon; they are generalized in the sense that they embody nucleon form factors and ordinary PDFs as limiting cases.

The theoretically cleanest process sensitive to GPDs is the Deeply Virtual Compton Scattering (DVCS) [Ji97b]. DVCS denotes exclusive production of high energy photons, where in contrast to Bremsstrahlung the photon is not emitted by the lepton but by one of the quarks inside the nucleon. In HERMES, DVCS is studied through lepton scattering on a nuclear target. This reaction receives contributions from both the DVCS process, whose origin lies in the strong interaction, and the electromagnetic Bethe-Heitler (BH) process. Note that the BH cross section can be precisely calculated in quantum electrodynamics (QED) using elastic form factors. Therefore the BH contribution can be subtracted with sufficient precision if the BH cross section is not strongly dominating the DVCS cross section. At HERMES kinematics, the BH contribution dominates by far, and hence a subtraction of the BH contribution would lead to large uncertainties. The BH/DVCS interference term $\mathcal{I}$ in the total photon production amplitude $\mathcal{T}$,

$$|\mathcal{T}| = |\mathcal{T}_{BH}|^2 + |\mathcal{T}_{DVCS}|^2 + \underbrace{\mathcal{T}_{BH}^{*}\mathcal{T}_{DVCS} + \mathcal{T}_{BH}\mathcal{T}_{DVCS}^{*}}_{Interference\ term\ \mathcal{I}} \quad ,$$

offers the possibility to directly access the DVCS amplitudes. The imaginary part of the interference term $\mathcal{I}$ can be isolated by measuring the angular dependence of the produced photon if polarized lepton beams are available. In order to access the real part in addition, lepton beams of both charges are needed. A determination of the angular dependencies in beam spin and beam charge asymmetries provides the possibility to access DVCS amplitudes and through them certain combinations of GPDs.

Exclusive reactions were already measured at HERMES [Air01, Air07a]. However the low momentum recoil nucleon in the final state of the DVCS process is produced at large laboratory angles and escapes detection by the HERMES spectrometer. Nevertheless, DVCS processes are successfully analyzed employing indirect methods to establish exclusivity of the data sample. However, background contributions, modelled in Monte Carlo, to the exclusive sample due to semi-inclusive DIS and intermediate Δ^+ resonances ($\sim$15%) are impossible to identify by these indirect methods, given the calorimeter resolution.

In order to improve the measurement of exclusive reactions, the HERMES collaboration decided in 2001 to design and construct a Recoil Detector [Her01] surrounding the target cell so that the recoiling target can be directly measured. Together with the information from the forward spectrometer, all reaction products for the exclusive reactions can be identified and their kinematics determined in the Recoil Detector acceptance. Hence, the background in the exclusive event sample will be strongly reduced. The HERMES Recoil Detector consists of three sub-detector components inside a superconducting magnet that provides a longitudinal magnetic field of 1 Tesla. From the beam line, surrounding the target cell inside the HERA lepton beam vacuum, going outside, the Silicon Strip Detector is positioned, followed by a Scintillating Fibre Tracker and a Photon Detector with three tungsten/scintillator layers. The Recoil Detector was installed in January 2006 and commissioning started in February.

The Recoil Detector will be also useful for other exclusive analysis, like hard exclusive meson or Λ-hyperon productions. For hard exclusive meson production, the main task of the Recoil Detector is to detect and identify recoil protons that are exclusively produced in conjunction with a neutral meson, like $e + p \rightarrow e + p + \rho^0 \rightarrow e + p + \pi^+ + \pi^-$. On the other hand the Λ-hyperons from the exclusive reactions $e + p \rightarrow e + K^+ + \Lambda$ can be detected in the Recoil Detector through their decay products $\Lambda \rightarrow p + \pi^-$, improving the semi-inclusive hyperon statistics.

The work presented in this thesis mainly consists of testing the Recoil Detector with cosmic rays and with the HERA lepton beam, in particular analyzing data related to the Silicon Strip Detector, and showing the potentiality of the data analysis in extracting the information of DVCS. The outline of the work is as follow: after this introduction, the first Chapter of this thesis introduces the theoretical framework of GPDs and the way to access them via DVCS. Moreover published HERMES DVCS measurements of beam spin and beam charge asymmetries, based on only forward going particles detections, will be presented. Chapter 2 concerns the setup of the HERMES experiment. After a brief description of the HERA accelerator and some of its technical specifications, the bulk of this Chapter presents the technical details of the HERMES spectrometer itself and its sub-components. In Chapter 3 a full description of the Recoil Detector with Monte Carlo detector performance will be presented. The Cosmic Ray Test Experiment performed in Spring and Summer 2005 for the Recoil Detector will be discussed in Chapter 4, focusing on the performance of the Silicon Strip Detector, one of the three sub-detectors of the Recoil Detector. The Chapter 5 concerns the performance of the Silicon Strip Detector with HERA lepton beam and Chapter 6 concerns the preliminary DVCS analysis based on 2006 data without the Recoil Detector and first Recoil Detector performance for such a data sample. This work is concluded by a Summary and an Outlook.

Chapter 1

Generalized Parton Distributions and Deeply Virtual Compton Scattering

In the theory of Quantum Chromo Dynamics (QCD), one of the main questions is the understanding of the substructure of hadrons. Therefore, most high energy experiments study Deep Inelastic Scattering (DIS), $e{+}p \rightarrow e{+}X$, by detecting only the scattered beam lepton (inclusive reactions), or in addition some of the hadrons (denoted by X) escaping the reaction (semi-inclusive reactions), or by determining the kinematics of all reaction partners (exclusive reactions). These processes are described in QCD by Parton Distribution Functions (PDFs), which encode the one-dimensional distribution of longitudinal momentum and polarization, carried by quarks, antiquarks and gluons.

By definition PDFs do not contain information on the three-dimensional distribution of the hadronic substructure. In order to extract the additional information, particle correlation functions have to be measured that depend on additional variables, characterizing e.g. the momentum difference of the *in* and *out* state. Therefore, processes where the nucleon remains intact are a natural process to study the three-dimensional structure. In such processes, either all produced particles have to be detected and clearly separated from the intact final state nucleon, or the missing mass has to be calculated in order to characterize the difference between the initial energy and the sum of the energy of all reconstructed particles in the detector. In particular Deeply Virtual Compton Scattering (DVCS), $e + p \rightarrow e + p + \gamma$, provides such a process, which constitutes a hard exclusive reaction. These hard exclusive reactions, e.g. DVCS, are described by particle correlation functions, called

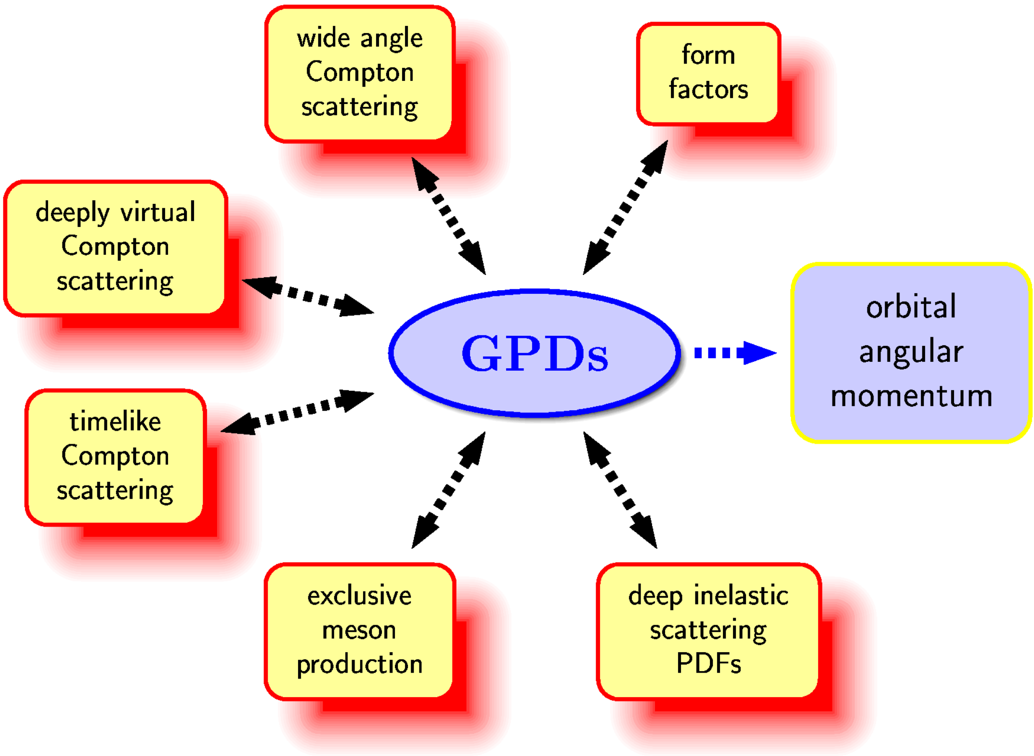

Figure 1.1: Schematic overview of some reactions and nucleon properties related to GPDs. Figure taken from [Web01].

Generalized Parton Distributions (GPDs) [Mul94].

1.1 *Generalized Parton Distributions*

GPDs have been extensively studied theoretically in recent years [Mul94, Ji97b, Die03]. They came into the focus of interest, after Ji has found that GPDs offer the possibility to determine the **total angular momentum** carried by quarks and gluons [Ji97a]. Nowadays, GPDs start to play a role in the studies of nuclear structure.

Although not complete, the schematic overview in Figure 1.1 visualizes the central role GPDs are playing in nucleon structure studies and it shows the exclusive processes which can be described in terms of GPDs. Measurements of these processes will facilitate to access them. The DVCS process appears to be the theoretically cleanest process to be interpreted in terms of GPDs since it involves only a single hadron. In contrast, exclusive meson production needs further non-perturbative information due to the involved meson distribution amplitude $\Phi(z)$. The process of timelike Compton scattering [Ber02], describing the production of a virtual photon which eventually converts into a lepton-antilepton pair, is suppressed by α_{em}^2 compared to the DVCS process. It is therefore experimentally difficult to access. Wide-Angle Compton Scattering is a process where the initial and final photons are real and the involved momentum transfer is large [Rad98].

1.1.1 *Properties of GPDs and the Total Angular Momentum of quarks in the Nucleon*

GPDs are universal non-perturbative objects, entering the description of hard exclusive electro-production processes. First implicitly introduced in [Mul94], they are generally defined for each quark flavor (u,d,s) and gluon (g) as a parametrization of matrix elements of light-cone operators [Rad96]. The matrix elements can be described as elements of the transition matrix between the initial and final hadron state.

The GPDs can be characterized by the following features:

- These GPDs depend on the longitudinal momentum fractions x and ξ where the initial and final proton move fast, and on the Mandelstam variable
$$t = (p - p')^2 \quad , \tag{1.1}$$
where p and p' are the initial and final proton four-momenta (Figure 1.2). The variable ξ, also called *skewedness* parameter, is related to x_{Bj} (Expression 1.9), the momentum fraction of the nucleon carried by the struck quark, as
$$\xi \approx \frac{x_{Bj}}{2 - x_{Bj}}$$
in the kinematic limit (Bjorken limit) of large photon virtuality and energy with x_{Bj} being fixed. The meaning of the longitudinal momentum fraction variables is that the parton with the longitudinal momentum fraction $x + \xi$ is removed from the proton and then put back with a longitudinal fraction $x - \xi$. Note that these longitudinal momentum

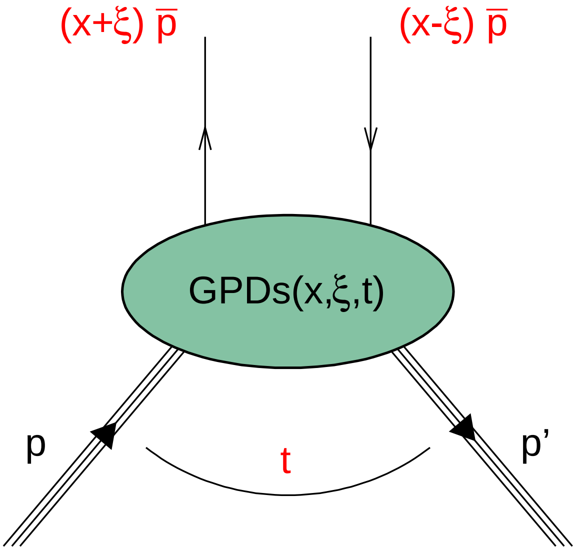

Figure 1.2: The GPD handbag diagram.

fractions are either positive or negative if the active parton is a particle or antiparticle.

- GPDs are defined in the interval $x \,\epsilon\, [-1,1]$, which is subdivided into three regions, shown in Figure 1.3 [Die03]:
    1. for $x \,\epsilon\, [\xi, 1]$: both momentum fractions $x+\xi$ and $x-\xi$ are positive, describing emission and reabsorption of a quark;
    2. for $x \,\epsilon\, [-\xi, \xi]$: $x+\xi \geq 0$ and $x-\xi \leq 0$, interpreted as an antiquark with momentum fraction $\xi - x$ emitted from the initial proton;
    3. for $x \,\epsilon\, [-1, -\xi]$: both momentum fractions $x+\xi$ and $x-\xi$ are negative, belonging to emission and reabsorption of antiquarks.
- In the case of the spin-1/2 nucleon the most important GPDs are the chirally-even GPDs $H^{q,g}$, $\tilde{H}^{q,g}$, $E^{q,g}$, $\tilde{E}^{q,g}$, defined for each quark flavor ($q =$ u,d,s) and gluon (g). Chirally-even means here that they do not flip the parton helicity [Hoo98]. They can be divided into unpolarized GPDs ($H^{q,g}$, $E^{q,g}$) and polarized ones ($\tilde{H}^{q,g}$, $\tilde{E}^{q,g}$). Of these, $H^{q,g}$ and $\tilde{H}^{q,g}$ conserve the nucleon helicity, while $E^{q,g}$ and $\tilde{E}^{q,g}$ can also flip it.

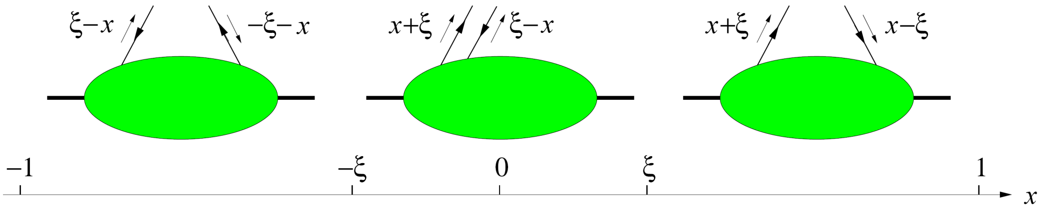

Figure 1.3: The parton interpretation of GPDs in the three x-intervals $[-1,-\xi]$, $[-\xi,\xi]$, and $[\xi,1]$.

The number of GPDs for spin-zero hadrons (pions and spin-zero nuclei) is reduced to one GPD $H^{q,g}$ for each quark flavor and gluon [Die03].

- The first moments of the helicity-conserving GPDs are related to the elastic form factors of the nucleon [Ji97a]:

$$\int_{-1}^{1} dx H^q(x,\xi,t) = F_1(t) \text{ Dirac form factor}$$

$$\int_{-1}^{1} dx E^q(x,\xi,t) = F_2(t) \text{ Pauli form factor}$$

$$\int_{-1}^{1} dx \tilde{H}^q(x,\xi,t) = G_A(t) \text{ Axial-vector form factor}$$

$$\int_{-1}^{1} dx \tilde{E}^q(x,\xi,t) = G_P(t) \text{ Pseudo-scalar form factor}$$

Since the result of the integration does not depend on ξ, one can choose $\xi = 0$. In the limit of vanishing momentum transfer $t \longrightarrow 0$, results

$$H^q(x,0,0) = q(x) \qquad \tilde{H}^q(x,0,0) = \Delta q(x) \quad . \tag{1.2}$$

For gluons they reduce to $H^g(x,0,0) = xg(x)$ and $\tilde{H}^g(x,0,0) = \Delta xg(x)$. The reduced distributions are the ordinary spin-independent density $q(x)$ and spin-dependent density $\Delta q(x)$ for quarks and $xg(x)$, $\Delta xg(x)$ for gluons. The corresponding relation for the distributions $E^{q,g}$ and $\tilde{E}^{q,g}$, which would express the *magnetic* density, can not be directly expressed in terms of any known parton distribution. For Expressions 1.2, $-1 \leq x \leq 1$ and negative values of x correspond to antiquark distributions according to:

$$q(-x) = -\bar{q}(x) \qquad \Delta q(-x) = \Delta\bar{q}(x) \quad .$$

- GPDs have a rich structure in the spin degrees of freedom of the partons and the nucleon. This is especially reflected in a relation between the second moment of a combination of GPDs with a given flavour a on the one hand, and the total angular momentum J^a, i.e. the sum of intrinsic and orbital angular momenta carried by quarks of the flavour a in the proton [Ji97a, Ji97b]:

  $$\lim_{t \to 0} \int_{-1}^{1} x[H^a(x,\xi,t) + E^a(x,\xi,t)]dx = J^a \quad . \tag{1.3}$$

  A determination of contributions J^a from all quark flavors gives the total quark angular momentum J^q which decomposes as

  $$J_q = \frac{1}{2}\Delta\Sigma + L_q \quad , \tag{1.4}$$

  where $\frac{\Delta\Sigma}{2}$ and L_q are the quark spin and the orbital angular momentum contributions, respectively. Using the information on $\Delta\Sigma$ available from inclusive and semi-inclusive polarized DIS [Air07b], this relation may be used to derive the contribution of the quark orbital momentum L_q to the nucleon spin, for whose determination no other way is known at present. It should be noted that this requires access to both unpolarized GPDs, H^q and E^q , and that it is necessary to be able to extrapolate to $t = 0$. This stresses the importance of measurements at low values of t.

1.2 *Deeply Virtual Compton Scattering*

The DVCS is a process in which a virtual photon γ^* interacts with a quark inside the hadronic target and produces a real photon γ. The hadronic target is left intact.

1.2.1 *Kinematics*

The electro-production (Figure 1.4) of real photons

$$e(k) + N(p) \to e(k') + N(p') + \gamma(q') \tag{1.5}$$

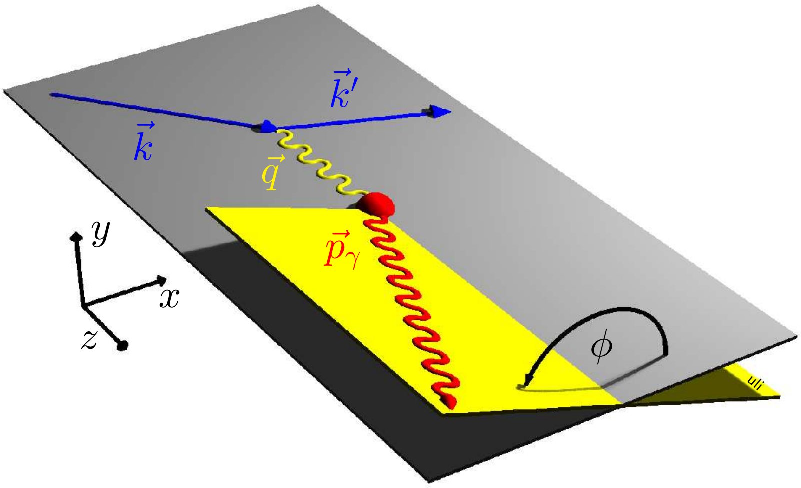

Figure 1.4: Diagram of the DVCS kinematics. The scattering plane (grey) is defined by the incoming and scattered electron momentum vectors $\overrightarrow{k}$ and $\overrightarrow{k'}$. The production plane (yellow) is given by the virtual and real photon momentum vectors $\overrightarrow{q}$ and $\overrightarrow{q'}$ ($\overrightarrow{p}_\gamma$). The angle between scattering and production plane defines the azimuthal angle ϕ.

is described in terms of the four-momenta of the incoming and outgoing electron (k, k') and nucleon (p, p'). The four-momentum transfer by the virtual photon is defined by

$$q^2 \equiv -Q^2 = (k-k')^2 \overset{lab}{=} 4\ E\ E'\ sin^2\frac{\theta}{2} \quad . \tag{1.6}$$

In the laboratory frame (lab) E and E' denote the initial and final electron energy and θ is the scattering angle of the electron. In a fixed target experiments with the target nucleon at rest, the variable ν, given by

$$\nu = \frac{p\ q}{M} \overset{lab}{=} E - E' \quad , \tag{1.7}$$

is the energy loss of the scattered electron. The squared invariant mass of the photon-nucleon system is given by

$$W^2 = (p+q)^2 \overset{lab}{=} M^2 + 2\ M\ \nu - Q^2 \geq M^2 \quad , \tag{1.8}$$

with M being the nucleon (proton) rest mass. Another important variable used to describe DIS events is the Bjorken variable

$$x_{Bj} \equiv \frac{Q^2}{2\ p\ q} \overset{lab}{=} \frac{Q^2}{2\ M\ \nu} \quad , \tag{1.9}$$

being interpreted as the momentum fraction of the nucleon carried by the struck quark. All variables described above (q^2, ν, W^2, x_{Bj}) are fully described by the electron kinematics. The Mandelstam variable t can be calculated either from the initial and final proton or photon four-momenta:

$$t = (p - p')^2 = (q - q')^2 \quad . \tag{1.10}$$

The $\theta_{\gamma^*\gamma}$ angle is the angle between the virtual photon and the real photon:

$$\theta_{\gamma^*\gamma} \equiv \arccos \frac{\overrightarrow{q} \cdot \overrightarrow{q'}}{|\overrightarrow{q}| \cdot |\overrightarrow{q'}|} \quad , \tag{1.11}$$

while the azimuthal angle ϕ (Figure 1.4) is defined as the angle between electron scattering plane and photon production plane:

$$\phi \equiv \arccos \left(\frac{(\overrightarrow{q} \times \overrightarrow{k'})(\overrightarrow{q} \times \overrightarrow{q'})}{|\overrightarrow{q} \times \overrightarrow{k'}||\overrightarrow{q} \times \overrightarrow{q'}|} \right) \frac{\overrightarrow{q'} \cdot \overrightarrow{q} \times \overrightarrow{k'}}{|\overrightarrow{q'} \cdot \overrightarrow{q} \times \overrightarrow{k'}|} \quad . \tag{1.12}$$

1.2.2 *Cross Section*

The DVCS final state is indistinguishable from that of the Bethe-Heitler (BH) process, (Figure 1.5), where the photon is radiated by the incoming or outgoing electron. This leads to an interference of the processes on the amplitude level.

The differential cross section for the *ep* scattering process with unpolarized protons and electrons is given by [Die97]

$$\frac{d\sigma}{d\phi \; dt \; dQ^2 \; dx_{Bj}} = \frac{1}{32 \; (2\pi)^4} \frac{x_{Bj} \; y^4}{Q^4} \frac{1}{\sqrt{1 + 4 \; x_B^2 \; M^2/Q^2}} |\mathcal{T}_{BH} + \mathcal{T}_{DVCS}|^2$$

where y denotes the fractional energy of the virtual photon with respect to the initial electron energy:

$$y \equiv \frac{p \; q}{p \; k} \overset{lab}{=} \frac{\nu}{E} \quad .$$

The BH contribution can be calculated in QED given the knowledge of electromagnetic Dirac and Pauli form factors of the proton. In practice, the BH contribution can be subtracted with sufficient precision only if the BH

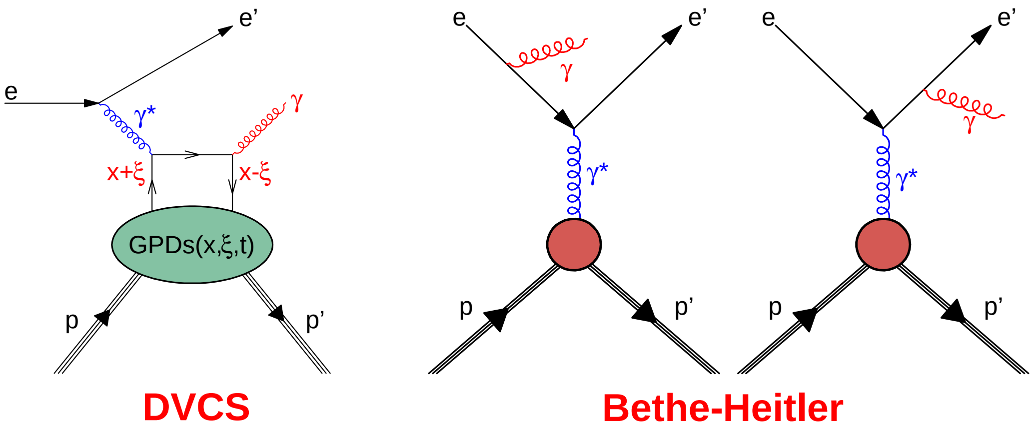

Figure 1.5: Feynman graphs of DVCS (left panel) and Bethe-Heitler (BH) process (right panel). Both processes lead to the same final state, thus their amplitudes interfere.

cross section is not strongly dominating the DVCS cross section. If the BH contribution dominates by far, a subtraction of the BH contribution would lead to large uncertainties. The situation for the kinematic regime in *ep* interaction at beam energy $E = 27.5$ GeV is shown in Figure 1.6 [Kor02] for the specific case that the produced photon is in the same plane as the incoming and outgoing electron, i.e., $\phi = 0$ or $\phi = \pi$. The differential cross sections for the DVCS, BH and total photon production processes are displayed as a function of the angle $\theta_{\gamma^*\gamma}$ (Expression 1.11). Note that contrary to its usual definition the polar angle $\theta_{\gamma^*\gamma}$ in Figure 1.6 can become negative. Positive values of $\theta_{\gamma^*\gamma}$ correspond to $\phi = 0$, negative ones to $\phi = \pi$. The DVCS cross section has its maximum at $\theta_{\gamma^*\gamma} = 0$, while the BH cross section has a three peak structure corresponding to the real photon being essentially collinear to the virtual photon or the incoming or outgoing electron, commonly referred to as Compton peak, Initial State Radiation (ISR) and Final State Radiation (FSR), respectively [Kor02]. In this condition the DVCS cross section is at least an order of magnitude smaller than the BH cross section, therefore the subtraction of the calculated BH cross section from a measured total photon production cross section would lead to large uncertainties [Kor02, Ell04].

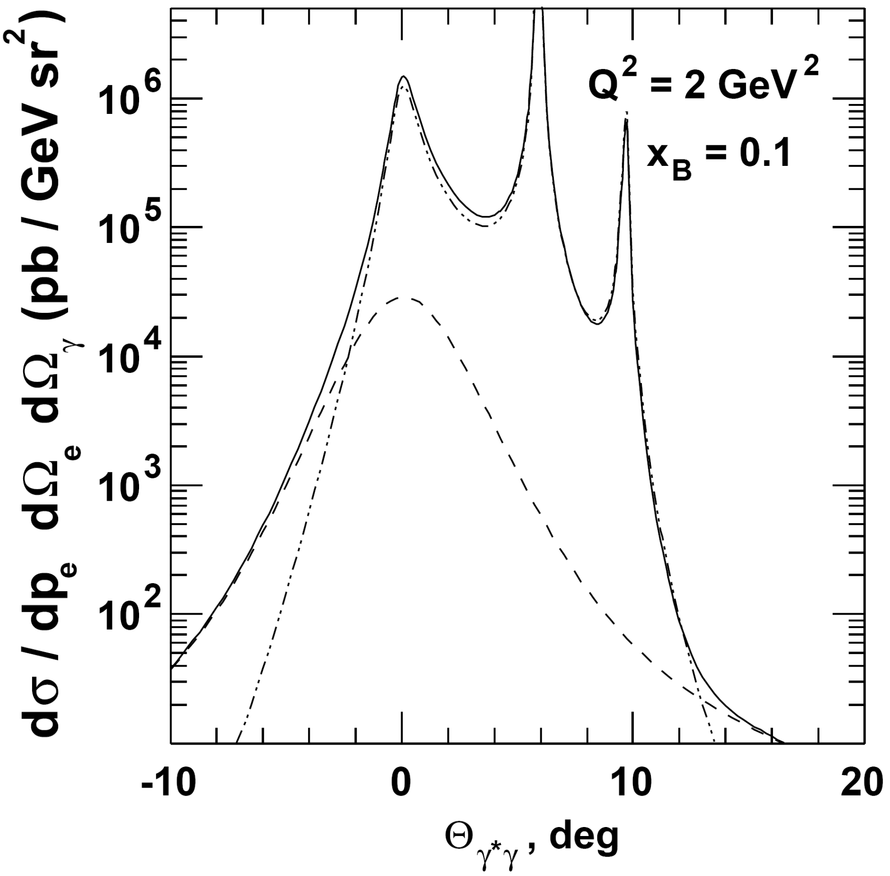

Figure 1.6: Differential in-plane cross section as a function of the angle $\theta_{\gamma^*\gamma}$ between the virtual photon and the real photon for DVCS (dashed line), BH (dashed-dotted line) and total photon production (solid line) in ep interaction at the beam energy $E = 27.5$ GeV for fixed values of x_{Bj} and Q^2. Positive values for $\theta_{\gamma^*\gamma}$ correspond to $\phi = 0$, negative ones to $\phi = \pi$. Figure taken from [Kor02].

1.2.3 *Azimuthal Asymmetries*

Another possibility to gain information on the DVCS contribution is to consider the interference term $\mathcal{I}$ in the total photon production amplitude $\mathcal{T}$,

$$|\mathcal{T}| = |\mathcal{T}_{BH} + \mathcal{T}_{DVCS}|^2 = |\mathcal{T}_{BH}|^2 + |\mathcal{T}_{DVCS}|^2 + \underbrace{\mathcal{T}_{BH}^* \mathcal{T}_{DVCS} + \mathcal{T}_{BH} \mathcal{T}_{DVCS}^*}_{\mathcal{I}} \quad ,$$

which offers the opportunity to access the real and imaginary part of the DVCS amplitude $\mathcal{T}_{DVCS}$. These can eventually be expressed in terms of the target GPDs. The three parts that make up the photon production cross section can be expanded in Fourier series. For an unpolarized proton target they read [Bel02]:

$$\begin{aligned}
|\tau_{BH}|^2 &= \frac{e^6}{x_{Bj}^2\ y^2\ t\ (1+4x_{Bj}^2\ M_p^2/Q^2)^2\ P_1(\phi)\ P_2(\phi)} \times \\
&\quad \times \left\{ c_0^{BH} + \sum_{n=1}^{2} c_n^{BH} \cos(n\phi) \right\} \quad , \qquad (1.13) \\
|\tau_{DVCS}|^2 &= \frac{e^6}{y^2\ Q^2} \times \\
&\quad \times \left\{ c_0^{DVCS} + \sum_{n=1}^{2} c_n^{DVCS} \cos(n\phi) + \lambda\ s_1^{DVCS} \sin(\phi) \right\}, \qquad (1.14) \\
\mathcal{I} &= \frac{\pm e^6}{x_{Bj}\ y^3\ t\ P_1(\phi)\ P_2(\phi)} \times \\
&\quad \times \left\{ c_0^{\mathcal{I}} + \sum_{n=1}^{3} c_n^{\mathcal{I}} \cos(n\phi) + \lambda \sum_{n=1}^{3} s_n^{\mathcal{I}} \sin(n\phi) \right\}, \qquad (1.15)
\end{aligned}$$

where the + (-) sign in the interference term $\mathcal{I}$ stands for a negatively (positively) charged lepton beam. The Fourier coefficients c_n and s_n depend on the kinematic variables x_{Bj}, y, Q^2 and t and on the beam as well as on the target polarization. Note that the BH propagators $P_1(\phi)$ and $P_2(\phi)$ [Bel02],

$$\begin{aligned}
Q^2\ P_1 &\equiv (k-q')^2 \quad , \\
Q^2\ P_2 &\equiv [(k-(p'-p)]^2 \quad ,
\end{aligned}$$

in the squared BH and in the interference term have an additional dependence on the azimuthal angle ϕ. They are approximately given by $P_i(\phi) = A_i + B_i cos(\phi)$, whereby B_i is at least suppressed like $1/Q^2$. The exact expressions for the Fourier coefficients for an unpolarized target and for the BH propagators are lengthy and therefore not shown here, but can be found in [Bel02]. Note that the dependence of the Fourier coefficients on the beam polarization λ has been taken out of the expressions given in [Bel02] and put into the Expressions 1.14 and 1.15 for later convenience.

The Fourier coefficients of the interference term ($c_n^{\mathcal{I}}$ and $s_n^{\mathcal{I}}$) are proportional to the DVCS amplitudes. Appropriate asymmetries are needed to disentangle the different contributions in order to extract them. The beam spin and the beam charge asymmetries are suitable for this purpose. They are described in the next two subsections.

Beam Spin Asymmetry A_{LU}

The beam spin asymmetry

$$A_{LU}(\phi) = \frac{d\overrightarrow{\sigma} - d\overleftarrow{\sigma}}{d\overrightarrow{\sigma} + d\overleftarrow{\sigma}} \quad ,$$

where A_{LU} denotes the asymmetry (A) using a longitudinally (L) polarized beam and an unpolarized (U) target, is a cross section asymmetry built from two measurements with opposite beam helicity denoted by arrows with opposite orientation. Assuming that the magnitude of the polarization is the same in both helicity states, only those Fourier coefficients in the Expressions 1.13 - 1.15 that depend on λ ($s_1^{\mathcal{I}}$, $s_2^{\mathcal{I}}$, $s_3^{\mathcal{I}}$ and s_1^{DVCS}) are left in the numerator and only those independent of λ (all others) contribute to the denominator. Among the four Fourier coefficients in the numerator only $s_1^{\mathcal{I}}$ is related to the leading twist-2 quark GPDs, while $s_2^{\mathcal{I}}$, $s_3^{\mathcal{I}}$ and s_1^{DVCS} are twist-3 contributions and therefore suppressed. The assumption that the denominator should be dominated by the $|\mathcal{T}_{BH}|^2$ contribution is supported by Figure 1.6 where the DVCS cross section is shown to be about an order of magnitude smaller than the BH one. The dominant contribution in the BH cross section itself originates from the c_0^{BH} term. Assuming that the BH propagators $P_1(\phi)$ and $P_2(\phi)$ in the numerator and in the denominator largely cancel each other, the beam spin asymmetry A_{LU} can be approximated at leading twist as

$$A_{LU}(\phi) \approx \pm \frac{x_{Bj}}{y} \frac{s_1^{\mathcal{I}}}{c_0^{BH}} sin(\phi) \quad . \tag{1.16}$$

Hence, if the above assumptions hold, the beam spin asymmetry should predominantly show a $\sin\phi$ modulation which changes its sign depending on the beam charge. The observation of an additional $\sin 2\phi$ and $\sin 3\phi$ dependence would probably allow access to the higher twist coefficients $s_2^{\mathcal{I}}$ and $s_3^{\mathcal{I}}$.

Beam Charge Asymmetry A_C

The beam charge asymmetry

$$A_C(\phi) = \frac{d\sigma^+ - d\sigma^-}{d\sigma^+ + d\sigma^-} \quad ,$$

is a cross section asymmetry built from two measurements with opposite beam charge where $d\sigma^+$ and $d\sigma^-$ denote the cross section measurements with positron and electron beams, respectively. The cross section difference in the numerator directly projects out the interference term $\mathcal{I}$ since it is the only term that depends on the charge (see Expressions 1.13 - 1.15), the denominator gets contributions only from the charge independent squared BH and squared DVCS term. Assuming an unpolarized beam ($\lambda = 0$), only the Fourier coefficients $c_n^{\mathcal{I}}$ contribute to the numerator. Among these, the coefficients $c_0^{\mathcal{I}}$ and $c_1^{\mathcal{I}}$ are related to the same leading twist quark GPDs, but $c_0^{\mathcal{I}}$ is kinematically suppressed like $1/Q^2$ compared to $c_1^{\mathcal{I}}$. The coefficient $c_2^{\mathcal{I}}$ arises at twist-3 level and the Fourier coefficient $c_3^{\mathcal{I}}$ originates from the twist-2 helicity-flip gluon GPDs, suppressed by α_s/π, or from twist-4 quark GPDs. Thus the leading term in the numerator is $c_1^{\mathcal{I}}$. As for the beam spin asymmetry, the denominator should be dominated by the BH squared term (see Figure 1.6), whereby the c_0^{BH} term gives the largest contribution to the BH squared term. Under the assumption that the BH propagators from the BH squared and from the interference term largely cancel each other, the beam charge asymmetry at leading twist is approximately given as

$$A_C(\phi) \approx -\frac{x_{Bj}}{y} \frac{c_1^{\mathcal{I}}}{c_0^{BH}} cos(\phi) \quad . \tag{1.17}$$

Consequently, a measurement of the beam charge asymmetry should predominantly reveal a $\cos\phi$ dependence, probably accompanied by $\cos 2\phi$ and $\cos 3\phi$ modulations.

1.2.4 *From Azimuthal Asymmetries to DVCS Amplitudes*

In terms of DVCS amplitudes, the leading Fourier coefficients accessible via the beam spin asymmetry ($s_1^{\mathcal{I}}$) and via the beam charge asymmetry ($c_1^{\mathcal{I}}$)

are proportional to the imaginary and the real part of the photon helicity conserving amplitudes $M^{1,1}$, respectively. Here $M^{\mu,\mu'}$ denotes the helicity amplitudes with an initial (final) state photon helicity μ (μ'), following the notation in [Die97]. In this case the helicity of the virtual and the real photon is the same. The Fourier coefficient $s_0^{\mathcal{I}}$ is related to the same amplitude, but it is kinematically suppressed like $1/Q^2$.

Beyond leading twist, the coefficient $s_2^{\mathcal{I}}$ ($c_2^{\mathcal{I}}$), accompanied by a $sin2\phi$ ($cos2\phi$) modulation, is related to the imaginary (real) part of the helicity non-conserving amplitudes $M^{0,1}$ and $M^{0,-1}$, corresponding to the virtual photon being longitudinal.

The Fourier coefficient $c_3^{\mathcal{I}}$ is accessible through $cos3\phi$ modulations and proportional to the real part of the photon helicity non-conserving amplitudes $M^{1,-1}$ and $M^{-1,1}$. The amplitudes $M^{1,-1}$ and $M^{-1,1}$ are the photon helicity-flip amplitudes, i.e., also the virtual photon is transverse but both photons have opposite helicity.

1.2.5 *From DVCS Amplitudes to GPDs*

In the following, the relation between the DVCS amplitudes and the GPDs is shown for the leading contributions only. Summarizing the leading twist approximation, the beam spin and the beam charge asymmetries

$$\begin{aligned} A_{LU} &\sim s_1^{\mathcal{I}} \ \sin(\phi) \sim Im(M^{1,1}) \ sin(\phi) \quad , \\ A_C &\sim c_1^{\mathcal{I}} \ \cos(\phi) \sim Re(M^{1,1}) \ \cos(\phi) \quad , \end{aligned}$$

give access to the imaginary and real part of the photon helicity conserving DVCS amplitude $M^{1,1}$, respectively. The DVCS amplitude

$$\begin{aligned} M^{1,1} = F_1(t)H_1(\xi,t) \quad &+ \quad \frac{x_{Bj}}{2-x_{Bj}}(F_1(t)+F_2(t))\tilde{H}_1(\xi,t) + \\ &- \frac{t}{4M^2}F_2(t)E_1(\xi,t) \end{aligned} \tag{1.18}$$

is given by a linear combination of the so-called Compton form factors (CFFs) H_1, $\tilde{H}_1$ and E_1, together with the Dirac and Pauli form factors F_1 and F_2, respectively. The involved CFFs entirely appear at twist-2 and in fact are convolutions of the hard scattering amplitude and the twist-2 GPDs H, $\tilde{H}$ and E.

At small values of x_{Bj} (t) the contribution from the CFFs $\tilde{H}_1$ (E_1) to the amplitude $M^{1,1}$ is suppressed (see Expression 1.18). Therefore the main contribution to the asymmetries in this kinematic region originates from the CFF H_1 and with

$$\begin{aligned} Im\ H_1(\xi,t) &= -\pi \sum_q e_q^2 (H^q(\xi,\xi,t) - H^q(\xi,\xi,t)) \quad , \\ Re\ H_1(\xi,t) &= \sum_q e_q^2 \left[P \int_{-1}^{1} H^q(x,\xi,t) \left(\frac{1}{x-\xi} + \frac{1}{x+\xi} \right) dx \right] \quad , \end{aligned}$$

it originates from the GPD $H^q(x,\xi,t)$. Here, P denotes Cauchy's principal value. Analogous expressions are valid for the other CFFs $\tilde{H}_1$, E_1 and $\tilde{E}_1$ which in principle can be accessed through other asymmetries measurable on longitudinally or transversely polarized targets.

1.3 *DVCS at HERMES*

Recent measurements of the beam spin asymmetry A_{LU} [Air01] published in 2001 and beam charge asymmetry A_C [Air07a] published in 2007 were carried out by HERMES, which employs a polarized lepton beam with an energy of 27.6 GeV scattered off unpolarized hydrogen. The HERMES experiment will be described in detail in the next Chapter.

Since HERMES is a fixed target experiment, its kinematic region is disjunct from that of the collider experiments. The total cross section as a function of the angle $\theta_{\gamma^*\gamma}$ between the virtual photon and the real photon for DVCS, BH and total photon production in ep interaction at the beam energy $E = 27.5$ GeV has been shown in Figure 1.6: DVCS amplitudes can only be accessed through the BH/DVCS interference term.

The asymmetries exhibit the expected $\sin\phi$ and $\cos\phi$ dependence (see Expressions 1.16 and 1.17) as shown in Figure 1.7. For A_{LU}, data taken during 2000 were used to extract the $\sin\phi$ moment of the observed real photon production cross section. During this data taking period, the positron beams were in positive and negative helicity states, resulting in 9387 DVCS events in total (4014 for positive helicity state and 5373 for negative one). The beam polarization had an average value of 55%. For A_C, data taken during

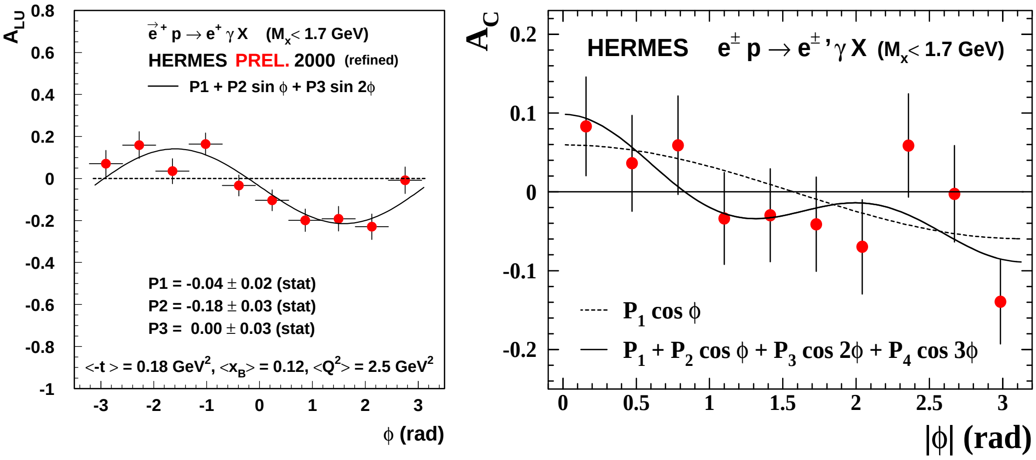

Figure 1.7: Asymmetries for the hard electro-production of photons off protons as a function of the azimuthal angle ϕ (Expression 1.12). The data correspond to the missing mass region between -1.5 and +1.7 GeV. Left: beam spin asymmetry A_{LU}; the solid curve represents a three-parameter fit where only a negative $\sin\phi$ amplitude equal to 0.18 survives; the horizontal error bars represent the bin width. Right: beam charge asymmetry A_C as a function of $|\phi|$; statistical uncertainties are shown; the solid curve represents the four-parameter fit: $(-0.011 \pm 0.019) + (0.060 \pm 0.027)\cos\phi + (0.016 \pm 0.026)\cos 2\phi + (0.034 \pm 0.027)\cos 3\phi$. The dashed line shows the pure $\cos\phi$ dependence.

1998 and 2000 using positron (2000) and electron (1998) beams were used, resulting in 10231 DVCS events in total (9516 for positron beams and 715 for electron beams).

Since HERMES was not able to unambiguously detect the full final state of the reaction, a missing mass technique was employed. Since at HERMES the recoiling proton could not be detected, events containing exactly one lepton with the beam charge and one photon (untracked cluster in the calorimeter) were selected. The missing mass M_x of the reaction $\overrightarrow{e^{\pm}} + p \to e^{\pm} + \gamma + X$ (see Figure 3.1) was required to be between -1.5 and $+1.7$ GeV, i.e., 3σ below and 1σ above the proton mass M_p. Negative missing mass values arise due to the finite resolution of the HERMES spectrometer. The lepton kinematics were required to satisfy 1 GeV$^2 < Q^2 <$ 10 GeV^2, $0.03 < x_{Bj} < 0.35$, $W > 3$ GeV, and $\nu < 22$ GeV. The real photon was identified by detecting an energy deposition above 5 GeV in the calorimeter in addition to a signal in the preshower detector, without an associated charged track in the back region of the spectrometer. The useful range of the polar angle $\theta_{\gamma^*\gamma}$ between the virtual and real photons lies between 5 mrad, limited mainly by the lepton momentum resolution and 45 mrad, imposed in order to improve the signal to background ratio. The average values of the kinematic variables are $\langle Q^2 \rangle = 2.5$ GeV^2, $\langle x_{Bj} \rangle = 0.10$ and $\langle -t \rangle = 0.12$ GeV^2. The obtained value for the $\sin\phi$ amplitudes in A_{LU} (left side in Figure 1.7) is -0.18 ± 0.03(stat) $\pm$ 0.03(sys). The constant term as well as the $\sin 2\phi$ amplitudes are compatible with zero. For A_C (right side in Figure 1.7) the shown four-parameter fit yields a non-zero $\cos\phi$ amplitude of 0.060 ± 0.027. The constant term as well as the $\cos 2\phi$ and $\cos 3\phi$ terms are compatible with zero.

1.3.1 *Constraining* J_u *vs* J_d

At present the only known strategy to *extract* GPDs from experimental measurements is to assume a functional form of GPDs with a number of adjustable parameters, and to fit these parameters by comparing the resulting observables with experimental data [Die03].

The theoretical calculations in function of $-t$ for the $e^+ + p \rightarrow e^+ + p + \gamma$ process shown in Figure 1.8 [Air07a] employ GPD models developed in [Van99a, Goe01]. These initial data can already be used to distinguish among theoretical models for GPDs. The only model parameters of interest are those that change the GPD H since the impact of the GPDs $\tilde{H}$ and E is suppressed at small value of x_{Bj} and $-t$, respectively (see Expression 1.18).

Four different parameter sets are selected by choosing either a factorized or a Regge-inspired t-dependence, each with or without the contribution of a negative value of the so-called D-term, which is related to the spontaneous breaking of chiral symmetry in QCD (for detail see [Pol99, Goe01]). The three data points at small $-t$ (the data at large $-t$ are not included in model calculations as it will be explained in Chapter 6) exclude the model based on the Regge-inspired t-dependence with the D-term contribution.

Within the next few years HERMES will be able to provide sufficient data to largely constrain the GPD H in the kinematic region of the experiment. It is natural to ask to what extent the GPD E can be accessed, which is the other important GPD necessary in order to determine J_q, the total orbital angular momentum of quarks in the nucleon [Ji97a, Ji97b] (see Expression

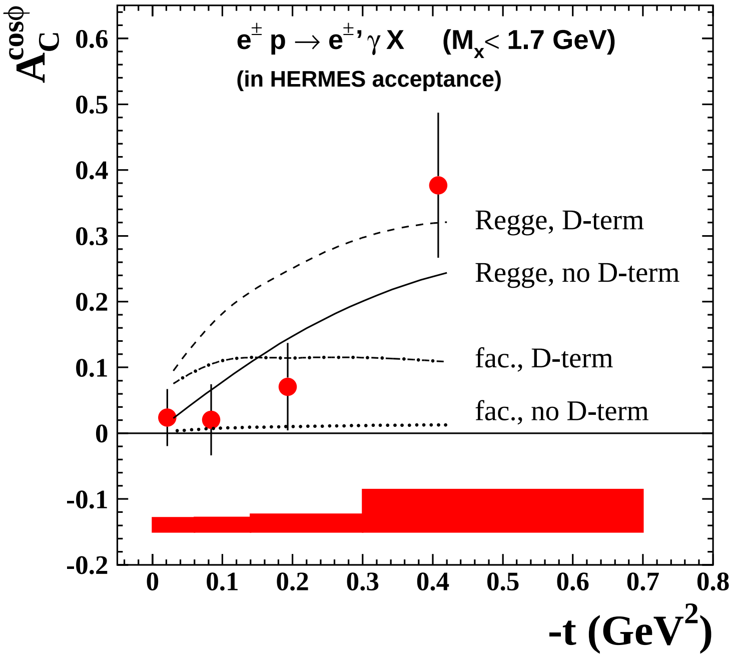

Figure 1.8: The published $-t$ dependence for $A_C^{\cos\phi}$. The calculations based on GPD models [Van99a, Goe01] use either a factorized t-dependence with (dashed-dotted) or without (dotted) the D-term contribution, or a Regge-inspired t-dependence with (dashed) or without (solid) the D-term contribution. Figure taken from [Air07a].

1.3). For an unpolarized proton target the contribution from the GPD E is suppressed with respect to H, but this is different for transverse target polarization [Bel02, Die03]. Using an unpolarized beam (U) and a transversely (T) polarized target, a $\sin(\phi - \phi_S) \cos\phi$ modulation in the DVCS Transverse Target Spin Asymmetry (TTSA) gives access to a combination of the GPDs H and E [Ell06, Ye06]. Here ϕ_S denotes the azimuthal angle of the target polarization vector with respect to the lepton scattering plane.

The results from HERMES data collected on a transversely polarized hydrogen target are shown in Figure 1.9 [Ye06]. They agree with the model calculations [Ell06] shown in the same Figure, which have been calculated for various values of J_u. Based on u-quark dominance the d-quark total angular momentum has been assumed to be zero. Since it was realized that the model calculations are largely insensitive to all model parameters but J_u and J_d, it

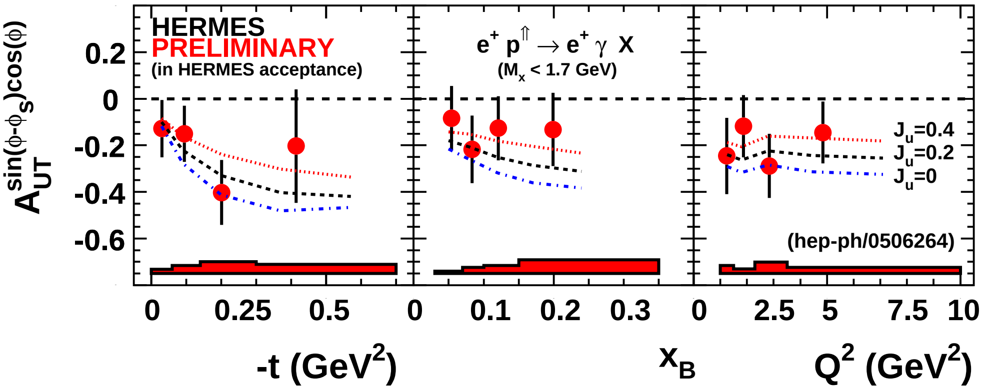

Figure 1.9: The $\sin(\phi - \phi_S)\cos\phi$ amplitude [Ye06] of the transverse target spin asymmetry as a function of $-t$, x_{Bj} and Q^2 in comparison to theoretical predictions from [Ell06].

is possible to constrain J_u and J_d [Ell06, Ye06].

Based on Figure 1.8, the set with the Regge-inspired t-dependence and without a contribution of the D-term (solid line in the Figure 1.8) have been chosen in order to determine the parameter space allowed for J_u and J_d [Ye06]. For different values of J_u and J_d these sets have been compared to the DVCS TTSA data shown in Figure 1.9, leading to a first model dependent constraint on J_u versus J_d shown in Figure 1.10 [Ye06]. The area in the (J_u, J_d)-plane, in which the reduced χ^2 value is not larger than one, is defined as the one standard deviation constraint on J_u vs J_d [Ye06]. It is obtained to be

$$J_\mathrm{u} + J_\mathrm{d}/2.9 = 0.42 \pm 0.21 \pm 0.06 \tag{1.19}$$

(Figure 1.10). The first uncertainty is due to the experimental uncertainty in the measured TTSA amplitude. The second one is a model uncertainty, obtained by varying from one to infinity the unknown profile parameter b which controls the skewedness dependence of GPDs [Goe01].

A model-dependent constraint on the total angular momenta of u-quarks and d-quarks, J_u and J_d, is obtained which provides the first constraint on the total angular momentum of quarks in the nucleon. However the work is still in progress. Further improvement can be expected, taking into account that the GPD H and therefore the available theoretical models will be well

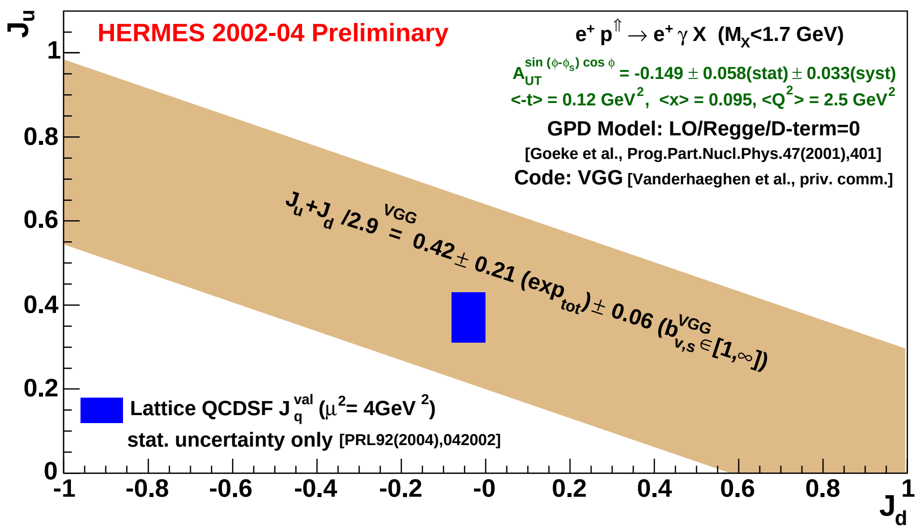

Figure 1.10: Model dependent constraint on the quark orbital angular momenta J_{u} and J_{d}. The theoretical calculation is done with the VGG code [Van01b]. Also shown is a result from the QCDSF collaboration [Göc01]. The work is still in progress. Figure taken from [Ye06].

constrained by the upcoming HERMES data, and that the data shown here is less than half of the data taken on the transversely polarized hydrogen target.

Chapter 2

The HERMES Experiment at HERA

The HERMES (HERa MEasurement of Spin) Experiment is located at the Deutsches Elektronen SYnchrotron (DESY) in Hamburg, Germany. Designed to investigate the spin structure of the nucleon, HERMES measures scattering reactions from polarized lepton beams on polarized or unpolarized fixed gas targets of various types. Scattered leptons and particles produced in deep inelastic lepton-nucleon interactions are detected and identified by a forward spectrometer with large momentum and solid angle acceptance, presented in detail in Section 2.3.

2.1 *The Polarized Electron Beam at HERA*

HERMES is situated in the east experimental hall of the HERA (Hadron-Electron Ring Anlage) collider ring, which has a circumference of 6.3 km. The collider consists of two storage rings with counter-rotating beams of protons and leptons. The proton beam has an energy of 920 GeV and the lepton beam an energy of 27.6 GeV. HERMES makes only use of the lepton beam. HERA can run with both electrons and positrons. For simplicity throughout the whole thesis electrons are used for both lepton species.

The HERA electron beam consists of individual bunches, which have a length of 27 ps and are separated by 96 ns. The average beam current at injection is up to 40 mA and then decreases exponentially, due to interactions with residual gas, with a beam life time of about 10 - 15 hours. The electron beam is initially unpolarized when it is injected into the HERA ring. However a transverse polarization of the electron (positron) beam anti-parallel (parallel) to the magnetic dipole builds up naturally through the Sokolov-Ternov effect [Sok64]: the circular motion of the electrons accelerated in a synchrotron causes the charged electron to emit synchrotron radiations; the emission of synchrotron radiation sometimes causes the electron to flip their spins, resulting in a beam which has a transverse polarization. The beam polarization rises exponentially with time:

$$P(t) = P_{max}(1 - e^{-t/\tau})$$

where t is the time elapsed since the injection of the beam into the accelerator ring and τ is the so-called *build up* time, the time taken to reach $(1 - \frac{1}{e}) \approx 64\%$ of the maximum possible polarization P_{max}. For an ideal machine without any depolarizing effects, the maximum achievable polarization is $P_{th} = 0.924$ [Lor97]. For the (ideal) HERA storage ring, operating at an energy $E = 27.6$ GeV, the theoretically expected value τ_{th} is 37 min. In a realistic storage ring depolarizing effects can, however, substantially reduce the maximum achievable polarization. The depolarizing effects also affect the actual rise time, which scales with P_{max} according to

$$\tau = \frac{P_{max}}{P_{th}} \cdot \tau_{th} \quad .$$

Thus for a typical asymptotic beam polarization $P_{max} = 0.55$, the rise time is about 22 min. Precise alignment of the machine quadrupoles and fine tuning of the orbit parameters is needed to achieve high polarization.

Based on the fact that the magnetic moment (spin) of charged particles precesses in a magnetic field, the transverse polarization of the beam can be rotated into the longitudinal direction. Such a rotation is performed by a spin rotator consisting of interleaved horizontal and vertical bending magnets [Buo86]. A pair of spin rotators is installed up- and downstream the HERMES experiment[1]. The upstream spin rotator rotates the direction of the beam polarization into the beam direction, while the downstream one rotates the direction of the beam polarization back into the vertical direction. Figure 2.1 shows a schematic diagram of the layout of the HERA facility as

---

[1] During the high luminosity upgrade of HERA in the years 2000-2001, two additional sets of spin rotators were installed for the H1 and ZEUS experiments.

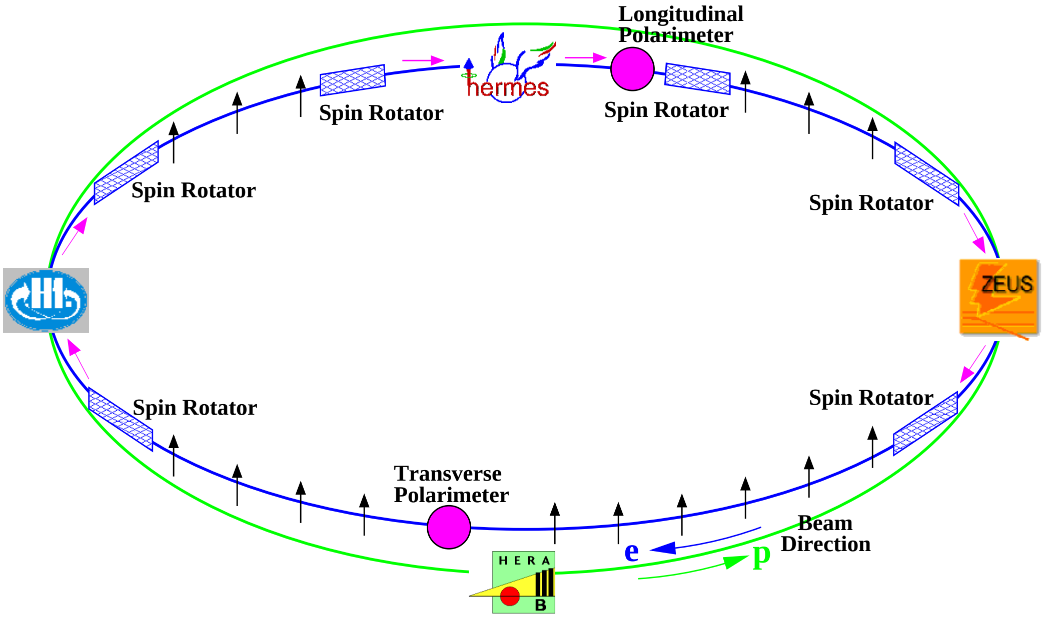

Figure 2.1: Schematic overview of the HERA collider ring at DESY, indicating the four experimental areas. The positions of the spin rotators for the electron beam is shown as well as the positions of both transverse and longitudinal polarimeters. The arrows denote the direction of the electron beam polarization.

well as the locations of the spin rotators. With this system longitudinal electron polarization has been achieved for the first time in 1994 in a high energy storage ring [Bar95]. Since then, the polarization direction has been reversed typically every few months by moving the magnets of the spin rotators.

The polarization of the electron beam is continuously monitored by two polarimeters (Transverse and Longitudinal Polarimeters, see Figure 2.1 for their location) which utilize the spin dependent cross section for Compton scattering of circularly polarized laser photons on the stored electrons. Transverse beam polarization leads to a small up-down spatial asymmetry of the back-scattered photons with respect to the orbital plane of the electrons for the two helicity states of the laser beam. Energy and vertical position of individual Compton photons are measured with the Transverse Polarimeter [Bar93] in the HERA West section. For 100% electron polarization the center of gravity of the vertical position of the Compton photons on the calorimeter, which is located 65 m behind the interaction point of the laser beam

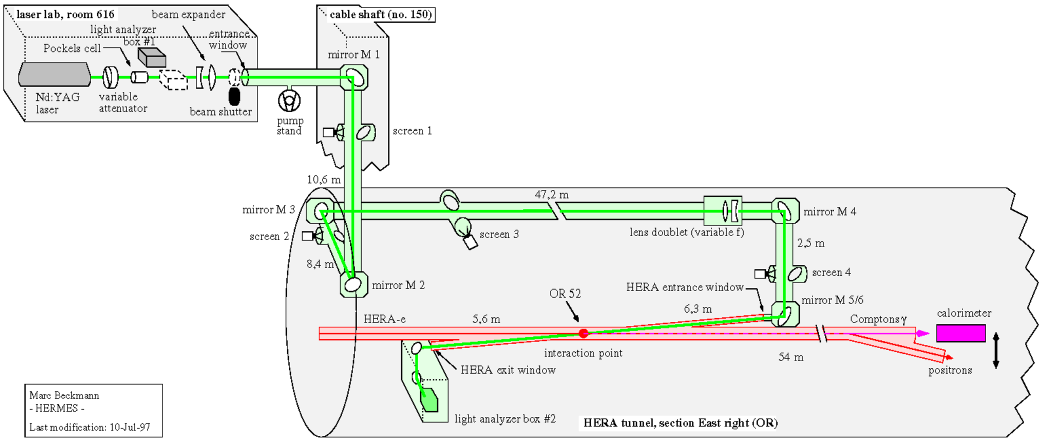

Figure 2.2: Schematic layout of the Longitudinal Polarimeter and its components.

and the electron beam, shifts by about 0.3 mm. Longitudinal beam polarization modifies the energy dependence of the cross section. The corresponding asymmetry in energy deposition of the back-scattered photons for the two helicity states of the laser photon beam is measured with the Longitudinal Polarimeter [Bec02] in the HERA East section, downstream of the HERMES experiment. This polarimeter normally works in the multi-photon mode: it measures the total energy deposited in the detector by $10^3 - 10^4$ Compton photons per bunch and also allows to measure the polarization of individual bunches. The schematic layout of the Longitudinal Polarimeter is shown in Figure 2.2. A measurement of the beam polarization to an absolute statistical accuracy of 0.01 requires typically one minute, the fractional systematic uncertainty of the Transverse Polarimeter is 3.4% [Bar93], and that of the Longitudinal Polarimeter 1.6% [Bec02]. A typical rise-time curve, measured simultaneously with both polarimeters is shown in Figure 2.3. The polarization quickly rises at the beginning and stays stable for the entire length of the data taking.

Longitudinal polarization was routinely obtained in the range 40% - 65% in the years 1995-2000. Due to the high luminosity upgrade of HERA in the years 2000-2001, longitudinal polarization of the beam was very low in the year 2002 but went back to between 40% and 55% in the years 2003-

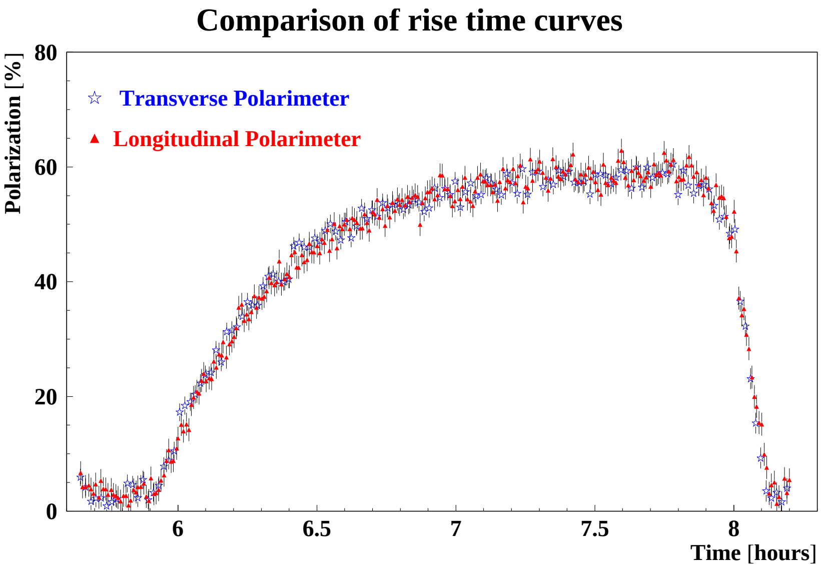

Figure 2.3: Polarization of the HERA electron beam.

2007.

2.2 *The HERMES Internal Gas Target*

The HERMES experiment uses a gas target internal to the storage ring. The gas enters a thinwalled cooled storage cell consisting of an open-ended elliptical tube made of ultra-pure aluminium with a uniform wall thickness of 75 μm. The target cell used between 1994 and 2005 had a length of 400 mm which optimized the performance with the polarized Atomic Beam Source (ABS)[2]. In 2006 the cell design was changed for the unpolarized running with the Recoil Detector, presented in Chapter 3. This cell was only 150 mm long and is shown in Figure 2.4.

Either polarized atoms or molecules are injected into the center of the target cell. The atoms diffuse to the ends of the target where they leak out and are pumped away by a high speed differential pumping system. A set of movable and fixed collimators is used to protect the target cell and the spectrometer from synchrotron radiation.

---

[2] The ABS [Nas03] supplied the target cell with polarized hydrogen or deuterium atoms.

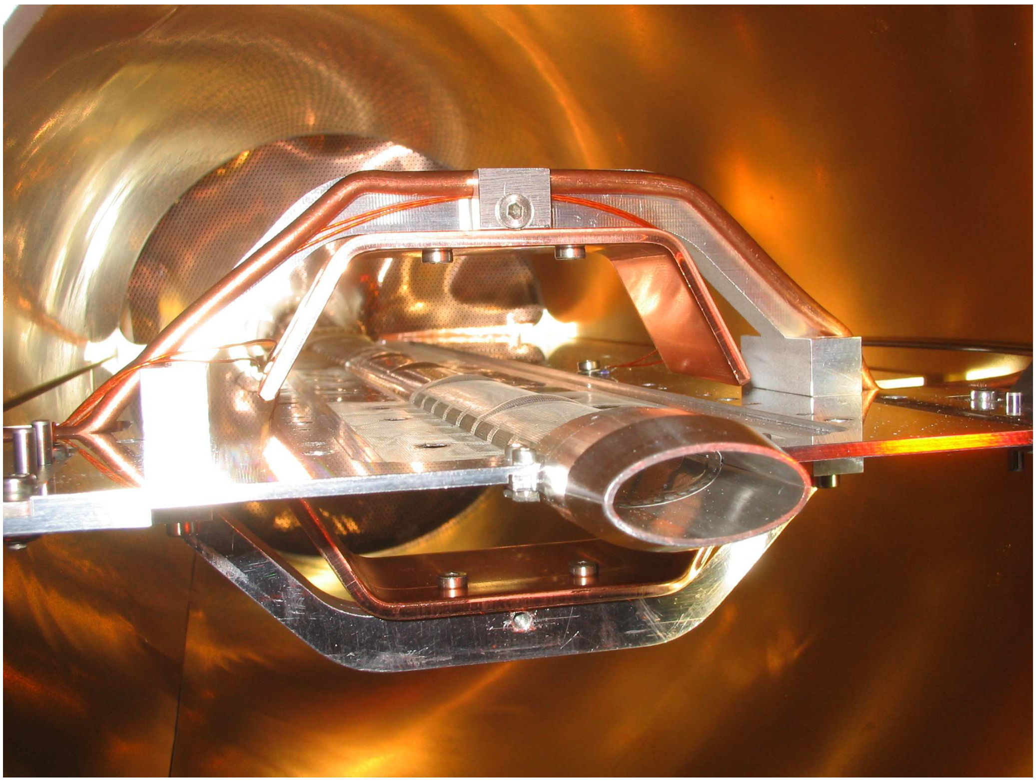

Figure 2.4: Upstream end of the HERMES target cell used for the unpolarized running. The beam enters the elliptical tube opening into the page.

Until 2005, the target could be operated in two modes: injecting polarized hydrogen/deuterium or a variety of unpolarized gaseous targets like hydrogen, deuterium, helium, nitrogen, krypton, neon and xenon. For the final data taking period the polarized target, consisting of the ABS, a Breit-Rabi Polarimeter (BRP) and a Target Gas Analyzer (TGA)[3], was removed to install the Recoil Detector.

For **unpolarized operation** (the only one available since 2006) the target gas is inserted into the storage cell by the Unpolarized Gas Feed System (UGFS). Typical target densities of $10^{15} - 10^{17}$ nucleons/cm^2 can be achieved with the UGFS, restricted ultimately by the deadtime of the HER-

---

[3] The BRP [Bau02] measured the atomic polarization of the gas sampled from the cell. The TGA [Bau03] measured the degree of dissociation of the target gas with a quadrupole mass spectrometer. Until 2000 a longitudinal target polarization was maintained, which then was changed to a transversely one.

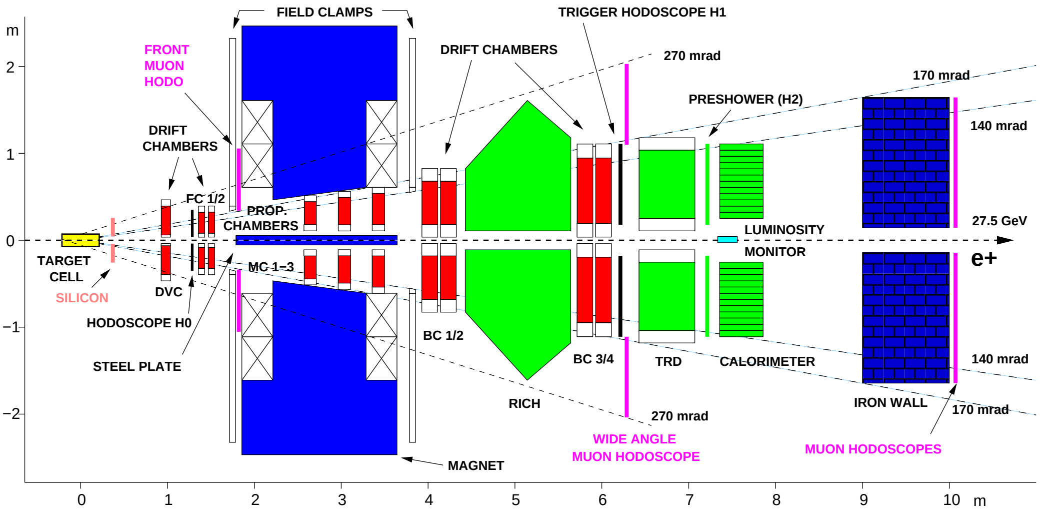

Figure 2.5: Schematic drawing of the HERMES spectrometer without the Recoil Detector. The tracking system (DVC, FC, MC, BC) is shown in red, the PID detectors (RICH, TRD, CALO) in green. The electron beam enters the spectrometer from the left, first traversing the target cell (yellow) and continuing along the symmetry axis of the top and bottom half of the spectrometer defining the z-axis of the HERMES coordinate system. Furthermore, the acceptance of the spectrometer and the back tracking system in the vertical direction is indicated which is the y-axis in HERMES coordinates. Finally, the x-axis of the HERMES coordinate system points into the plane.

MES Data Acquisition, increasing current in the HERMES front region due to Møller-Bhabha electrons. Only unpolarized Hydrogen targets will be used for the analysis in this thesis.

2.3 *The HERMES Spectrometer*

A schematic side view of the HERMES spectrometer [Ack98] is shown in Figure 2.5. It is a forward spectrometer with a dipole magnet surrounding the electron and proton beam pipes, providing an integrated field of 1.3 Tm. The magnet gap is divided into two identical sections, *top* and *bottom*, by a horizontal septum plate that shields the electron and proton beams from the spectrometer's magnetic field. Consequently, the spectrometer is constructed as two identical halves, mounted above and below the beam pipes. Both beams go through the spectrometer, separated by 72 cm. The HERMES coordinate system has the z axis pointing along the beam direction, the x axis horizontal and pointing outside the HERA ring and the y axis vertically upwards. Scattered electrons and hadrons produced in the inelastic reactions can be detected and identified within an angular acceptance ±170 mrad horizontally and ±(40-140) mrad vertically. Track reconstruction is provided by the spectrometer's Front drift Chambers (FC), Drift-Vertex Chambers (DVC), Back drift Chambers (BC) and proportional Magnet Chambers (MC) which also help match tracks in the forward and backward regions after deflection by the magnetic field. The spectrometer also possesses several instruments which provide particle identification (PID). These are the Transition Radiation Detector (TRD), a Ring Imaging Cherenkov (RICH) Detector and a preshower detector (H2). Additional PID is provided by the electromagnetic calorimeter (CALO) which also provides an energy measurement for electrons and photons. The standard HERMES trigger for DIS events is provided by a combination of the hodoscopes H1, H2 and the CALO which makes the decision of whether to run the trigger system as an electron or hadron trigger, depending on the energy deposition. Luminosity is determined by a dedicated monitor (LUMI) which detects Møller and Bhabha scattering events from the beam-target interaction. The whole spectrometer, apart from the target and the muon wall, is mounted on a movable platform to allow access to the HERA tunnel in case of major repairs or replacement of accelerator components. The total length is restricted to about 8 m and all the detectors are very tightly packed.

2.3.1 *Tracking System*

The HERMES tracking system consists of drift chambers in front of and behind the spectrometer magnet and proportional chambers mounted inside the magnet opening. All chambers measure the horizontal coordinate x with a plane of vertical wires (X-plane) and two coordinates u and v with wire planes which have their wires titled by ±30° (U-plane, V-plane) with respect to the wires in the X-plane (Figure 2.6). Each drift chamber consists of six layers of drift cells, where each layer is constructed of a plane of alternating anode and cathode wires between the cathode foils, while the foils belong to the neighboring cell as well, if there is one. Two consecutive planes have

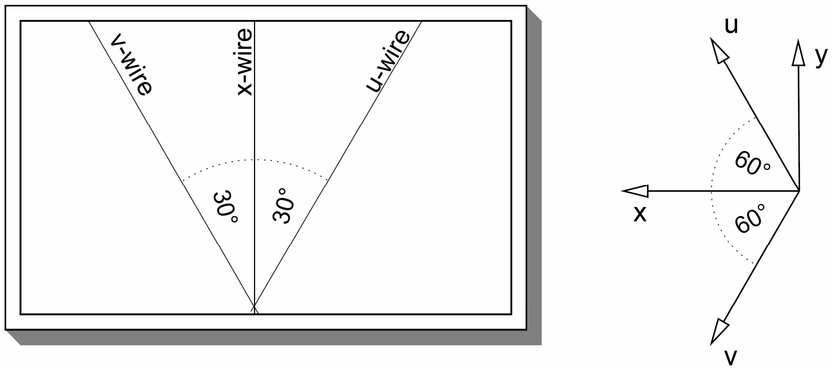

Figure 2.6: Drift chamber wiring scheme and the direction of their projections x, u and v. z points along the beam direction [Wan96].

the same wire inclination, while their drift cells are staggered by half a cell width to avoid left-right ambiguities (configuration XX' UU' VV'). The DVCs [Blo99] help to increase the redundancy of the tracking system in the front region and have a larger geometrical acceptance than the other detectors extending vertically from ±35 mrad to ±270 mrad and covering ±200 mrad horizontally, mainly to increase the efficiency for the detection of events from charmed particle decays. The width of the drift cell is 6 mm and the total number of wires is 1088. The non-flammable gas mixture is the same as for all the other drift chambers: $Ar/CO_2/CF_4$ (90%/5%/5%), the spatial resolution per plane (σ) is 220 μm.

The FCs [Bra01] provide good spatial resolution immediately in front of the magnet. They are drift chambers with a cell width of 7 mm, resulting in 2304 channels. The measured spatial resolution per plane is 225 μm.

The MCs [And01] are multiwire proportional chambers with a spacing of the read-out wires of 2 mm and a corresponding resolution per plane of 700 μm. They are located in the gap of the magnet and were originally intended to help resolve multiple tracks in case of high multiplicity events and to improve track reconstruction in case of missing planes in the front region. Since low background and good performance of the front detectors have made this unnecessary, their primary function is now the momentum analysis of relatively low energy particles from the decay of Λ hyperons or K_S mesons, for example. Each module has three planes of the configuration

XUV; the total number of channels is 11008 and the gas mixture used is $Ar/CO_2/CF_4$ (65%/30%/5%).

The BCs [Ber95, Ber98] are drift chambers with a cell width of 15 mm. The active areas of the chambers are chosen according to their z-position and the acceptance of the spectrometer, resulting in 7680 channels. The measured resolution per plane is in average $\sim$285 μm with a minimum of about $\sim$230 μm in the middle of the drift cell.

Alignment of all tracking detectors is achieved by special alignment runs in which the magnet is switched off and the straight particle tracks are used to align front and back chambers with respect to each other. An efficient reconstruction code (HRC)[4] using a tree-search algorithm is employed to allow for a very quick determination of particle tracks from a given set of detector hits, which is possible due to the similar layout of each drift chamber. Afterwards each track is reconstructed under the assumption that front- and back-partial track have to form a continuous curve (forced-bridging). The momentum of a particle is then calculated from its deflection in the magnetic field, which provides also the particle charge. The achieved momentum resolution was between 0.7 and 1.25% over the entire kinematic range of the experiment [Ack98] before the installation of the RICH detector in the beginning of 1998 and is between 1.5 and 2.5% since then [Air05]. The uncertainty in the scattering angle is smaller than 0.6 mrad.

2.3.2 *Particle Identification System*

The HERMES spectrometer provides an excellent electron-hadron separation (contamination less than one percent) using four PID detectors: the RICH detector, the TRD, the preshower H2 and the CALO. Each of these four detectors is able to differentiate between hadrons and electrons, however each detector varies with regard to its relative effectiveness to do so. In order to improve the separation of hadrons from electrons, the hadron-electron identification for each of the four detectors is combined. The RICH, designed for the separation of pions, protons and kaons, contributes to the electron-hadron separation only for particles with energies below about 4 GeV. Since this analysis deals with particles with higher energies only, the RICH is not

---

[4] HERMES Reconstruction Code.

used and is therefore not described any further. For a detailed description see [Asc00, Ako02].

The Transition Radiation Detector

Transition Radiation (TR) is emitted by charged particles that cross a boundary between two media which have different dielectric constants. Usually TR belongs to the X-ray region of the electromagnetic spectrum. The probability for a particle to emit a photon per interface is approximately $\frac{2}{3}\alpha$, where $\alpha = 1/137$ is the fine structure constant. In the ultra-relativistic regime, the mean energy W of the emitted TR caused by the passage of a particle i from vacuum into a medium with plasma frequency ω_p depends linearly on $\gamma = E_i/M_i$ [Art75]:

$$W = \frac{2}{3}\alpha\omega_P\gamma. \tag{2.1}$$

The plasma frequency in a material is a function of its electron density n_e:

$$\omega_P = 4\pi\alpha\frac{n_e}{M_e} \tag{2.2}$$

where M_e is the rest mass of the electron. Since γ is much higher for electrons than for hadrons, the dependence of the TR energy yield on γ is a useful property for differentiating between electrons and hadrons.

From Expressions 2.1 and 2.2 it can be shown that the optimal radiator material should have a high electron density. In order to increase the probability of TR emissions in the HERMES TRD, multiple boundaries are necessary. The material should also be highly transparent to the X-rays. These requirements are satisfied by a polypropylene radiator. The choices of fibre thickness (17 - 20 μm) and packing density (0.10 g/cm^3) of this porous material are optimized for the electron energy range of the experiment. The bulk thickness of the radiator is limited by the X-ray absorption and is chosen to be 6.5 cm.

In addition to the radiator described above, the HERMES TRD contains planar proportional wire chambers as X-ray detectors (there are a total of 12 MWPCs). For optimal X-ray absorption, a high Z gas is required. For this reason the wire chamber is filled with a mixture of Xenon (90%) and CH_4 (10%) gas. CH_4 is used as a quenching agent to control the electron multiplication in the chamber.

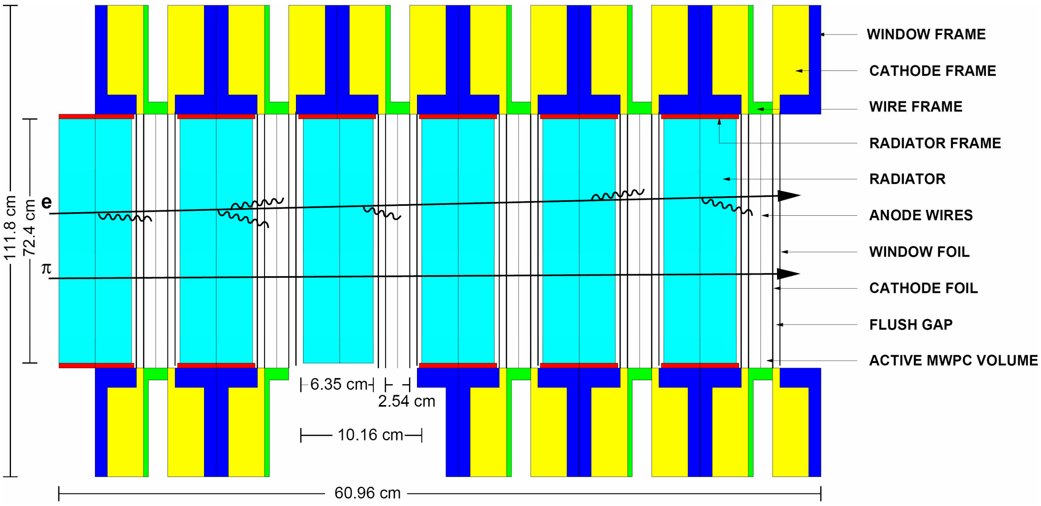

Figure 2.7: Schematic view of the TRD.

A radiator and a wire chamber constitute one module of the TRD. Each half of the detector consists of 6 such modules used in succession (Figure 2.7). When particles ionize the medium, secondary high energy electrons are frequently produced. These are known as δ-rays and constitute the background to the TRD signal. Use of several modules in succession permits a module by module comparison of energy deposition, which in turn allows the elimination of the majority of the δ-rays. A truncated mean method may be used for illustration: since δ-rays are characterized by high energy deposition the module with highest energy deposition is excluded from the calculation of the mean value of energy deposition for each hit. As shown in Figure 2.8, the use of the 6 modules and the truncated mean method improves the electron-hadron separation.

The Preshower Detector

Energy loss per unit thickness dE/dz is significantly higher for electrons than for hadrons: in addition to collisions with electrons within the material, a significant portion of the energy is lost through radiation [Leo94]. At HERMES energies where the radiative energy loss dominates, the radiated photons are sufficiently energetic to produce e^+ e^- pairs. These pairs also radiate, with

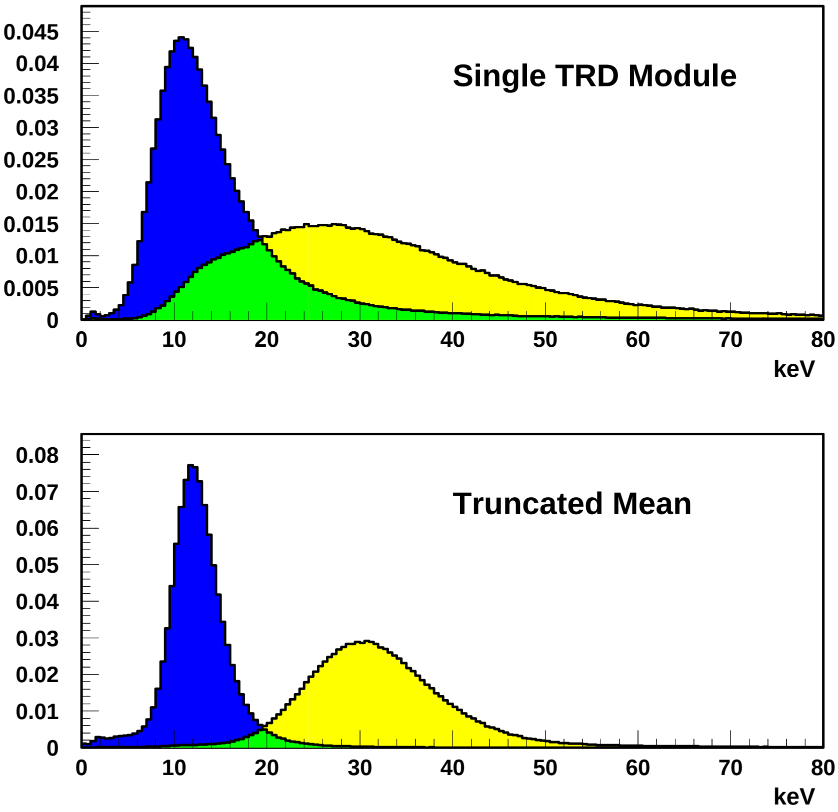

Figure 2.8: Response of the TRD detector for a single module and with the truncated mean. Light (yellow) and dark (blue) shading represents electron and hadron distributions respectively. The intermediate shading (green) represents the region where the two distributions overlap [Kai97].

subsequent pair production. Rapid multiplication of the numbers of electrons and positrons occur and an electromagnetic shower is produced. With a sufficiently thick material of high Z it is possible to use the high dE/dz for electrons to initiate an electromagnetic shower. This principle is used in the H2 at HERMES which consists in each detector half of 42 vertical 1 cm thick scintillator paddles with an area of 9.3×91 cm^2. The paddles are staggered with an overlap of 2-3 mm to avoid insensitive areas between them. Each scintillator is optically coupled via a light guide to a photomultiplier at the outside of the detector (Figure 2.9).

The preshower detector consists of the hodoscope H2, preceded by a 11 mm thick lead shield (two radiation lengths) which causes the majority of

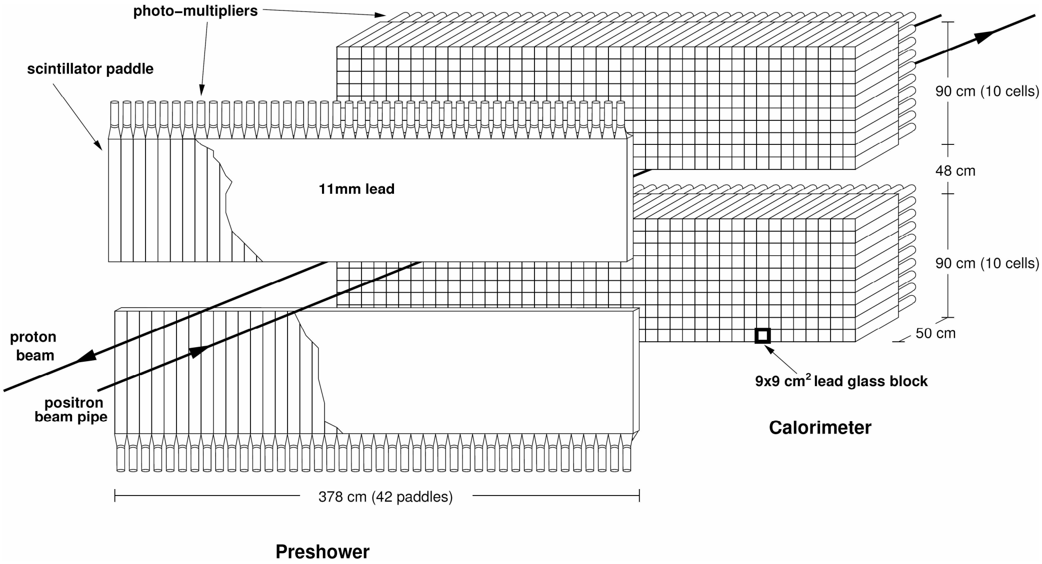

Figure 2.9: Schematic drawing of the lower half of the preshower and calorimeter detectors. The preshower detector is preceded by a 1.1 cm thick lead shield causing electrons and photons to start electromagnetic showers. The calorimeter consists of lead-glass blocks with a front area of 9 × 9 cm^2 and a length of 50 cm corresponding to about 50 radiation lengths.

electrons and photons to produce electromagnetic showers before entering the CALO. The electron-hadron separation is based on the fact that electrons, in contrast to hadrons, have a very high probability to produce electromagnetic showers and thus deposit more energy in the scintillators than hadrons which mostly lose energy by ionization only. The response of the preshower detector is shown in Figure 2.10.

It is important to note that photons can produce electromagnetic showers as well, and thus the preshower, besides the CALO, is the only detector capable of detecting photons. However, it does not provide a measurement of the energy or position of the photon.

The Electromagnetic Calorimeter

The HERMES CALO (Figure 2.9) contains 420 cells in each half of the detector. The cells, which are square in cross section, are constructed from a glass made of 51.23% Pb_3O_4, 41.57% SiO_2, 7% K_2O and 0.2% Ce in weight

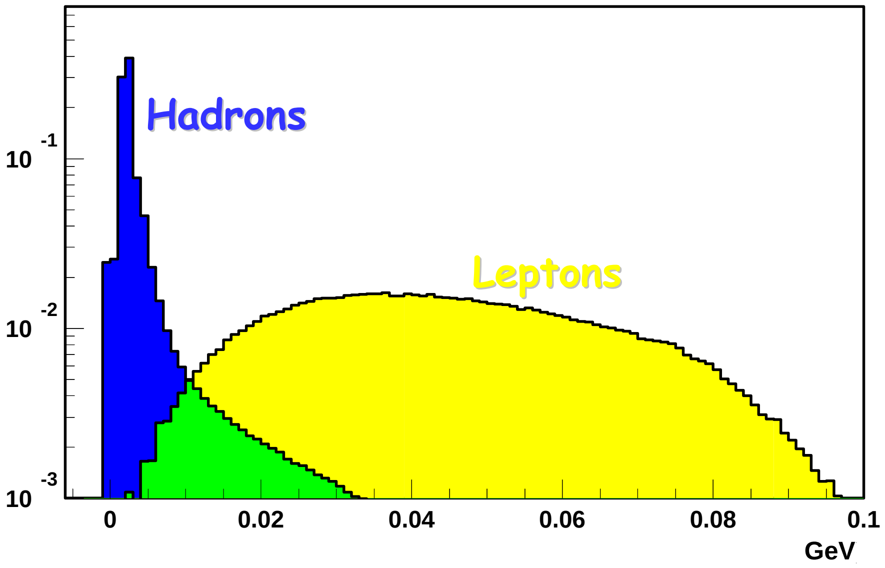

Figure 2.10: Normalized response of the preshower detector. Light (yellow) and dark (blue) shading represents electron and hadron distributions respectively. The intermediate shading (green) represents the region where the two distributions overlap.

proportions. They were polished, wrapped with 50 μm thick aluminized mylar foils, and covered with a 125 μm thick tedlar foil to provide light isolation. The glass blocks have a radiation length of 2.78 cm and an index of refraction of 1.65 [Fan96]. With cell dimensions of $9 \times 9 \times 50$ cm^3, each cell is 18 radiation lengths thick. As the shower is quenched in the cells, particles emit Cherenkov radiation which is detected by the PMT tubes. Each cell is coupled to a photomultiplier tube thereby forming a total of 840 channels. Due to the fact that showers may extend over adjacent cells the measurements are summed over a 3×3 block array with the center of the shower in the middle of the block with the most energy.

The discrimination between electrons and hadrons of the CALO is based on the different topologies of electromagnetic and hadronic showers. Hadronic showers typically start much later and spread much wider than electromagnetic showers. With the chosen size of the lead-glass blocks, more than 99% electromagnetic shower energy is contained in a matrix of 3×3 blocks (defined as a cluster), while a large part of the hadronic shower energy leaks out of

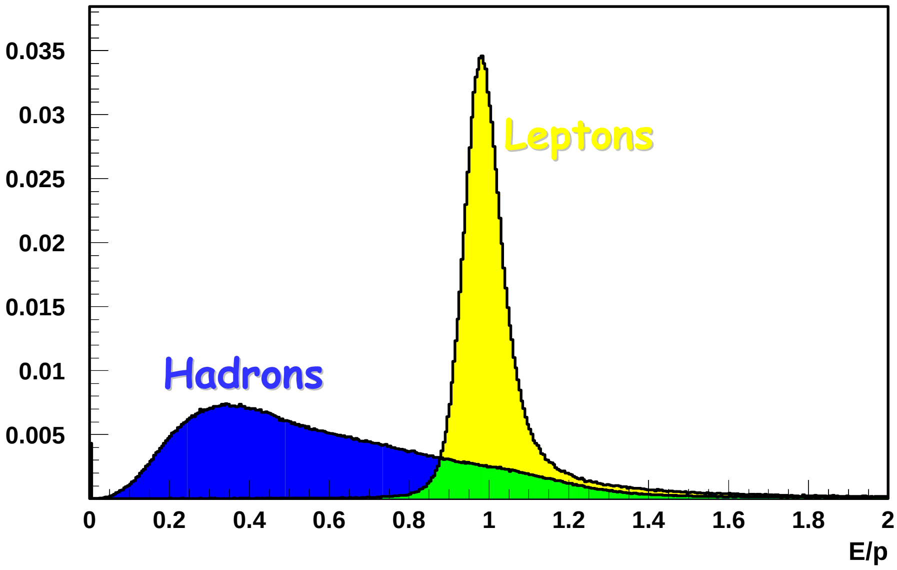

Figure 2.11: Normalized response of the CALO. Light (yellow) and dark (blue) shading represents electron and hadron distributions respectively. The intermediate shading (green) represents the region where the two distributions overlap.

the CALO. A valid PID parameter is the ratio of the detected shower energy E_{calo} in the nine-block cluster to the momentum P of the incident particle measured by the tracking chambers. This ratio (E_{calo}/P) is typically unity for electrons and photons and less than unity for hadrons, allowing a good degree of separation between the two (Figure 2.11).

The energy resolution of the CALO for scattered electrons can be described by the following parametrization [Ava98]:

$$\frac{\sigma(E)}{E}[\%] = \frac{5.11 \pm 1.1}{\sqrt{E(GeV)}} + (2.0 \pm 0.5) + \frac{10.0 \pm 2.0}{E(GeV)} \quad .$$

Impact positions of electrons and photons in the CALO can be obtained from the energy distribution inside the nine-block cluster. It can be calculated by the following energy-weighted average position of the cluster:

$$\begin{aligned} x &= \frac{\sum_{i=1}^{9} x_i \sqrt{E_i}}{\sum_i \sqrt{E_i}} \\ y &= \frac{\sum_{i=1}^{9} y_i \sqrt{E_i}}{\sum_i \sqrt{E_i}} \end{aligned}$$

where x_i and y_i are the central coordinates of the i-th block, and the square root of the corresponding energy, $\sqrt{E}_i$, is used as the weight w_i. The position resolution can be evaluated by checking the difference between the positions of scattered electrons obtained in this way and the positions reconstructed from the tracking chambers [Ava98]. The above position reconstruction algorithm does not account for the exponential shape of the lateral shower profile and has been found to lead to a bias of several centimeters [Ely02]. An alternative algorithm, which uses a logarithmic weight, $w_i = max\{0, 4.8 + ln(E_i = E)\}$, improves significantly the resolution to approximately 0.5 cm [Ell04].

There is no separate energy reconstruction method for electrons and photons, i.e., it is assumed that the shower development is at least similar. This is probably true for photons which convert into lepton pairs in the preshower and thus, like most of the electrons, start the electromagnetic shower before reaching the CALO. Photons which do not convert in the preshower will most likely start the shower inside the CALO, i.e., much later. This might lead to a reduced loss of light due to attenuation in the CALO and thus to an increased signal in the photomultipliers resulting in an overestimated photon energy.

PID System Performance

The responses of the three PID detectors described above are combined to provide good hadron rejection. Using a probability based approach, the quantity PID_2 defined as

$$\text{PID}_2 = \log_{10}\left(\frac{P^e_{Cal}P^e_{Pre}}{P^h_{Cal}P^h_{Pre}}\right) \quad ,$$

where P^i_j is the probability that a particle of type i produced a given response in detector j. The P^i_j are determined by comparing the detector responses for each track to typical response function for each detectors. Such functions are referred to as parent distributions [Ack98]. Combining PID_2 with the TRD response, yields are very good hadron-electron separation (better than 98% with a contamination of less than 1%, Figure 2.12) with a clean electron sample at positive PID_2 values and large TRD signals.

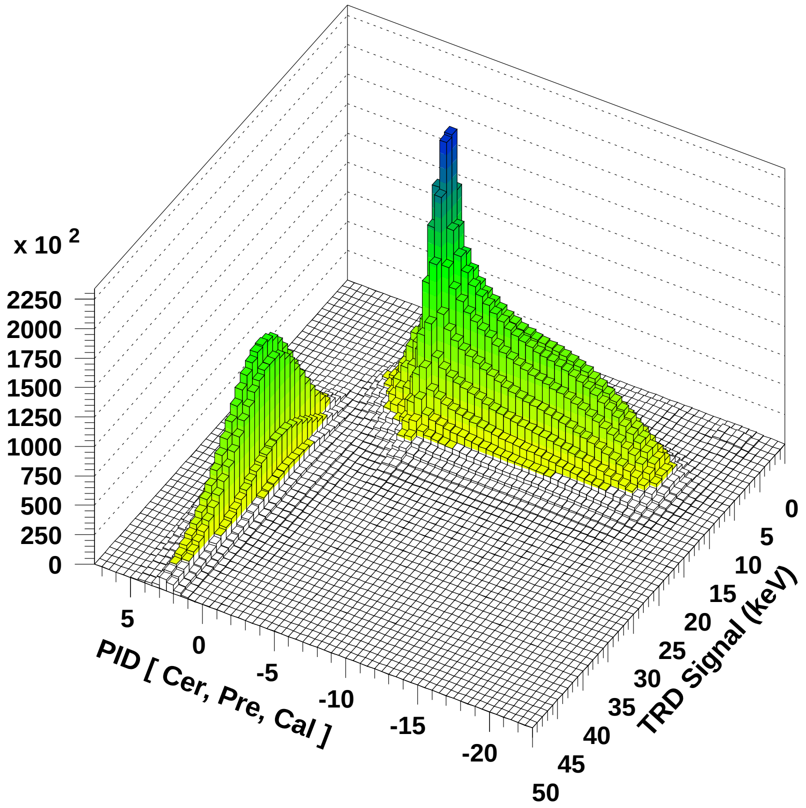

Figure 2.12: Hadron and electron separation achieved with HERMES PID detectors. Electrons appear at positive PID_2 and large TRD signal values.

2.3.3 *Luminosity Monitor*

In order to do absolute measurements of e.g. cross sections, and to be able to compare data sets of different years or polarizations, it is very important that the luminosity is determined precisely. In HERMES this is done either by counting the number of DIS events in a data set, or by using the luminosity monitor [Ben01]. Determining the luminosity can be done using a well known physics process, with a sufficiently high cross section to keep both systematic and statistic error low. An example of such process is the elastic scattering of beam particles off electrons from the target gas. In the case of an electron beam the process is called Møller scattering ($e^-e^- \rightarrow e^-e^-$), for a positron beam the process is referred to as Bhabha scattering ($e^+e^- \rightarrow e^+e^-$). An additional reaction which can be used in the case of a positron beam is the

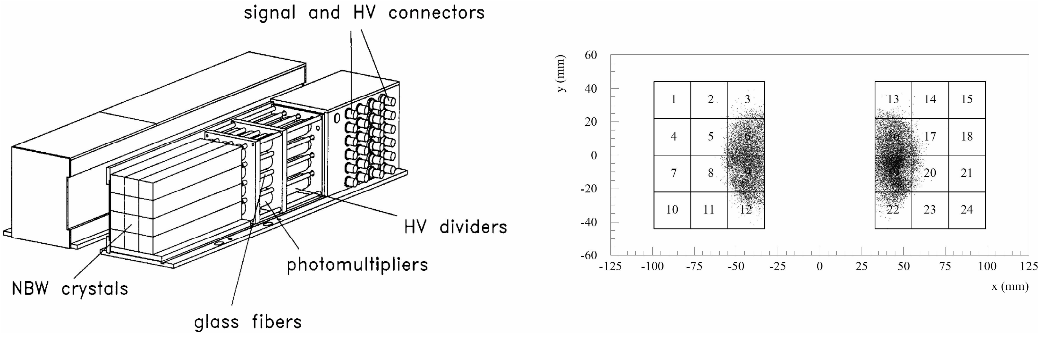

Figure 2.13: Schematic view of the luminosity monitor. On the right a front view with the reconstructed impact points from elastic scattering can be seen. The elliptical beam profile is well reflected

annihilation of an electron and positron into a pair of photons. All these reactions have small scattering angles and leave both particles with a similar amount of energy.

The luminosity monitor is built out of two symmetrical halves positioned on the left and right from the HERA electron beam pipe. Each halve is built out of 12 $NaBi(WO_4)_2$ Cherenkov crystals, each with dimensions $2.2 \times 2.2 \times 20$ cm^3. The blocks are read-out by photomultipliers. Due to high radiation doses during beam injection and acceleration, the luminosity monitor was placed on a movable table allowing it to be moved in position right before data taking. When a physics run is about to be finished, the luminosity monitor is moved back into a position where it is safe from synchrotron radiation. A schematic view of the luminosity monitor can be seen from Figure 2.13. The luminosity monitor has its own dedicated read-out scheme. This scheme allows a dead time free operation of the luminosity monitor.

Since the luminosity monitor is positioned outside of the standard HERMES acceptance, it requires its own dedicated trigger in order to select desired processes. Most background events will deposit energy in only one side of the luminosity monitor, while Bhabha or Møller events will have an equal energy deposition in both halves. Triggering occurs when signals in both luminosity detector halves exceed a 4.5 GeV threshold. The motivation for this choice can be seen in Figure 2.14. The absolute luminosity is then given

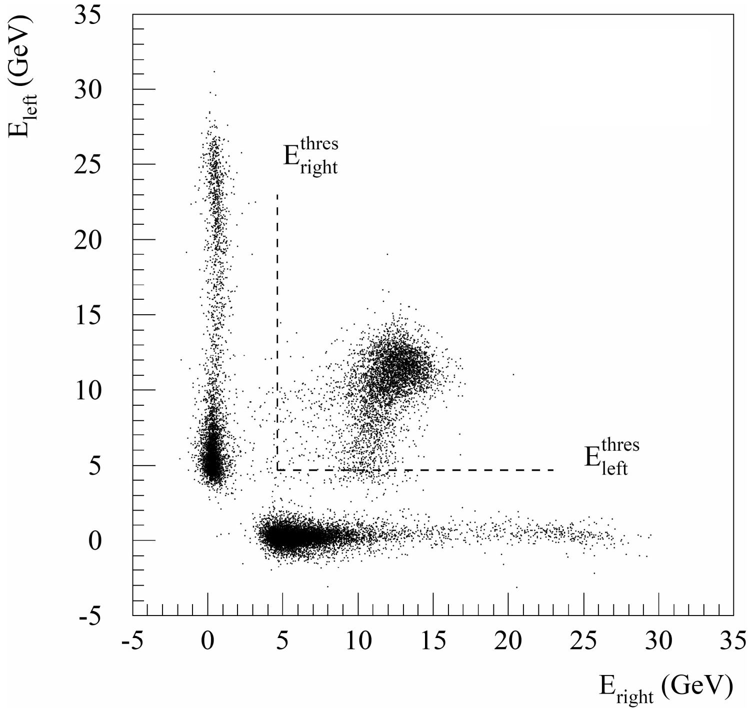

Figure 2.14: Energy deposited in the left luminosity monitor halve versus the right luminosity monitor halve. The trigger threshold is indicated in the figure. Energies of both halves add up to about 27.5 GeV, the Hera beam energy.

by the measured coincidence rate times the luminosity constant. The latter is obtained from the precisely known Bhabha or Møller cross sections with the knowledge of the detector efficiency and acceptance. The systematic uncertainty for the absolute luminosity measurements is $6.3 - 6.4\%$ and that for the relative luminosity measurements $0.9 - 1.5\%$ [Ben01].

2.3.4 *The HERMES Trigger*

The trigger initiates the read-out of the detector for an event which is considered to be of interest. The main physics trigger (trigger 18 for the top of the spectrometer and trigger 26 for the bottom of the spectrometer) should start the read-out if a candidate DIS event took place. An event is considered a candidate DIS event if the scattered electron traverses one full detector half including detection in the CALO with an energy above a preset threshold. For a fast decision on the particle type and trajectory, the hodoscope H1 is used in coincidence with the preshower and the CALO. H1 is placed directly in front of the TRD in the back region of the spectrometer (Figure 2.5). Its setup is similar to the hodoscopes H2 as described previously in the subsection 2.3.2.

Trigger 18/26 requires the following conditions:

- A signal in H1;
- A signal above the minimum ionizing signal in the preshower to indicate passage of an electron;
- The sum of the signals in two neighboring CALO columns has to be above a certain threshold. The data used in this analysis was collected with thresholds of 1.5 GeV and 3.5 GeV;
- All signals have to arrive in coincidence with the bunch crossing signal from the accelerator. In addition, particles originating from the HERA proton beam and thus entering the spectrometer from the rear are excluded by timing restrictions.

The purity of the DIS trigger is good for a high CALO threshold (3.5 GeV) and acceptable for a low threshold (1.4 GeV). For a 3.5 GeV CALO threshold, two thirds of the triggers have tracks, 95% of reconstructed tracks come from the target and one third has accompanying electrons. For a 1.4 GeV CALO threshold, the physics trigger rate increases by a factor of about 6 while the fraction of DIS electrons only goes up by about 10%. About two thirds of the events have tracks, but only 70% of the tracks come from the target.

Chapter 3

The HERMES Recoil Detector: Benefits and Design

In 2001 the HERMES collaboration decided to build a Recoil Detector around the target cell for detecting recoiling protons and making event identification more exclusive. A description of the recoil sub-detectors will be given, going from the inside out. Moreover in the last Section detector performance, obtained with Monte Carlo simulations, will be presented.

3.1 *Missing Mass Technique for DVCS measurement*

Until 2005 HERMES was not able to unambiguously detect the full final state of the DVCS reaction: the recoiling proton could not be detected and events containing exactly one electron and one photon were selected in order to extract DVCS asymmetries, as discussed in Section 1.3.

A missing mass technique is then employed to extract the sample of exclusive events. For scattering on hydrogen, the missing mass should then be equal to the proton mass M_p if the proton stays intact and the photon is the only particle produced. Otherwise the process exhibits a higher missing mass. The squared missing mass

$$M_x^2 = (q + p - q')^2 \quad ,$$

with q, p and q' (Expressions 1.5 and 1.6) being the four-momenta of the virtual photon, the target nucleon and the real photon, respectively, is cal-

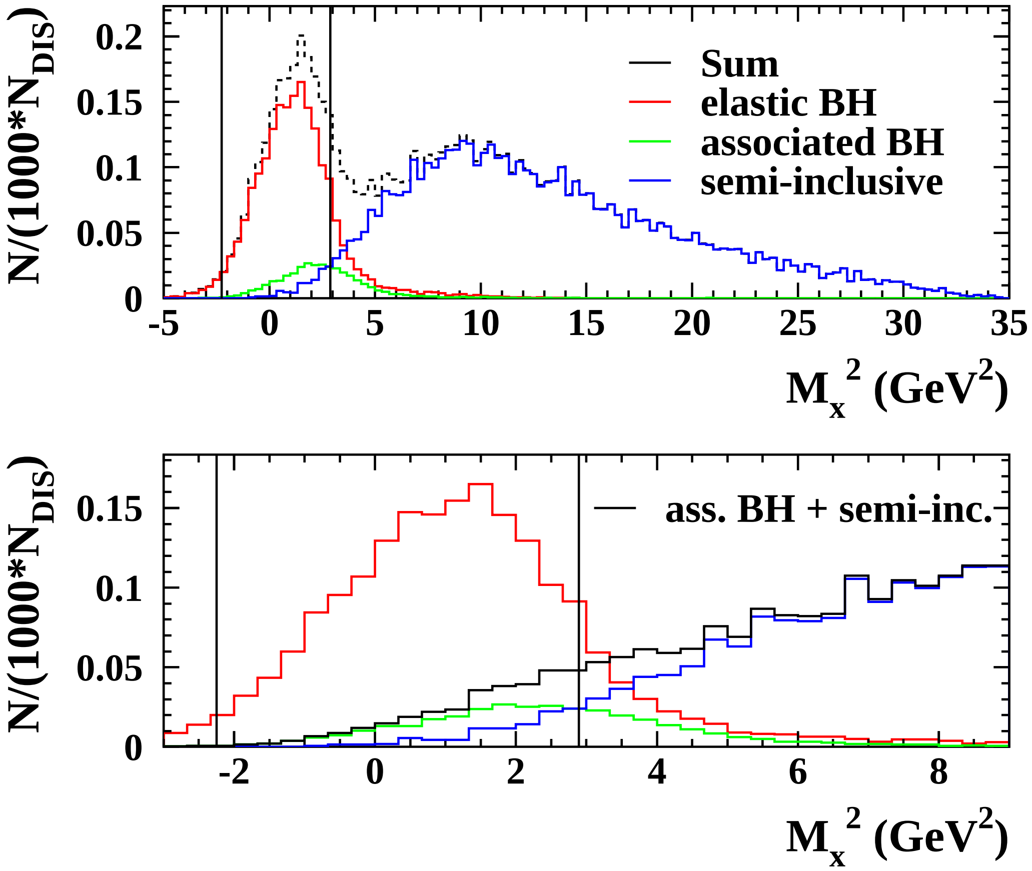

Figure 3.1: Squared missing mass distribution in the full kinematic range (upper panel) and in the small M_x^2 region (lower panel) showing the exclusive and the semi-inclusive area. The different backgrounds leaking into the exclusive region are explained. The vertical lines indicate the exclusive bin (-2.25 GeV^2 $< M_x^2 <$ 2.89 GeV^2). The data sets are normalized to the respective number of DIS events.

culated for every single photon event[1]. Its distribution is shown in Figure 3.1. Due to the limited photon resolution of the HERMES spectrometer the exclusive peak is quite broad (missing mass resolution $\Delta M_x^2 = 1.5$ GeV^2) and even extends to negative values in which case $M_x = -\sqrt{-M_x^2}$ is defined.

In order to define the exclusive sample, the missing mass constraint of -1.5 GeV $< M_x <$ +1.7 GeV is used for the HERMES DVCS analysis. The

---

[1] Sample of events with exactly one charged track, i.e. the scattered electron, and exactly one cluster in the CALO with no track (trackless cluster) assigned to it. For detail see Section 6.4.2.

size of this exclusive bin is indicated by vertical lines in Figure 3.1.

Moreover t (Expression 1.10) has to be calculated using the virtual and real photon kinematics

$$t \overset{lab}{=} -Q^2 - 2E_\gamma \left(\nu - \sqrt{\nu^2 + Q^2} \cos\theta_{\gamma^*\gamma} \right) \quad , \tag{3.1}$$

and consequently is affected by the photon energy resolution as well. Hence, the $-t$ distribution of exclusive events, just like the M_x^2 distribution, extends to negative values (see Section 6.4.3 and Figure 6.6). Both variables are related to each other via

$$M_x^2 = M_p^2 + 2M_p(\nu - E_\gamma) + t \quad . \tag{3.2}$$

The limited missing mass resolution of the spectrometer is not sufficient to identify non-exclusive events where an intermediate Δ^+ resonance is created (associated BH in Figure 3.1) or semi-inclusive events where one of the produced particles is a π^0. This type of background contributes to about 15% [Air01] (10% for associated BH and 5% for semi-inclusive) to the exclusive sample.

3.2 *Benefits with the Recoil Detection*

Improving the study of hard exclusive processes, HERMES required a novel detector surrounding the internal gas target. A Recoil Detector [Her01] surrounding the target cell (Figure 3.2) was proposed to enhance the acceptance of the main spectrometer and detect recoiling target nucleons. The direct measurement of recoiling nucleons will then allow to distinguish exclusive events from the non-exclusive background.

The detection of recoil particles in the measurement of DVCS at HERMES will have two main benefits. One is the rejection of events in which a real photon is accompanied by Δ^+ resonance production instead of a proton. The Δ^+ resonance will decay into a nucleon and a pion. Since these are produced back-to-back in the rest frame of the Δ^+, most of the time they will have a transverse momentum component with respect to the direction of the recoil momentum, and thus violate coplanarity with the reaction plane. This can be used to minimize the resonance contamination of the sample. A

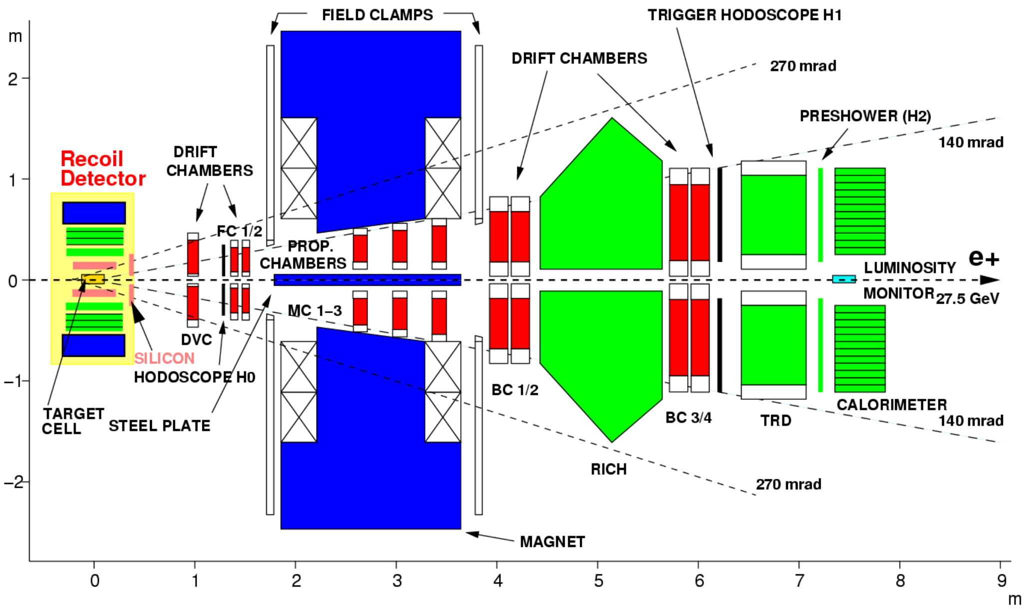

Figure 3.2: Schematic drawing of the HERMES spectrometer indicating the position of the Recoil Detector surrounding the target cell. The electron beam enters the spectrometer from the left.

selection in *coplanarity and transverse momentum* exploits the fact that the momentum vector of the recoiling nucleon has to coincide with the scattering plane of the electron. The two parameters of the cut are illustrated in Figure 3.3. The azimuthal angle ω is defined as the angle between the missing transverse momentum $p_{t,miss}$ calculated from the spectrometer information and the reconstructed transverse momentum of the recoil proton $p_{t,rec}$. The second parameter is the ratio R of the absolute values of the two transverse momenta.

The second benefit of recoil detection for DVCS lies in the reconstruction of the kinematics of the recoil particle. Whereas the determination of the variables Q^2 and x_{Bj}, or W^2, depends solely on the reconstruction of the scattered electron, $-t$ depends on the reconstruction of the real photon, as seen in Expression 3.1, if the recoil particle is not detected. As a result, the resolution in t, as reconstructed from the real photon's four-momentum is rather poor, approximately 0.17 GeV^2 (see Section 3.9.2, Figure 3.31). This variable can alternatively be determined when the four-momentum of the

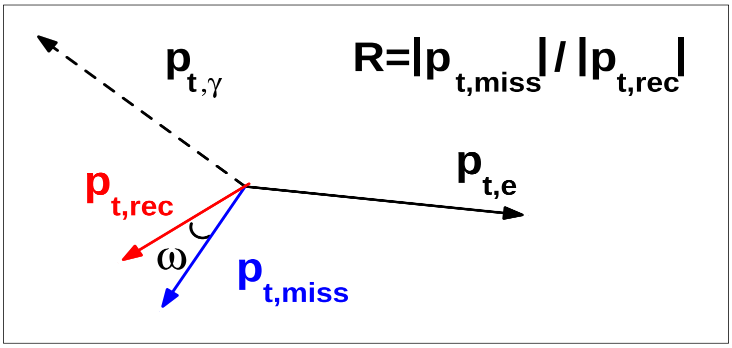

Figure 3.3: Transverse momentum and coplanarity cut parameters. $p_{t,\gamma}$ and $p_{t,e}$ are the transverse momenta of photon and electron measured by the spectrometer, $p_{t,miss}$ the missing transverse momentum calculated from them, $p_{t,rec}$ is the transverse momentum of the recoil proton measured by the Recoil Detector. The angle ω between $p_{t,miss}$ and $p_{t,rec}$ and the ratio R of their absolute values are the two cut parameters.

recoiling proton is measured, as seen in Expression 1.1. In this case the resolution in t depends only on the resolution in the proton four-momentum reconstruction.

3.3 *Design Requirements*

The design requirements on the Recoil Detector are defined by the kinematics and the nature of the particles involved in the exclusive reactions, as well as by the expected background reactions. The main background in the exclusive area results from events with intermediate Δ^+ production (Figure 3.1). Hence the particle types that are in principle to be detected are protons, pions and photons from π^0 decay.

All exclusive physics processes that will be investigated produce a low momentum recoil proton at large laboratory angles. Figure 3.4 shows the kinematic distribution of recoil protons in terms of momentum p and polar laboratory angle θ at an incident electron energy of 27 GeV [Her01]. The top side of the plot shows the correlation for the DVCS events and for the events associated with the BH/DVCS interference. The bottom left plot is for exclusive ρ^0 vector meson production and the bottom right plot shows the correlation for background processes where an intermediate Δ^+ resonance is

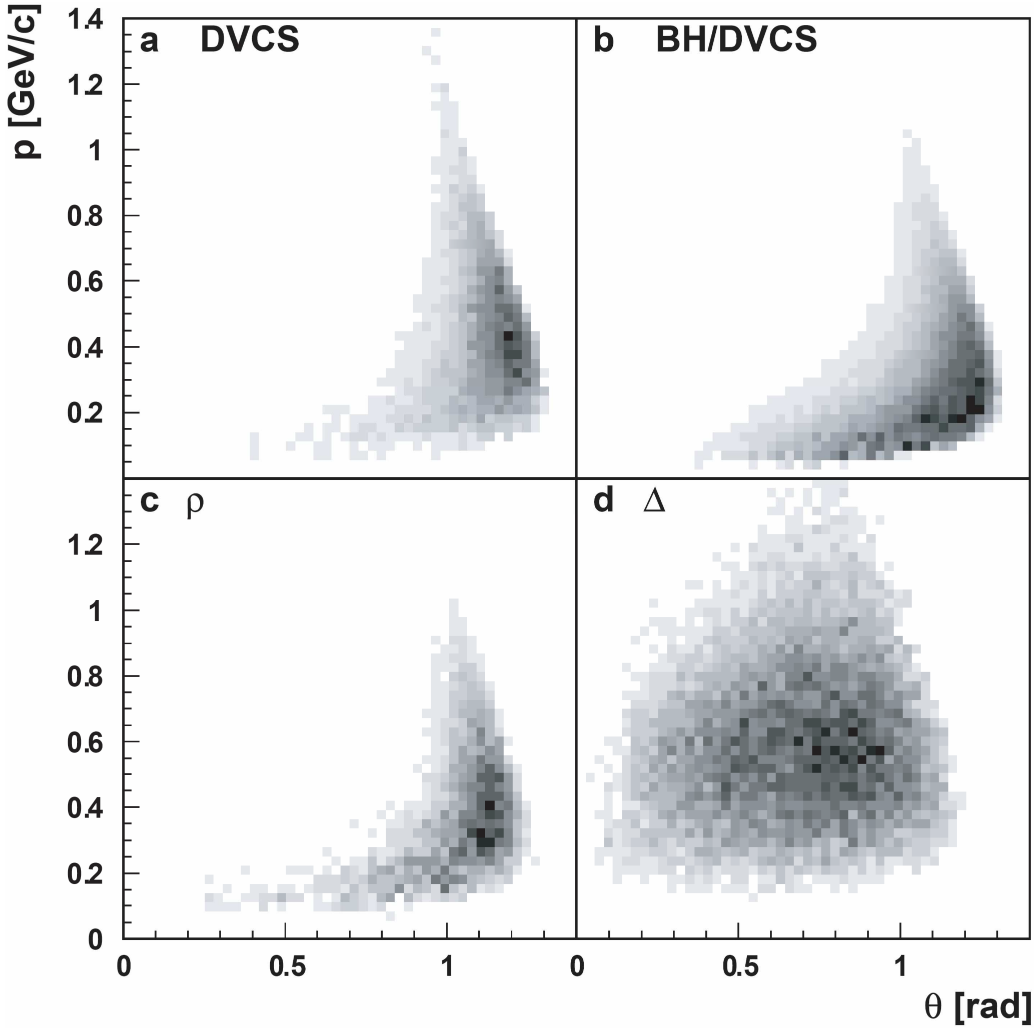

Figure 3.4: Kinematics of recoil protons in exclusive processes. The momentum of recoil particles versus (scattering) angle is shown for (**a**) DVCS, (**b**) BH/DVCS interference, (**c**) ρ^0 production and (**d**) the Δ^+ resonance [Her01].

produced. From the Figure it is clear that the resulting desired coverage of the Recoil Detector is 0.1 to 1.35 rad ($6^\circ - 80^\circ$) in polar angle and the momentum of the recoiling proton in the DVCS process never exceeds 1.3 GeV/c and most of the events even stay in the range below 0.8 GeV/c. For ρ^0 production the momentum limit of the recoil protons amounts to 1.1 GeV/c. The low momentum cut-off of the detector should be as low as possible. The bulk of the statistics is located at angles between 0.5 and 1.3 rad and momenta between 50 and 600 MeV/c. The protons from intermediate Δ^+ resonances have momenta below 1.4 GeV/c, while the pions typically have momenta below 800 MeV/c (see Figure 3.28).

The momenta of particles detected in the forward spectrometer are much larger than those of the particle(s) detected by the Recoil Detector. As a result, the invariant mass resolution is dominated by the resolution of the spectrometer. Even a perfect Recoil Detector cannot improve this situation. Due to the suggested application of the detector its resolution only has to be as good as required by the resolution of the spectrometer. This can be translated into a required resolution of 0.05 rad in the azimuthal angle ϕ around the beam axis, while the resolution for the transverse momentum component should be smaller than 10%. If the detector resolution is better, this will only have a marginal impact on the background rejection [Her01].

Currently the resolution in t provided by the spectrometer is only 0.17 GeV^2 for BH/DVCS events, mainly due to the photon energy resolution, as seen in Expression 3.1. This is not sufficient to measure a good t-dependence. The minimum requirement is that the t-resolution for BH/DVCS is improved to the same value of 0.07 currently available for exclusive ρ^0-production. The four-momentum p' of the recoil proton can be used directly to determine the value of t via the relation $t = (p' - p)^2$ (Expression 1.1) where p is the four-momentum of the target proton. No information from the main spectrometer enters into this calculation; the t-resolution therefore only depends on the momentum resolution of the Recoil Detector. Hence a good momentum resolution of the Recoil Detector is important. As the t-dependence will have to be used for extrapolations towards $t \to 0$ (see Section 1.1.1) the t and p resolutions are especially important at low momenta and low values of t.

Given the right kinematics a pion, e.g. from a Δ^+ decay, could be mistaken for a recoil proton. This can be avoided for negative pions through charge determination using the deflection of the track in a magnetic field. To additionally reject positive pions a particle identification capability of the detector is required. As hardly any pions from Δ^+ decays can be expected at momenta above 800 MeV/c, this defines the required momentum range for pion/proton separation. The desired performance is hard to quantify, but a

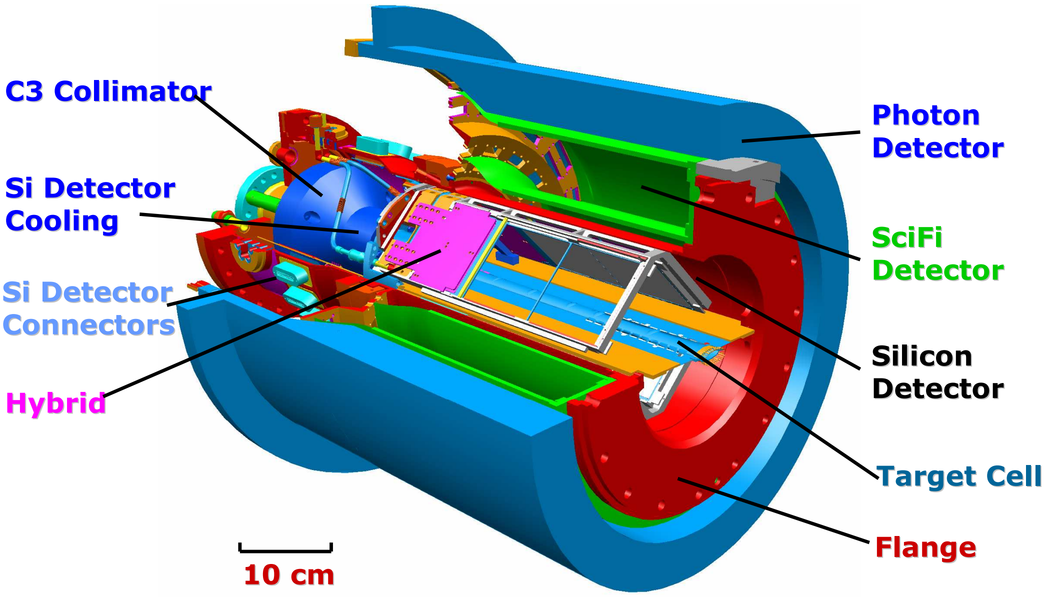

Figure 3.5: Schematic drawing of the Recoil Detector and its support structure. The Silicon Strip Detector surrounding the target cell is located within the beam vacuum inside the scattering chamber. Continuing outwards are the two concentric barrels of the Scintillating Fibers and finally the Photon Detector. The surrounding superconducting magnet is not shown. The electron beam enters from the left side, where an additional collimator protects the Recoil Detector from synchrotron radiation.

rejection factor of 10 or more for positive pions should be sufficient.

The best possible combination of detectors was found to be a solenoidal magnet combined with layers of tracking detectors. A solenoid magnet is required to protect the inner detectors from intense Møller background. A rather strong field is needed to obtain sufficient track bending over a distance of about 20 cm. Moreover neutral pions, coming from intermediate Δ^+ production, decay immediately into photons, therefore photon detection is required as well.

3.3.1 *Recoil Detector Design*

The final design of the Recoil Detector is shown in Figure 3.5. The Recoil Detector consists of three separate detectors, all surrounded by a superconducting 1 Tesla solenoid magnet not shown in Figure. The beam enters the detector from the left hand side. The Silicon Strip Detector is the innermost and surrounds the 75 μm thickness target cell within the beam vacuum of the HERA ring and inside the scattering chamber. The scattering chamber consists of two sections. The downstream part surrounding the target cell is made of aluminium with a wall thickness of 1.2 mm, governed only by mechanical constraints. In contrary, the upstream part, where due to kinematics no recoiling nucleons are expected, is a stainless steel service chamber with feedthroughs for electronic and cooling connections for the Silicon Strip Detector and the target cell. The next detector, outside the scattering chamber, is the Scintillating Fibre Tracker detector. The outermost detector is the Photon Detector which consists of several layers of converter and scintillator material, located within the magnet, and surrounding the Fibres. As mentioned, all three sub-detectors are within a 1 Tesla longitudinal magnetic field which is generated by the superconducting solenoidal magnet.

The technical details of the different sub-systems of the Recoil Detector and the expected detector performance will be described in the next Sections.

3.4 *The Target Cell*

The HERMES recoil target cell has been already discussed in Section 2.2 and shown in Figure 2.4: its wall thickness is 75 μm[2] and the volume containing the gas is 15 cm long instead of 40 cm, target length during polarized operation until 2005. This change in length was done to match the length of the Silicon Strip Detector. Figure 3.6 [Leo94] shows calculated range curves of different heavy particles in Aluminium. Knowing the density of Aluminium (2.71 g/cm^3), the lowest kinetic energy of protons coming from the target is ∼3 MeV, corresponding to a proton momentum of ∼75 MeV/c. As the target gas was no longer polarized, it was no longer necessary to cool the target with gas helium to increase the density, therefore water at 8°C is used. This cooling reduces mechanical stress caused by temperature gradients and in second order it keeps the cell temperature as constant as possible in order to have a target gas density which is controllable.

---

[2] The initial Recoil Detector project foresaw the use of 50 μm thickness target cell, but it was dis-installed after few months of HERMES data taking due to problems with electron beam, as it will be discussed in Chapter 5.

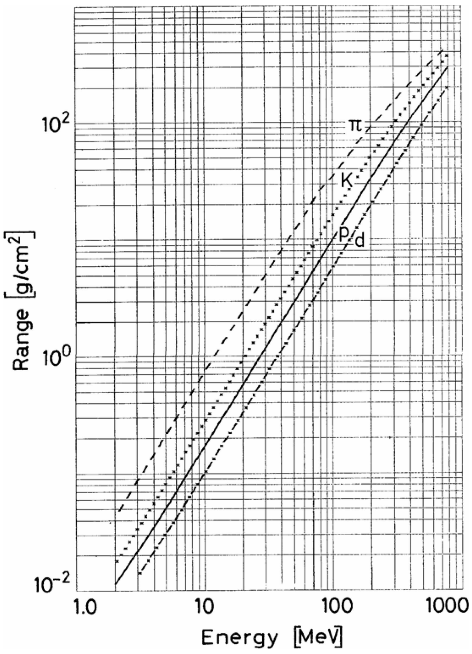

Figure 3.6: Calculated range curves of different heavy particles in Aluminium [Leo94].

3.5 *The Silicon Strip Detector*

The first sub-detector closest to the beam axis is the Silicon Strip Detector (SSD). The working principle of a silicon detector depends on the fact that a charged particle produces electron-hole pairs along its track in the material. As shown in Figure 3.7, n-type silicon with high resistivity is used as the base material on which p+ diode strips with aluminum contacts are implanted. This side of the sensor is called p-side. For a double-sided silicon detector, n+ electrode with much higher donor density compared with the base n-type material is similarly implanted. Then in the presence of an electric field which reversely biases the p-n diode of the silicon sensor, the particle produced charges drift oppositely towards the electrodes where the charges are collected. The collected charges then produce a signal on the electrode which is then read-out by a charge sensitive preamplifier. With the electrodes divided into narrow strips, the position information is obtained. An introduction to silicon microstrip detectors can be found in [Pei92].

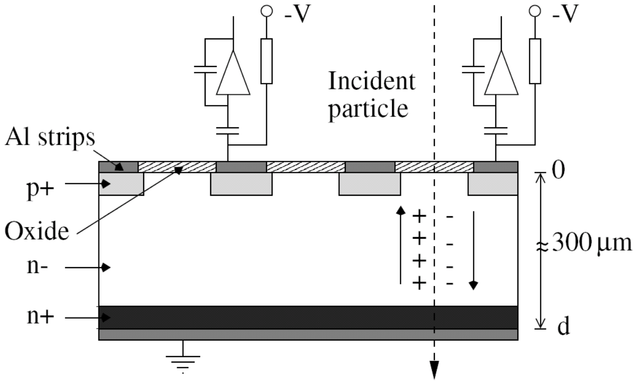

Figure 3.7: Schematic representation of the basic operation of a silicon microstrip detector. A charged particle will produce electron-hole pairs along its track. The charges created in the depleted region is collected and converted to signals by the charge sensitive preamplifiers.

3.5.1 *Energy Deposition in Silicon*

In this subsection the process of energy deposition in a layer of silicon will be presented with emphasis on the energy range in which the SSD will operate. Ionizing radiation creates electron-hole pairs in the n-doped silicon. Holes drift towards the p+ and electrons to the n+ side of the detector. In general the average energy loss (stopping power) of an ionizing particle inside a material is given by the Bethe-Bloch formula [PDG98]:

$$-\frac{1}{\rho}\frac{dE}{dx} = -\kappa\, z^2 \frac{Z}{A}\frac{1}{\beta^2}\left(\frac{1}{2}\ln\frac{2\, m_e\, c^2\, \beta^2\, \gamma^2\, T_{max}}{I^2} - \beta^2 - \frac{\delta}{2}\right) \quad , \tag{3.3}$$

where:

- $\kappa = 4\,\pi\, N_A\, r_e^2\, m_e\, c^2$ ($= 0.3071 \frac{MeV \cdot cm^2}{g}$);
- z = Charge of incident particle (in units of elementary charge);
- Z = Atomic number of absorbing material (14 for Silicon);
- A = Atomic weight of absorbing material (28.09 for Silicon);
- T_{max} = Maximum kinetic energy transferred to an electron in a single collision $= 2\, m_e\, c^2\, \beta^2\, \gamma^2$ (if $m_e \ll M$ where M is the mass incident particle);

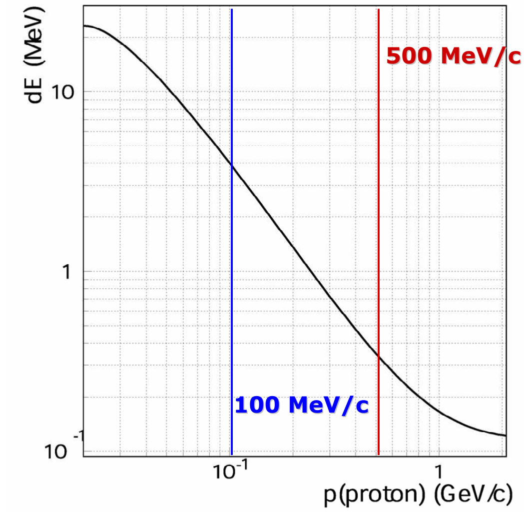

Figure 3.8: Bethe-Bloch for protons in a 300 μm silicon layer. The two vertical lines represent momenta equal to 100 and 500 MeV/c.

- I = Mean excitation energy (173.0 eV for Silicon);
- δ = *Density effect* correction to energy loss by ionization.

This formula is plotted in Figure 3.8 for ionizing protons passing through a 300 μm thick silicon layer for the momentum range relevant for the SSD. The density effect has been neglected since only momenta up to 1.4 GeV/c are expected. Particles with an energy corresponding to the minimum plateau of the Bethe-Bloch are defined as *Minimum Ionizing Particles* (MIP).

A particle traveling through a certain material becomes more ionizing towards the end of its path, therefore its energy loss versus penetration depth is a typical Bragg curve. The range R of a particle with a kinetic energy E_0 which stops inside the absorbing material is calculated by integrating the Bethe-Bloch formula (Expression 3.3):

$$R(E_0) = \int_0^{E_0} \left(\frac{dE}{\rho dx}\right)^{-1} dE \quad .$$

For low energies the Bethe-Bloch formula goes as $\sim 1/\beta^2$ ($= \sim 1/E_0$) so the range can be approximated to be:

$$R(E_0) = \int_0^{E_0} \frac{1}{\rho} \frac{dE}{cE^a} = \frac{1}{\rho} c_r E_0^b \quad ,$$

with b and c_r fitting parameters. Using the measured energy range the parameters c_r and b have been fitted in the range 40 to 170 MeV/c and are:

$$c_r = 3.258 \times 10^{-3} \frac{g}{cm^2}; \qquad b = 1.70 \quad .$$

For other energies fitting parameters are given in [Bic67].

A particle traveling through the silicon deposits an energy of

$$E_{dep} = E_0 - E_{\text{fin}} \quad , \tag{3.4}$$

where E_{fin} is the energy of the particle after passing the silicon. If now the range of a particle in a piece of silicon is t then it has lost an amount of energy equal to $E_0 - E_{\text{fin}}$. Hence:

$$\int_{E_{\text{fin}}}^{E_0} \left(\frac{dE}{\rho dx}\right)^{-1} dE = t \quad .$$

Calculating now the range $R(E_{\text{fin}})$ of a particle with energy E_{fin}:

$$\begin{aligned} \int_0^{E_{\text{fin}}} \left(\frac{dE}{\rho dx}\right)^{-1} dE &= \int_0^{E_0} \left(\frac{dE}{\rho dx}\right)^{-1} dE + \int_{E_{\text{fin}}}^{E_0} \left(\frac{dE}{\rho dx}\right)^{-1} dE \quad , \quad \text{and} \\ \frac{1}{\rho} c_R E_{\text{fin}}^b &= \frac{1}{\rho} c_R E_0^b - t \quad . \end{aligned}$$

Then from Expression 3.4:

$$E_{dep} = E_0 - \left(E_0^b - \frac{t\rho}{c_R}\right)^{\frac{1}{b}} \quad .$$

Applying this formula the energy deposition in the two silicon layers can be calculated. In Figure 3.9 the energy deposition in the first layer is plotted versus the energy deposition in the second layer for protons hitting the detector perpendicularly. Protons with momenta lower than ∼106 MeV/c get stuck in the first layer of silicon. Protons with momenta between ∼106 MeV/c and ∼130 MeV/c punch through the first layer but get stuck in the second layer. If the momentum of a proton is higher than ∼130 MeV/c it punches through both silicon layers.

Due to the possibility of large energy transfer in a single collision, the energy deposition inside thin layers of detector material is not Gaussian.

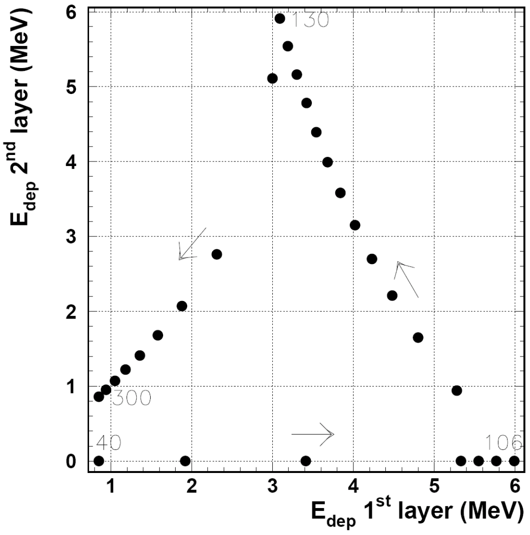

Figure 3.9: Energy deposition in two layers of 300 μm silicon for protons hitting the silicon perpendicularly. The arrows indicate increasing proton momenta. Protons with $p < 106$ MeV/c get stuck in the first layer, if 106 MeV/c $< p <$ 130 MeV/c then the protons punch through the first layer but get stuck in the second. For $p >$ 130 MeV/c the proton punches through both layers.

Therefore a difference between the most probable and the average energy deposition arises. The distribution should be approximated by a Landau curve [Gru96]:

$$L(\lambda) = \frac{1}{\sqrt{2\pi}} e^{-\frac{1}{2}(\lambda + e^{-\lambda})}$$

$$\lambda = \frac{\Delta E - \Delta E^W}{\xi} \tag{3.5}$$

where $\xi = \frac{\kappa}{2}\rho\frac{Z}{A}(\frac{z}{\beta})^2$, ΔE the actual energy loss, and ΔE^W the most probable energy loss. ΔE^W can be determined by taking the mean of Expression 3.5:

$$\Delta E^W = -\xi < \lambda > + < \Delta E > \quad . \tag{3.6}$$

The mean energy loss $< \Delta E >$ of a proton in a silicon layer is known from the Bethe-Bloch formula (Expression 3.3). $< \lambda >$ can be calculated by:

$$< \lambda >= \frac{1}{\sqrt{2\pi}} \int_{-\infty}^{+\infty} \lambda e^{-\frac{1}{2}(\lambda + e^{-\lambda})d\lambda} = \gamma + \ln 2 \quad ,$$

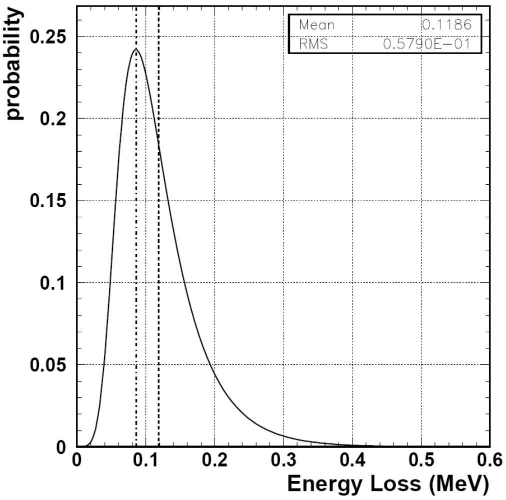

Figure 3.10: Energy loss distribution for minimum ionizing protons with normal incidence in 300 μm silicon. The distribution is represented by a Landau curve. The dashed (dash-dotted) line represents the average (most probable) energy loss.

where γ is Euler's constant. Evaluating Expression 3.6 for a MIP gives $\Delta E^W = 85.5$ keV. Knowing that 3.6 eV is needed to create one electron-hole pair in silicon [Leo94], a signal of ~24000 electrons is *most probable* appearing for the energy deposition of a MIP. The Landau distribution for minimum ionizing protons with normal incidence in 300 μm silicon is shown in Figure 3.10. Looking back at Figure 3.9 the expected signals can now be calculated for the mentioned momenta: a proton with momentum ~106 MeV/c will deposit ~6 MeV in the first energy layer, corresponding with a signal of ~51 MIPs. For a momentum of 130 MeV/c there will be a deposition of ~3.1 MeV (~5.9 MeV) in the first (second) layer, corresponding with a signal of ~26 MIPs (~50 MIPs). A 300 MeV/c proton will deposit ~0.8 MeV in both layers, giving a signal of about 7 MIPs. Most recoil particles will cross the SSD not perpendicularly but at an angle of between around 0.8 - 1.4 rad. A dynamic range of 70 MIPs ensures that those particles can be detected.

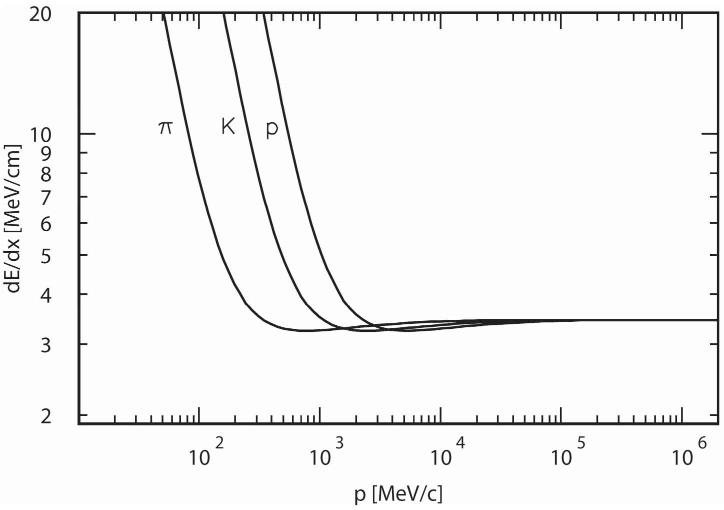

Figure 3.11: Mean energy deposition as a function of momentum for pions, kaons and protons.

3.5.2 *SSD Conceptual Design*

Due to the very low energy of the recoil protons (Figure 3.4), it is necessary to minimize the amount of material between the interaction point and the detector. Therefore the SSD is located inside the scattering chamber within the beam vacuum in order to detect low momentum recoil protons that would otherwise be stopped inside the scattering chamber: only protons with kinetic energies of ∼14 MeV, corresponding to a momenta of ∼160 MeV/c, can pass through the 1.2 mm thickness scattering chamber (Figure 3.6). For this reason, all of the components and techniques used for the SSD must be vacuum compatible.

The momentum and particle type of the detected particle are determined from the energy deposited in the silicon layers (Figure 3.11). Since the resolution has to be as good as required by the resolution of the spectrometer, a poor angular resolution is acceptable for the SSD and for this reason a relatively large strip pitch of ∼1 mm is chosen.

The SSD consists of 8 modules mounted in two layers symmetrically around the target cell in roof-shaped structures (Figure 3.12). The two layers are separated by 1.5 cm in which the inner ones are 5.75 cm away from the center of the scattering chamber (HERA beam axis). Not shown in Figure

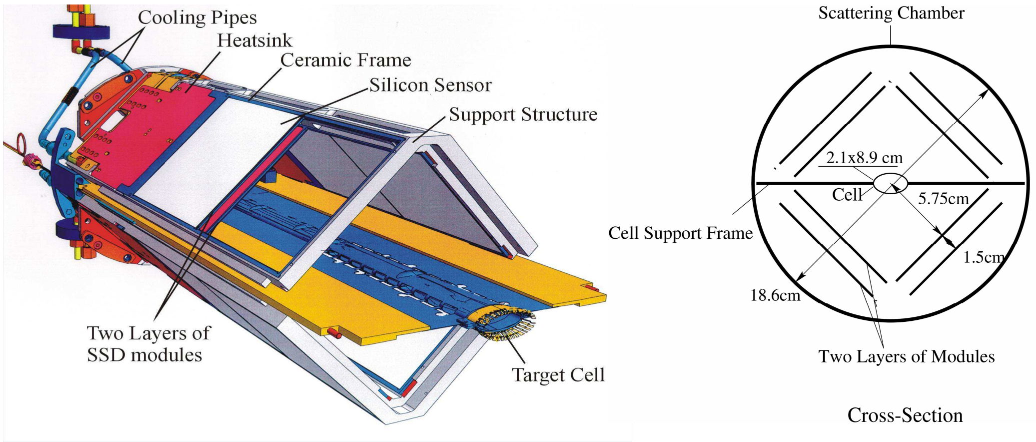

Figure 3.12: Silicon Strip Detector with the Target Cell. The SSD consists of 8 modules mounted in two layers symmetrically around the target cell. The panel at the right hand side shows the relative position of the SSD in the scattering chamber with the target cell.

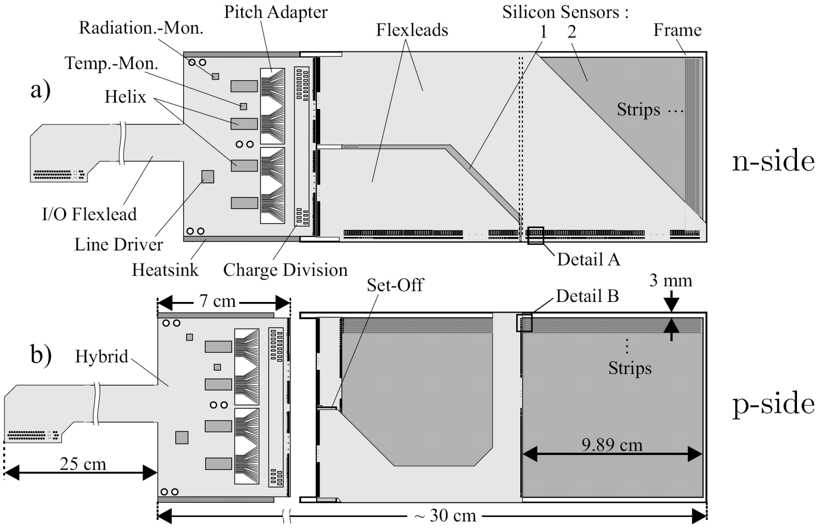

Figure 3.13: N-side (a) and P-side (b) of a SSD Module. It mainly consists of two double-sided silicon sensors (right side) and two hybrids with the read-out electronics (left side).

3.12 but shown in Figure 3.13 is the detector read-out hybrids, which are the circuit boards containing the HELIX3.0 read-out chip (discussed in the next subsection) and on board electronics. They are glued to a 0.5 mm thick aluminium plate and then to a 5 mm thick aluminum heatsink. Figure 3.13 shows the structure of one detector module [Rei04]. The main components include two TIGRE (The Tracking and Imaging Gamma Ray Experiment) sensors and two read-out hybrids with digital control and analog read-out circuits. The double-sided silicon TIGRE sensors are from Micron Semiconductors Ltd [MicUK] with a size of 9.9×9.9 cm^2. The active thickness of the sensors is in average 300 μm. The delivered batch of 25 good TIGRE sensors has a varying thickness of 295 - 316 μm, values measured by the manufacturer and confirmed using a micrometer screw on the supplied test-structures. On each side of the sensor there are 128 strips with a 758 μm wide pitch. The total surface area of the 16 silicon sensors constituting the SSD is 0.16 m^2, resulting in 4096 strips. The strip directions of the p-side and the n-side in one sensor are arranged perpendicularly to each other so that 2-dimensional position information is available. The electric connection from the detector strips to the hybrids is achieved by 50 μm thick polyimide foils (flexleads or flexfoils) [Her01]. Space constraint made it impossible to route the signals away from the sensors. Therefore the flexfoils had to be placed on top of the sensors. The material thickness was minimized so to produce as small a disturbance as possible. The inner modules have their n-side facing towards the cell and p-side facing towards outside, while the outer modules have their n-side facing towards outside and p-side facing towards the cell. This implies that the long flexfoils of the n-side face the target cell and the wall of the scattering chamber, while the short flexfoils on the p-side are between the 2 module layers. This minimizes the material between the two silicon layers where the particles may have very low momentum. A photograph of 2 silicon modules mounted on the support of the scattering chamber is shown in Figure 3.14.

3.5.3 *SSD Read-out*

The energy range of the recoil protons makes the design of the read-out electronics challenging. For protons at normal incidence the energy deposited in the silicon varies between 6 MeV and 86 keV. This corresponds to a dynamic range of 70. The HELIX read-out chips were considered for use with the SSD. HELIX 128-3.0 [Fal99] was designed by the ASIC laboratory of the

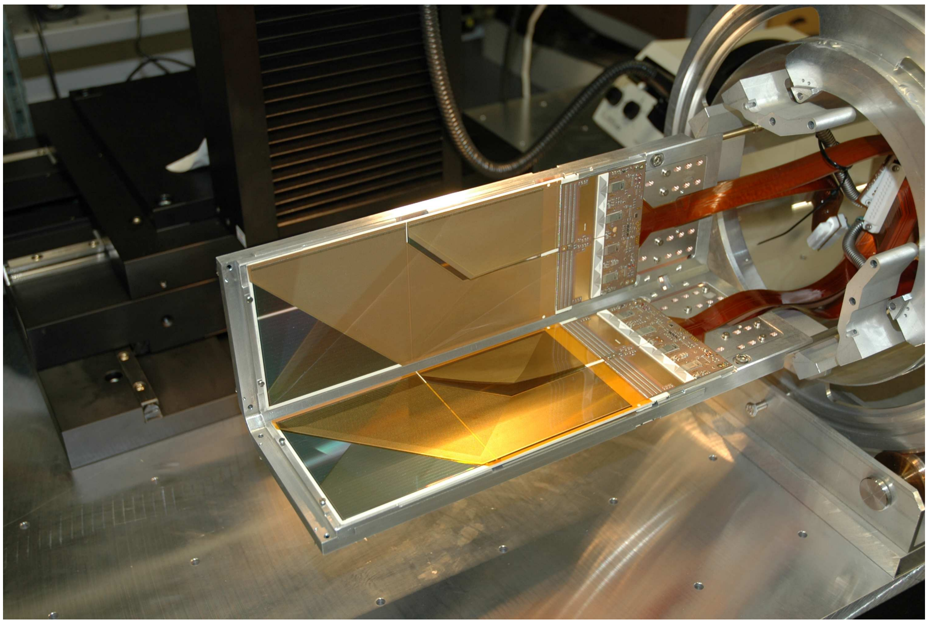

Figure 3.14: Photograph of 2 silicon modules mounted on the support of the scattering chamber.

Heidelberg University and manufactured in the 0.8 μm CMOS process by AMS (Austria MikroSysteme International GmbH). It was designed for the HERA collider experiments at DESY. The clock frequency was designed to match the HERA bunch crossing of 10 MHz. The HELIX is schematically depicted in Figure 3.15. The chip itself consists of 128 input channels which all have a charge sensitive preamplifier, followed by a CR-RC shaper. The latter is needed to have the signal shaped within 1 clock cycle of 100 ns. After the shaper there is a capacitor array, referred to as a pipeline, where the signal can be stored until read-out. Every clock cycle a different pipe cell is addressed. The pipeline depth is 128 + 8, so the maximal delay between signal and trigger is over 12 μs. The chip has a multi-event buffer of 8 events. Whenever a trigger occurs, the charge stored on one of the pipe cell condensators is read-out via the pipe amplifier. The analog signal from all 128 channels then is serialized to form the *AnalogOut* signal which is sent to the external world. The analog signal is followed by a trailer of 8 bits giving information about the pipe-cell where the charge was stored. There exists the possibility to daisy chain several chips together, to extend the amount of

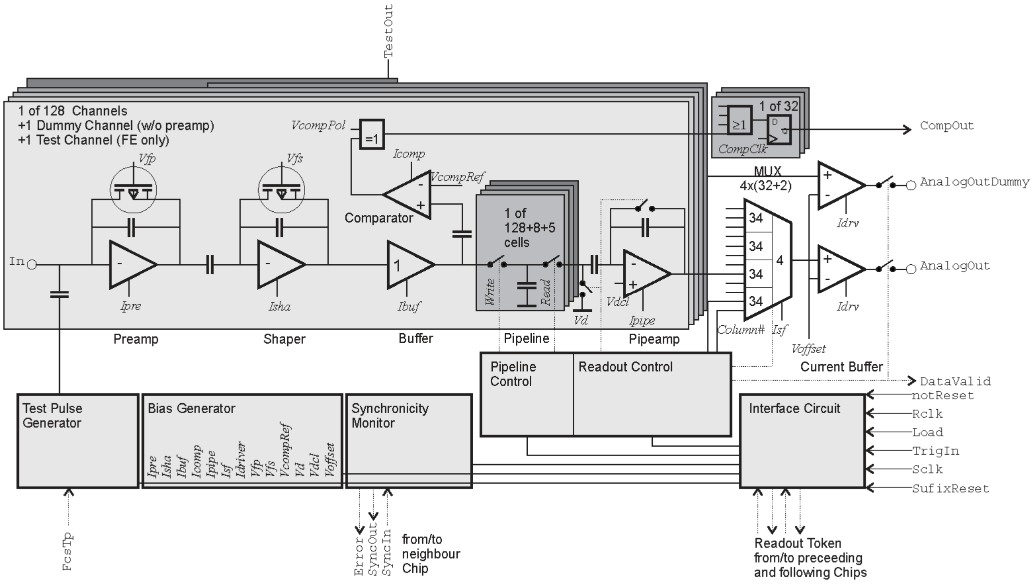

Figure 3.15: Schematic diagram of HELIX128 [Tru00].

input channels from 128 to any multitude of that number. A possible broken chip can be excluded from the daisy chain via a fail-safe mechanism. The HELIX 3.0 also features a comparator which can be used to trigger on the analog input. If the output of the preamplifier-shaper combination is above a certain reference voltage a trigger is generated.

For the HELIX 128-3.0 the dependance of the chip's response on the injected charge is linear in the range of |10| MIPs. This is not sufficient to detect slow protons (up to 50 MIPs ≈ 6 MeV deposited energy). A possible way to extend the dynamic range is charge division. The chosen method is shown in Figure 3.16. The signal from the detector can be divided by a coupling capacitor into High Gain (HG) and Low Gain (LG) read-out channels. In order to avoid difficulties caused by the crosstalk, independent chips for the HG and the LG channels are used. The response of two channels, coupled by a 10 pF capacitor, to the injected positive charge with TIGRE sensors not connected can be seen in Figure 3.17 [Kop02]. In such a configuration the dynamic range is extended to |40| MIPs for the LG channel. It can be made even wider by decreasing the value of the coupling capacitor.

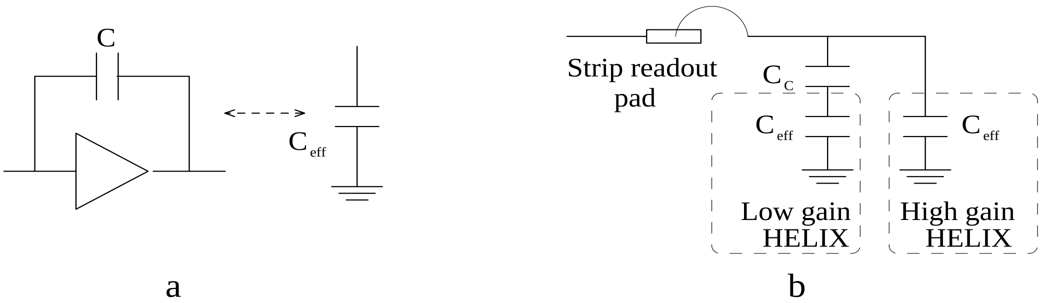

Figure 3.16: **a** Equivalent schematic of the charge sensitive HELIX128 preamplifier. It can be represented as effective capacitance $C_{\text{eff}} = G \cdot C$, where G is the gain of the preamplifier. **b** Schematic view of charge division. Capacitance C_c can be varied for the dynamic range adjustment.

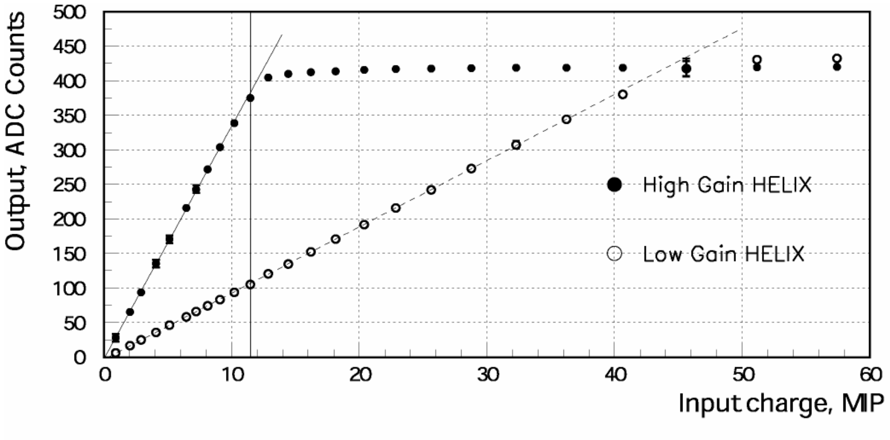

Figure 3.17: Responses of HG and LG HELIX128 channels coupled by a 10 pF capacitor to the injected positive charge with TIGRE sensors not connected [Kop02]. If the HG channel gets saturated, the signal from the LG channel is used.

Additional electronics is needed outside the vacuum to operate the detector: an analogue digital converter, a sequencer for addressing the HELIX chips (HLCU), an auxiliary module (ACC) and high - as well as low - voltage power supplies. This layout will be presented in the Section 4.1.

Timing

In order to get a constant calibration, using a 1 MIP signal which is the lowest signal from a particle above pedestal, it is necessary to sample the data at the peak of the output. This ensures that the signal is at its strongest and that the measurements can be compared to any others made. Three things must be taken into consideration to achieve this:

- *Latency* - a term describing the number of clock cycles between the read pointer and the write pointer in the setup: if an external trigger is applied the chip stops and goes back a number of cells (latency) to find the charge that was stored for the time of triggered event;
- *Clock Delay* - a term describing when the clock pulse arrives and when the trigger pulse in generated;
- *Clock Difference* - a term that describes the delay between sampling for the n-side data and the p-side data. This third term is necessary due to the increased mobility of electrons in the n-side as opposed to the mobility of holes in the p-side, causing the n-side detector to respond faster than the p-side. Therefore the output peak from the n-side detector arrives at the read-out chip before that of the p-side

Figure 3.18 illustrates the meanings of Clock Delay and Clock Difference. The Latency and Clock Delay are dependent upon the setup of the experiment and are unique for every situation, whereas the Clock Difference is bound to the Clock Delay.

The Latency is varied through the settings range to find the signal from the detector. Once the signal has been located, the Clock Delay is varied in order to produce the highest output from the n-side detector. Finally the Clock Difference setting is varied to produce the highest possible output for the p-side detector.

3.6 *The Scintillating Fibre Tracker*

3.6.1 *SFT Conceptual Design*

The Scintillating Fibre Tracker (SFT) is the second detector located after the SSD, going from inside out. Charged particles of higher momenta which escape the scattering chamber are detected by the SFT. Their momentum is determined by the deflection of their track in the longitudinal magnetic field

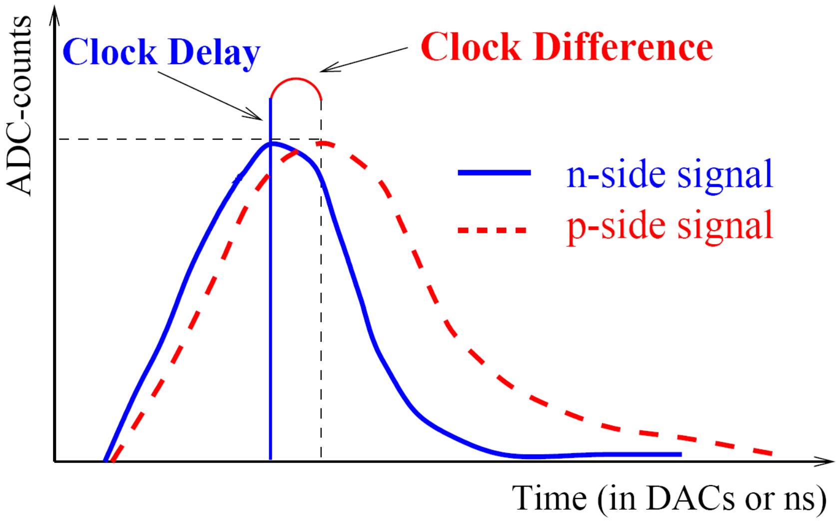

Figure 3.18: An illustration of the differences between the Clock Delay and the Clock Difference. These sampling parameters should be the same for each module, but vary by a value equivalent to ∼1 ADC count [Hri05].

which also allows the identification of the sign of the charge. The radius of curvature ρ in meters of a particle track in a magnetic field is given by

$$\rho = \frac{p_\perp}{0.3 \cdot eB}$$

with $p_\perp$ (GeV/c) being the transverse momentum with respect to the magnetic field B (T) and e being the particle charge. For a momentum positive particle of 500 MeV/c in 1 T magnet, the radius of curvature ρ is about 1.5 m.

The SFT consists of two concentric barrels (with an inner diameter of 109 mm and 183 mm of the inner and outer layer respectively) of 1 mm diameter scintillating fibres, each with a thickness of 4 mm and a length of 280 mm. Each barrel consists of two layers: the fibres of the inner layer are aligned parallel to the beam, while the fibres of the outer layer (stereo layer) are inclined by 10° (Figure 3.19, left side). This configuration allows the determination of a space point of a particle track for each barrel. Each layer in turn consists of two sub-layers that are shifted by half a fibre such that the 2$^{\text{nd}}$ sub-layer is put into the grooves formed by the first sub-layer (Figure 3.19, right side). The inner barrel consists of 657 fibres per sub-layer

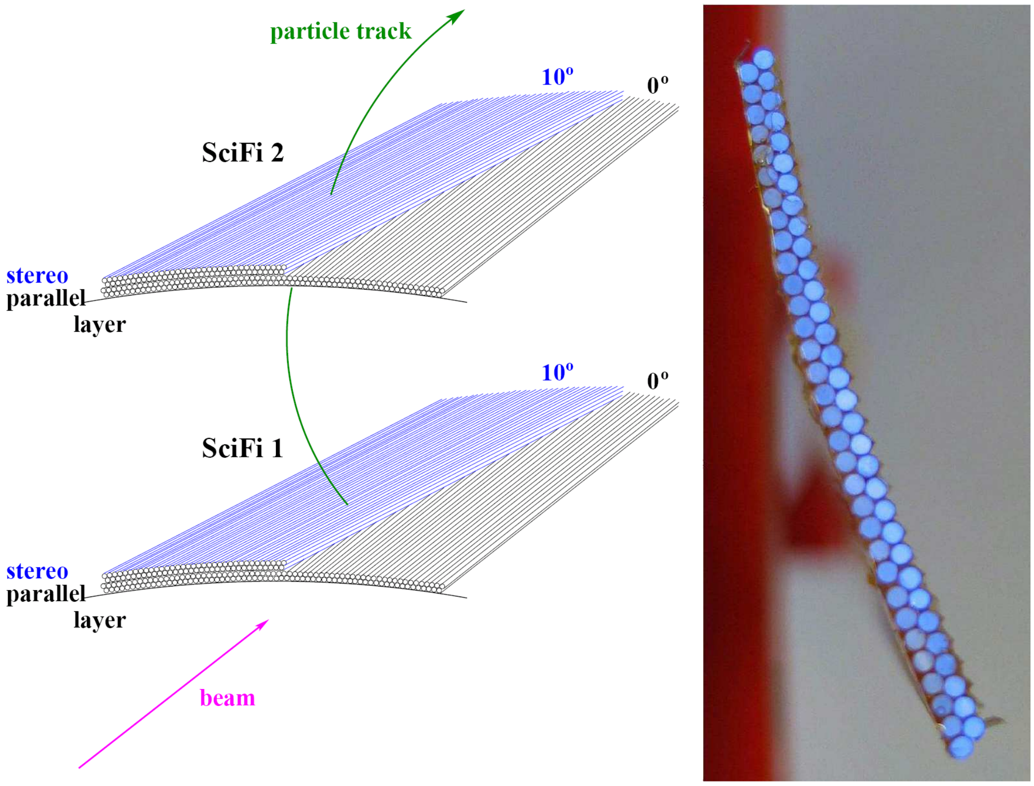

Figure 3.19: Left: the schematic view of fibre layout in the SFT. The fibres of the inner sub-layer are orientated parallel to the beam axis. Fibres wrapped around the barrel in a helix-shaped in the outer sub-layer form a stereo angle of 10° with respect to the beam direction. Two sub-layers are built into each of the parallel and stereo layers of either barrel. Right: Picture of the one fibre layer. Two sub-layers of fibres with a diameter of 1 mm form one layer.

in the first layer and 660 fibres per sub-layer in the second layer; the outer barrel consists of 1098 fibres per sub-layer in the first layer and 1090 fibres per sub-layer in the second layer, resulting in 7010 fibres in total. The sub-layers are assembled in modules such that single modules with defects can be discarded. A maximum distance between inner and outer barrel is desirable in terms of maximizing the lever arm for momentum resolution. However, the outer dimensions of the SFT are constrained by the scattering chamber and the Photon Detector. The spatial resolution σ of two staggered layers, neglecting contributions from multiple scattering, is given by [Coo95]

$$\sigma \propto \frac{D}{\sqrt{12}}$$

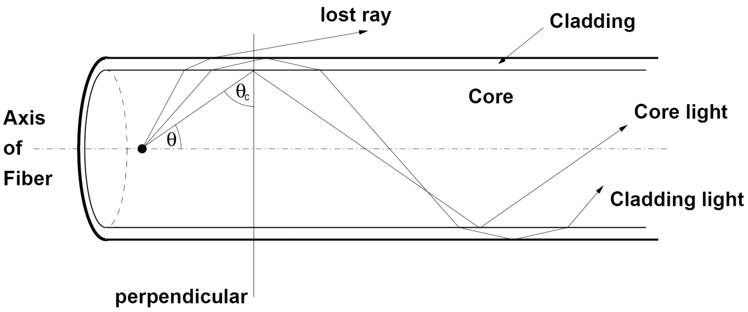

Figure 3.20: Light propagation in a scintillating fibre for light rays emitted on-axis.

with D being the fibre pitch between the staggered layers. In case of a fibre pitch of 0.5 mm for a 1 mm fibre, the expected spatial resolution σ is 150 μm.

The energy loss in the scintillating fibres, depending on the particle type and its momentum, will be used for PID. Therefore the read-out of the SFT has to provide not only information on the space point of the particle track but also on the deposited energy.

3.6.2 *Scintillating Fibres*

Scintillating fibres consist of a core in which the scintillation light is produced, surrounded by one (single-clad) or two (multiclad) cladding layers. Choosing the index of refraction of fibre core and cladding appropriately light transport inside the fibre due to total internal reflection becomes possible. The scintillation light contained within the total reflection cones, which are determined by the critical incidence angle θ_C, in case of the fibre core given by

$$\theta_C^{core} = \sin^{-1}\left(\frac{n_{clad}}{n_{core}}\right)$$

with n_{core} and n_{clad} being the index of refraction of the corresponding fibre part, is then trapped inside the fibre core and transported along its axis (Figure 3.20).

The fibre core consists of polystyrene[3] mixed with scintillation dopants, usually organic compounds. These dopants determine the scintillating and optical properties of the fibre, e.g. radiation hardness.

---

[3] $C_6H_5CH = CH_2$

characteristic	**value**
peak emission	450 nm
attenuation length	> 4 m
decay time	2.8 ns
cladding thickness	30 μm

Table 3.1: Properties of Kuraray SCSF-78M multiclad scintillating fibres of 1 mm diameter [CatKur].

The fibre cladding consists of polymethylmethacrylate (PMMA)[4] and fluorinated PMMA for the outer cladding in case of multiclad fibres. There are no additional scintillating dopants present in the cladding so that no scintillation occurs within the cladding layer. Also the cladding serves two secondary purposes. It protects the core from mechanical damage thus ensuring perfect surface conditions for total reflections and it also prevents primary scintillation light leaking into neighbouring fibres.

The fraction of trapped light is then guided along the axis to the fibre end. Before it reaches the fibre end, some light will be lost. Detracting from the amount of light that reaches the end of the fibre some losses, caused by an overlap of the emission and absorption band of the fibre dopants leading to self-absorption of the scintillation light, do exist. These light losses are increased by Rayleigh scattering on small density fluctuations in the core, especially for wavelengths below 400 nm [Leu95]. Furthermore, small imperfections at the core-cladding interfaces cause small reductions from unity for the total reflection coefficient and inducing thus further light losses [Alt99]. At the fibre end, Fresnel's losses due to reflections occur depending on the coupling material. Fresnel's losses R are described by

$$R = \left(\frac{n_{core} - n_{clad}}{n_{core} + n_{clad}} \right)^2 \quad .$$

For a core-air interface, Fresnel's losses amount to approximately 5%.

Kuraray SCSF-78M with a diameter of 1 mm were chosen as active material for the SFT. The basic characteristics of this fibre type are given in Table 3.1. The cladding thickness amounts to 3% of the overall diameter for inner and outer cladding each, i.e. the active fibre core has a diameter of

---

[4] $C_5H_8O_2$

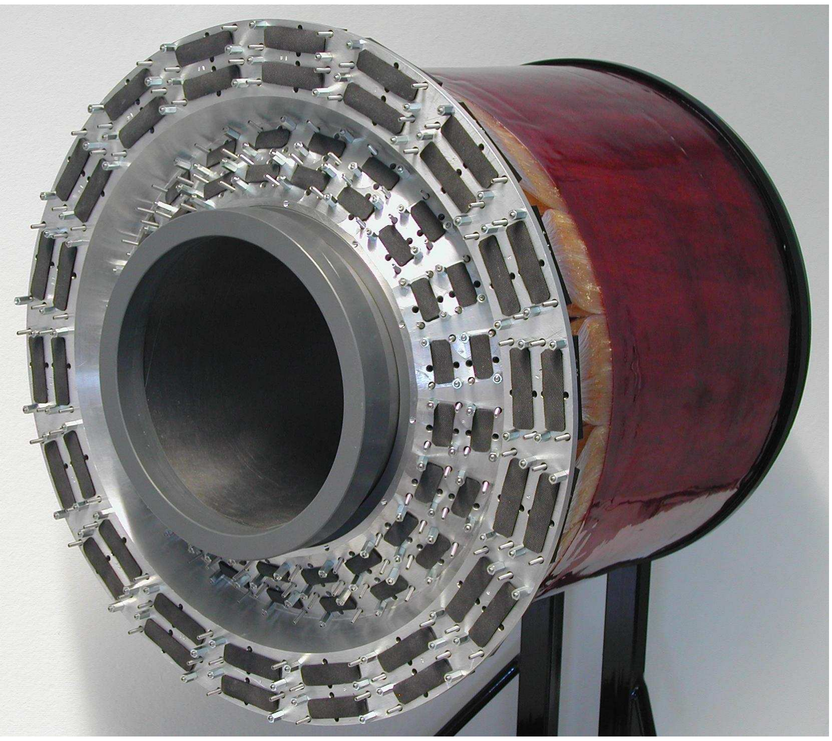

Figure 3.21: Picture of the completed SFT mounted to a dummy scattering chamber. Protective caps are put onto connectors. Kapton film on outer barrel serves as protection from mechanical influences.

0.94 mm. The tolerance in diameter is specified by the manufacturer to be below 2% [CatKur].

The scintillating fibres are connected via 4 m long light guides made of clear fibres to Multi-Anode Photo-Multiplier Tubes (MAPMT). The completed SFT mounted on a dummy scattering chamber is shown in Figure 3.21.

3.6.3 *Optical SFT Read-out*

The read-out of the scintillating fibres faces several difficulties. First of all the Recoil Detector is surrounded by a solenoidal magnet with a field strength of 1 T. Secondly, the available space in the upstream area is very limited because of pumps for the vacuum system and cabling of the other sub-detectors. A combination of clear fibres acting as light guides and Photo Multiplier Tubes

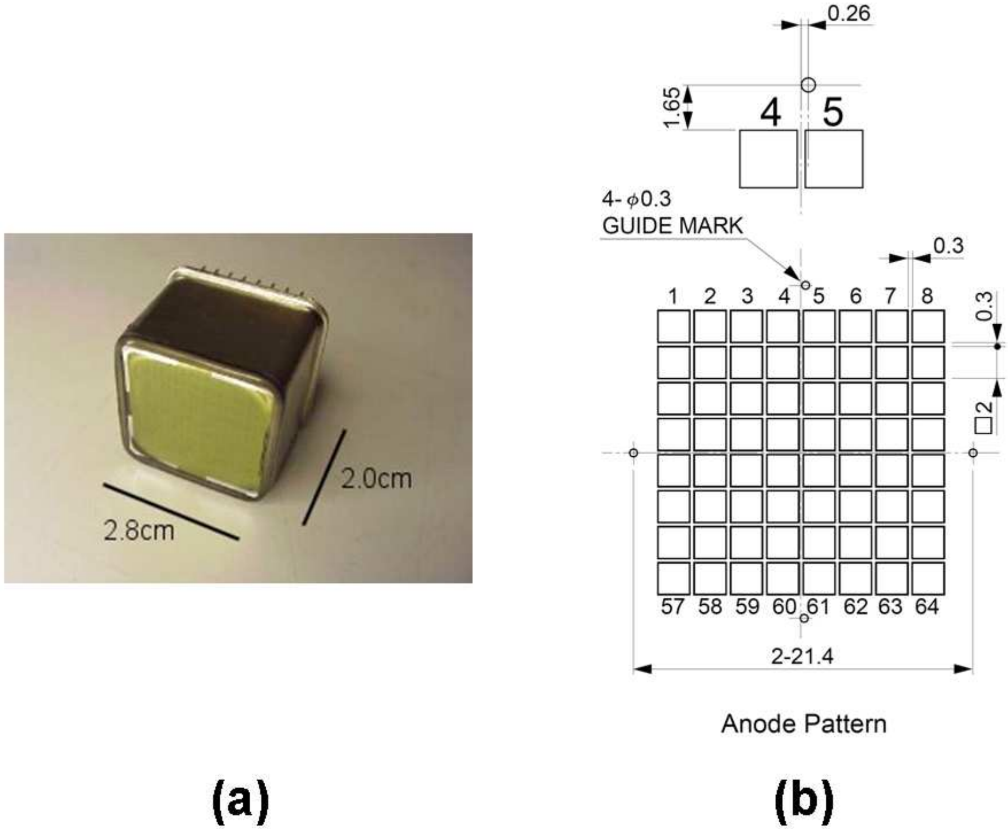

Figure 3.22: **(a)** Hamamatsu R5900-00-M64 Multi-Anode Photo-Multiplier Tube (MAPMT) without housing and voltage divider; **(b)** Layout of MAPMT cathode plane and correlation to reference marks.

is used to accomplish the read-out of the scintillating fibres.

As the total number of fibres amounts to 7010, a compact light detecting device is mandatory. In addition, a linear response and a large dynamic range are required as the deposited energy ΔE will be used for PID purposes. In total 78 MAPMT H7546 from Hamamatsu, employing a metal channel dynode structure with 64 channels, fulfill all demands. The total number of read-out channels amounts to 4822, since one MAPMT pixel is used to collect light from two outer barrel fibres. With compact outer dimensions (Figure 3.22**a**) the 64 channels are arranged in an 8×8 array with a pixel size for each channel of 2×2 mm^2. A schematic overview of the photocathode layout and pixel size is shown in Figure 3.22**b**. The metal channel dynode structure is an array of small linear focused dynodes, which leads to negligible crosstalk in the dynode structure itself [Yos97]. The spectral response of the employed bialkali photocathode ranges from 300 - 650 nm with a maximum sensitivity at 420 nm (quantum efficiency is 23.1%) which is close to the peak emission wavelength of the selected SCSF-78M fibres (Table 3.1). Given the fast signals from scintillating fibres (Table 3.1) a fast rise time of 1.5 ns of the H7546 MAPMT suits these needs. The typical gain for the envisaged working voltage is of the order of 3×10^5 at an operating voltage of 800 V. Gain uniformity across all anodes of a MAPMT is typical 1:3 [Pho00] and is improved to 1:2 for MAPMTs preselected by Hamamatsu [Sei04] which is important for measurements of the deposited energy ΔE (since the working voltage defining the gain cannot be adjusted for each channel individually but only in common for all channels). The MAPMT response is reported to be linear up to currents of 0.1 mA [Enk98] and depends only weakly on the operation temperature. The single electron peak was shown to be always well separated from the dark current [Enk98]. Individual calibration of each pixel allows to account for possible gain variations.

The MAPMTs are sensitive to magnetic fields, especially along the dynode axis. Variations in gain of up to 10% for a field of 35 Gauss are reported by Hamamatsu, which excludes mounting these MAPMTs close to the active SFT components inside the Recoil Detector magnet as fringe fields of several hundred Gauss are expected given model calculations of the magnetic field. Additional shielding with μ-metal and soft iron allows for a maximum field strength of the fringe fields of 50 Gauss which can be achieved by a distance of 2.5 m between MAPMT and solenoid axis.

The scintillation light has therefore to be transported from the active SFT part to the MAPMTs. Clear fibres constitute the best solution since they possess similar optical properties as the scintillating fibres and can be shaped to fit the available space. In order to minimize optical crosstalk on the MAPMT cathode the light guide fibres have to be centered on the corresponding pixel. Optical crosstalk is typically in the order of 2% for a 1 mm fibre centered on the pixel within 0.2 mm [Yos97]. Unfortunately, the center position of the cathode is not exactly correlated with the MAPMT housing. Therefore the center position of each MAPMT cathode with respect to the housing has to be determined. Measuring the position of three of the guide marks on the MAPMT cathode with a precision of approximately 10 μm allows to determine the cathode center position with sufficient accuracy to achieve the above mentioned optical crosstalk level. Deviation up to 0.5 mm has to be taken into account for the actual connection between the light guide and the respective MAPMT.

The connection of light guide fibres to the active SFT part at one end and to the MAPMTs at the other imposes several conditions on the light guide design. Firstly, the number of channels of a MAPMT fixes the number of fibres in a light guide. Sharing of fibres between different MAPMTs is not practical as the whole set-up has to be light tight and each light guide should, in principle, be mountable individually for easy inspection and testing. Furthermore, each light guide needs to be centered precisely on the corresponding MAPMT. The connection of the light guide to the individual scintillating fibres of the SFT has to be precisely aligned as well in order to avoid additional light losses at the connection. To ease restrictions, a slightly larger diameter of 1.1 mm for the light guide fibres is chosen in comparison to 1 mm for the scintillating fibres. 1.1 mm clear multiclad Kuraray fibres are chosen due to their superior attenuation length (9 m) and radiation hardness [Asc97].

The transmission efficiency between scintillating and clear fibre depends, apart from precise alignment, on the distance of their end-faces. The gap width was varied up to 2 mm and the change in transmission recorded. The decrease in light yield is approximately linear to the gap width and was found to be 12% for a 100 μm wide gap [Chu96]. The use of optical grease as couplant was discarded as it enhances crosstalk at the corresponding connection and introduces a time dependent behaviour of the coupling efficiency [Aot95]. This implies the necessity of precisely processed fibre surfaces for the light guide and scintillating fibres of the SFT. The best surface quality was achieved with a two-step procedure, first using a standard ten-blade cutter for coarse machining and then employing a diamond fly-cut tool yielding optical quality surfaces. Transmission efficiencies of 90 - 95% are reported for this kind of coupling [Aot95, Chu96, Asc97] and are achieved within SFT connector design constraints as well.

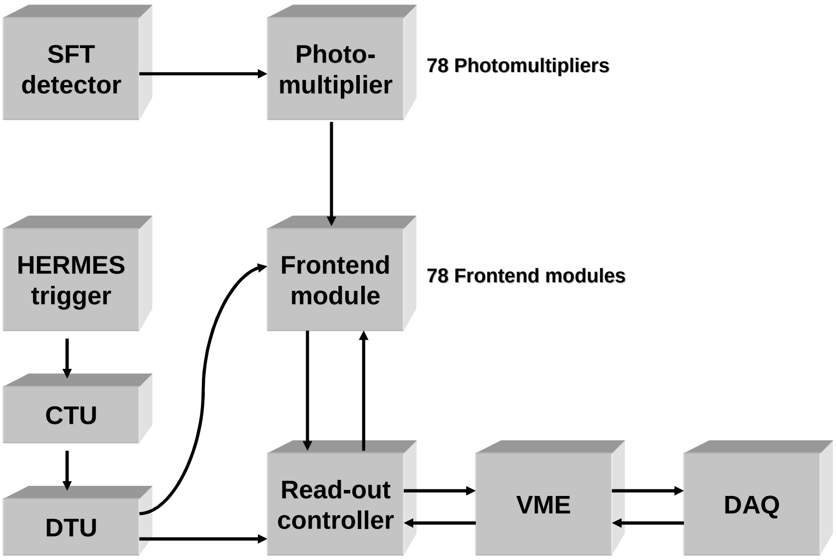

Figure 3.23: Block scheme of the read-out system for the SFT.

The readout electronics for the SFT uses the design of the HADES RICH readout [Kas99]. The simple block diagram shown in Figure 3.23 describes the principles of this readout concept. Analog signals from the MAPMTs are processed and digitized in 64-channel preprocessing Frontend Modules (FM). The digital values (corresponding to a pulse height above threshold of the analog signals) for each channel are transferred through a VME-bus based Readout Controller (RC) to the VME-bus and further by an VME-to-VME interface to the HERMES DAQ system. Zero suppression is enabled on each FM. The Central Trigger Unit (CTU) and the Detector Trigger Unit (DTU) are VME-bus-cards which convert incoming trigger signals and send it to the FM and the RC, respecting dead time and busy states of the readout system.

The FM is a 64 channel data acquisition system on a small PCB. One FM is needed for each MAPMT. In total 78 FMs are needed to read-out the complete SFT. Five FMs are grouped and daisy-chained onto one back plane. 16 back planes is needed in total. Since one RC can handle 8 of these back planes, two RCs are needed. Counting one CTU, one DTU and one VME to VME interface, five VME modules in total are needed to readout the complete SFT. A small custom VME crate is sufficient for this purpose and can be located close to the detector.

The main components of the FM are four GASSIPLEX chips for analog signal processing. Each is a 16-channel analog integrated circuit which uses the peaking time of the integrated and shaped signal as a delay, allowing an external trigger to memorize the information by a Track-and-Hold analog circuit. Using negative input signal, the GASSIPLEX works in a dynamic range up to 500 fC with a gain of 2.2 mV/fC. The GASSIPLEX outputs are connected to half-flash ADCs operating at 20 MHz via a fast video multiplexer. The resulting 10 bit binary words are processed in a pipelined logic inside a re-programmable field programmable gate array (FPGA) which performs signal discrimination, adds a channel number to each data word and generates a hit address list for the 64 input channels. Valid data words are memorized in the first level pipe.

The readout of the data from the FMs is accomplished by the RC. Up to eight FM ports are connected to a passive backplane by a 50-pin ribbon cable. Each port is equipped with its own FPGA performing basic functions of the command and data transfer protocol. The ports are driven in an interlaced mode with effective clock frequency on the port cable of about 4 MHz, while the RC is internally operated at 40 MHz. After a 2$^{\text{nd}}$ level trigger signal the data from the 1$^{\text{st}}$ level pipe in the FMs are transferred to the 2$^{\text{nd}}$ level pipe on the RC. These also provide an extension of the fibre addresses to ensure a unique channel number in the whole readout system. This results in 32 bit wide data words. Using a common VME-bus CPU, a transfer rate of about 20 MByte/s to the VME-bus can be achieved.

3.7 *The Photon Detector*

The outermost sub-detector is the Photon Detector (PD). The PD improves the capability of the Recoil Detector to suppress background by rejecting events in which an intermediate Δ^+ resonance is produced. This is achieved by detecting at least one of the photons into which a neutral pion emitted from a Δ^+ decay subsequently decays. Direct measurement of π^0 particles becomes possible upon detection of two separate decay photons. Also, the first layer of the PD improves the pion/proton separation capability of the SFT, a pion rejection factor of 10 is expected for momenta up to 800 MeV/c

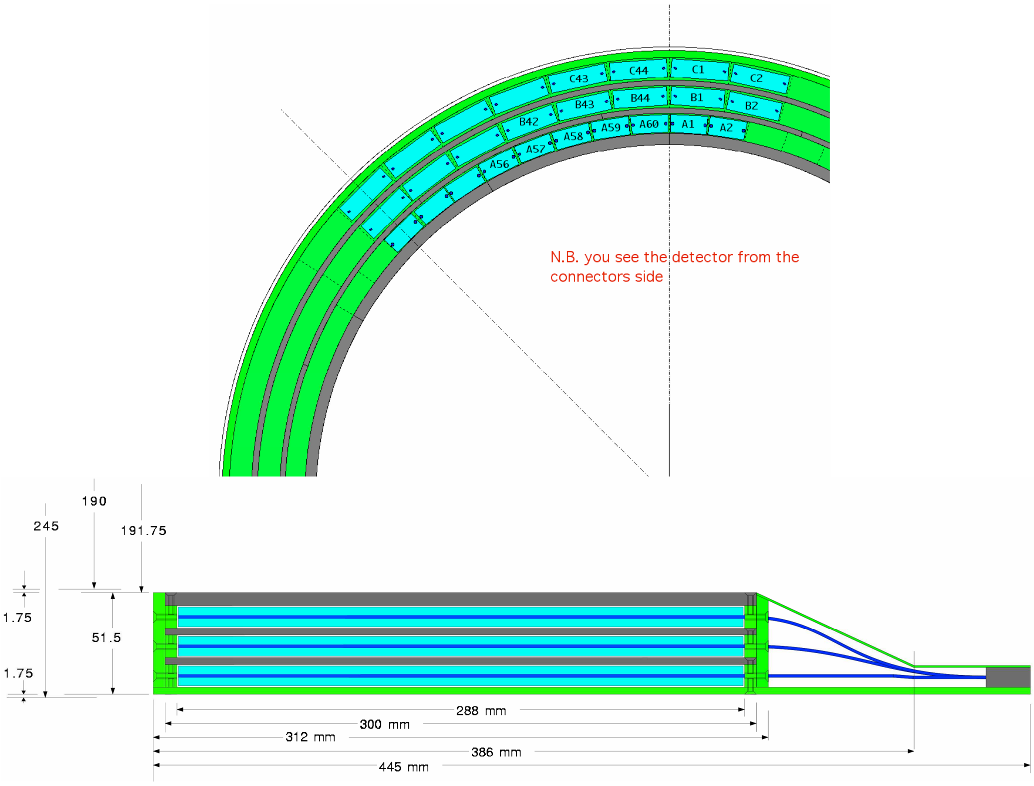

Figure 3.24: Schematics of the PD [Tyt03]. Upper diagram is shown from upstream perspective with numbering scheme, lower diagram shows longitudinal cross-section. Grey shalding represents tungsten preshower layer, blue represents scintillator material.

[Her01]. Finally, the PD provides a trigger for cosmic ray events, providing a method to align the sub-components of the Recoil Detector. The PD is constructed from six layers, alternating between a tungsten converter layer from which incident charged particles produce electromagnetic showers, and a scintillator layer which detects these showers. Figure 3.24 illustrates the geometry of the PD, and Figure 3.25 is a photograph of the detector taken during its construction. The inner layer is segmented into 60 trapezoidal blocks aligned parallel to the beam axis, the middle and outer layers are segmented into 44, aligned at +45 and −45 degrees to the beam. Scintillation light produced by incident photons or cosmic ray particles is collected by two light guide fibres in grooves on the sides of each scintillator block. The

Figure 3.25: Assembling of the PD. The scintillator strips of the outer stereo layer are visible, as are wavelength shifting fibres and the connector rings.

light guides are connected to 64 channel Hamamatsu PMTs and the signal is read-out via 32 channel CAEN QDC v792. The PD is positioned between the second layer of the SFT and the recoil magnet, its extent having inner and outer radii of 190 mm and 250 mm respectively [Tyt03].

The PD efficiency is constrained mainly by geometry. It is known that decay photons are often emitted at low polar angles. Photons emitted at 220 mrad will enter the standard HERMES acceptance while up to 400 mrad photons will not be detected at all. Despite the 2π azimuthal coverage of the PD, its length is restricted to roughly that of the Recoil Detector. Detection probabilities are calculated to lie between 77 and 80% for a single photon, the situation is much worse for a pair of photons from the same vertex and in this case the probability lies between 18 and 20% [Her01].

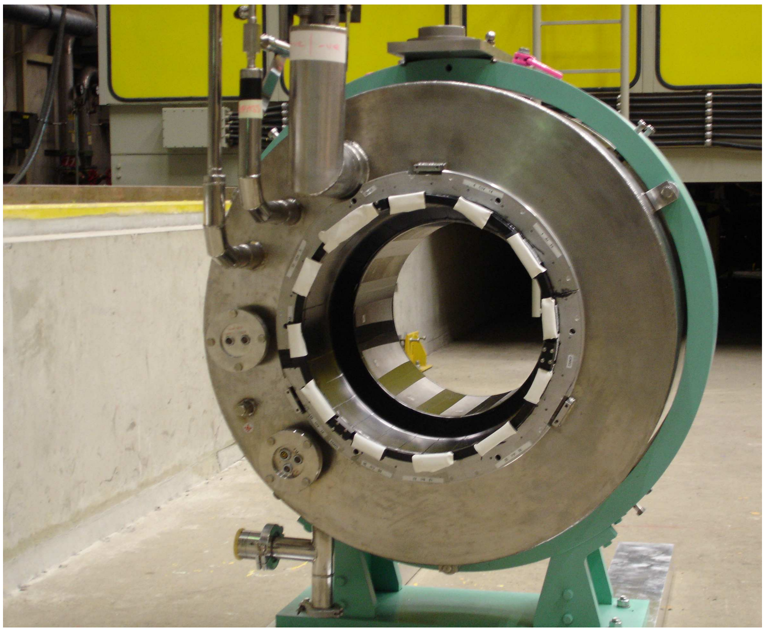

Figure 3.26: Photograph of the Recoil Detector Superconducting Magnet.

3.8 *The Superconducting Magnet*

The Recoil Detector is finally surrounded by a Superconducting (SC) 1 Tesla solenoid magnet. The primary purpose of the Recoil Detector SC magnet is to provide a means for the SFT to measure track momentum by bending charged particle tracks in a 1 T magnetic field. Additionally, the magnet protects the SSD and SFT from background electrons emitted from Møller scattering events by allowing these electrons to spiral forward in the magnetic field.

A 20% or better field homogeneity is required to ensure the momentum resolutions of the SSD and SFT detectors are smoothly connected. A 0.7 T field strength near the beam line is adequate to sufficiently reduce Møller background. A SC coil was chosen due to space constraints within the experimental area. Liquid helium is supplied to the magnet to allow it to be cooled down to a working temperature. The magnet, constructed by the Efremov Institute in St. Petersburg, it is shown in Figure 3.26.

3.9 *Expected Detector Performance*

3.9.1 *Kinematic Coverage*

The acceptance of the SSD and SFT is optimized to match the recoil proton kinematics shown in Figure 3.4. As the SSD is placed inside the beam vacuum, the lowest momenta that can be detected are given by a threshold due mainly to the aluminium target cell (75 μm thickness), to the kapton foil (50 μm thickness) and to the inner silicon module (300 μm thickness). For the requirement of a signal in both silicon layers this threshold is 135 MeV/c; if only a signal in the first layer is required this threshold drops to an average value of 106 MeV/c.

The acceptance in the azimuthal angle ϕ is given by the position and size of the second layer of the SSD. The necessity of a holding structure for the SSD, the equal size of different SSD modules and the necessity to have space between the target cell and the SSD lead to an acceptance of about 4.8 rad or 76% of 2π. For the first layer of SSD alone this would increase to 5.7 rad or 90%. The SFT alone would have a ϕ acceptance of 2π, neglecting the support structure of the target.

The kinematic distributions for the recoil protons in the Recoil Detector acceptance from the different physics processes of interest, based on Monte Carlo before the production of the detector, are shown in Figure 3.27. The boxes indicate the acceptance of SSD and SFT. Distributions without boxes have been already shown in Figure 3.4. There are only small differences between the kinematic distributions for recoil protons from DVCS and exclusive meson-production. However, the actually measured BH/DVCS process yields comparatively more statistics at lower momenta. The protons resulting from Δ^+ decays have on average lower angles and higher momenta compared to *direct* protons. A large fraction of them is therefore not seen by the Recoil Detector.

In addition to the recoil proton all other potential reaction products (see Figure 3.1) should be detected if possible, especially pions and photons resulting from Δ^+ decays; neutron detection is not possible in this design. The distribution of momentum versus polar angle for positive pions from Δ^+ decays is shown in Figure 3.28, together with a box that indicates the

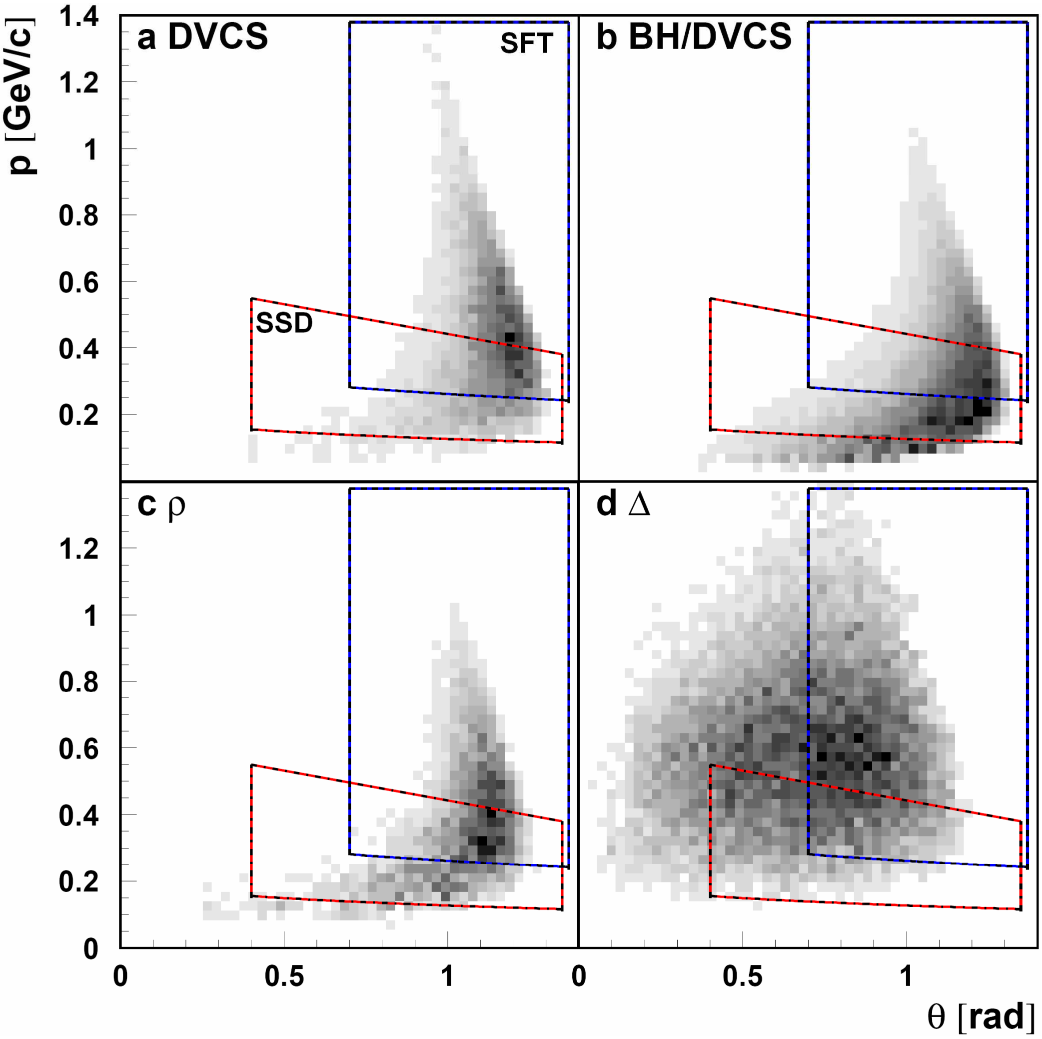

Figure 3.27: Recoil proton momentum versus polar angle with respect to the beam for (**a**) DVCS only, (**b**) BH/DVCS, (**c**) exclusive ρ^0-production, (**d**) Δ^+ decays. The lines indicate the kinematic coverage by SSD (red) and SFT (blue). Studies based on Monte Carlo before the production of the detector.

acceptance of the SFT. The central part of the distribution is covered, but especially at lower angles a lot of statistics is lost. If also the detection efficiency of the SFT is taken into account, about 44% of the pions will be detected. The geometry of the setup makes it impossible to extend the detector further downstream to cover smaller polar angles.

Two-thirds of all Δ^+ resonances decay into a neutral pion and a proton;

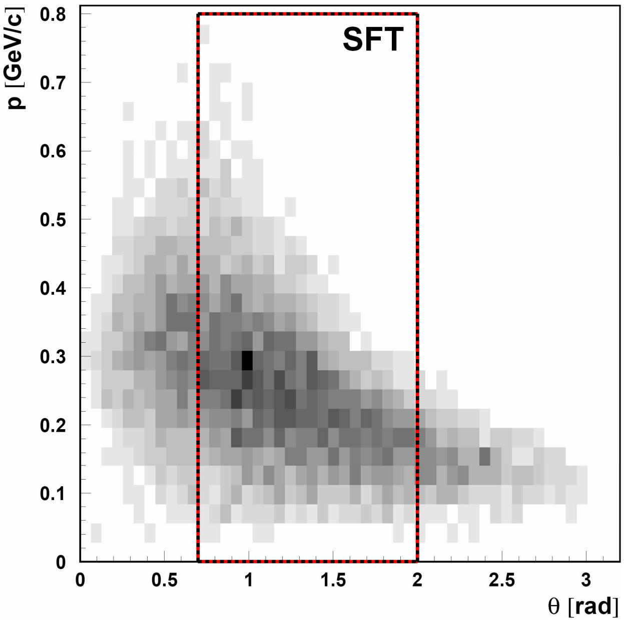

Figure 3.28: Distribution of momentum vs polar angle for π^+ from Δ^+ decays. The box indicates the acceptance of the SFT.

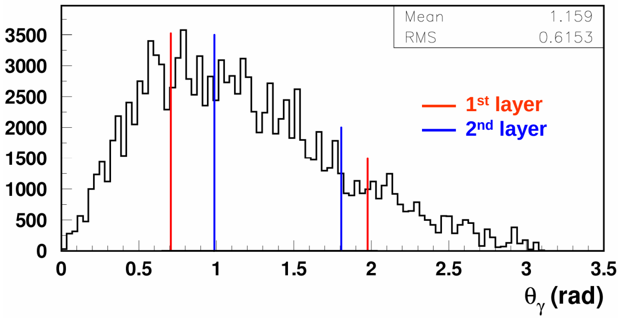

Figure 3.29: Angular spectra for photons resulting from neutral pions from Δ^+ decays. The lines indicate the acceptance of the first two layers of the PD.

the neutral pion in turn decays into two photons. Figure 3.29 shows the angular spectrum for the photons together with lines indicating the acceptance of the first two layers of the PD. For the generation of this spectrum a production vertex at the target center is assumed. In the case of π^0 decays the PD will detect one of the decay photons in 80% and both decay photons in about 20% of the cases [Her01].

3.9.2 *Resolution in p, t and ϕ*

For the SSD and the SFT two different methods are used to measure the momentum of the recoil particles. The method for the SSD is based on the total energy deposition in both layers of silicon in combination with the reconstructed track direction. The method for the momentum reconstruction with the SFT is based on the deflection of the particle tracks in the magnetic field. The resulting momentum p of the particles in combination with the polar and azimuthal angles θ and ϕ yields all three components of the particle momentum. The precision of the momentum measurement with the SSD is limited by the statistical fluctuations in the energy deposition and the nature of the dependence of the energy loss on the momentum. As seen in Figure 3.8 up to 500 MeV/c the energy loss for protons is a steep function of momentum making it well suited for momentum reconstruction. At higher momentum the dependance on momentum decreases leading to an increased momentum uncertainty. For the SFT this limit results mostly from the magnitude of the longitudinal magnetic field, from the fiber size, from the diameter of the detector and from the multiple scattering in the material in front of the detector and in the inner barrel of the SFT.

Resolution studies were carried out based on Monte Carlo before the production of the detector [Her01]. Figure 3.30 shows the resolution for proton momenta; if momentum is measured by the SSD the resolution rises from 1.5% at momenta below 200 MeV/c (stopped protons) to about 9% at 500 MeV/c. The resolution provided by the SFT for protons below 500 MeV/c ranges between 13% and 20%. For the upper momentum cut-off of the SSD a detection threshold of 3 MIPs was assumed. No assumption was done on detector noises. The increase towards lower momenta for the SFT is caused by multiple scattering. Above 500 MeV/c the recoil proton momentum is reconstructed only by the deflection in the magnetic field, with a constant resolution of about 13% for a magnetic field of 1 Tesla. The momentum resolution delivered by the SFT for pions from Δ^+ decays is about 10%. In contrast to the SSD, the SFT needs the position of the electron beam for the momentum reconstruction. The typical beam drift in the HERMES target region is of the order of 1 mm. A Monte Carlo simulation to study the effect

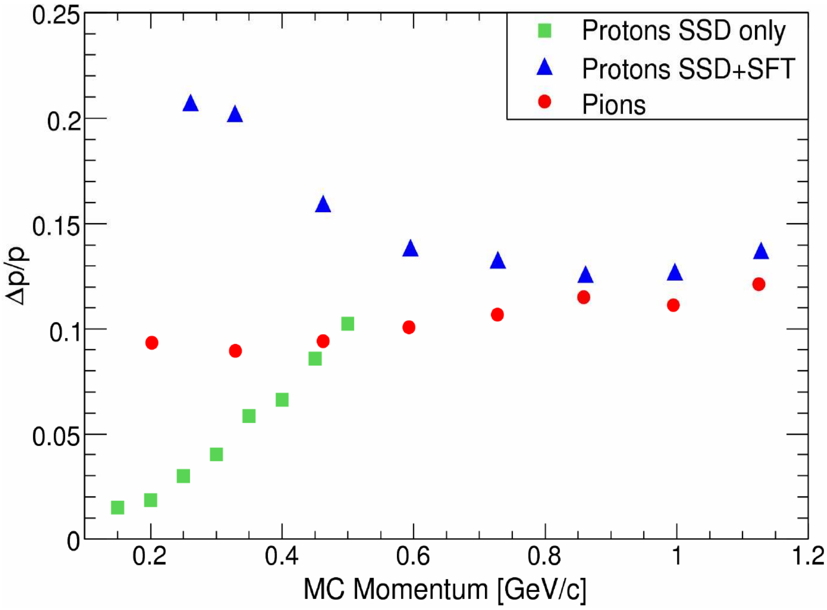

Figure 3.30: Momentum resolution for SSD and SFT [Her01].

of the shifted beam showed that this degrades the momentum resolution of the SFT by a few percent.

As mentioned in Section 3.3, the variable t can be now determined from the momentum of the recoil proton alone (Expression 1.1). Hence, for events with low momentum recoil protons, the good momentum resolution of the SSD determines the resolution in t. The right panel of Figure 3.31 shows the t resolution obtained by the forward spectrometer for BH/DVCS and exclusive ρ^0 production. Compared to this t resolution, the Recoil Detector provides an improvement by about an order of magnitude for DVCS events at low values of t. At medium values of $-t$ (0.25 - 0.5 GeV^2), where the SFT will mainly be used, the resolution in $-t$ is improved by a factor of two for DVCS events and about the same for exclusive ρ^0 production.

As it will be discussed in Section 6.4.3, the extraction of azimuthal asymmetries as a function of values of t implies the problem that results are shown in an unphysical region where no comparison to theoretical predictions is possible, since the $-t$ distribution of exclusive events extends also to negative values (Figure 6.6). In order to eliminate this feature without detecting the hadronic final state, a price has to be paid: if the process is elastic, energy

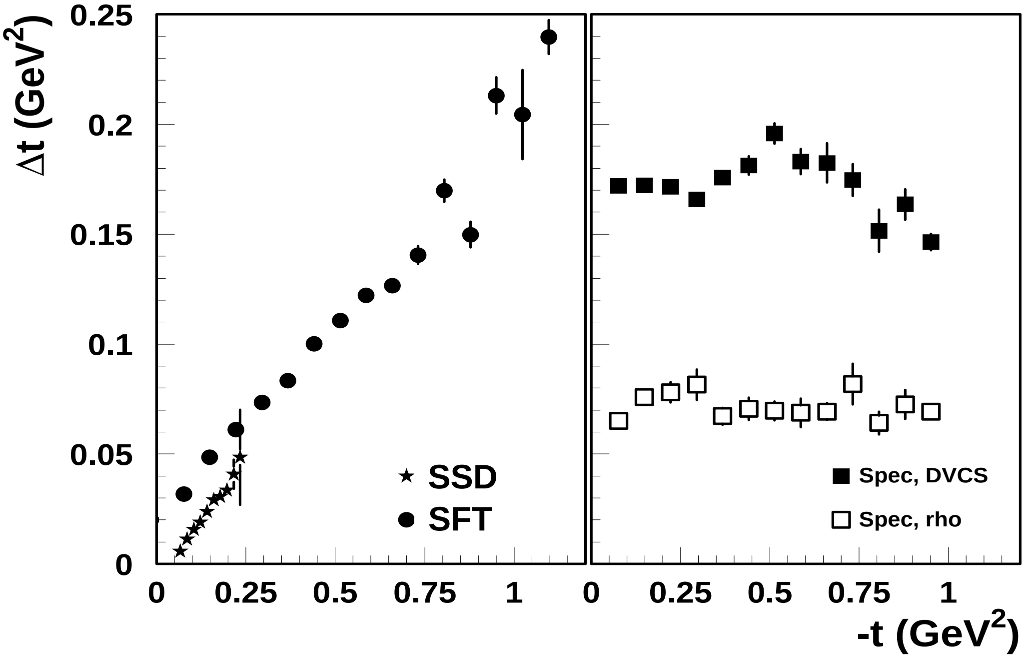

Figure 3.31: Resolution in $-t$ for SSD and SFT for DVCS (left) and for the forward spectrometer for ρ production and DVCS (right). Monte Carlo simulation.

and momentum conservation can be used to remove E_γ from the calculation of t, resulting in a closed expression t_c (Expression 6.1) where the proton mass is assumed to be equal to the missing mass. Consequentely the t resolution of the spectrometer is improved (Figure 3.32). Comparing the spectrometer t_c resolution and the t resolution for the two recoil sub-detectors obtained from the proton momentum, at low momenta the SSD has a much better resolution than the spectrometer and covers values of up to $t = 0.2$ GeV^2. The SFT on the other hand starts at $t = 0.1$ GeV^2 but does not improve the t resolution. Since this measurement is totally independent from the measurement provided by the spectrometer, the combination of both results may still have a reduced error.

The angular resolution provided by SSD and SFT for the azimuthal angle ϕ for the BH/DVCS events is shown in the two panels of Figure 3.33. The result has an average values of 0.031 rad for the SSD and 0.008 rad for the SFT.

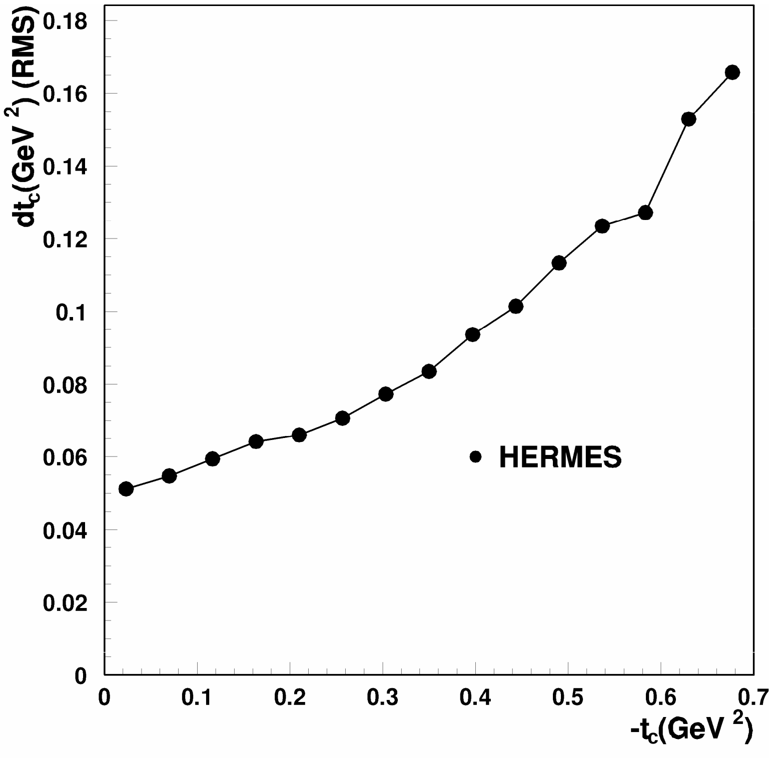

Figure 3.32: The resolution in t_c for the HERMES spectrometer.

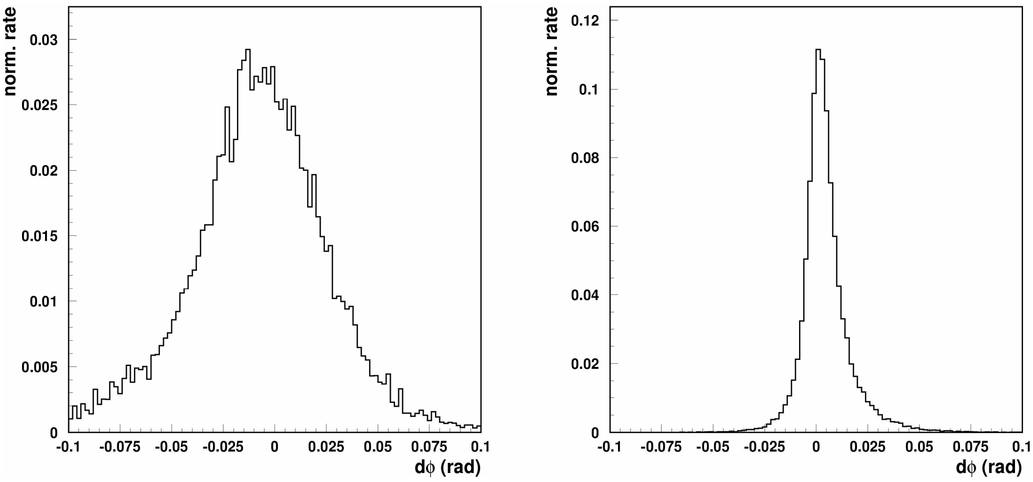

Figure 3.33: Resolution dϕ in the azimuthal angle around the beam. Left panel: SSD, right panel: SFT.

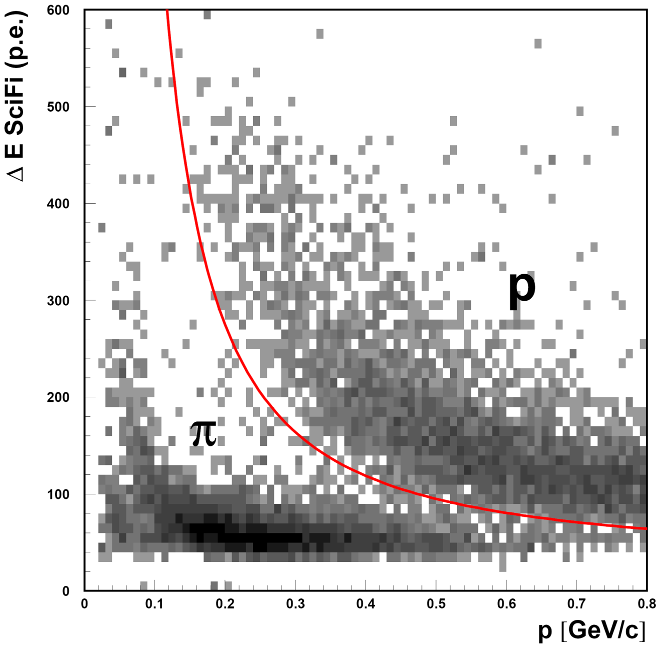

Figure 3.34: Energy deposition versus momentum for pions and protons from Δ^+ decays. The line indicates a possible hyperbolic PID cut. The energy deposition is given in photoelectrons, the momentum measurement is provided by the SFT. Monte Carlo simulation.

3.9.3 *Particle Identification*

The Recoil Detector must be able to distinguish between pions and protons to positively identify the recoil proton. The parameter to use for pion/proton separation is the energy deposition ΔE in the different detector layers, since the ΔE is different for different particles with same momenta (Figure 3.11). For low momenta below 250 MeV/c protons produce large signals in the SSD and no signal in the SFT, because they do not reach it. Pions in the same momentum range produce a signal in the SFT but small signals in the SSD: from the Figure 3.11 it can be noticed that 200 MeV/c pions in the silicon deposit the same energy lost by protons of 1300 MeV/c. As a result an almost complete separation of protons and pions can be expected at these momenta.

Figure 3.34 shows a possible hyperbolic PID cut. In the range of 250 to 450 MeV/c, as determined by the SFT, a momentum dependent cut on the total energy deposition in the SFT provides an adequate particle identifica-

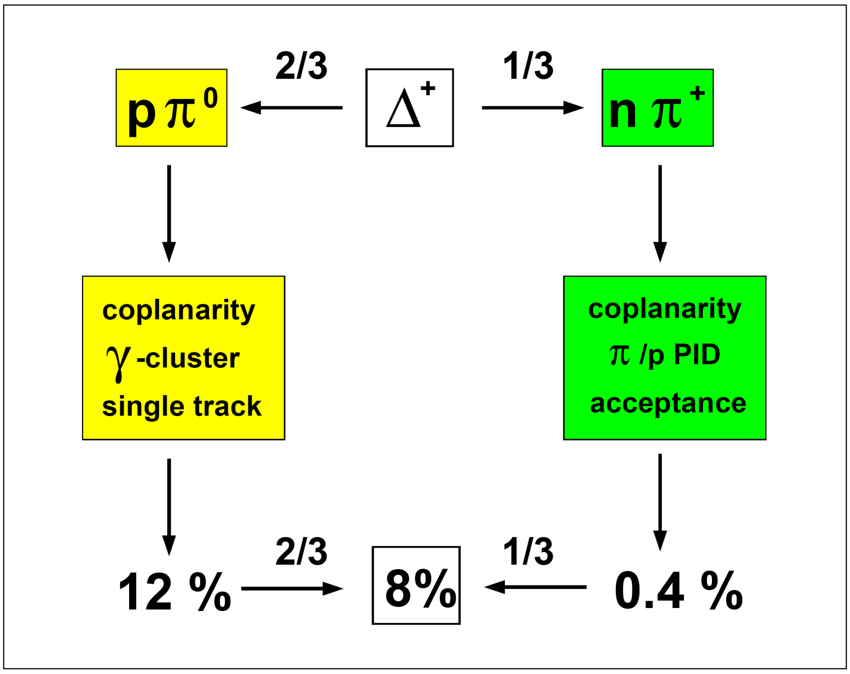

Figure 3.35: Schematics overview of the Δ^+ resonance background suppression.

tion, achieving 90% proton efficiency while rejecting about 98% of the pions, corresponding to an average rejection factor for positive pions of about 50. For momenta above 650 MeV/c the pion rejection factor drops below 10. It is expected that the additional information from the PD will allow to achieve pion rejection factors of 10 or more up to 800 MeV/c.

3.9.4 *Background Suppression*

Figure 3.35 illustrates how the background from intermediate Δ^+ production in BH/DVCS events can be suppressed. About two-thirds of all Δ^+ resonances decay into a proton and a neutral pion. Only 12% of these events pass the rejection cuts requiring exactly one track in the Recoil Detector that passes the coplanarity and matching transverse momentum cut and no additional untracked cluster in the PD. The remaining third decays into a neutron and a positive pion. As can be seen from Figure 3.28 only about 44% of the positive pions are within the acceptance and about 90% of these can be rejected by a PID cut (Figure 3.34). The additional application of

Parameter	**Ideal Performance**	**Detector Performance**
p acceptance	50 - 1400 MeV/c	135 - 450 MeV/c SSD 250 - 1400 MeV/c SFT
θ acceptance	0.1 - 1.35 rad	0.4 - 1.35 rad SSD 0.7 - 1.35 rad SFT
ϕ acceptance	2π	4.8 rad SSD 2π SFT
p resolution	<10%	3 - 9% ($p < 500$ MeV/c) 13% ($p > 500$ MeV/c)
t resolution	<0.07 GeV^2	0.01 - 0.07 GeV^2 ($t < 0.3$) 0.07 - 0.2 GeV^2 ($0.3 < t < 1.0$)
ϕ resolution	<0.05 rad	0.031 rad SSD 0.008 rad SFT
π^+ rej. factor	>10	>10 ($p < 650$ MeV/c)
Δ^+ suppression	>90%	92%

Table 3.2: Overview of requested and expected detector performance according to Monte Carlo simulation.

the coplanarity cut reduces the percentage of Δ^+ decays that pass the cuts to only 0.4%. Therefore in total about 92% of all Δ^+ resonances background events can be rejected. The average Δ^+ contamination inside the DVCS analysis with missing mass technique was estimated to be 10% [Air01]. The combined information from the Recoil Detector will allow to reduce this value to less than 1%.

3.9.5 *Detector Performance Overview*

Table 3.2 shows an overview of the ideal performance based on the DVCS and background processes as stated in Section 3.3 and the projected detector performance based on Monte Carlo studies. In general the detector design meets all the requirements to study the DVCS process. The main exception is the low-momentum cut-off of the SSD at 135 MeV/c. This value follows from the thickness of the target cell wall, the kapton foil and the first silicon layer. The lower boundary of the θ acceptance results from this thickness as well. The design parameters of the SSD have been optimized and the detector has been placed inside the beam vacuum to minimize the material thickness. The given detection threshold does not compromise the physics goals: a further improvement would be marginal since protons with lower momentum are mostly produced in the BH process than in the DVCS process (Figure 3.27). The detector performance is summarized by the reduction by 92% of the background due to intermediate Δ^+ production.

3.10 *Test Beam Experiments*

Prototypes of different detector components were tested in various test beams ranging from low energy protons to mixed pion/proton beams and up to high energy electrons.

The first test beam at the Erlangen tandem accelerator (August 2002) demonstrated that the proposed SSD system can fulfil all the design requirements and that a detector calibration at this facility is possible [Kra05]. Protons of 6.22, 7.00, and 8.00 MeV kinetic energy were used and a surface barrier diode behind the detector served as a trigger detector. As the diode was calibrated using an α-source, the energy deposition in the SSD could be directly measured during the test beam. Thus the calibration was almost independent of energy loss calculations.

The test beam at DESY in December 2002 [Gre02] features a 6 GeV electron beam which was used to test the position dependence of the SSD performance with MIPs. These measurements were performed using a Si-telescope as reference detector. The efficiency of the module was measured to be $\varepsilon = 98.73\%$. The energy response was homogeneous sensor to sensor.

A first test including all the prototypes of the detectors was possible during the GSI test beam (December 2003) [Sei04]. At the GSI accelerator a secondary hadron beam of momenta between 300 MeV/c and 900 MeV/c was supplied. The beam consisted of pions, protons and deuterons. The test setup is schematically shown in Figure 3.36. Since the beam momentum was given at the exit window of the beam-pipe, the SSD was installed as the first device in order to obtain the best possible measurement of deposited energy vs. momentum. Behind it a multi-wire proportional chamber (MWPC) was mounted for reasons of beam diagnosis. One SFT module and one prototype PD module were installed behind the MWPC. Three different scintillation counters were used as trigger detectors and for time of flight separation of the three particle types.

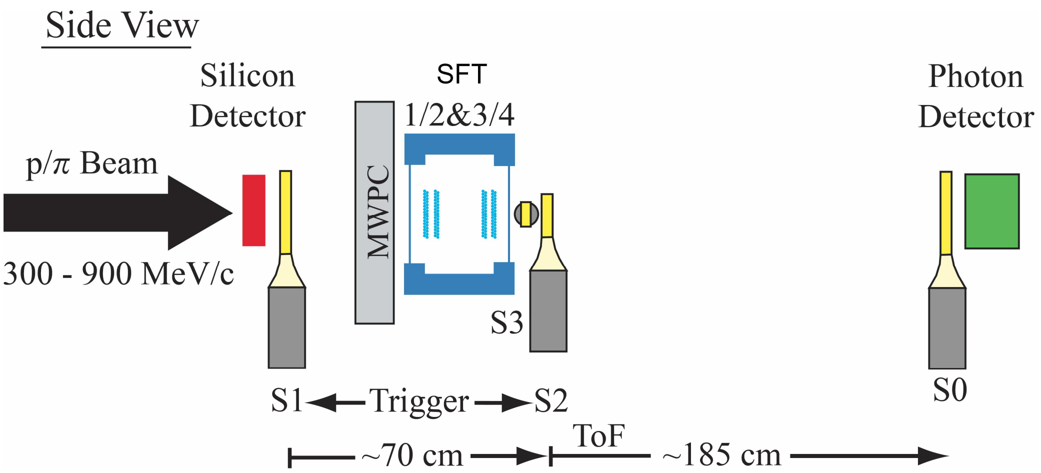

Figure 3.36: Schematic drawing of the GSI test experiment setup [Sei04] indicating the position of all sub-detector prototype modules. The secondary beam enters from the left. The scintillators (S0, S1 and S2) are used for triggering and Time-Of-Flight measurement. Scintillator S3 is employed for efficiency determination of the SFT prototype modules. The Multi-Wire Proportional Chamber (MWPC) provides position measurements.

The three particle types were clearly separated with an efficiency exceeding 99% for all momenta and particle species measured. All prototypes fulfill or exceed the design criteria.

In February 2005, few months before final installation in HERMES, the Recoil Detector (including the SC recoil magnet) was completely assembled in the HERMES experimental hall outside the interlock region and tested with cosmic rays. Results from this test experiment will be shown in the next Chapter.

Chapter 4

Recoil Test Experiment with Cosmic Rays: SSD Performance

A few months before installation in HERMES, the Recoil Detector (including the recoil magnet) was completely assembled in the HERMES experimental hall outside the interlock region. Figure 4.1 shows the fully assembled Recoil Detector on right side, the SFT light guides in the middle and the SFT electronics on left side. From April to August 2005 the Recoil Detector took cosmic data in order to identify and solve problems connected to the whole detector and to its separate sub-systems. In practise this cosmic ray test experiment was carried out in order to test the Recoil Detector assembly, the Recoil Detector with magnetic field, the SSD in vacuum and to check the detector performance.

The detector was operated continuously in several data taking modes, save for regular short periods when the detector modules needed to be switched off to prevent damage (e.g. when ramping the magnet up and down), or when other maintenances were being carried out.

The SSD performance with cosmic rays is presented in this Chapter. Before discussing results, the layout of the silicon module control is presented.

4.1 *Layout of the Silicon Module Control*

Every SSD module is connected through the Analog Clock Control (ACC) module with the HeLix Control Unit (HLCU) and the HELIX ADC (HADC). The HLCU module serves as a controller for the HELIX chip, and the HADC is the ADC for the SSD. Both these modules are VME based and were

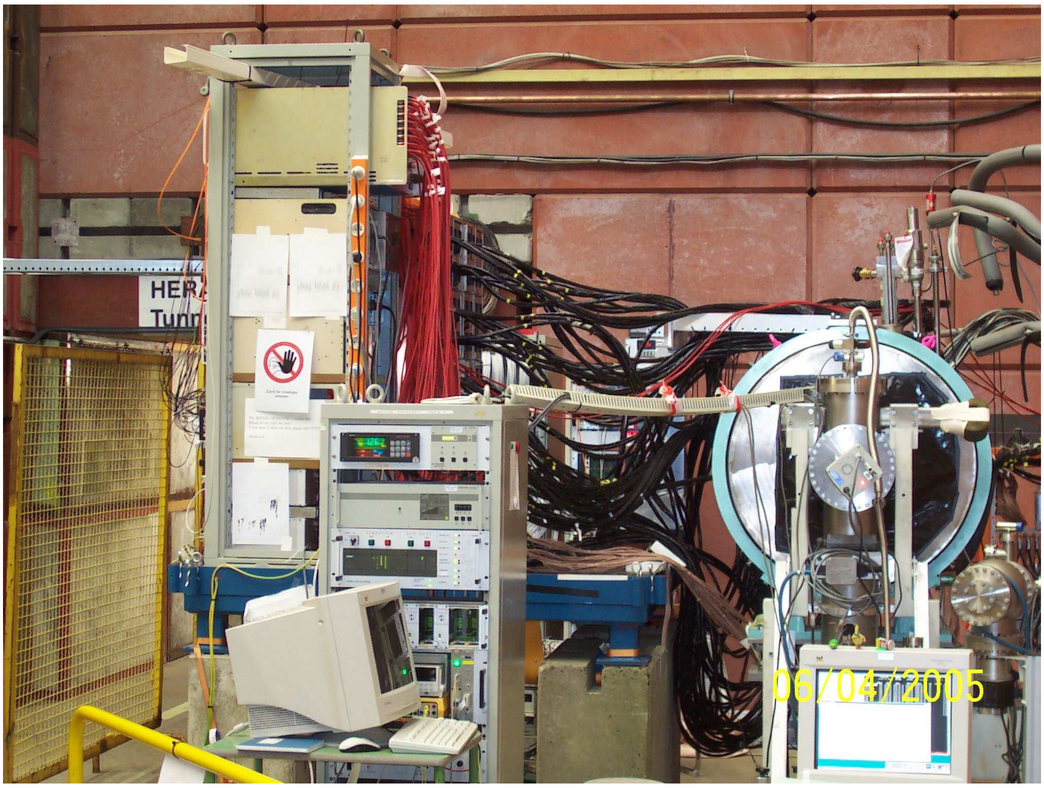

Figure 4.1: Picture of the fully assembled Recoil Detector in the HERMES experimental hall outside the interlock region. The Detector is on right side, the SFT light guides in the middle and the SFT electronics on left side.

designed by Nikhef, Amsterdam and built by The University of Glasgow. As the HADCs and the HLCUs were located during HERMES data taking in the electronics trailer, which is located about 30 meters from the interaction point, a dedicated repeater board was designed. This board is the ACC which will be located close to the SSD itself. An additional functionality of the ACC is the distribution of the required low voltage and bias voltage to the sensors. Moreover, it houses the interface to the radiation and temperature sensors on the hybrid. The DAQ chain is depicted in Figure 4.2.

4.1.1 *Controlling and Programming - HLCU*

The HLCU provides the clock and trigger signals to the HELIX chip [Fal99]. Its outputs are organized in two groups of signals: *current* and *TTL* signals.

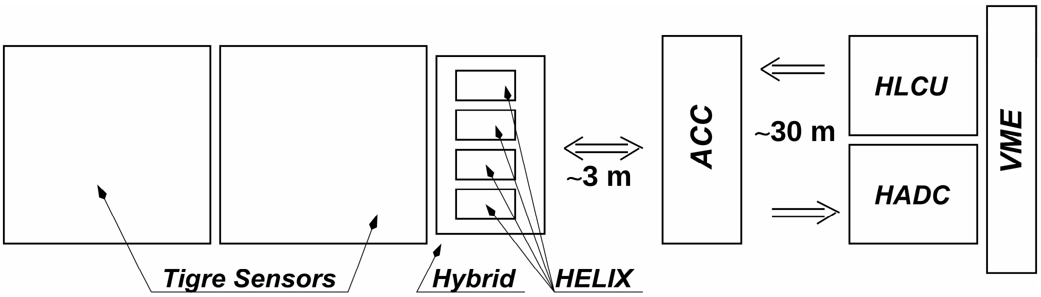

Figure 4.2: Schematic diagram of the silicon module control sequence. The module contains 8 chips for read-out, 4 chips per side.

The *current* group contains the LVDS (*Low Voltage Differential Signaling*) signals. The Clock (defines the ADC sample time) and the trigger (marks a pipeline for read-out) for both N and P side are of this type. The *TTL* group contains the TTL (*Transistor-Transistor Logic*) signals *reset* (defines the start of writing data to the pipeline), *Sload* (defines a data download sequence), *test-pulse N* and *test-pulse P* (generate a test signal at the input stage of each channel) with their respective grounds. Up to four chains of SSD modules can be connected to the HLCU. The HLCU has four inputs: clock, trigger, reset, and test-pulse input.

The HLCU also contains several programmable delays: the Clock Delay between the incoming and outgoing clock and the Clock Difference between P and N side, needed to cope with the different mobility of electrons and holes in silicon. All delays are programmable in steps of 0.5 ns. The delays are needed to get an optimal signal out of the sensors (see Section 3.5.3).

4.1.2 *Module Read-out - HADC*

The HADC module digitizes the analog signal coming from the HELIX chips. On every active phase of the clock, one channel is digitized. Two hybrids can be connected to one HADC. The HADC module also performs zero suppression (pedestal subtraction) and common mode noise calculation and correction. A definition of common mode noise is given in the next Section.

4.1.3 *Interfacing - ACC*

The ACC serves as a repeater board for the signals coming from the HLCU, and has some line drivers to send the HELIX analog out to the HADC in the electronics trailer. The ACC also accepts the ±2 V lines from the low voltage power supply as well as the bias voltage. Since the low voltage directly connects to the preamplifier, it is very important to make the low voltage as free as possible of noise. All TTL signals needed for the logic devices on the hybrid are set between -2 and +2 V before being sent to the hybrid. As a consequence, the entire hybrid is working between these two voltages relative to the 70 V bias potential. Additionally, the ACC also contains the interface for the radiation and temperature monitors on the hybrid. One ACC module is needed for every SSD module.

4.2 *Representation of the SSD Chip's Output Signal: Pedestal and Common Mode Noise*

When the HELIX chip receives a trigger signal, the signals of its 128 channels stored in the pipeline, corresponding to that trigger, will be read-out. The HELIX output of one event coming from several sources can be written as:

$$PH_i^k = S_i^k + P^k + N_i^k + CMN_i \quad , \tag{4.1}$$

in which:

- i denotes the event number,
- k denotes the HELIX channel number,
- PH_i^k is the ADC output in counts of the k^{th} HELIX channel from the i^{th} event,
- P^k is the DC offset (pedestal) of the k^{th} channel,
- S_i^k is the real signal of the k^{th} channel from the i^{th} event,
- N_i^k is the random (or correlated) noise of the k^{th} channel from the i^{th} event,

- CMN_i (Common Mode Noise) is a random voltage offset common for all the channels at the chip, which may be due to a common change of the working environment, such as temperature, low voltage power supply for the chip, or electrical pickup which affects all channels equally.

To get the pedestal values, *pedestal runs* are taken when there are no real signals (for example, there is no particle crossing the detector). The pedestal for each channel can then be computed:

$$P^k = \frac{1}{N_{event}} \sum_{i=1}^{N_{event}} \left(PH_i^k\right) \quad .$$

The pedestals are first subtracted for each HELIX channel from the raw data before future analysis. The CMN for each event is estimated as:

$$CMN_i = \frac{1}{N^*_{channel}} \sum_{i=1}^{N^*_{channel}} \left(PH_i^k - P^k\right) \quad ,$$

where $N^\star_{channel}$ denotes the channels of one HELIX chip being selected to calculate the CMN. The HADC modules were designed to choose the first 16 channels not hit by particles within the first 32 channels of the chip. The variance (rms) of the CMN from a certain number of events is then an estimation of the common mode noise level, which can be calculated as:

$$CMN_{rms} = \sqrt{\frac{\sum_{i=1}^{N_{event}} (CMN_i - \overline{CMN})^2}{N_{event} - 1}} \quad .$$

The variance of the common mode noise is a measure of the entity of the common mode noise level on an event by event basis. $S_i^k + N_i^k$ measured by the detector can then be computed by subtracting the pedestal value P^k for channel k and the common mode noise CMN_i from the measured ADC output PH_i^k as:

$$S_i^k + N_i^k = PH_i^k - P^k - CMN_i \quad ,$$

which is the best estimate of the signal induced by the charge generated in the detector. The average value of N_i^k must be zero as the pedestal correction P^k accounts for any constant DC offset. The effect of the noise N_i^k is then to broaden the measured signal. The variance of the noise N^k_{rms} is then a measure of the broadening of the measured signal due to noise. It is calculated as:

$$N^k_{rms} = \sqrt{\frac{\sum_{i=1}^{N_{event}}(PH^k_i - CMN_i - S^k - P^k)^2}{N_{event}-1}} \quad .$$

4.3 *SSD Noise Studies*

4.3.1 *Silicon Mapping*

At the beginning of the cosmic ray test experiment, a well defined nomenclature has been introduced for each of the three sub-detectors. For the SSD the format S[12][IO][1-4] has been used, where 1 or 2 refers to the upstream and downstream respectively. The "I" refers to the inner detectors and "O" refers to the outer detectors. The numbers 1 through 4 are defined to be one of the four quadrants of the SSD. The position of module 1 is arbitrarily chosen to be the lower left quadrant when viewing the detector looking downstream with y pointing upward and x pointing to the left (Figure 4.3). The other quadrants, 2 through 4, are then numbered in a clockwise direction. The inner modules have their N-side facing towards the cell and P-side facing towards outside, while the outer modules have their N-side facing towards outside and P-side facing towards the cell. The strip directions of the P-side and the N-side in one sensor are arranged perpendicularly to each other: P-side strips are parallel to the beam direction and therefore they measure ϕ angle while N-side strips are perpendicular to the beam direction and therefore they measure θ angle. In the Figure 4.3 the numbering of the P side strips is indicated (1 - 128). For each quadrant the P side strips for inner and outer modules are organized in such a way that the sum between one inner strip and its opposite outer strip is always 129.

4.3.2 *HADC Read-out*

The HADC has two main different read-out modes. In the *serial* or *unsparsified* operation mode all enabled channels are read-out when a trigger occurs, while in the *sparse* operation mode only channels that are enabled and triggered (have a signal above a threshold) are read-out. For pedestal

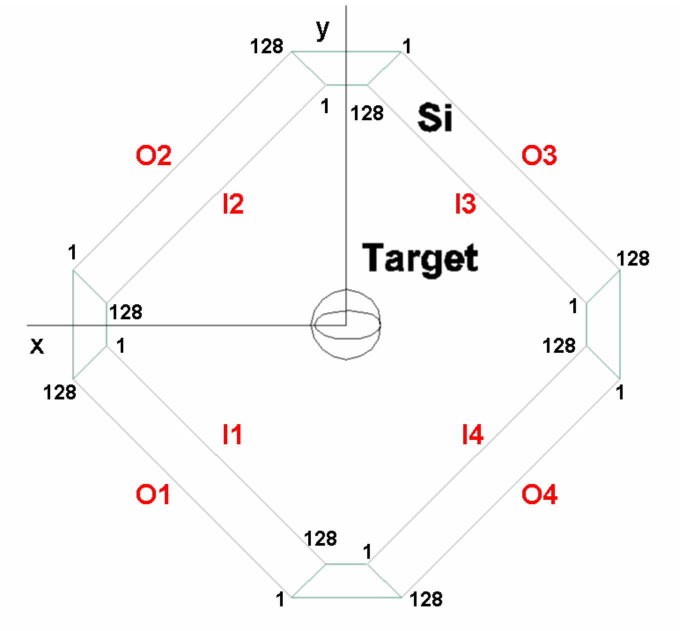

Figure 4.3: Silicon mapping. For the SSD the format S[12][IO][1-4] is used: 1 or 2 refers to the upstream and downstream respectively, "I" refers to the inner detectors and "O" refers to the outer detectors, the numbers 1 through 4 refers to the four quadrants of the SSD. The position of quadrants are numbered in a clockwise direction 1 through 4 starting from the lower left quadrant when viewing the detector looking downstream with y pointing upward and x pointing to the left. In the Figure the numbering direction of the P side strips (parallel to the beam) are indicated.

and sigma studies the unsparsified read-out mode is used, since information for all channels is needed to evaluate sigma values. For *normal* running, since the SSD consists of 4096 strips and 8192 read-out channels (Section 3.5.2), the sparse operation mode is necessary to use, since the total time needed to read-out the detector decreases, as it serves no purpose to acquire data from empty channels.

4.3.3 *Pedestal and CMN*

The pedestal runs (random trigger) supply the information about position and width of the pedestals for all channels of all HELIX chips, both HG and LG.

The data is read-out from the sensor and initially saved on the DAQ PC

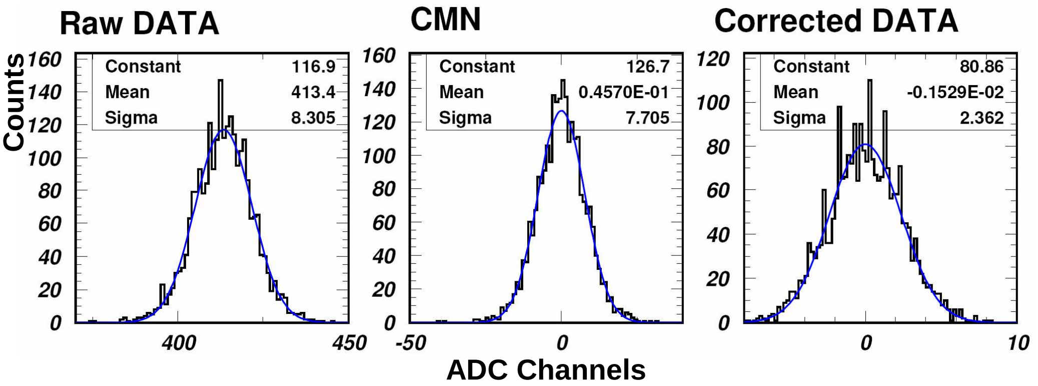

Figure 4.4: Raw ADC output (left panel), CMN (middle panel) and signals (and noises) after CMN correction and pedestal subtraction (right panel) are computed for a pedestal run when there is no particles going through the detector.

as a set of binary files that are later converted into n-tuple format by a C converter routine. These n-tuple files contain all data for each channel. For the pedestal and sigma studies, the options of HADC modules to subtract the pedestal values and to correct for the CMN are not used.

Due to the large number of the channels, pedestal signals are fitted automatically assuming a gaussian shape. Typical data taken during a pedestal run collected for one channel of a HELIX chip in the cosmic ray test experiment is shown in Figure 4.4. The left panel shows a histogram of the raw ADC output values PH_k^i (Expression 4.1). The mean of the histogram is the measure of the pedestal for this channel, which is about 413 ADC Channels. The middle panel shows a histogram of the CMN computed for all 2500 events in that run. The width of the CMN distribution is a measure of how large are the influences to the detector which affect all channels simultaneously on an event by event basis. In this example the CMN distribution has a width of $\sigma = 7.7$ ADC Channels. In the right panel the response of the detector is shown after the subtraction of the pedestal offset and the correction for the CMN. The average is now zero, as it should be, for data where no charge is injected in the read-out electronics and the width of the distribution is reduced from 8.3 ADC Channels to 2.4 ADC Channels, showing the importance of the CMN correction and measuring the residual electrical

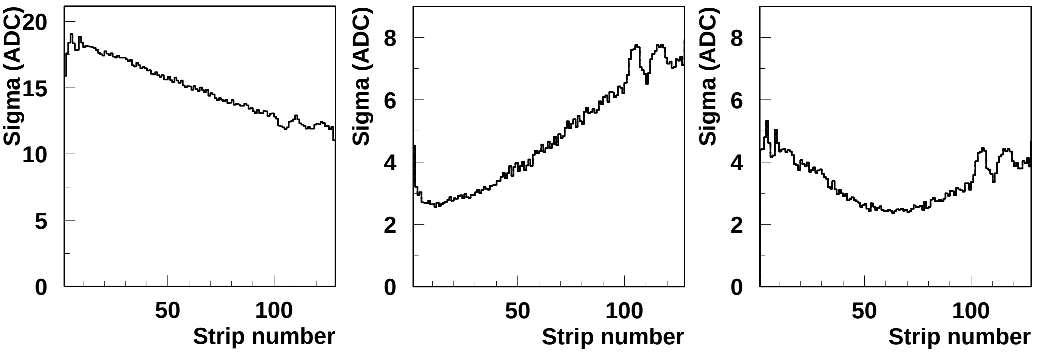

Figure 4.5: Noise performance of HG chips. Left: pedestal sigmas versus the strip number. Middle: noise after CMN correction (using the first 16 channels) versus the strip number. Right: noise after CMN correction (using 128 channels) versus the strip number.

noise.

4.3.4 *Noise and CMN Behaviour*

The noise of the channels is defined as standard deviation σ of the Gaussian fit of pedestal distribution (value 8.3 ADC Channels in the Figure 4.4 on the left panel; the value 2.4 ADC Channels on the right panel defines noise after CMN correction).

In this test experiment it is observed that for the HG chips and for few LG chips noise decreases roughly linearly versus the HELIX channel number. Such a behaviour is shown as an example for a HG chip in Figure 4.5 on the left panel. Therefore, when CMN is evaluated from the first 16 HELIX channels for such chips, noise of the first several HELIX channels is always much smaller than the one of the last channels (Figure 4.5, middle panel). In the same Figure on the right panel, noise corrected for the CMN evaluated over 128 channels is shown for completeness: it has a parabolic shape, resulting in less noise in the middle of the chip compared to the noise in edges. However, an overall improvement in noise can be noticed calculating the CMN over 128 channels.

During HERMES data taking the sparse operation mode will be used. The unsparsified operation mode in HERMES cannot be used at all, otherwise the HERMES deadtime will be dominated by the SSD. The sparse mode can only be used after the pedestal subtraction and the CMN correction. Both have to be done at an early stage and cannot be done off-line. Unfortunately the HADC modules are planned to choose only the first 16 channels of the chip to calculate the CMN, as already mentioned in Section 4.2. Limitations in the HERMES DAQ imposed time restrictions on how long the HADC has to process the data after a trigger is generated, and there was not sufficient time available to make a more complicated CMN subtraction algorithm. Therefore from now on only CMN calculated over the first 16 channels will be treated in this thesis.

It is also observed that the CMN corrected noise and the width of the CMN distribution of the outer modules are typically higher than the corresponding inner modules, and that the HG chips have higher noise and CMN width than the corresponding LG chips. As an example, Figure 4.6 shows the CMN corrected noise (upper panel) and the CMN distributions (lower panel) for the best LG chip (left plots) as well as for the corresponding best HG chip (right plots).

The mean of widths of the CMN distributions for all the LG chips is found to be equal to 3.5 ADC Channels (Figure 4.7, left panel) and for all the HG chips is found to be equal to 11 ADC Channels (Figure 4.7, right panel).

The mean of the CMN corrected noise for all the LG chips is found to be equal to 2.5 ADC Channels (value pretty constant along all the chip) and for all the HG chips is found to be equal to ∼5 ADC Channels, being 2.5 ADC Channels for the first HELIX channels of the chip and ∼8 ADC Channels for the last ones.

4.3.5 *Dead or Noisy Channels*

Based on the output pedestal distributions and sigma values for single channel, it is possible to identify channels which don't have any response to charge produced in the corresponding strip of the sensor (dead channels) or have a sigma value much higher than the mean of sigma values of their closer channels (noisy channels). Figure 4.8 shows examples of noises after CMN correction versus the strip number for four chips. Spikes, corresponding to channels with high sigma values, can be easily noticed.

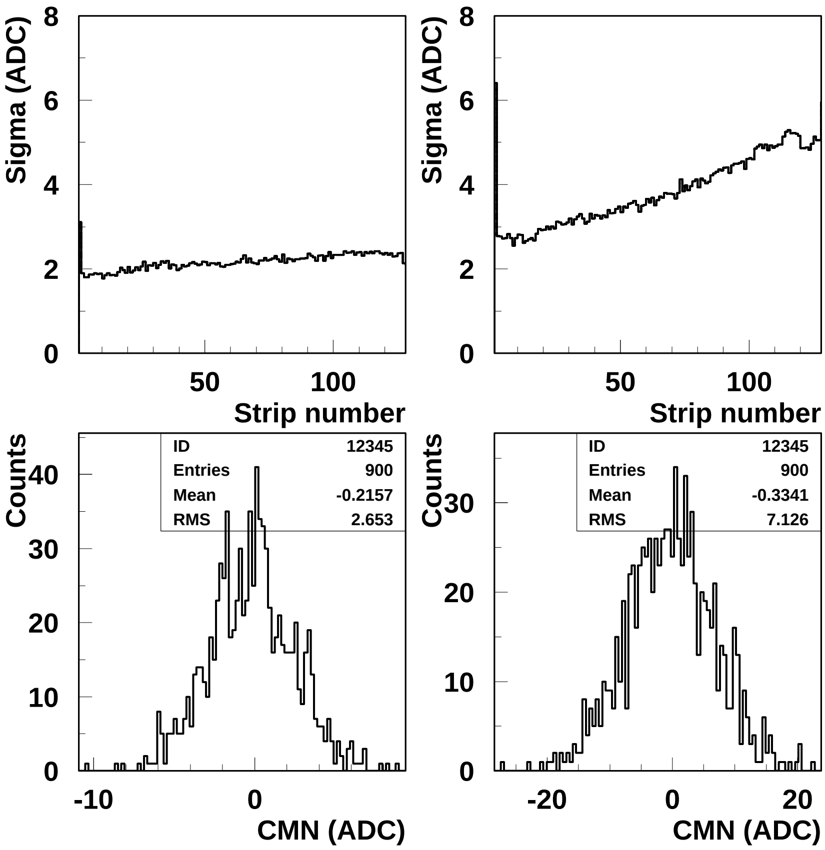

Figure 4.6: CMN corrected noise (upper part) and CMN distributions (lower part) for the best LG chip (left plots) and the corresponding best HG chip (right plots).

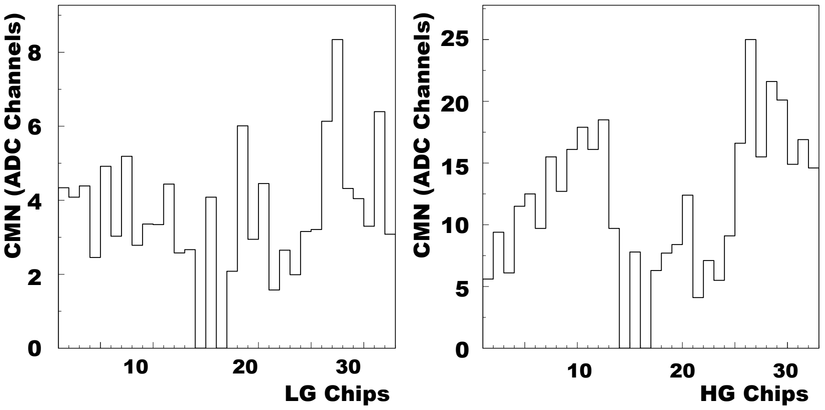

Figure 4.7: Widths of the CMN distributions for all the LG chips (left panel) and for all the HG chips (right panel).

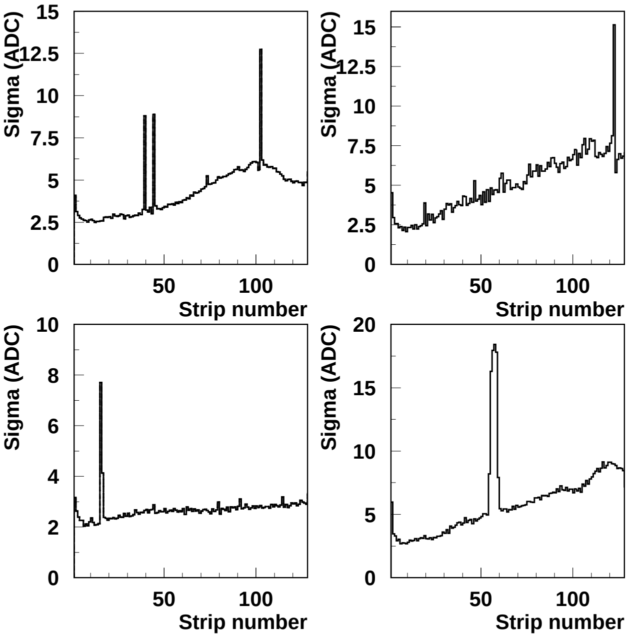

Figure 4.8: Noises for four chips after CMN correction versus the strip number. Spikes corresponding to channels with high sigma values can be easily noticed.

Sometimes it is also observed that the first channel of the chips is more noisy than the corresponding closer channels in the same chip. Figure 4.9 shows examples of noises after CMN correction versus the strip number for four other chips. Spikes in the first channel of the four chips can be easily noticed.

Only 1% of the total number of channels for all the 8 SSD modules is found to be noisy: they are directly deleted from the DAQ.

4.3.6 *Further Noise Studies*

Several measurements have been performed for the SSD to investigate its noise behaviour and to make it as low as possible. In the previous test beam [Gre02], the noise for the LG and HG chips was found to be almost independent on strip number and equal to $2-3$ ADC Channels, resulting in a signal to noise ratio (evaluated only for HG chips) equal to $5-6$ for MIP signals. In this test experiment only LG chips and first channels of HG chips can almost reproduce well the same noise performance. Instead noise level in

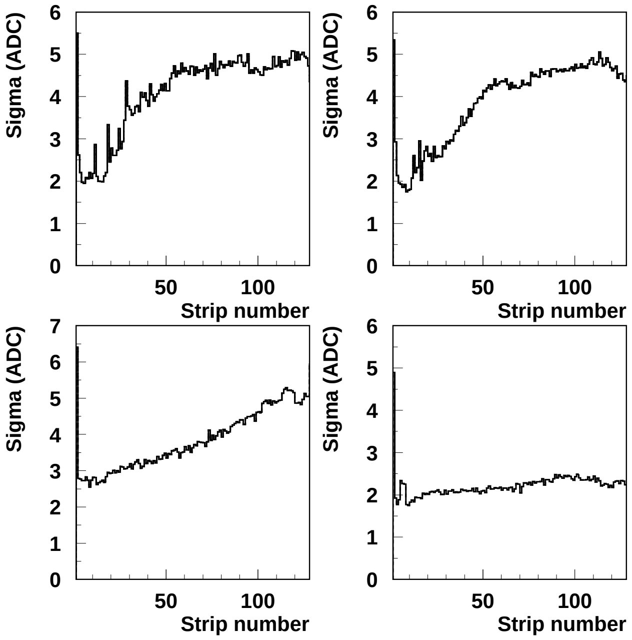

Figure 4.9: Noises for four chips after CMN correction versus the strip number. Spikes in the first channel with a high sigma value can be easily noticed.

the last channels of HG chips can even reach a mean of $7-8$ ADC Channels, resulting in a signal to noise ratio equal to 2 for MIP signals, as discussed in the next Section.

The first feature found in this test experiment is that the low voltage greatly influenced the noise: values were set in order to optimize the noise. Unfortunately, with the exception of the low voltage, no way was found to reduce the noise during the test experiment.

A new bench test was possible in September '05 in order to improve the SSD noise. This bench test was carried out during the dismounting of the Recoil Detector from the HERMES experimental hall in order not to interfere with the development of the other sub-detectors. To protect the final SSD modules, the final detector was not used: a spare scattering chamber, a spare silicon support structure, and a dummy connector chamber were used to make the test. An identical geometry of the final system was guaranteed. A Radio Frequency (RF) shield constructed with 125 μm Mylar and 125 μm Cu which can line the scattering chamber was manufactured.

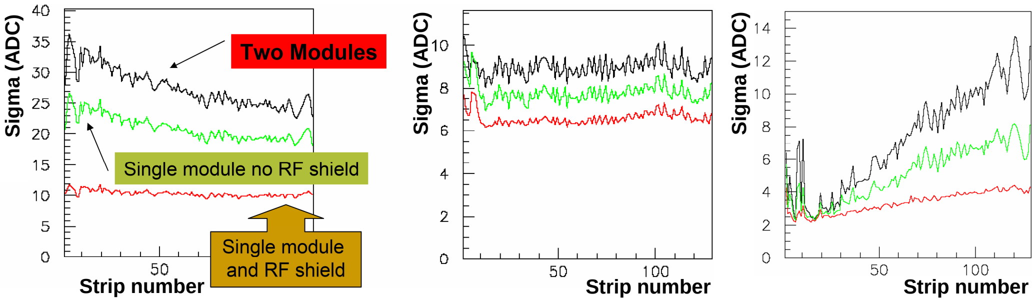

Figure 4.10: Noises for a HG chip (left panel) and LG chip (middle panel) with no CMN correction versus the strip number during the bench test. On the right panel CMN corrected noise for a HG chip [Ste05].

Tests with single module were performed in order to study the effect of an additional shielding and the effect of changing the grounding scheme. The noise level of the SSD module in the test chamber is less than the noise of the outer layer in the cosmic ray test experiment: noise similar to that seen in the previous test beam [Gre02] is observed. Tests with two modules were also performed: noise levels similar to those seen in the cosmic test experiment are observed when two modules are put together. Figure 4.10 [Ste05] shows, for three different conditions, noises for a HG chip (left panel) and LG chip (middle panel) with no CMN correction versus the strip number during the bench test. The linear decreasing of the pedestal sigmas versus the HELIX channel number for HG chips disappears when only one SSD module is installed inside the scattering chamber with the RF shield. When CMN correction is applied (right panel), the noise level decreases drastically reaching values obtained in the previous test beam. This bench test indicates that SSD modules are effecting each other inside the scattering chamber. Modules can couple to one another capacitively through the support structure. An improvement was got by changing the grounding scheme of the detector modules: the reference potential of all silicon modules was capacitively connected to the support structure. After this no change is observed if one or two modules are in operation, as documented by Figure 4.11 [Ste05]. Noise levels similar to those seen in the previous test beam [Gre02] are observed, even if a noise behaviour dependent on the strip number is still present.

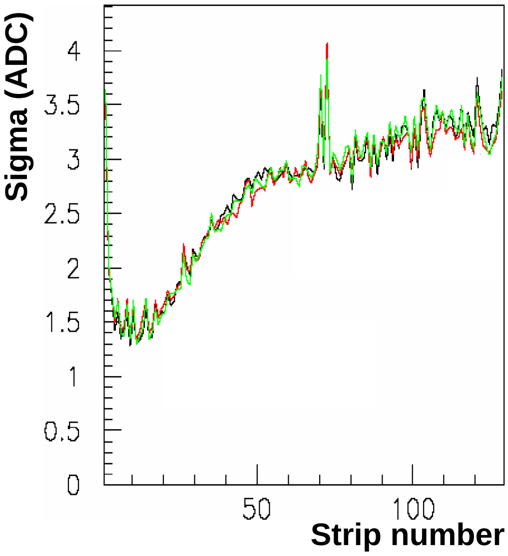

Figure 4.11: CMN corrected noise for a HG chip after connecting the reference potential of all silicon modules to the support structure [Ste05].

4.3.7 *Cosmic Test Noise Conclusions*

Several measurements have been performed for the SSD to investigate its noise behaviour. After first noise optimization, carried out varying the low voltage values, it has been noticed that only LG chips can reproduce same noise performance as seen in the previous test beam [Gre02]. For HG chips it has been observed that noise of last several HELIX channels is always much higher than the one of the first channels. During running period, unfortunately, nothing else has been found which has a positive influence on the noise. In September '05 it was possible to carry out a dedicated bench test, which has indicated that SSD modules are effecting each other inside the scattering chamber. An improvement is obtained by capacitively coupling the reference potential of all silicon modules to the support structure. Noise levels similar to those seen in the previous test beam were then observed, even if a noise behaviour dependent on the strip number was still present.

Additionally a further correction at the software level, that deletes the noise dependence on the strip number, is being investigated and it will be used for the data taken during HERMES running. This software off-line correction will be presented in the next Chapter.

4.4 *SSD Response to Cosmic Rays*

4.4.1 *Cosmic Trigger*

As discussed in Section 3.7, the PD can provide a trigger for cosmic ray events, since its cosmic signals are far away from the pedestal position. Several cosmic triggers have been used for this test experiment: the most used one is mainly a *logical OR* between all lower strips in the A layer. The A layer of the PD corresponds to the inner layer containing scintillating blocks parallel to the beam axis. The other two layers are called B and C layers. The trigger rate of the logical OR is about 15 Hz. Almost all cosmic particles are MIPs. From now on the word MIP is used to identify cosmic particles, well knowing that MIP is only an abstract concept.

However the logical OR doesn't help in extracting MIP signals for the SSD. The MIP signal is expected to have an amplitude of ∼15 ADC Channels. Therefore a clear separation between pedestal and MIP signals is almost impossible due to the high noise level, in particular in the last several channels of the chips, where the pedestal sigma can even reach 8 ADC Channels (Figure 4.5 and Figure 4.8).

A cosmic trigger that partially reduces the probability to extract noise in the detector is mandatory. In the PD MIPs are selected by requiring a signal (above pedestal mean + 28 times noise) in one photon scintillator above and one below the SSD (e.g. strip 58 and 33 in the A layer, Figure 4.12). In Figure 4.13 a typical MIP signal for the PD [VHa05] is shown. The upper plot shows a cosmic spectrum for strip 58 in A layer without any requirement on signal. The lower one shows the same plot, requiring a signal above pedestal mean + 28 times noise in coincidence with the opposite strip 33 in A layer. The trigger rate from this PD coincidence is ∼50 hits/hr.

4.4.2 *Multiplicity and ADC signals*

As already explained, for *normal* running, the sparse operation mode is used, therefore the pedestal subtraction and the CMN correction are performed by the HADC modules. After pedestal determination and subtraction for each channel, a further offset equal to 50 ADC Channels is added to all channels of all the HELIX chips. This offset avoids signals with negative ADC Channels

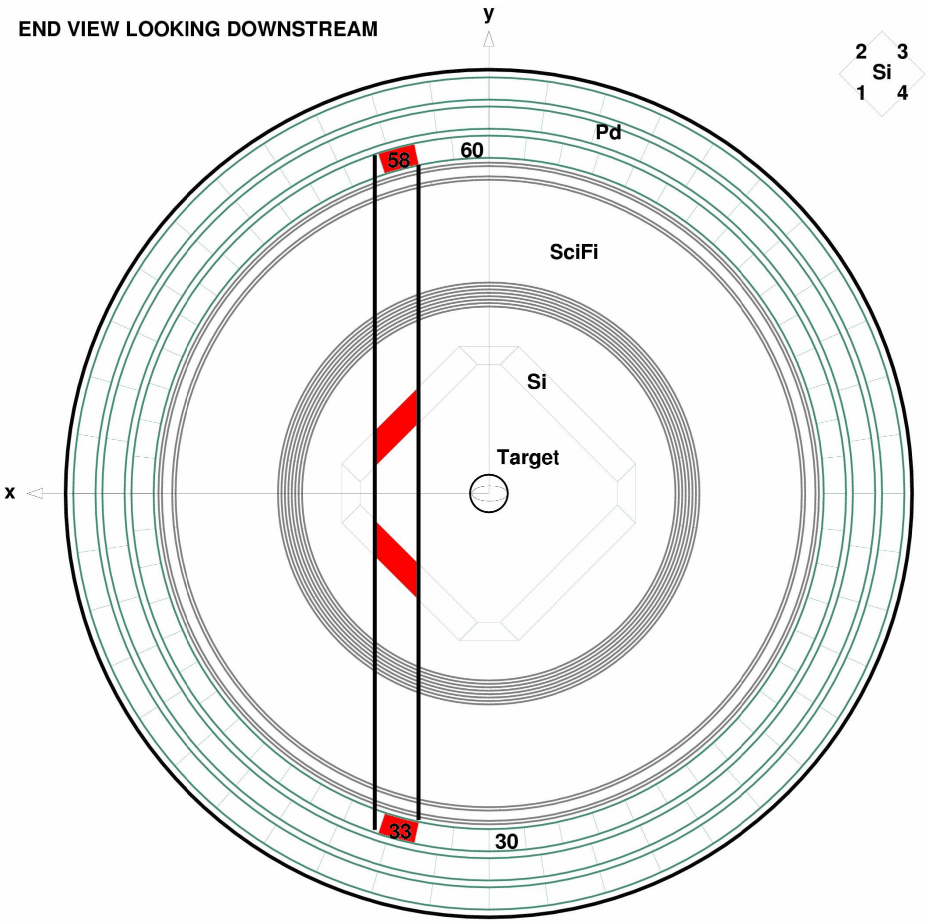

Figure 4.12: Cosmic trigger used to study SSD. In the PD MIPs are selected by requiring a signal (above pedestal mean + 28 times pedestal sigma) in one photon scintillator above and one below the SSD (58 and 33 in the A layer).

after HADC CMN correction. Finally a 10 ADC Channels hard threshold is applied on data.

In addition to the PD cosmic trigger shown in Figure 4.12, a signal in every silicon sensor (eight-fold coincidence, four in the P side and four in the N side) is required together with a multiplicity less than 20 hits for each event and for each sensor. The multiplicity is the number of strips for each event with a signal greater than 10 ADC Channels hard threshold. Since the MIP signal is the lowest one above pedestal for the silicon, only HG chips

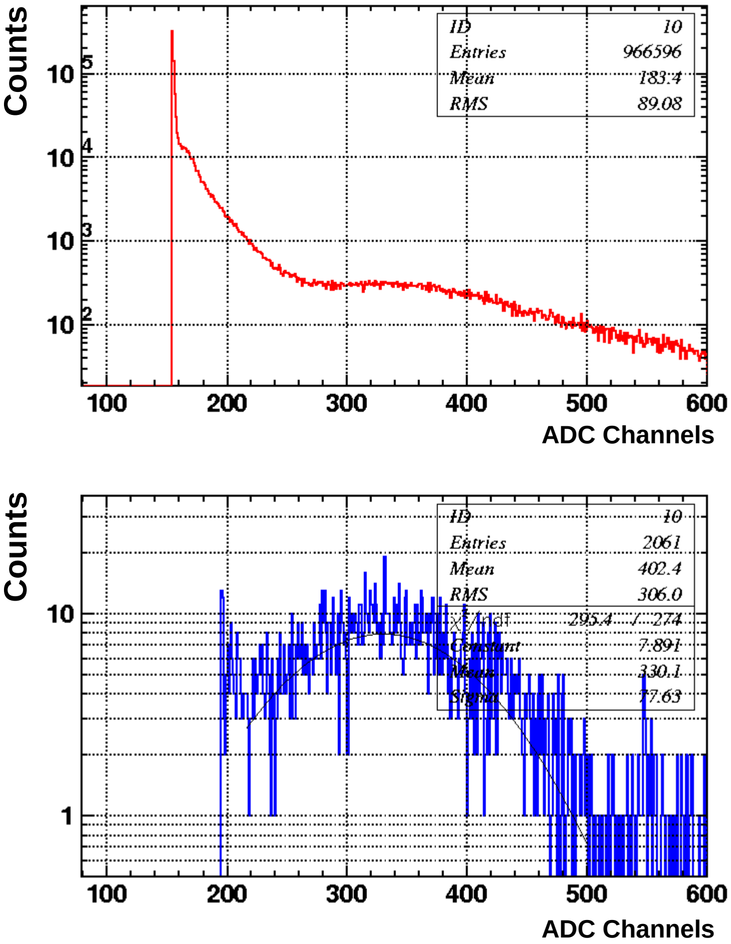

Figure 4.13: Typical cosmic spectra for the PD [VHa05]. Upper plot: cosmic spectrum without any requirement on signal in strip 58 in A layer. Lower plot: cosmic spectrum for strip 58 in A layer, requiring a signal above pedestal mean + 28 times noise in coincidence with the opposite strip 33 in A layer.

are read-out. The effective rate for a silicon sensor is reduced further by acceptance: a trigger rate ~4 hits/hr is recorded.

Figure 4.14 shows typical multiplicity spectra for a P side (left panel) and for a N side (right panel) silicon sensor. The mean of the multiplicity is around three strips, a value higher than expected due to the high noise level. For a MIP, if no noise appears in the detector and no threshold is applied on data, the expected multiplicity is three strips, due to crosstalk and to the 45° incidence angle of the MIPs that produces clustering. As soon as a great hard

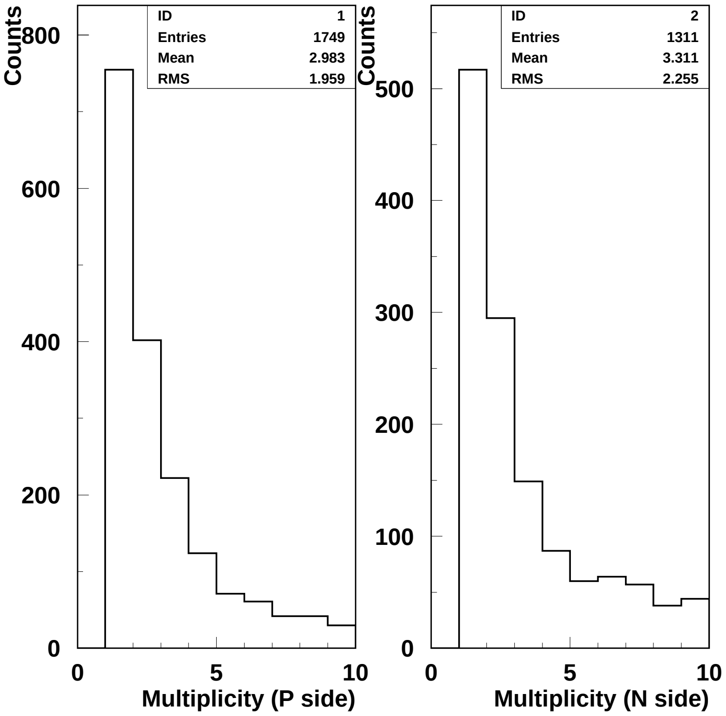

Figure 4.14: Typical HG multiplicity spectra for a P side (left panel) and a N side (right panel) silicon sensors.

threshold (10 ADC Channels) is applied on data, clustering and especially crosstalk are suppressed, resulting in a multiplicity less than 2 strips.

Figure 4.15 shows a typical ADC spectrum (pedestal position is at 50 ADC Channels) for all the strips for a P side silicon sensor: after all requirements to signals, a great separation between pedestal and MIP signal is still not evident, even if a different slope is presented in the plot around 70 ADC Channels.

Figure 4.16 shows typical ADC spectra, obtained from taking only into strips with the maximum ADC value for each event, in order to suppress noise hits. The two plots (left for P side, right for N side) are fitted with a Landau-Gaussian convolution curve. This convolution fit accurately reflects the noise in the signal due to the electronics and has a χ^2 parameter ≤ 1. This is better by half an order of magnitude than the χ^2 parameter of a pure Landau fit, which was used in the previous test beam analysis [Gre02] and

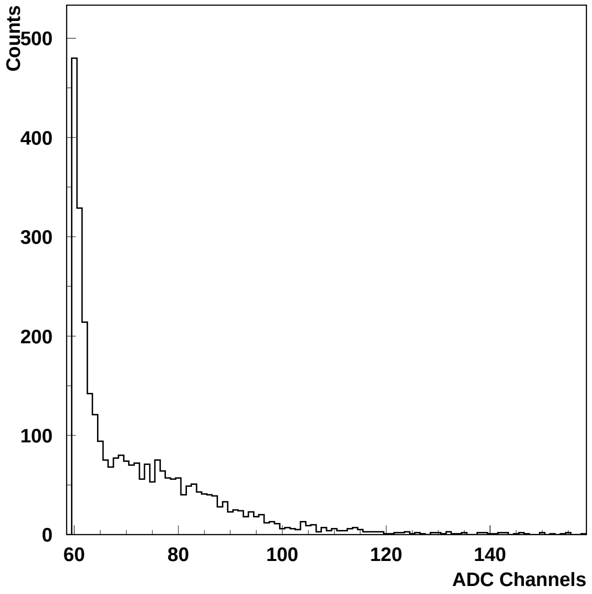

Figure 4.15: Typical HG ADC spectrum for a P side silicon sensor. The pedestal position is at 50 ADC Channels.

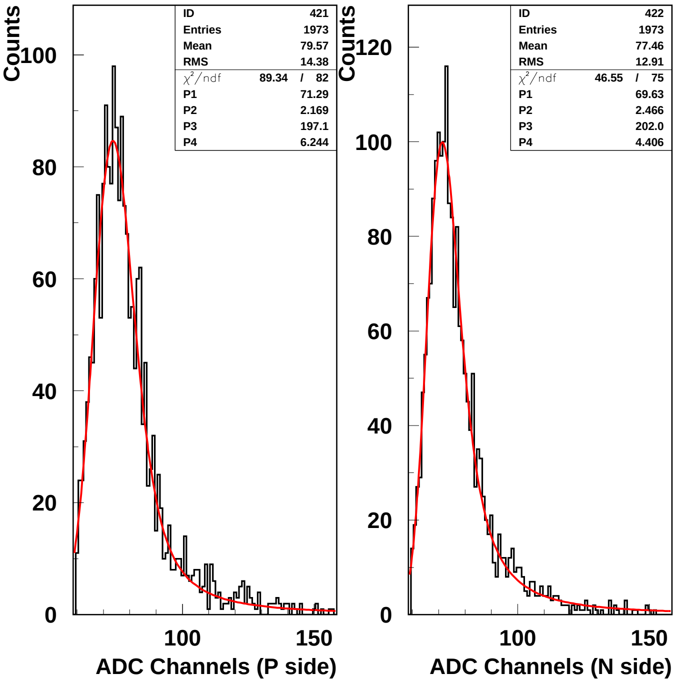

Figure 4.16: MIP signal plots (left for P side, right for N side), with a Landau-Gaussian convolution fit. The peak value $P1$ is the sensor's most probable response to a MIP. The pedestal position is at 50 ADC Channels.

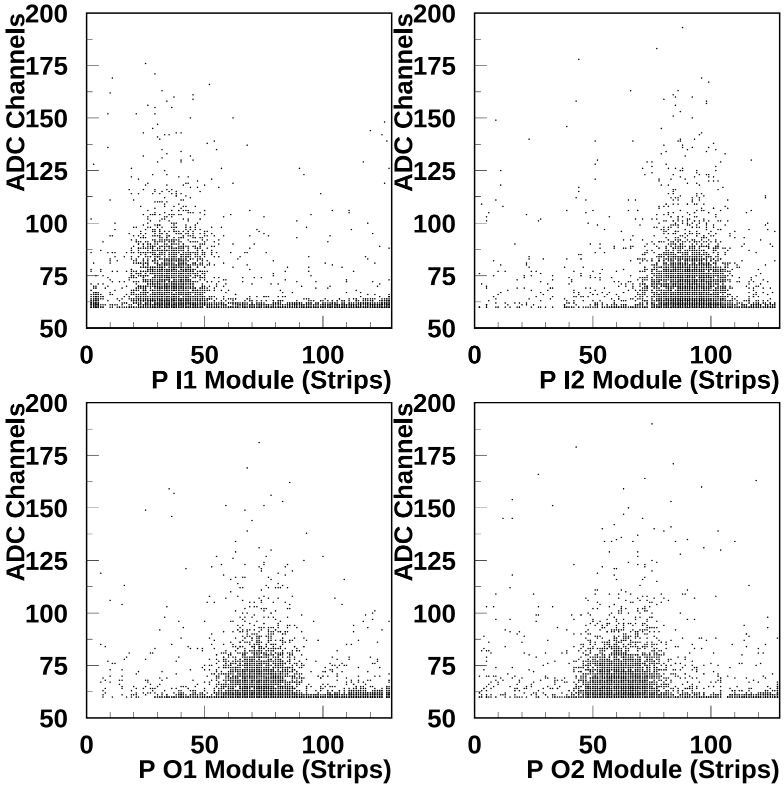

Figure 4.17: ADC Channel signals versus the number of strips for the 4 P side sensors (I1, I2, O1, O2) interested by the PD cosmic trigger. Due to the chosen PD strips for the trigger (58 and 33 in A layer, Figure 4.12), the expected MIP signals lie in the middle of the four silicon sensors.

represents a significant improvement of previous studies. The peak value on this fit, shown as parameter $P1$, is the sensor's most probable response to a MIP. Taking into account the pedestal position (50 ADC Channels), the most probable response to a MIP, crossing the SSD perpendicularly, corresponds to $\sim$14 ADC Channels, being $\sim$20 ADC Channels the signal corresponding to a MIP with an incidence angle of 45°. Due to the noise level into the detector, the signal to noise ratio for MIP signals results to be equal to 5.5 for the first channels of the chip, decreasing up to less than 2 for the last HELIX channels.

Figure 4.17 shows ADC Channel signals versus the number of strips for the four P side sensors (I1, I2, O1, O2) selected by the PD cosmic trigger. Due to the chosen PD strips for the trigger (58 and 33 in A layer, Figure

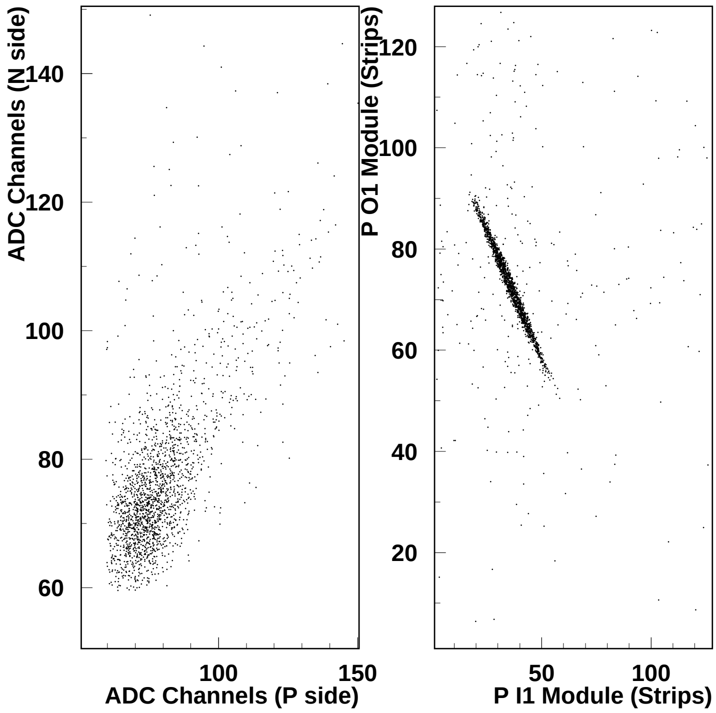

Figure 4.18: Left: typical correlation between P side and N side. Right: typical correlation between inner and outer module strips (P side). Strips with the highest ADC signal for each event are taken into account.

4.12), the expected MIP signals lie in the middle of the four P side sensors, as P strips are parallel to the PD strips in A layer. Since N side strips are perpendicular to the PD strips, the expected MIP signals in the N side silicon sensor lie over all the plane. In the same Figure the higher noise level in the last channels of the chips compared to that of channels in the beginning of the chip can be easily noticed.

When a charged particle goes through the SSD, an amount of electron-hole pairs is created in the silicon. Under normal operating conditions, the SSD is fully depleted with the bias voltage of 70 V across the detector. The generated charge then drifts to the corresponding side. As equal number of electrons and holes are generated by the particles passing through the detector, equal charge should be collected on the P and N side strips. Figure 4.18 on the left panel shows a typical correlation between P and N side signals: only strips with the maximum ADC value for each event are taken

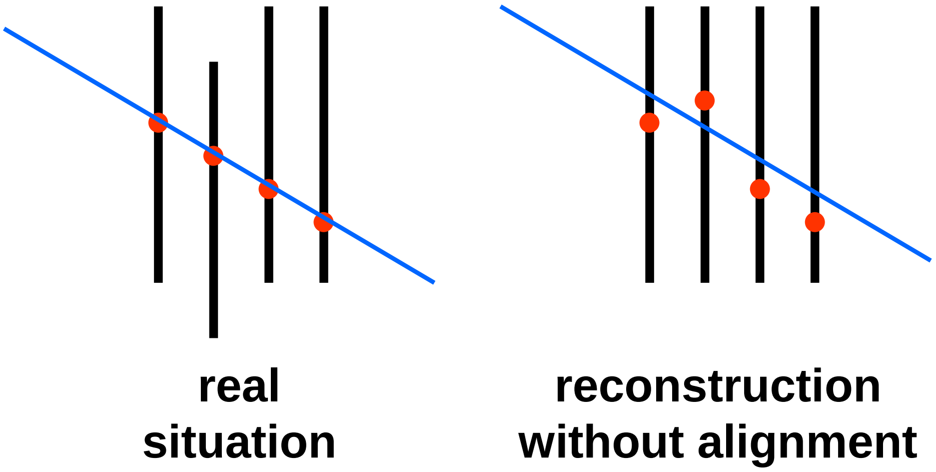

Figure 4.19: The alignment problem.

into account. A slope ∼1 can be evaluated from the Figure.

When a particle goes through the SSD, a signal appears on both the inner and outer modules. Figure 4.18 on the right panel shows a typical correlation between inner and outer module strips (P side): strips with the maximum ADC value for each event are taken into account. The reconstruction is quite linear and follows the different disposition of inner (I1) and outer (O1) strips (see Figure 4.3).

4.5 *Alignment and Residuals*

The main goal of alignment is to determine the real position of the sub-detectors, in order to be considered in the reconstruction tracking code. Otherwise an assumption of the sub-detectors in perfect position will be made with a resulting not correct estimate of track parameters.

The two part of Figure 4.19 illustrate the problem. A general very simple case is shown, with just one misalignment. What happens in reality is described on the left part of Figure. The particle (blue line) passing trough the real detector lets its signature: hits (red circles). The hits are collected and used by the reconstruction code in order to reconstruct the track. If the alignment is not corrected, the reconstruction code will see the right panel in the Figure, i.e. non-aligned hits. It will then reconstruct a bad quality track, or even no track at all if the misalignments are very large. In any case, track parameters will be seriously affected. That's why alignment is mandatory.

The distances between the red circles and the fitted track (blue line) are larger on the right figure. These distances are the *residuals*, and a good way to align detectors is to minimize them.

In order to evaluate SSD residuals a detailed knowledge of the mechanical structure of the detector is essential. A simple reconstruction tracking code free of magnet effect is used. When a track is fitted in a misaligned environment, six parameters (three translations and three rotations) which are not depending on the tracks but on the detector position, are considered. It becomes evident that residuals are a function of alignment parameters.

The data selection criteria for cosmic ray tracks are: in the A layer of the PD MIPs are selected by requiring a signal (above pedestal mean + 28 times noise) in five photon scintillators above and five below the SSD; in addition a signal in each P side silicon sensor is required (four-fold coincidence) with a multiplicity equal to one. The four SSD hits are then fitted by a straight line, since data with recoil magnet off are considered (Figure 4.20).

Figure 4.21 [Yas05] shows residual distribution for a large number of tracks for one silicon sensor, ignoring alignment parameters. As already noticed the residual distribution measures the quality of the alignment: for a perfectly aligned detector a gaussian centered at zero is observed with a width corresponding to the intrinsic resolution of the detector only if number of points in tracks is large (the intrinsic spatial resolution for a particle which produces a signal only in one strip with normal incidence is strip/$\sqrt{12} \sim 219$ μm). In case of only 2 points, lieing in tracks, residuals for a straight line are zero by definition. In this case, 4 points lie on tracks and, according to Monte Carlo [Yas05], the residuals are expected to be 0.220 strips ($\sim$167 μm) with ideally aligned detector, smaller than the intrinsic spatial resolution. A width equal to 282 μm (0.372 strips) is obtained from Figure 4.21.

Based on the residuals, a χ^2-like function can be constructed:

$$\chi_r^2 = \sum_i \frac{res_i^2(\alpha_j)}{\sigma_i^2} \quad ,$$

where the index i denotes a sum over all hits of all tracks in the sample

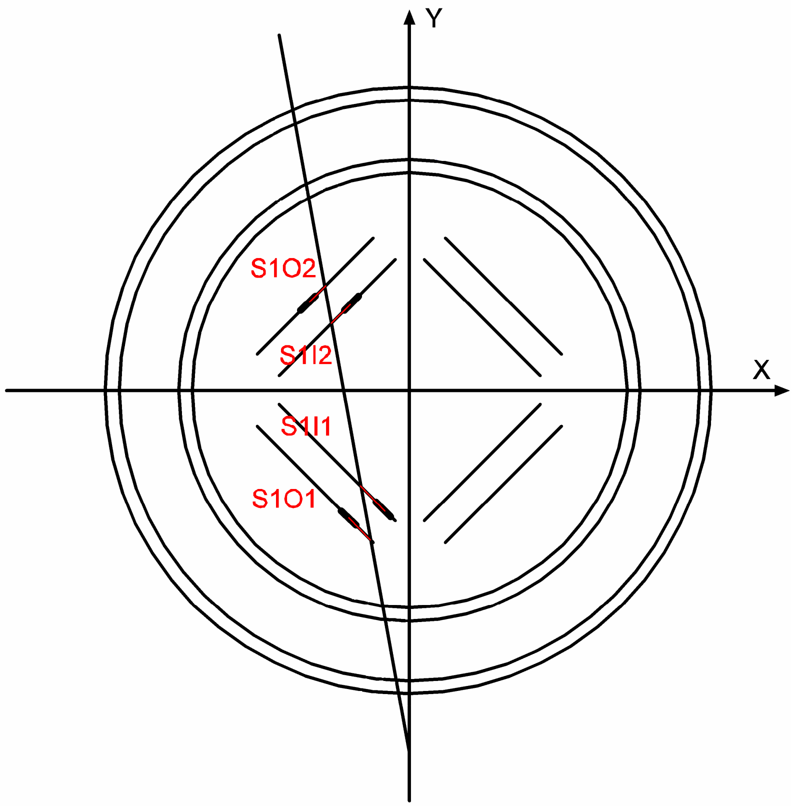

Figure 4.20: Simple reconstruction tracking code: four SSD hits are fitted by a straight line, since data with recoil magnet off are considered.

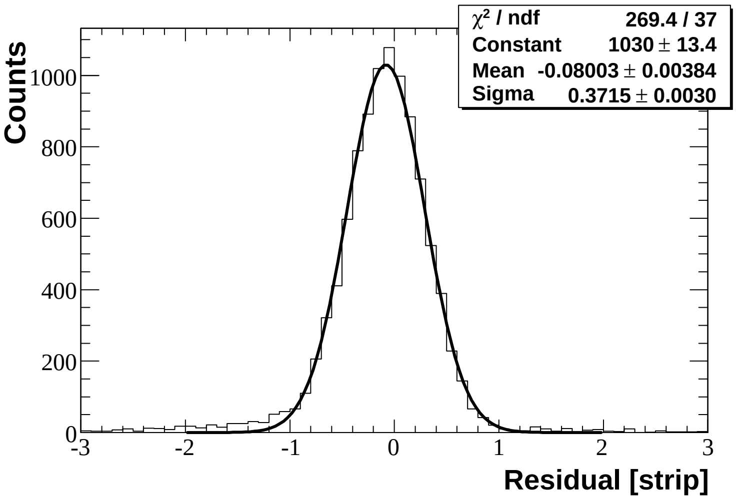

Figure 4.21: Residual distribution for a large number of tracks for SSD [Yas05].

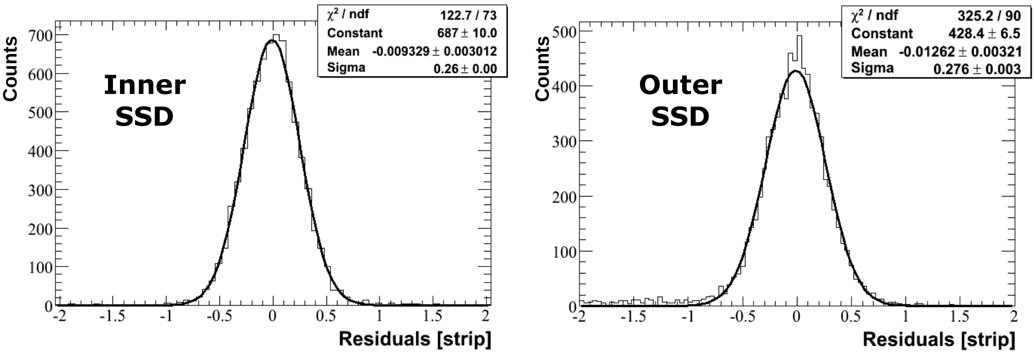

Figure 4.22: Residual distributions for inner and outer SSD after alignment [Yas07].

used and $res(\alpha)$ is the residual in function of the alignment variables α_j. σ, chosen to be strip/$\sqrt{12}$, is the intrinsic detector resolution. The alignment itself is done by minimizing the value of this χ^2_r in function of the alignment variables for a large sample of straight tracks.

Each track is then fitted with a straight line taking into account the six alignment parameters at current iteration. New residual distributions for inner and outer SSD are shown in Figure 4.22 [Yas07]. Widths of the two distributions equal to ∼200 μm (0.26 strips) are obtained, closer to the Monte Carlo value (∼167 μm). Results of the residuals are confirmed also with HERA lepton beam free of magnet effect.

4.6 *Efficiency*

Efficiency is the ratio of the number of particles detected to the number of particles which have struck the envelope limiting the sensitive volume of the detector.

In order to study efficiency, same MIP selection, used for residual evaluation, is considered: in the A layer of the PD MIPs are selected by requiring a signal (above pedestal mean + 28 times noise) in five photon scintillators above and five below the SSD. To study efficiency for one silicon sensor, only one hit in three silicon sensors is required, neglecting any condition in the silicon plane under study. The three SSD hits are then fitted by a straight

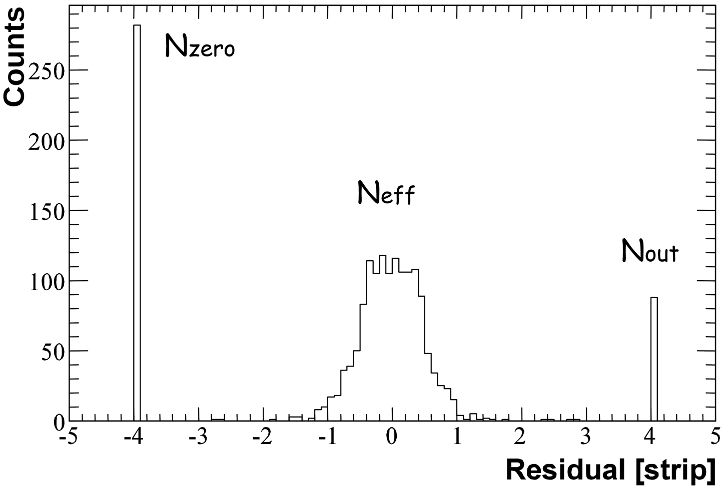

Figure 4.23: Efficiency studies for one silicon sensor [Yas05].

Detector	Efficiency
S1I1P	79.1 ± 1.0
S1I2P	87.6 ± 1.0
S1O1P	60.0 ± 0.9
S1O2P	85.0 ± 0.9
S2I1P	83.3 ± 0.9
S2I2P	90.3 ± 0.9
S2O1P	46.8 ± 1.0
S2O2P	76.8 ± 1.1

Table 4.1: Efficiencies for different silicon sensors [Yas05].

line. Figure 4.23 [Yas05] shows results for one silicon sensor: N_{zero} on the left represents the number of counts in which the silicon plane under study has no hit; N_{out} on the right represents the number of counts in which the residual for the silicon plane under study is greater than three strips, and therefore deleted from the efficiency evaluation; in the middle residual plot is shown containing events in which the silicon plane has one hit.

Table 4.1 [Yas05] shows efficiencies for different P side silicon sensors. Even if the noise level is high in comparison with the test beam in 2002 and no software noise correction is applied on data, the mean efficiency of a silicon sensor is ∼80%. Only module O1 has a low efficiency, due to a higher noise in comparison with the other silicon modules.

4.7 *Conclusions*

A few months before installation in HERMES, the Recoil Detector was completely assembled in the HERMES experimental hall outside the interlock region in order to take cosmic data.

Usefully, the cosmic ray test experiment helped to improve the understanding of the mechanical setup of the Recoil Detector and provided the possibility to anticipate some of the problems likely to arise during its installation into the spectrometer. In particular during cosmic data taking a lot of fibers in the SFT light guides were found broken next to the connectors due to an improper handling. They were rebuilt during December ’05, with great care. The magnet and vacuum tests were carried out successfully.

The cosmic ray test experiment also allowed the integration of the entire detector into the HERMES data acquisition system.

A total of 2 TByte of raw data was collected during the operating period of the test experiment, using the cosmic trigger generated by the PD. Mainly these data were used for the calibration of SFT and PD as well as for the development of software for the internal alignment of the detector with straight tracks.

From the SSD point of view, many noise studies were carried out: it was observed for HG chips that noise of last several HELIX channels was always much higher than in first channels, resulting in a signal to noise ratio equal or less than 2 for MIP signals. Although the high noise level, MIPs were detected, whose most probable signal was measured to be equal to $\sim$14 ADC Channels for a normal incidence. Residuals and efficiency were also evaluated: residuals were found to be equal to 0.27 strips, close to the obtained Monte Carlo value and mean efficiency was found to be $\sim$80%, a bit lower than efficiency evaluated in the previous test beam in 2002. Only in September ’05 the noise level was partially solved connecting the reference potential of all silicon modules to the support structure. A further correction on software level will be presented in the next Chapter.

Chapter 5

SSD Performance with HERA Lepton Beam

The Recoil Detector was installed in HERMES in January 2006 and started to take data in February '06 with a polarized electron beam. Figure 5.1 shows a picture of the HERMES target region with the lepton beam pipe at left side, the Recoil Detector in the middle and the SFT light guides at right side. The HERA beam enters into the page. The first target cell installed with the Recoil Detector in HERMES had a thickness of 50 μm, in order to lower the low momentum cut-off of the SSD.

The interlock was set on the 25^{th} of January '06 and HERA machine setup finished on the 18^{th} of February '06. Once stable beam conditions were established, the commissioning of the Recoil Detector with beam could begin. The Recoil Detector SC magnet was in routine operation since the 9^{th} of March '06 after which the tracking in the magnetic field using the SFT was possible. RF noise introduced by the beam bunches in the SSD and temperature excursions exceeding 100° C in the target cell were serious problems in the first months of operation. Figure 5.2 [Ste06] shows on the left panel the SSD pedestals versus the strip number for one sensor chip during electron HERA running: the SSD commissioning couldn't begin due to a non-defined pedestal structure. The same Figure on the right panel shows the temperature excursions of the target cell.

At the end of March '06, the target cell was damaged (Figure 5.3) while it was being inspected which resulted in large radiation doses to the SSD at the beam injection. This required rebuilding the SSD in April - June '06. All the read-out chips on the inner SSD modules were replaced. An additional

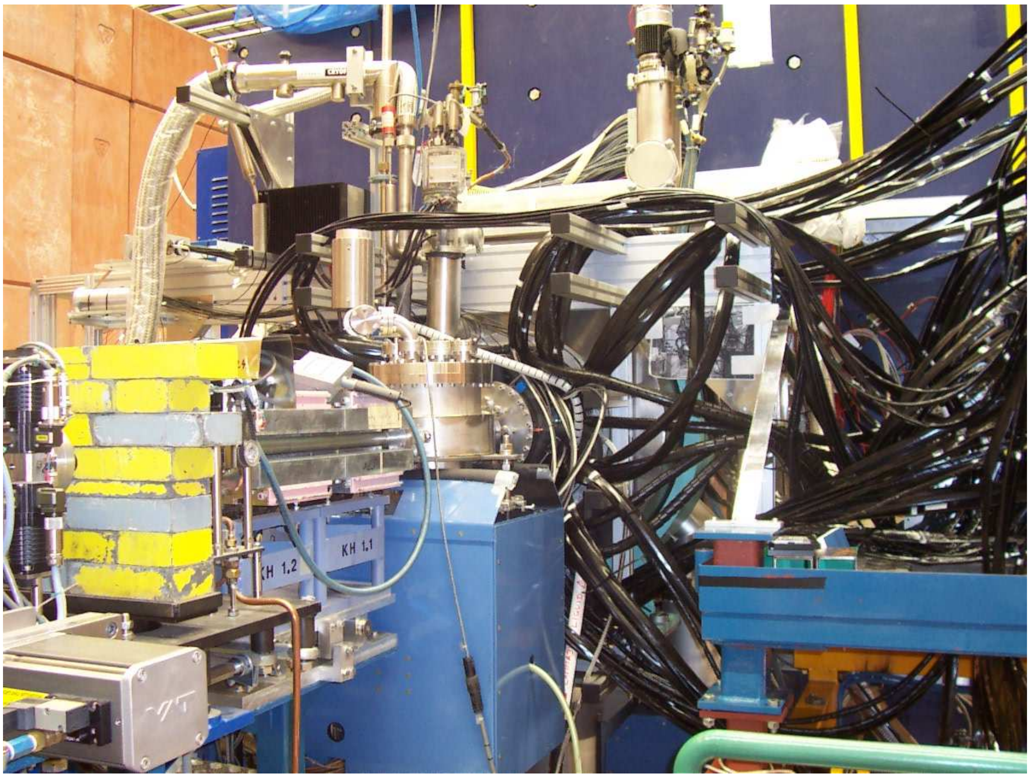

Figure 5.1: Picture of the HERMES target region in which the lepton beam pipe at left, the Recoil Detector in the middle and the SFT light guides at right can be easily noticed. The HERA beam enters into the page.

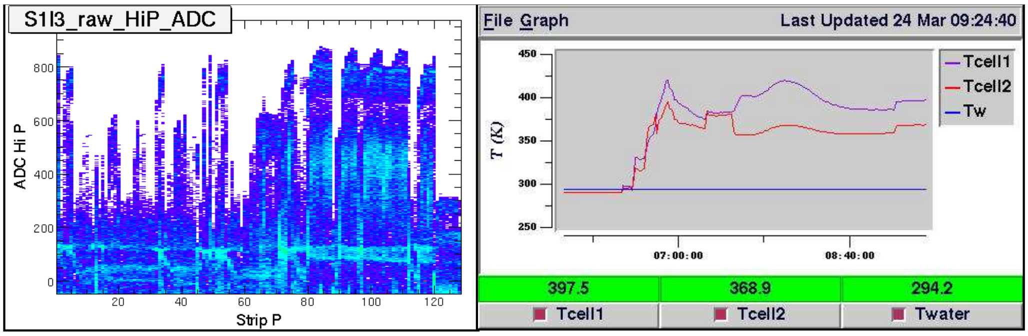

Figure 5.2: Left side: SSD pedestals versus the strip number for one sensor chip during electron HERA running. Right side: the temperature excursions of the target cell.

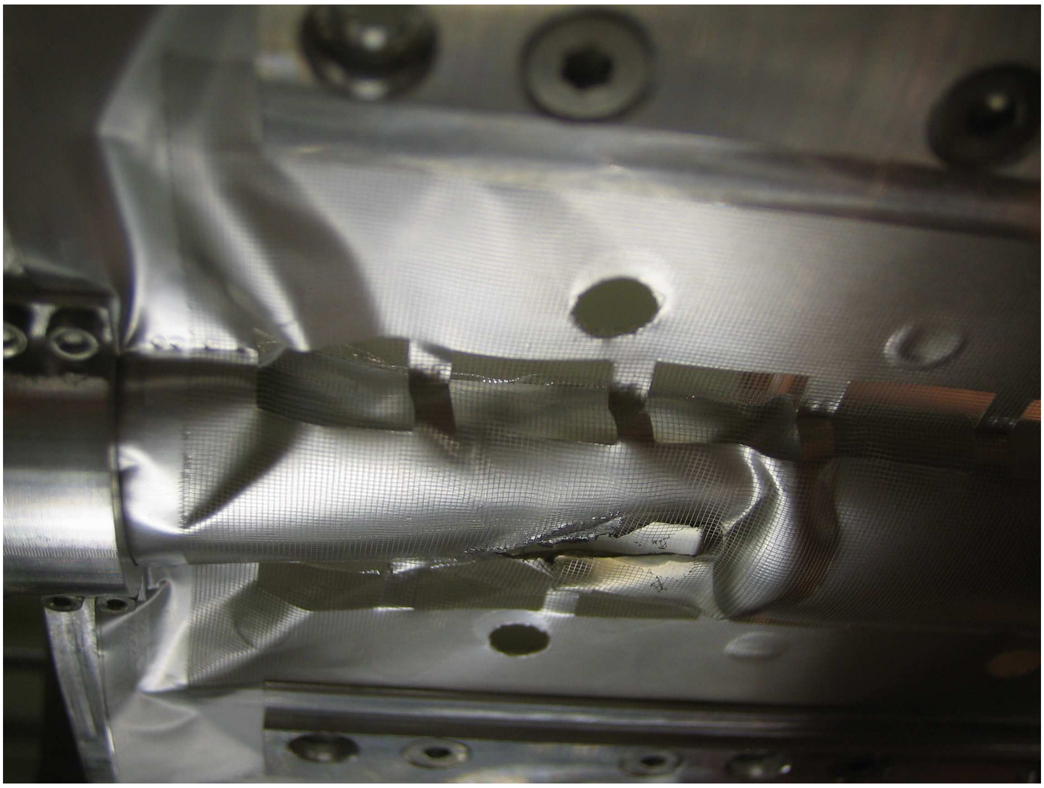

Figure 5.3: The target damaged in March '06.

RF shield (made of 20 μm of kapton and 8 μm of copper) to surround the SSD was constructed. Moreover it was decided to re-change the thickness of the target cell, building a new one with a thickness of 75 μm.

HERA switched the beam charge from negative to positive at the end of June '06, when the repaired SSD including the RF shield were re-installed. Also the new target cell of 75 μm thickness together with an improved cooling system were installed. Therefore, unfortunately, no data with electron beam is available with an operational SSD.

The data taking restarted in the middle of July '06 with no interruption till the June 30^{th} '07, last day of HERA running. After the re-installation of repaired silicon modules, noise problem in the SSD disappeared as documented in the Figure 5.4 [Ste06] left panel, in which same quantities displayed in the Figure 5.2 on the left panel are shown for positron HERA running. The Figure 5.4 on the right panel shows the temperature of the new target

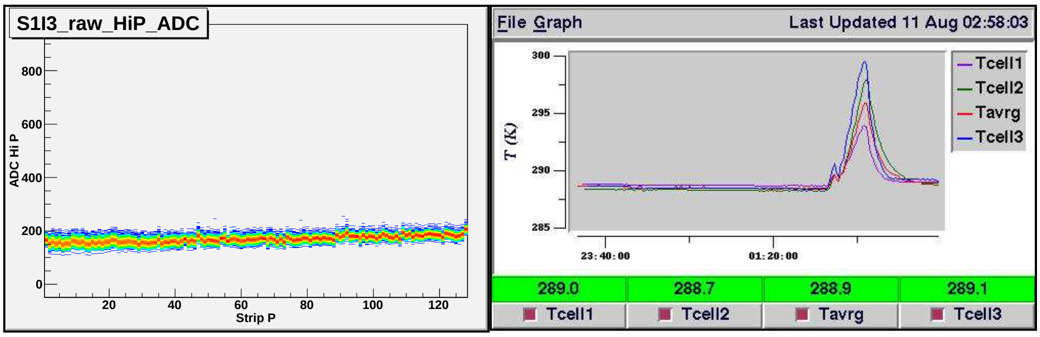

Figure 5.4: Left: First pedestals with a repaired SSD versus the strip number for one sensor chip during positron HERA running. Right: the temperature of the new target cell: the temperature excursion of 10° C is caused by the positron injection.

cell: the temperature increases only about 10° C during positron injection. The well defined pedestal structure allowed to start the commissioning of the SSD, in particular noise and timing studies, finished in September '06. Since then, the Recoil Detector was fully operational and it ran stable for 10 months without any problems.

In this Chapter the SSD first response to HERA positron beam is discussed as well as its correlation with the spectrometer.

5.1 *Pedestal and Noise*

Figure 5.5 shows typical pedestal means, evaluated from gaussian fits, and typical pedestal gaussian widths (sigmas) without beam (left panel) and with beam (right panel) for 128 channels of a LG and a HG sensor chip. The silicon pedestals and sigmas are quite stable to different HERA machine conditions. Pedestal sigma values are evaluated after CMN correction.

Measurements [Ye02], made with a prototype detector and an antenna along the target cell axis to simulate the effect of the HERA beam, indicated that a change in the pedestal level of about 1-2 channels was to be expected as the HERA beam current decayed over a fill from 30 to 10 mA. However a small fraction of the strips ($\sim$0.5%) showed a strong RF coupling between the beam and the detector. Pedestal measurements were collected every two hours during data taking to measure the correlation between the beam

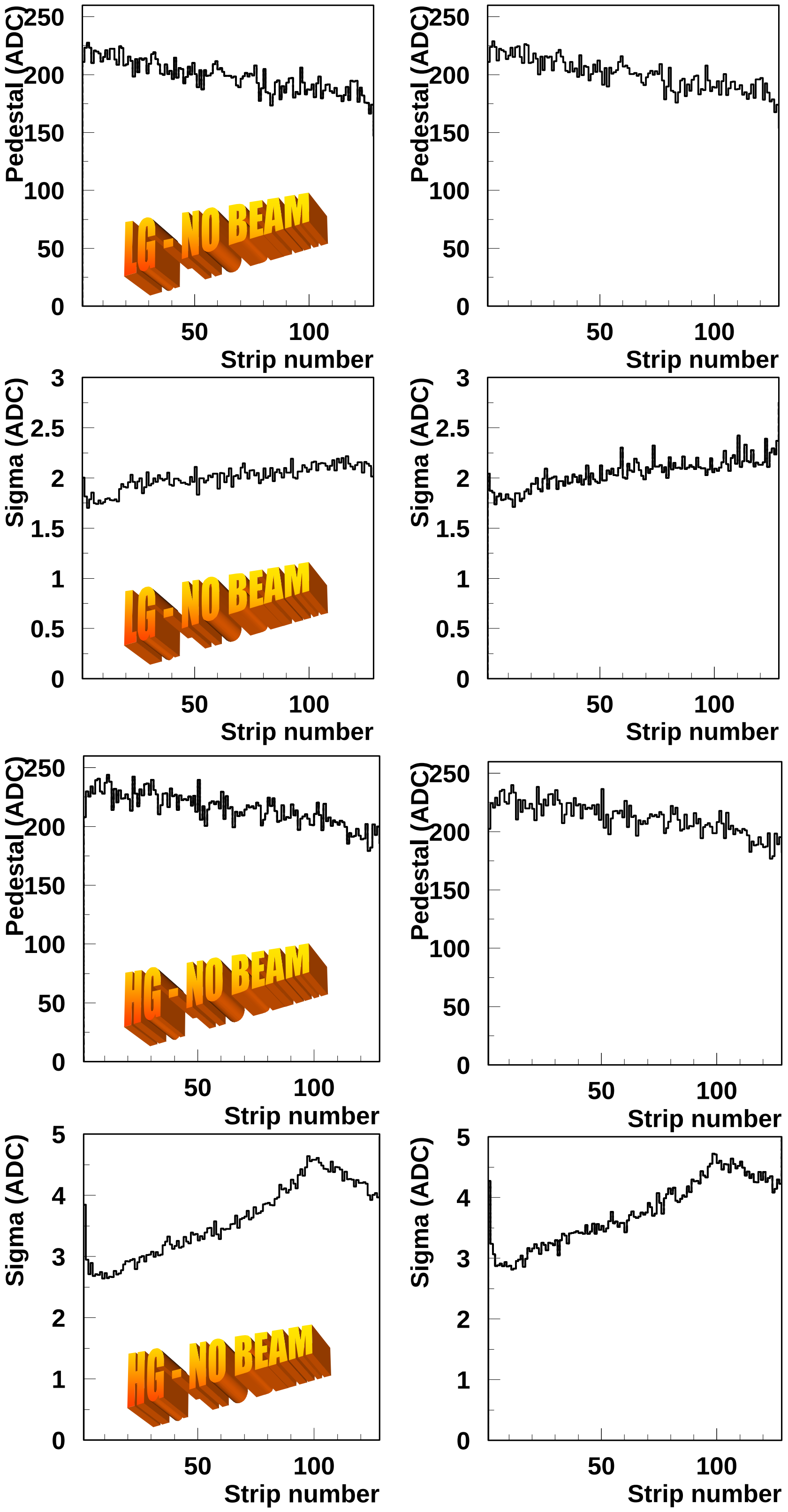

Figure 5.5: Typical pedestal means and their relative gaussian widths (sigmas) without beam (left side) and with beam (right side) versus the strip number for a LG and a HG chip. The sigma values are evaluated after CMN correction.

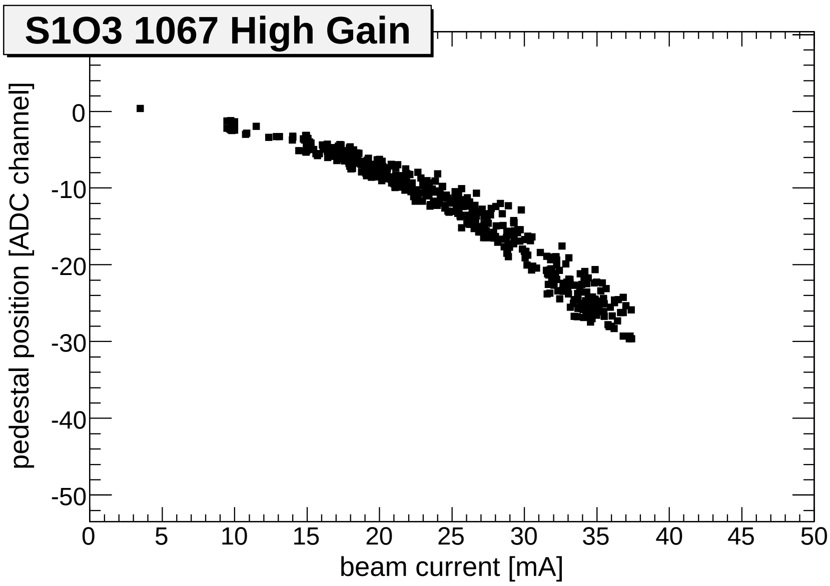

Figure 5.6: The dependence of the strip pedestal as a function of the positron current in HERA is shown for one strip [Mus07]. The strip was selected to be one of the few which couples strongly to the beam.

current and the pedestal for all strips. Figure 5.6 [Mus07] shows the change in pedestal as a function of beam current over 1.5 months of data taking for one of the strips which coupled strongest to the beam. For channels with more than 1 channel drift the dependence was fit with a third order polynomial and applied as a correction to the data.

As already seen in the cosmic ray test experiment, the CMN corrected noise of a LG chip is pretty constant versus the strip number. Instead this doesn't happen for HG chips. Figure 5.7 shows examples of CMN corrected noises for different bad HG chips with HERA beam: noise values can even reach at the last channels of the chip $10 - 15$ ADC Channels. From the cosmic ray test experiment, a signal equal to $\sim$14 ADC Channels is expected for a MIP with an incidence angle of 90°, resulting in a signal to noise less than two in the end of the sensor.

Since one of the SSD goals is to provide spatial information for MIPs, it should be strongly suggested to investigate the possibility to reduce noise in the last HELIX channels (Figure 5.7) at software level.

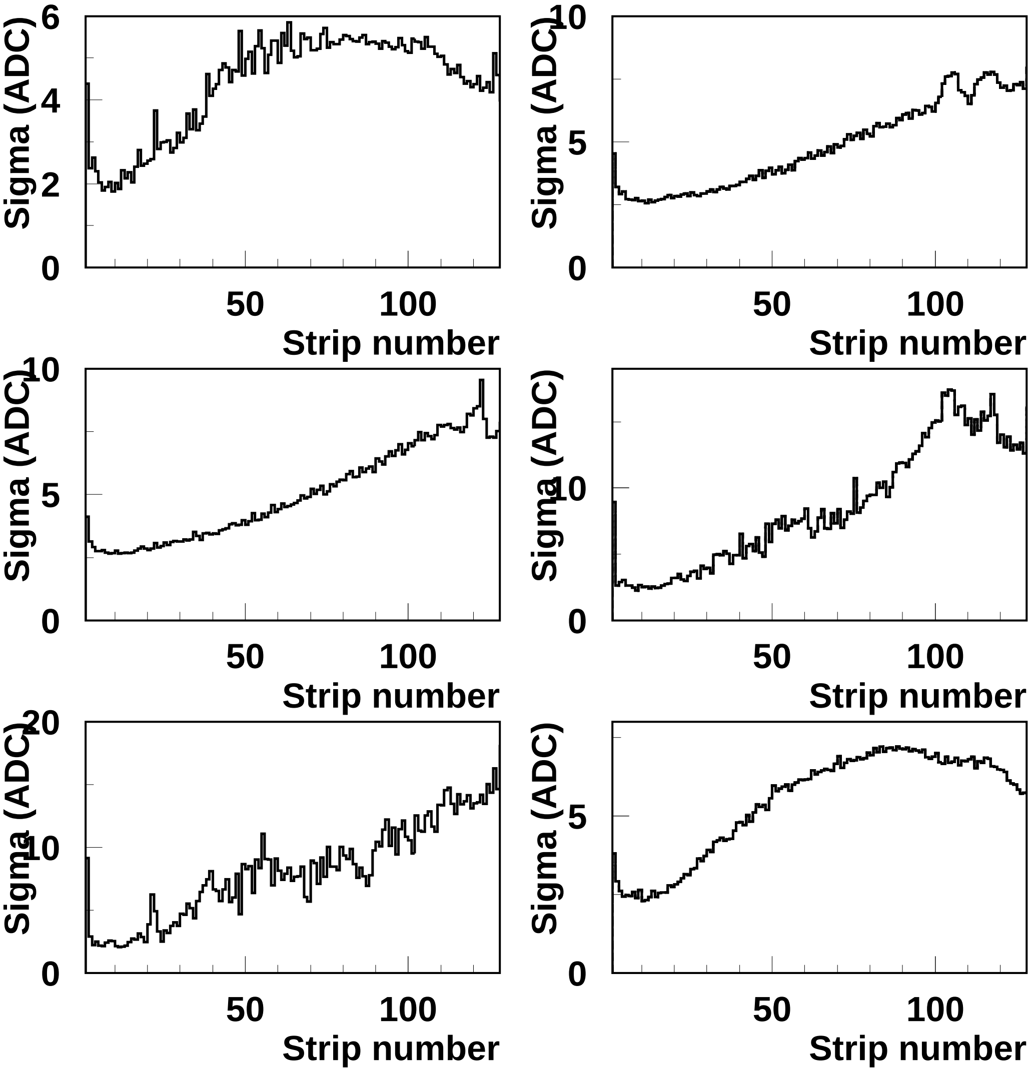

Figure 5.7: Examples of CMN corrected noises for different bad HG chips versus the strip number.

5.2 *Software Correction: Semi-Sparse Running Mode*

5.2.1 *Correlated Noise*

Few runs, during HERMES data taking, were taken in unsparsified operation mode, where all enabled channels are read-out, in order to study the SSD response on event by event level. The pedestal subtraction and the CMN

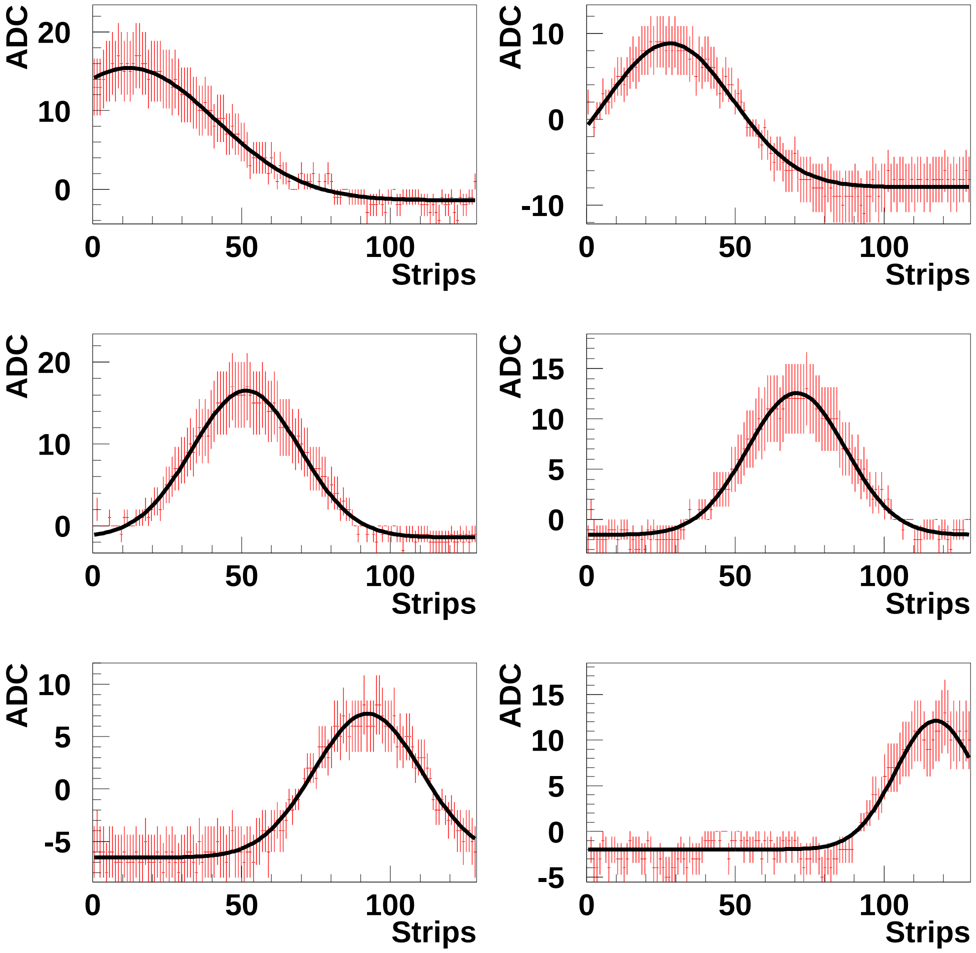

Figure 5.8: Typical unsparsified data of six different events for a HG chip. Data are fitted with a constant added to a gaussian function.

correction are performed by the HADC modules. The study on event by event level allows to determine if the source of noise has a defined behaviour or if the noise variation is random and doesn't depend, for example, on strip number. In principle the software correction can be possible in the first case, knowing the noise behaviour in the chip; in the second case, the software correction cannot be possible at all, being the noise random and therefore not fitted at all.

Figure 5.8 shows examples of unsparsified data for a HG chip for six different events, after pedestal subtraction and CMN correction performed by the HADC modules. Fortunately SSD unsparsified data seem to be not random and follow a well defined structure: the noise in the detector appears to be correlated and can be modelled by a function or by a combination of functions. In this case data can be easily fitted with a constant added to a gaussian function:

$$C + A \cdot exp\left[-\frac{1}{2}\cdot\left(\frac{strip - \overline{strip}}{\sigma}\right)^2\right] \quad . \tag{5.1}$$

The obtained values for the four unknown parameters (C, A, $\overline{strip}$, σ) for a given chip result to be in the range:

$$\begin{aligned} C &: [-8, 1] \text{ ADC Channels;} \\ A &: [5, 20] \text{ ADC Channels;} \\ \overline{strip} &: [-20, 150] \text{ Strip number;} \\ \sigma &: [14, 20] \text{ Strip number.} \end{aligned}$$

The fit fails for the ~20% of data, indicating that the SSD noise does not really observe a fixed behaviour, described by Expression 5.1. The remaining 20% can be fit with multiple Gaussian. However, to a first approximation, Expression 5.1 can be considered as the **correlated noise model** for the SSD.

5.2.2 *"Semi-Sparse" Running Mode*

Fortunately unsparsified data show a well defined structure as seen in Figure 5.8, allowing to reduce noise on software level. The best way to correct data would be to read the SSD in unsparsified operation mode, to see the behaviour of each chip and to subtract data using the function that fits SSD unsparsified response. But, as discussed in previous Sections, the unsparsified operation mode in HERMES cannot be used at all, otherwise the HERMES deadtime will be dominated by the SSD. On the other hand the noise information will be completely lost if the sparse operation mode will be used.

Therefore a combination of serial and sparse mode, called *semi-sparse* mode, is proposed to read data. Mainly a semi-sparse operation mode is a sparse mode with the addition in the read-out of some strips, called *unsparsified*, in order to monitor the pedestal stability and the sigma behaviour. The unsparsified strips will still permit to estimate a set of functions. A smaller distance between two unsparsified strips increases the accuracy in function estimation. But, on the other hand, a large distance between two unsparsified strips increases the read-out speed, and, then, decreases the deadtime.

In this case a compromise has to be found: the number of unsparsified strips, chosen to be always read-out, must allow to reduce successfully noise but at the same time the number must not reduce too much the read-out speed. Unsparsified strips are proposed to be equidistant with a distance of 8 strips (starting from the 20^{th} strip). Therefore in total 14 unsparsified strips are proposed to read-out for each sensor.

Since Expression 5.1 is not valid for all the data, a general spline interpolation is used to correct data. The spline interpolation is presented in next Section.

5.2.3 *Spline Interpolation Correction*

Interpolation between known data points is used to estimate an unknown fitting function. Interpolation methods can be divided into two main categories [Hen82, Pre95]:

- Global interpolation. This method relies on a single equation that fits all the data points. This equation is usually a high degree polynomial equation. Although this method results in a smooth curve, it is usually not well suited, as it observes severe oscillations and overshoots at intermediate points.

- Piecewise interpolation. This method relies on a polynomial with a low degree between each pair of known data points. If a first degree polynomial is used, it is called linear interpolation. For second and third degree polynomials, it is called quadratic and cubic splines, respectively. The higher the spline degree, the smoother the curve. Splines of degree m will have continuous derivatives up to the $m-1$ degree at the data points.

Linear interpolation results in a straight line between each pair of points with all derivatives discontinuous at the data points. To obtain a smoother curve, cubic splines are frequently used. They are continuous up to the second order derivative at the data points. Furthermore, its second derivate is zero at the end points.

Consider a collection of known points $(x_0,\, y_0)$, ... $(x_i,\, y_i)$, ... $(x_n,\, y_n)$. To interpolate between these data points using cubic splines, a third degree polynomial is constructed for each point. The equation to the left of point $(x_i,\, y_i)$ is indicated as f_i with a y value of $f_i(x_i)$ at point x_i. Similarly, the equation to the right of point $(x_i,\, y_i)$ is indicated as f_{i+1} with a y value of $f_{i+1}(x_i)$ at point x_i.

The cubic spline function, f_i, is usually constructed based on the following criteria:

- Curves are third order polynomials: $f_i(x) = a_i + b_i x + c_i x^2 + d_i x^3$;
- Curves pass through all the known points: $f_i(x_i) = f_{i+1}(x_i) = y_i$;
- The slope, or first order derivative, is the same for both functions on both sides of a point: $f_i'(x_i) = f_{i+1}'(x_i)$;
- The second order derivative is the same for both functions on both sides of a point: $f_i''(x_i) = f_{i+1}''(x_i)$;

This results in a matrix of $n-1$ equations and $n+1$ unknowns. The two remaining equations are based on the border conditions for the starting point, $f_1(x_0)$, and end point, $f_n(x_n)$.

Then cubic splines equations are combined, and the $(n+1)$ by $(n+1)$ tri-diagonal matrix is solved to yield the cubic spline equations for each segment [Hen82, Pre95]. As both the first and second order derivatives for connecting functions are the same at every point, the result is a smooth curve.

The 14 unsparsified strips are used to evaluate the equation coefficients event by event. Then the resulting spline interpolation is used to subtract data. Figure 5.9 shows serial data (upper panel) with CMN correction (left side) and with CMN and spline corrections (right side). From the comparison of the two plots, a great improvement in noise can be seen after the spline

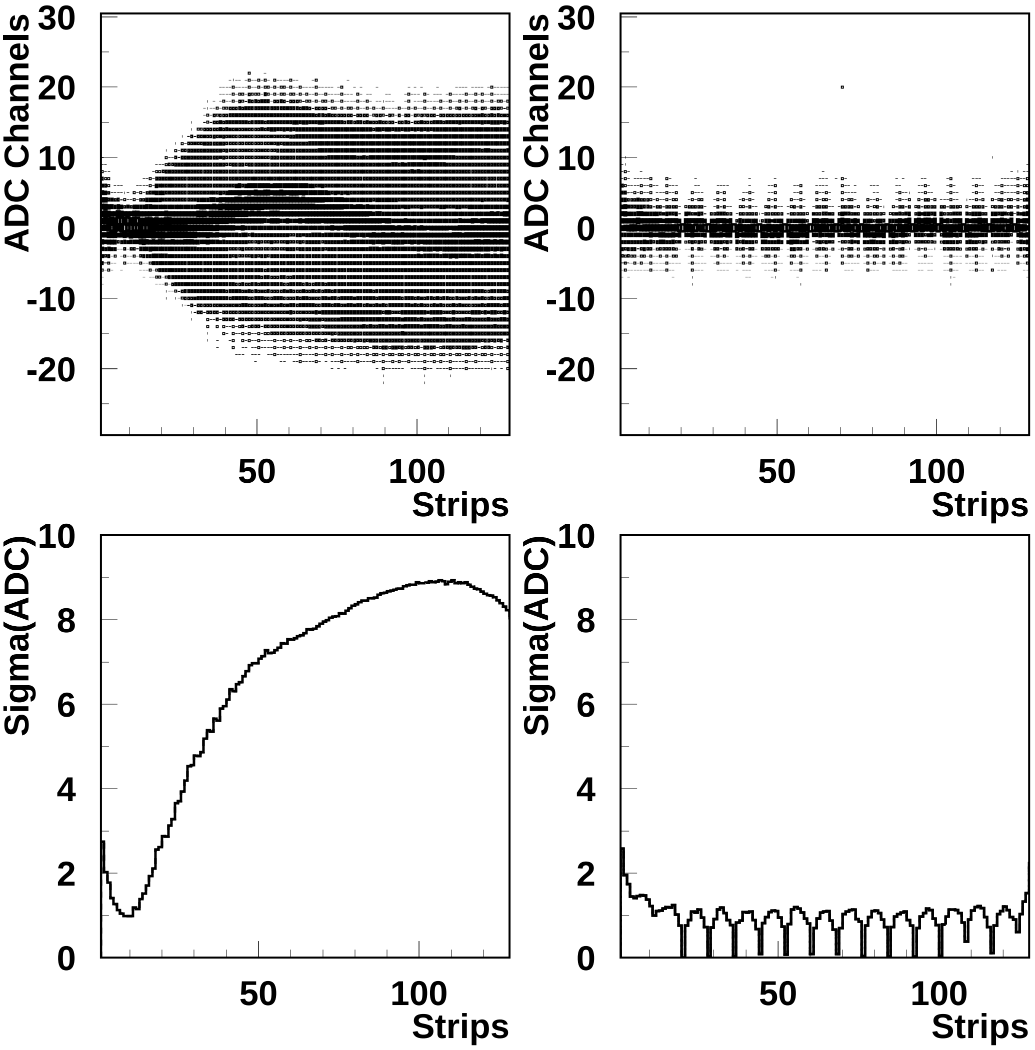

Figure 5.9: Bi-dimensional plots (upper panel) and corresponding sigma values (lower panel) with CMN correction (left side) and with CMN and spline corrections (right side). The corrected ADC values corresponding to the unsparsified strips become equal to zero, when the spline correction is applied event by event.

correction. Figure 5.9 shows in the lower panel noise values (left side) and noise values after spline correction (right side): great improvements can be easily noticed, reaching a sigma value equal to 1 ADC Channel, besides a constant linear behaviour along all the sensor. Typical sigma values obtained after spline correction are in the range $1-2$ ADC Channels, resulting in a

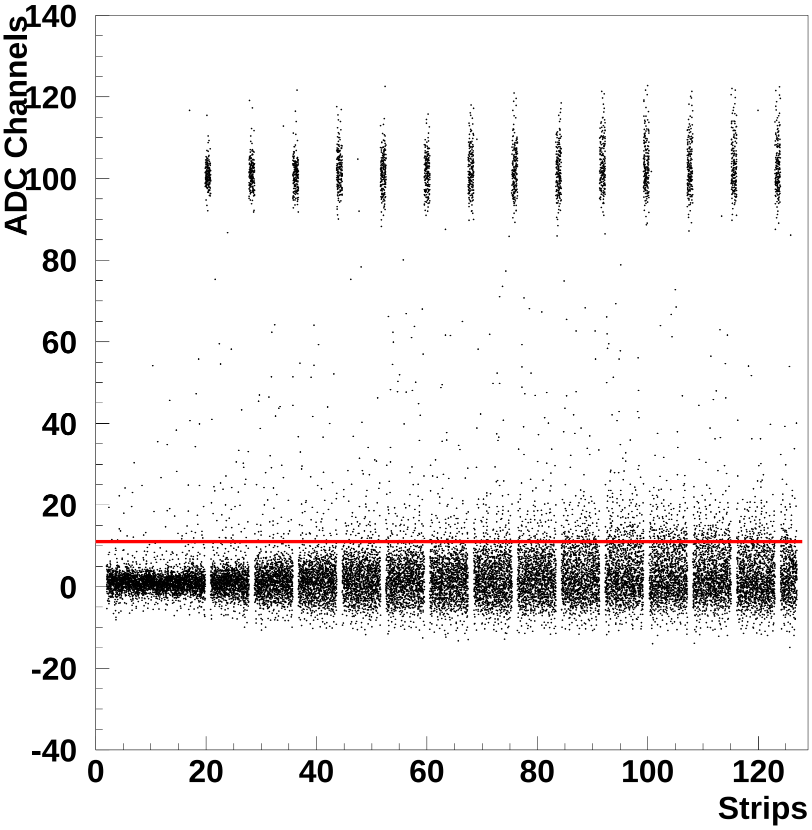

Figure 5.10: A typical bi-dimensional plot of a serial operation mode (pedestal subtracted and CMN corrected) with every 8^{th} strip (starting from the 20^{th} strip) shifted by 100 ADC Channels. For the *semi-sparse* running mode a 10 ADC Channels hard threshold is applied on data (red line).

signal to noise ratio for a MIP particle better than 7.

The number 14 constitutes 11% of the total number of silicon strips. It was decided to use 14 strips as the studies of the event-by-event data showed this was sufficient to accurately determine the shape of the correlated noise while not having a large impact on the deadtime of the HERMES trigger. In order to be always read-out, the unsparsified strips are shifted by 100 ADC Channels. Figure 5.10 shows a typical bi-dimensional plot of a serial operation mode (pedestal subtracted and CMN corrected) with every 8^{th} strip (starting from the 20^{th} strip) shifted by 100 ADC Channels. The *semi-sparse* operation mode is obtained with a 10 ADC Channels hard threshold, applied on data (red line).

5.2.4 *Hit-Rejection Algorithm: MC Predictions*

As seen in the previous subsection, cubic spline equations are built using 14 unsparsified strips. When the spline correction is applied event by event, the corrected ADC values corresponding to the unsparsified strips become equal to zero (Figure 5.9, lower panel, left side). If particles, going through the SSD, lose energy in the unsparsified strips (it can happen in ∼30% of all events, considering also clustering and crosstalk), the spatial and energy information recorded in those strips are lost since the corrected ADC value becomes zero after the spline correction. To avoid the loss of information in those strips and to improve the efficiency, an algorithm is necessary to reject unsparsified strips with a signal from the spline equation evaluations.

In order to evidence unsparsified strips with signal, a cut condition is used:

> *If the signal related to one unsparsified strip (x) is greater than the mean of the signals related to the four neighbour unsparsified strips (x-2, x-1, x+1, x+2) added to their rms value, it is considered as a good signal and the strip (x) is excluded from the evaluation of the spline equations. Otherwise it is considered as pedestal signal and, therefore, taken into account for the spline calculation.*

In order to see the impact of this *hit-rejection* algorithm in efficiency and in energy deposition resolution for unsparsified strips, a Monte Carlo study is performed.

In the Monte Carlo, Expression 5.1 is used to reproduce the noise in the detector. The correlated noise model adds algebraically correlated noise hits to good signals. Moreover an uncorrelated noise equal to 1 ADC Channels (sigma value) is added to the resulting ADC value. Figure 5.11 shows serial real data (left side) and Monte Carlo data (right side) after CMN corrected. From the comparison it can be noticed that the real data are reproduced with the same shape by the noise model (Expression 5.1).

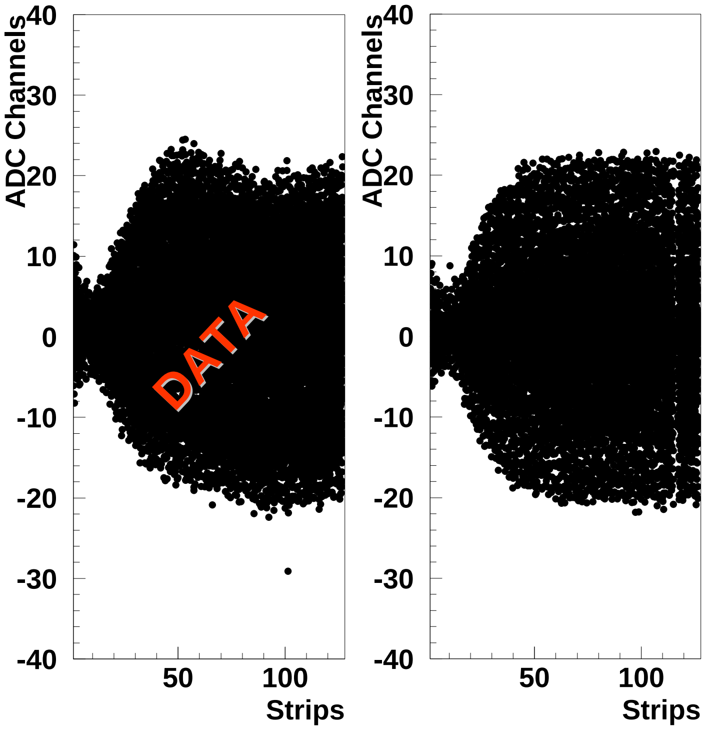

Figure 5.11: Serial real data (left side) and Monte Carlo data (right side).

Monte Carlo DIS events are generated in order to study efficiency and energy deposition resolution for unsparsified strips. From now on, the name *neighbouring strips* indicates strips neighbour to the unsparsified strips.

Figure 5.12 shows on the left side a typical ADC spectrum for neighbouring strips when the highest ADC value appears in the unsparsified ones. Therefore the ADC spectrum mainly represents crosstalk and clustering data. In this case the spline correction efficiency, that means the efficiency of the hit-rejection algorithm to consider a signal as a good hit instead of a noise hit, is 96%. The Figure on the right side shows a typical ADC spectrum for unsparsified strips when the highest ADC value appears in the neighboring ones. In this case the spline correction efficiency is much lower, around 70%.

Energy deposition resolution can be evaluated as:

$$f = \frac{rE_{corr} - rE}{rE} \quad , \tag{5.2}$$

where rE_{corr} is the energy deposited by particles in the SSD, calculated by

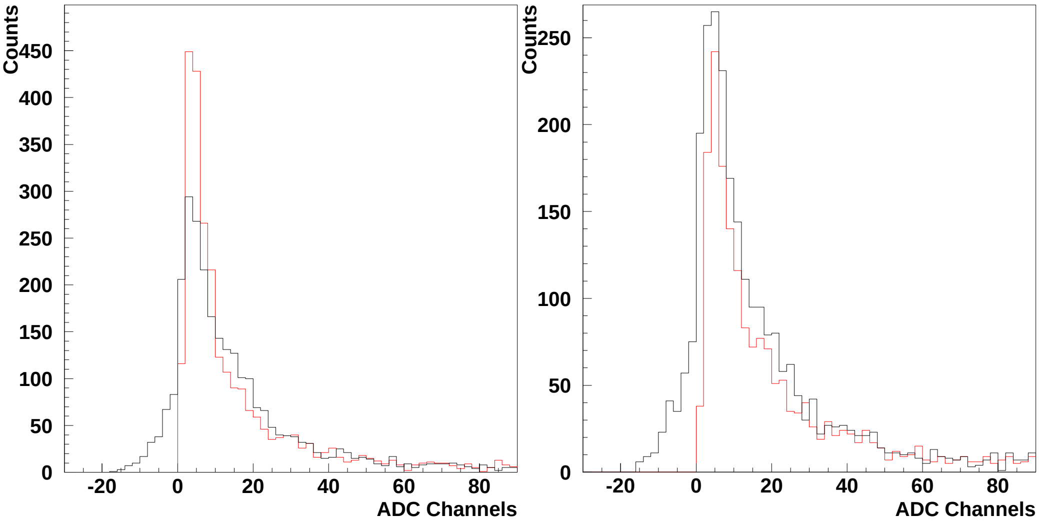

Figure 5.12: Typical ADC spectrum for neighbouring strips (left side) when the highest ADC value appears in the unsparsified ones, and ADC spectrum for unsparsified strips (right side) when the highest ADC value appears in the neighbouring ones. The black lines represent MC data without spline correction, while the red lines represent MC data with spline correction.

means of ADC data after spline correction, while rE is the theoretical energy deposition given directly by Monte Carlo for each particle. Figure 5.13 shows Expression 5.2 when the highest ADC value appears in the neighbouring strip. Two peaks can be noticed in the plot: one centered at zero value represents a good energy deposition reconstruction, the other, centered at -0.3 value, represents a very bad energy deposition reconstruction, leading to a RMS value greater than 0.15. The second peak is primarily due to a wrong evaluation of crosstalk, being the mean value two times the crosstalk estimation (∼15%).

According to Monte Carlo predictions, the critical case is when the highest signal appears in the neighboring strips, obtaining a low spline correction efficiency (70%) and a wrong estimation of particle energy deposition (resolution greater than 0.15, RMS value). An improvement of the hit-rejection algorithm is strongly necessary in order to increase the efficiency in this particular case.

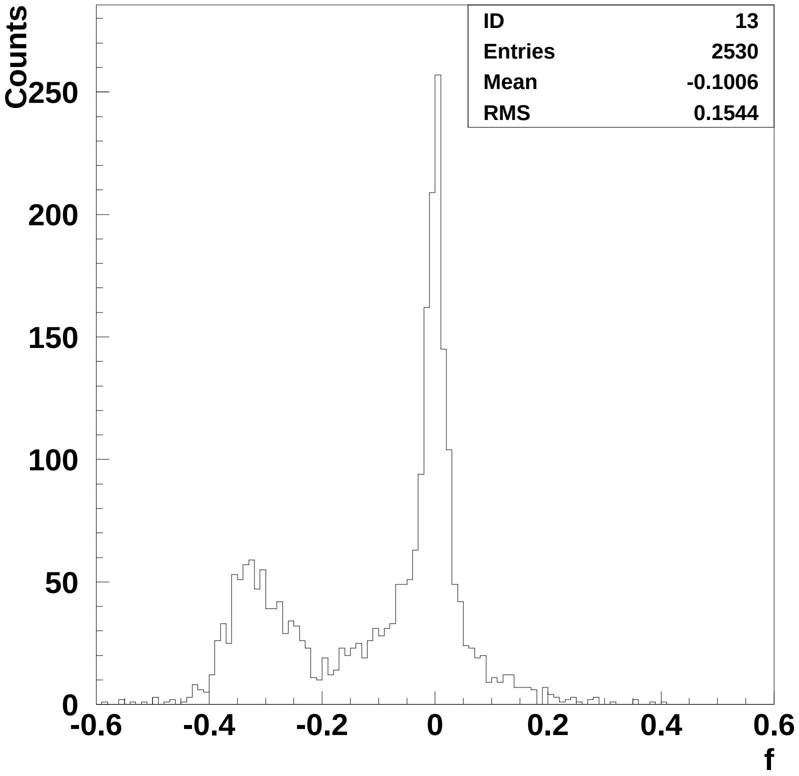

Figure 5.13: Distribution of the energy deposition resolution (f, Expression 5.2) when the highest ADC value appears in the neighboring strips.

A further condition is introduced:

> *If the highest ADC value appears in the neighbouring strips, the corresponding unsparsified strip is not taken into account into the spline equation evaluation.*

Figure 5.14 shows on the left side a typical ADC spectrum for unsparsified strips when the highest ADC value appears in the neighboring ones (same plot at Figure 5.12 right side). The black line represents MC data without spline correction, while the red line represents MC data with spline correction. After considering the new hit-rejection algorithm, an increase in the peak counts (up to 450) for the red line is noticed. By comparing with the same plot at Figure 5.12, where the peak counts is 250, a spline correction efficiency equal to 96% is obtained. The Figure on the right side shows the

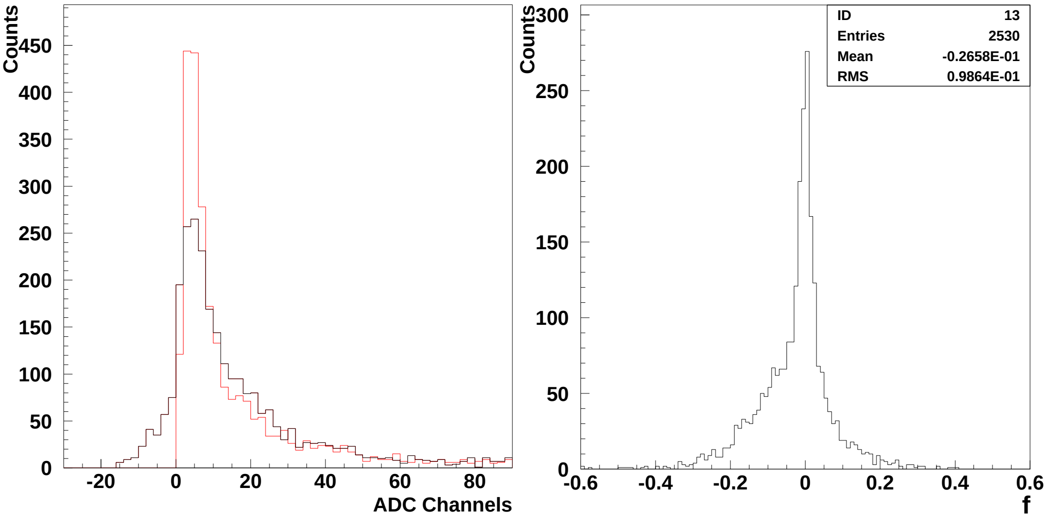

Figure 5.14: A typical ADC spectrum (left side) for unsparsified strips when the highest ADC value appears in the neighbouring ones. The black line represents MC data without spline correction, while the red line represents MC data with spline correction. Energy deposition resolution distribution (f, Expression 5.2, right side) when the highest ADC value appears in the neighbouring strips.

distribution of the energy deposition resolution f (Expression 5.2) when the highest ADC value appears in the neighbouring strips (same plot at Figure 5.13). By comparing Figure 5.14 right side with Figure 5.13 an improvement in the energy deposition resolution can also be noticed: the peak centered at $f = -0.3$ in Figure 5.13 disappears, indicating that the energy deposition reconstruction is correct when crosstalk and clustering are considered. After this new hit-rejection algorithm, a resolution of the energy deposition better than 0.1, RMS value in Figure 5.14 on the right side, can be reached.

5.2.5 *Noise Conclusions*

In the cosmic ray test experiment many tests have been carried out in order to reduce the noise but unfortunately on hardware level there has been no possibility to delete the dependence of the noise in strip number. Since the signal to noise ratio for MIPs has been found to be less than two, it has been investigated a possibility to correct data on software level. Fortunately the noise in the detector appears to be correlated and can be modelled. In order to estimate the spline interpolation, semi-sparse operation mode is used to read-out the SSD: unsparsified strips have been chosen to be equidistant with a distance of 8 strips (starting from the 20^{th} strip). Therefore in total 14 unsparsified strips, shifted by 100 ADC Channels, have been read-out for each sensor. The resulting spline interpolation is used to subtract data: a great improvement has been obtained, getting a signal to noise ratio for MIPs better than 7. The software correction is improved by a hit rejection algorithm, considering the case in which particles lose energy in the unsparsified strips.

From now on, data shown will be evaluated after CMN and spline corrections with the previous hit-rejection algorithm.

5.3 *SSD First Response*

The upper part at Figure 5.15 shows typical ADC spectra (pedestal subtracted) for all the strips for a P side (left panel) and a N side (right panel) silicon sensor. The black lines represent the HG chip, while the red lines represent the LG chip. The behaviour of the ADC spectra is an indication that most of particles produced in the HERMES target cell, crossing the SSD, and then the Recoil Detector, can be considered as MIPs. In the cosmic ray test experiment a signal equal to ∼14 ADC Channels is expected for a MIP with normal incidence. The peaks around 750 (left) and 600 ADC Channels (right) represent the ADC overflow: they are not a spike as the pedestal mean (subtracted) is not equal to all strips. The Figure on the lower part shows typical multiplicity spectra for a P side (left panel) and a N side (right panel) silicon sensor. The mean of the multiplicity is around 2 strips, which is the value expected for a particle which goes through the detector, as discussed in the previous Chapter.

For every hit on a strip, the signal is split in a HG and LG signal according to Section 3.5.3 and Figure 3.17. In the cosmic ray test experiment, only HG chips have been used, since MIPs deposit only a small amount of energy which is below threshold in the LG chips. Figure 5.16 shows a typical correlation between HG and LG values for a P side silicon sensor (left panel) and for a N side silicon sensor (right panel) for all events and all strips. The HG

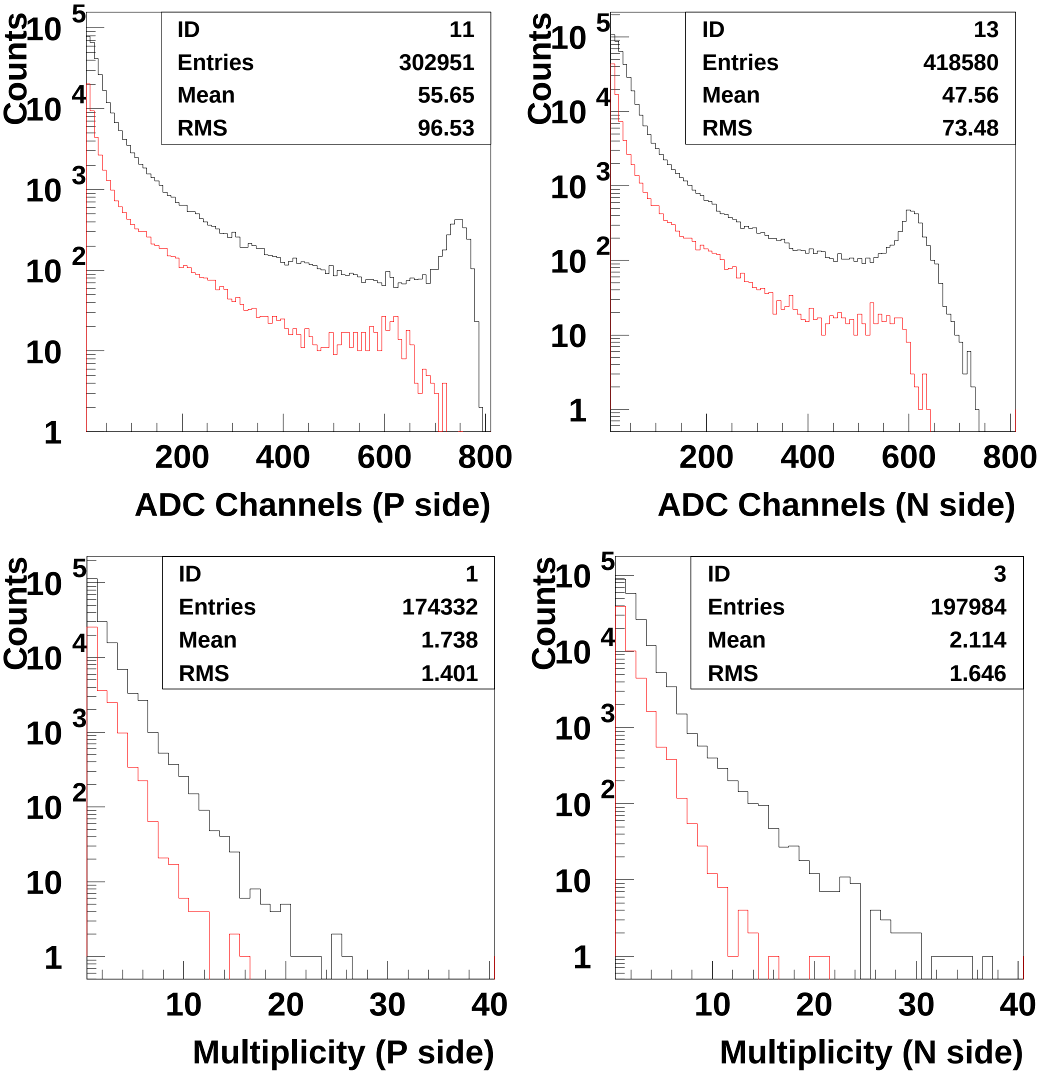

Figure 5.15: Typical ADC spectra (upper part) and multiplicity (lower part) for a P side (left) and a N side (right) silicon sensor. The black lines represent the HG chip, while the red lines represent the LG chip.

channel gets saturated for P side at ∼750 ADC Channels, for N side at ∼600 ADC Channels. If HG gets saturated, LG signals are used. From the Figure, HG/LG ratio can be evaluated and results to be ∼4, expected value.

Figure 5.17 shows a typical correlation between P and N side signals: left plot is for a HG chip while right one is for a LG chip. Figure 4.18, in

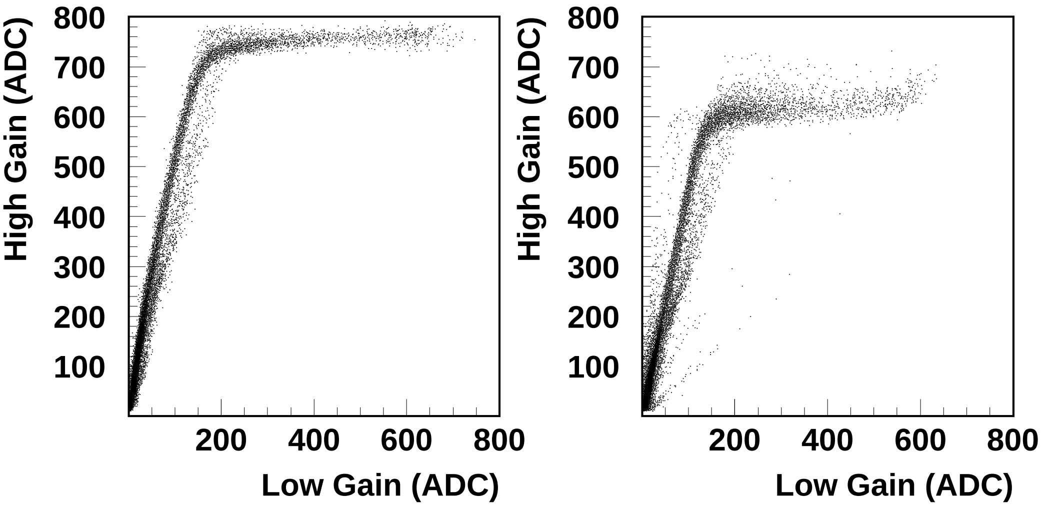

Figure 5.16: Typical correlation between HG and LG signals. Left plot is for a P side sensor, right one is for a N side sensor.

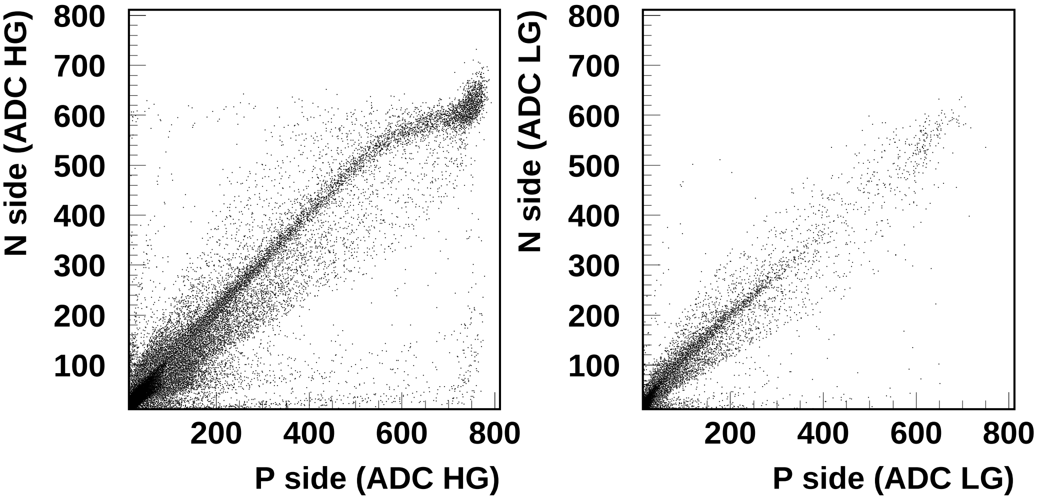

Figure 5.17: Typical correlation between P side and N side. Left plot is for a HG chip, right one is for a LG chip. Strips with the highest ADC value are taken into account.

the previous chapter, on the left panel is the corresponding plot for MIPs. Only strips with the highest ADC value are taken into account in these two plots. Excluding the non-linear part for the HG plot due to the previous evidenced saturation of the N side, a slope equal to one, expected value, can

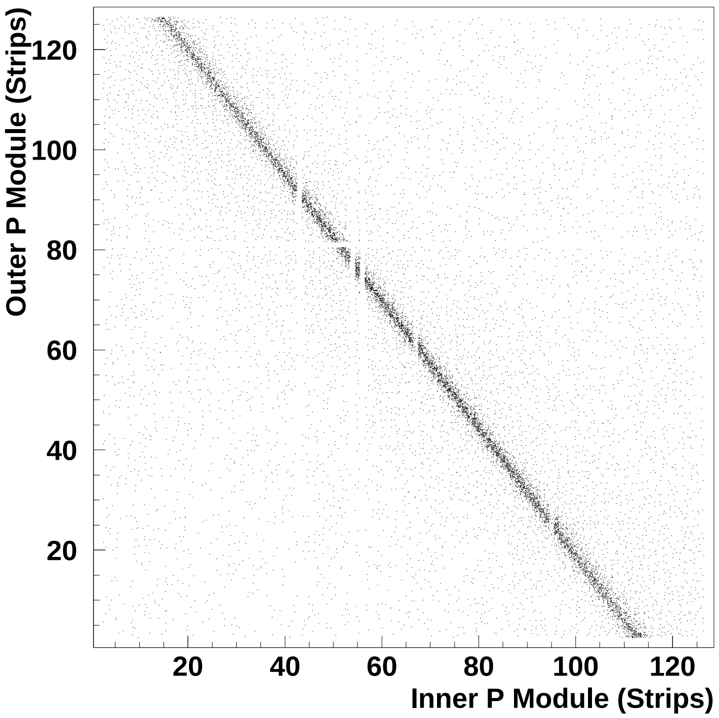

Figure 5.18: Typical correlation between inner and outer module strips (P side). Strips with the highest ADC value are taken into account.

be evaluated from the Figure.

When a particle goes through the SSD, a signal appears on both the inner and outer modules. Figure 5.18 shows a typical correlation between inner and outer module strips (P side): strips with the highest ADC value are taken into account. Figure 4.18 on the right panel is the corresponding plot for MIPs. In that plot, due to the cosmic trigger, only a part of SSD has been covered by MIP signals. In this case signal appear along all the sensors: the reconstruction is quite linear and follows the different disposition of inner and outer strips (see Figure 4.3).

Figure 5.19 shows a typical correlation between inner and outer module ADC signals. Left plot is for a P side sensor, HG chip, while right one is for a N side sensor, LG chip. The corresponding theoretical plot has been shown and discussed in Figure 3.9, Section 3.5.1. However, especially for HG chips, the shape is not triangular as only strips with the highest ADC value

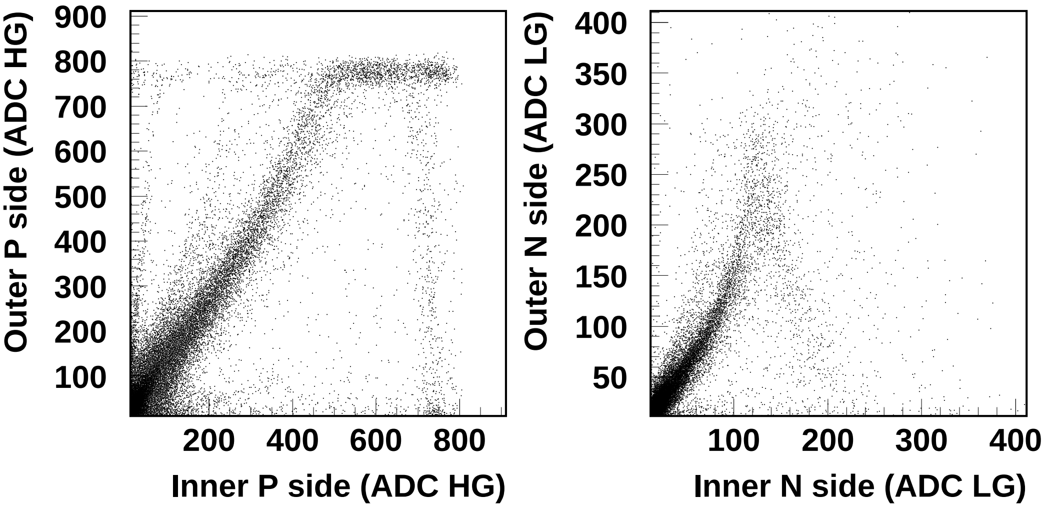

Figure 5.19: Typical correlation between inner and outer module ADC signals. Left plot is for a P side sensor, HG chip; right one is for a N side sensor, LG chip. Figure structure already discussed in the section 3.5.1 (Figure 3.9).

are taken into account.

5.4 *Correlation Recoil Detector-Forward Spectrometer*

In the previous Section first SSD response to HERA positron beams has been shown. SSD signals have been extracted without any conditions to the forward spectrometer.

In this following Section first recoil signals are extracted for a sample of $e^+ - p$ elastic scattering events. In an elastic process the same particles are present both before and after the scattering. The target remains in its ground state, absorbing merely the recoil momentum and hence changing its kinetic energy. The scattering angle and the energy of the positron and the production angle and energy of protons are unambiguously correlated. Elastic scattering represents the cleanest way to see a correlation for the first time between the forward spectrometer and the Recoil Detector. This sample of events can also be used as a tool for the recoil external alignment.

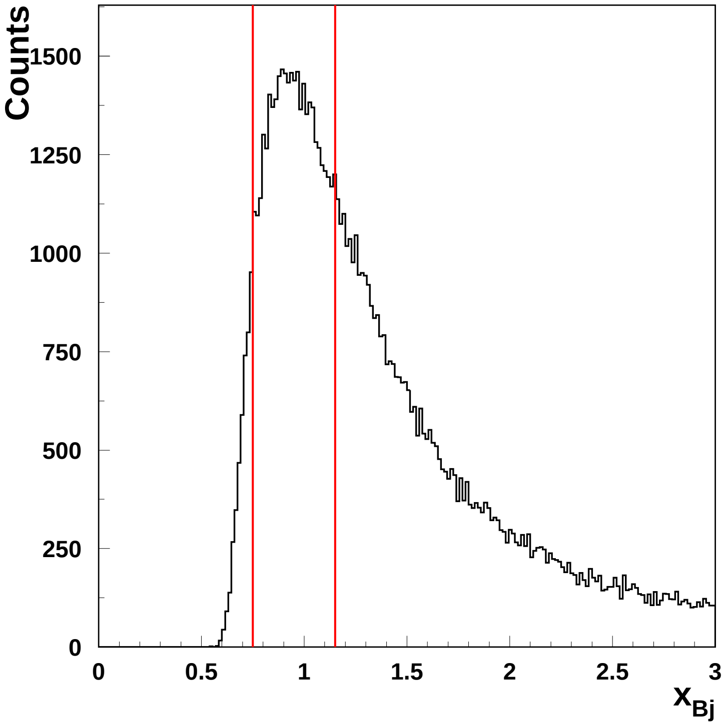

Figure 5.20: x_{Bj} variable (Expression 1.9) for events with positron momentum greater than 26.5 GeV. The red lines indicate the elastic events candidates.

5.4.1 *Elastic Event Selection*

In the forward spectrometer, events with one single charged track identified as a positron, fulfilling certain constraints, by HRC (described briefly in Section 2.3.1) are selected. HRC produces tracking and particle identification information. The reconstructed vertex is the point of closest approach of the track to the beam. The vertex range is chosen to be 0 cm $< z_{vertex} <$ 25 cm, wider than the cell dimension (15 cm) due to the poor resolution of the spectrometer for such a sample. The positron momentum is chosen to be greater than 26.5 GeV. The last constraint of this event sample is applied to the x_{Bj} variable (Expression 1.9), whose value is 1 for elastic scattering: its range is chosen to be $0.75 < x_{Bj} < 1.15$, indicated by vertical lines in Figure 5.20.

With this elastic sample, Recoil Detector signals are extracted for the first time. Since the Recoil Detector has been an upgrade of the HERMES spectrometer, a different reconstruction tracking code has to be used to extract tracking and particle identification information for the Recoil Detector. The reconstruction code will be briefly presented in the following Section.

5.4.2 *External Tracking Code (XTC)*

The HERMES Recoil Detector presents a difficult environment in which to perform tracking, where the track reconstruction code must fulfil the following requirements:

- The ability to find tracks using a limited (≤ 5) number of space points;
- The ability to find tracks in an inhomogeneous magnetic field;
- Good track fitting performance in the inhomogeneous field;
- Fast execution speed, generally required of tracking code.

Space points are the calculated positions on the detector plane transformed into the coordinate system required by the tracking algorithm.

In accordance with previous detector upgrades the tracking code for the HERMES Recoil Detector is implemented into a code called XTC (eXternal Tracking Code) in order not to interfere with the stable and proven HERMES reconstruction code HRC. In addition to the tracking, XTC contains subroutines which perform tasks such as clustering for the sub-detectors, space point reconstruction and interfaces to the ADAMO (Aleph DAta MOdel) libraries which provide the database scheme for HERMES.

A charged particle which passes through a segmented detector (e.g. a microstrip or fibre detector) generally deposits energy in a region which spans more than one strip or fibre. Clustering refers to a procedure applied to each sub-detector (SSD, SFT, PD) in which detector signals from physically adjacent strips or fibres are combined in order to obtain a more accurate estimate of the position (in the coordinate system of the detector plane) where the incident particle strucks. A clustering routine also typically uses calibration information to convert the detector signal from ADC pulses into an energy deposition measurement.

The Recoil Detector SC magnet generates a 1 Tesla magnetic field in which charged particles are deflected. The momentum of a charged particle traveling in a homogeneous, longitudinal magnetic field is proportional to its (constant) radius of curvature. The Recoil Detector SC magnet produces an inhomogeneous field, however, so tracking routines must be modified in order to reconstruct particle momenta more accurately. For this purpose a magnetic field map is required.

Tracking with the Recoil Detector is subject to various other specific challenges. Although the average number of good physics tracks inside the recoil acceptance is expected to be small, background contributions from noise or collimator scattering are expected. Furthermore, the amount of material passed by the particles through the recoil detector can lead to significant changes in the track parameters especially at low momenta.

At present status the XTC for the Recoil Detector is still in progress and not yet finished.

5.4.3 *Recoil Detector-Spectrometer Correlation*

Correlation between forward spectrometer and Recoil Detector is shown in Figure 5.21 where the difference between the z_{vertex} extracted by the forward spectrometer for the positron track and the z_{vertex} evaluated by XTC[1] for elastic protons crossing the Recoil Detector is displayed for elastic candidate events. For each event with a recognized positron, a single track into the Recoil Detector is required. A mean difference different than zero is found due to the fact that the external alignment between Recoil Detector and forward spectrometer is still not in production.

Figure 5.22 [Vil07b] shows the azimuthal angle ϕ and the $\sin\theta$ (polar angle) measured by the Recoil Detector for the scattered proton versus the same quantities reconstructed by the spectrometer for the positron track. The gap in the azimuthal angle results from the spectrometer acceptance.

---

[1] At the moment the tracking code XTC is not unique. In this thesis *Method 7* is used.

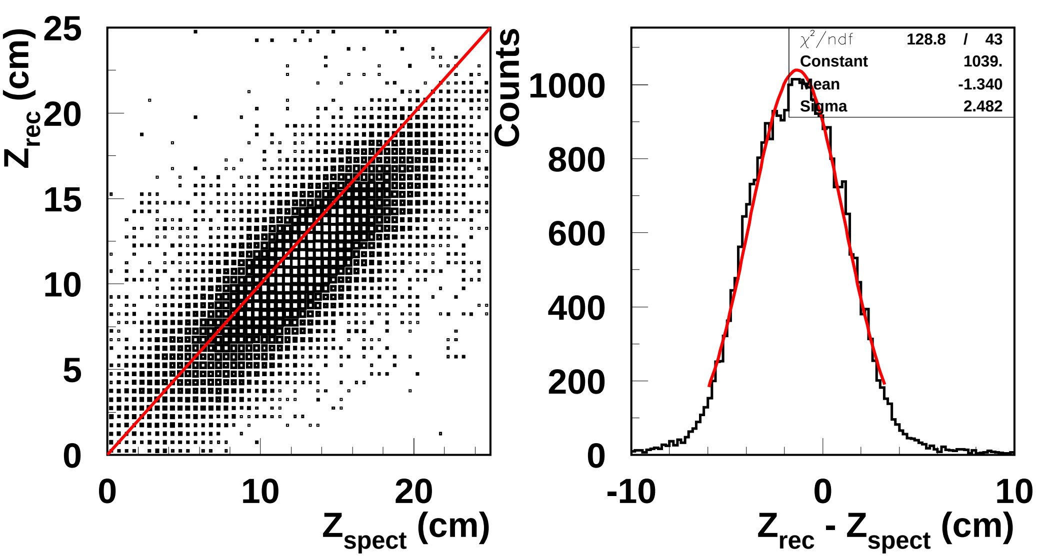

Figure 5.21: Difference between z_{vertex} extracted by the forward spectrometer for the positron track and z_{vertex} evaluated by XTC for elastic protons crossing the Recoil Detector.

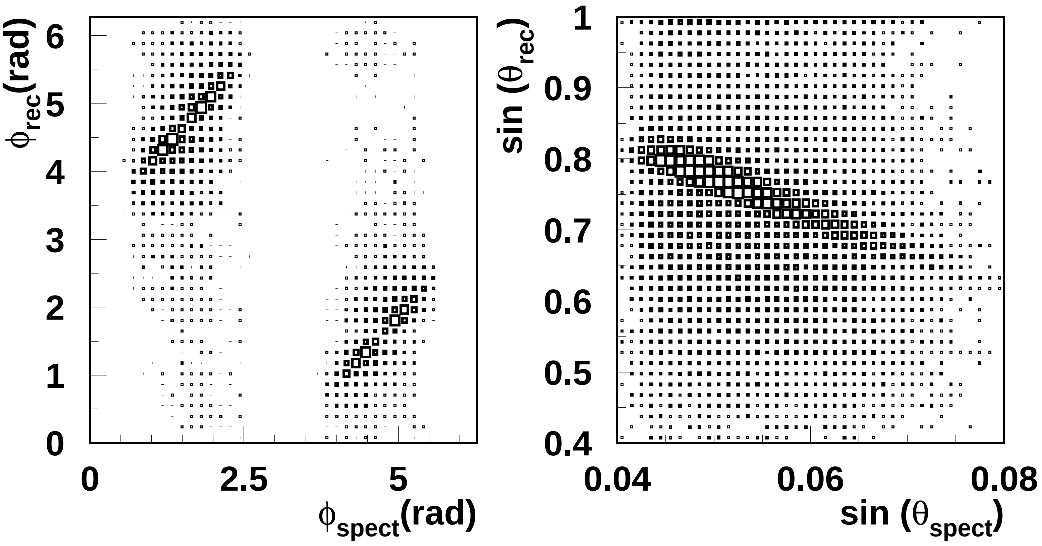

Figure 5.22: The azimuthal angle ϕ and the $\sin\theta$ (polar angle) measured by the Recoil Detector for the scattered proton versus the same quantities reconstructed by the spectrometer for the positron track.

5.5 *Summary*

The Recoil Detector was installed in January 2006 and took first data in February. The tracking in the magnetic field using the SFT was possible with the Recoil Detector SC magnet. In March the target cell was damaged while it was being inspected which resulted in large radiation doses to the SSD when the beam was injected. This required rebuilding the SSD in March - June. End of June HERA switched the beam polarity from negative to positive. The data taking was continued with the fully installed Recoil Detector in July 2006 till the 30^{th} of June 2007, last day of HERA running. Therefore unfortunately no data with electron beam is available with an operational SSD.

With positron beams it has been observed for bad HG chips that noise of last several HELIX channels was always much higher than the one of the first channels, resulting in a signal to noise ratio equal or less than 2 for MIP signals. A dedicated software noise correction by means of spline interpolation leads to a signal to noise ratio equal or better than 7, constant along all the sensors.

Correlation between HG and LG signals, P side and N side signals as well as inner and outer module signals has been shown. Moreover Recoil Detector signals have been extracted for the first time for events with one single charged track identified as a positron by the forward spectrometer. Even if the reconstruction tracking code for the Recoil Detector is still in progress, correlation between the Recoil Detector and the forward spectrometer for this event sample has been shown to be good.

In the next Chapter, preliminary DVCS analysis based on data without the Recoil Detector will be carried out as well as the extraction of first Recoil Detector physics signals based on single photon event sample.

Chapter 6

First Recoil Signals for DVCS Analysis

6.1 *Introduction*

The HERMES data taking stopped on the 30^{th} of June '07, the last day of HERA operation. Figure 6.1 shows the last fill of the HERMES data taking. A fill denotes the time period in which the measurement uses the same filling of the HERA electron ring. It lasts typically 8-14 hours. On the HERMES monitor stable current for protons and exponential behaviour current for positrons in function of time can be easily noticed.

In the years 2006-2007, HERMES took data with **only** unpolarized hydrogen and deuterium targets while HERA was filled with electrons and positrons. Figure 6.2 shows the collected statistics in these two years of HERMES operation with only the forward spectrometer (Figure 2.5). In the first half of 2006 HERMES took data with electron beams in both helicities, collecting, with the forward spectrometer, 7.4 millions of DIS events with hydrogen targets and 1.4 millions of DIS events with deuterium targets. HERA switched the beam charge from negative to positive in the end of June '06, leaving it positive till the end of data taking. With positron beams in both helicities, the forward spectrometer collected 40 millions of DIS events with hydrogen targets and 10 millions of DIS events with deuterium targets.

The beam polarization in the 2006 data sample was very similar in the positive helicity state (36%) and in the negative helicity state (-32.5%).

In the years 1996-2005, HERMES took data mainly with longitudinal (1996-2000) and transverse (2001-2005) polarized hydrogen and deuterium

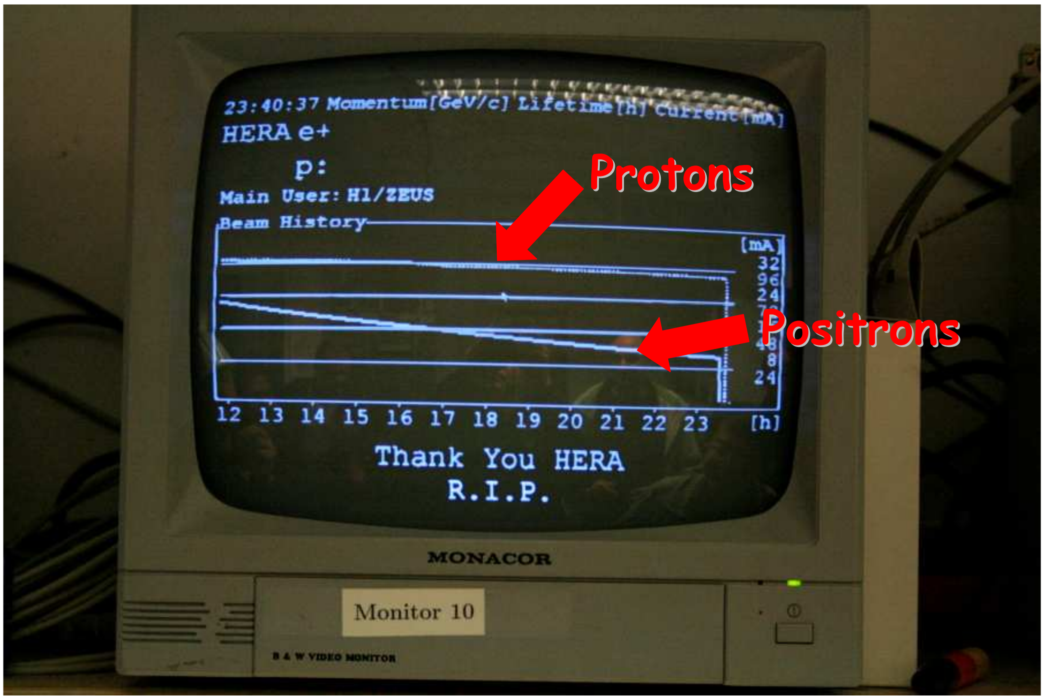

Figure 6.1: The HERMES monitor shows the last HERA fill.

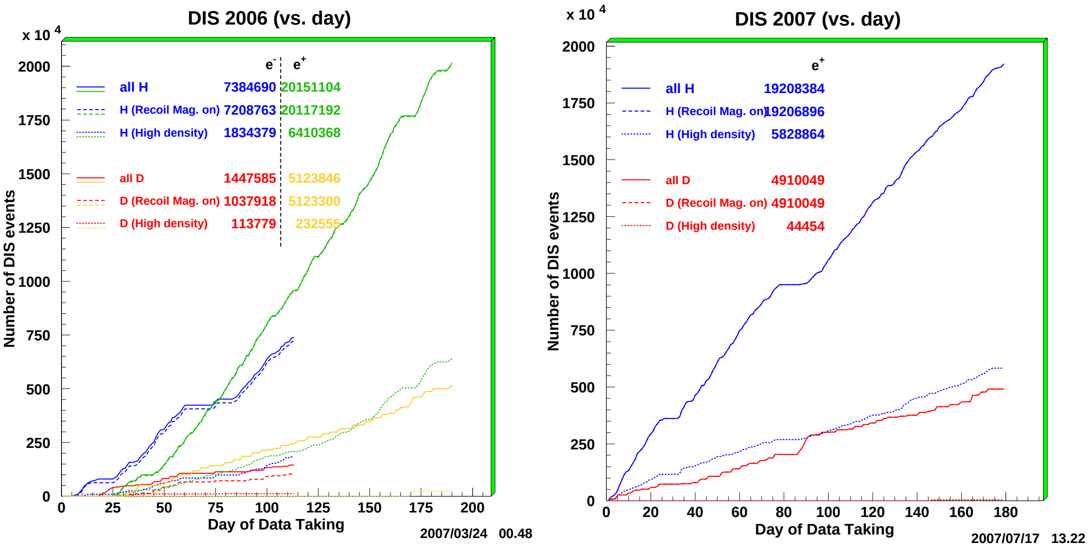

Figure 6.2: Number of DIS events versus days of data taking for 2006 (left panel) and for 2007 (right panel) for hydrogen and deuterium targets collected with the HERMES forward spectrometer.

gases injected by the ABS. The UGFS injected unpolarized molecular gases in place of the ABS when HERMES was running in the so-called *high-density mode*. The type of gas injected by the UGFS was changed between fills and running periods. The gases used were hydrogen, deuterium, helium, nitrogen, krypton, neon and xenon. High-density running was enabled during the final hour of each electron fill after the beam current had dropped from around 40 mA to approximately 15 mA. This mode of operation was due to the requirements from the collider experiments at HERA running in parallel to HERMES; the beam current had to remain above a certain amount in order to allow H1 and ZEUS to operate.

Due to the commissioning of the Recoil Detector, the number of DIS events collected for an exclusive analysis with the Recoil Detector (recoil exclusive analysis) is much lower than the number of accumulated DIS events shown in Figure 6.2. As already discussed in the previous Chapter, no data with electron beams are available with an operational SSD. Only the SFT was fully operational, with which 2.5 millions of DIS events were collected with hydrogen targets and 0.5 millions of DIS events with deuterium targets. With positron beams the Recoil Detector started to be fully operational in September '06, and since then 28 millions of DIS events were collected with hydrogen targets and 7 million of DIS events with deuterium targets.

The final statistics over the complete period of HERMES running for unpolarized hydrogen targets can allow to reproduce the published HERMES DVCS results (beam spin asymmetry A_{LU} and beam charge asymmetry A_C), based on the missing mass technique (see Section 3.1), with error bars reduced by a factor of 9, comparing to the two plots shown in Figure 1.7.

Statistics collected with the Recoil Detector can allow to extract recoil exclusive DVCS A_{LU}, suppressing background coming from semi-inclusive events and events with intermediate Δ^+ production (see Figure 3.1). The recoil exclusive DVCS A_C could not be easily extracted with only an operational SFT: as the SSD was not operational with electron beams, recoil protons with low momentum transfer $-t$ were not detected, therefore up to $t = 0.2$ GeV^2 improvements in t resolution are lost (Figure 3.31). Moreover the PID performance and the background suppressions cannot be guaranteed with only the SFT.

At present status, only 2006 data are ready for being analyzed. DIS and DVCS events selected by the forward HERMES spectrometer are used to extract A_{LU} and A_C, which are then compared to the previous published results (Figure 1.7). In order to extract A_C both beams have to be used. Then first signals from the Recoil Detector are shown for this data sample with positron beams.

In order to describe the extraction of the event samples for the DVCS analysis, the HERMES data structure and the various selection criteria applied to the data are explained in the next Sections. The reliability of the data produced during the running of the HERMES experiment is heavily dependent on the performance of each sub-component of the HERMES spectrometer and on the quality of the beam provided by the HERA accelerator. Data samples containing recorded events during a period of sub-system malfunction or instability are discarded during the analysis; only samples satisfying specific performance criteria remain.

6.2 *Data Structure and Production*

HERMES data sets are divided into fills, runs and bursts. After a trigger occurs during the measurement, the data acquisition system translates the response from all detectors into a digital form and stores it in a file on a hard disk. A file size of 500 MB determines a run which is typically achieved after 5-10 minutes of data taking depending on the event rate. Every 10 seconds the so-called slow-control data is read-out. This arbitrarily chosen time period defines a burst. Slow-control data is not related to a single event but to the performance of the beam, the target, and the detectors which change on a longer time scale. After a run is completed the file is stored on hard disk and copied in parallel to the DESY tape robot.

The raw data which are stored in EPIO (Experimental Physics Input Output) format are processed by a chain of analysis programs. The process of reading the raw data and computing the physical tracks and particle energies is called a data production. In a data production the raw data are analyzed in main steps. First the EPIO data are read from robot and converted in physical quantities using the HERMES DeCoder (HDC). With the knowledge of the design of the sub-detectors and specific mapping and calibration files the HDC program decodes the EPIO files into specific quantities for each sub-detector, e.g., hit positions in wire-maps, energy depositions or timing information. The output format is based on the tabular structure of the Aleph DAta MOdel (ADAMO) database and the output file is directly sent into the HRC program, described briefly in Section 2.3.1. This program combines the individual detector responses in conjunction with alignment and calibration information in order to reconstruct tracks in the spectrometer and clusters in the CALO respectively. The slow-control data, on the other hand, are combined with external data provided by the experts of the detector subsystems, into a single slow-control data file for each fill. In a last step all data relevant for physics analysis are calculated from the HRC output and the slow-control files and merged into a single file for each run, the so-called micro-Data Summary Tape (μDST). The first production called the "a" production uses the calibration data from the previous year. Its purpose is to be used for calibration of the detectors. The second pass over the data, the "b" production, is the first complete information set with calibrated detectors. These files are usually the ones used for the physics analysis.

6.3 *Data Quality*

The decision whether accumulated data is of sufficient quality to be used for analysis purposes or not is done on the run and burst level. On the run level the notes in the electronic logbook made by the people on shift during data taking are taken into account. On the burst level slow-control data are used.

The 2006 b2 μDST production is used for this analysis. Hydrogen targets are selected. Only runs marked as analyzable in the electronic logbook are taken into account. The following data quality cuts are used at the burst level:

- there are no HV trips in the FCs and BCs;
- there are no dead blocks in the CALO or luminosity monitor or H2;
- the TRD is functioning during the burst: the TRD affects the particle identification performance and is therefore monitored to ensure that

it experiences no high voltage trips and that its performance is stable over time;

- the beam polarization value is provided by at least one of the two polarimeters;
- the burst is not longer than 11 seconds: as the burst is the time unit between two consecutive scalar events, the burst length should not be too long in order to have trustworthy scalar data;
- the burst is not the first burst in a run: the first burst in a run is always omitted, since the initial phase of a run includes various initializations of detectors;
- the dead time is reasonable: the dead time is calculated as the ratio of generated triggers over accepted triggers. The dead time obviously is always smaller than one. Large dead times correspond to large backgrounds, therefore these data sets should be rejected.

At the moment no assumption is done on the performance of the Recoil Detector, since the first purpose is to compare 2006 DVCS A_{LU} and A_C to the previous published results (Figure 1.7), extracted with the missing mass technique.

6.4 *Event Selection*

In a first step, events where the scattered electron can be identified within certain kinematic boundaries are selected. The number of these so-called DIS events has to be counted for normalization purposes. In a second step DIS events are selected if they have exactly one charged track, i.e., the scattered electron, and exactly one photon fulfilling certain constraints. These events are called single-photon events. The third sample consists of the single-photon events which are likely to be produced exclusively, i.e. as described by Expression 1.5, and are therefore called exclusive events. With this exclusive event sample A_{LU} and A_C can be extracted.

6.4.1 *DIS Events*

Events containing at least one charged reconstructed track are called DIS events if at least one charged track meets the following requirements. The track traverses one full spectrometer half and produces a signal in the CALO, i.e. it is not bent out of the acceptance by the spectrometer magnet. A projection of the back track, as given by the BCs, to the position of the CALO satisfies the fiducial constraints $|x_{calo}| < 175$ cm and 30 cm $< |y_{calo}| < 108$ cm. This corresponds to the track not being incident in the outermost $2/3$ of the outer row or column of CALO blocks. Otherwise the energy might leak out of the sides of the CALO, thus leading to a wrong reconstruction. A correct energy reconstruction in the CALO is necessary for the PID system described in Section 2.3.2 which must identify the track as an electron in this case.

As can be seen from Figure 2.5 there are field clamps in front and behind the magnet, requiring additional cuts to the track parameters. The absolute value of the x position of the track at the front (rear) field clamp is smaller than 31 (100) cm; the absolute value of the y position of the track at the septum plate (rear field clamp) is larger (less) than 7 (54) cm. Particles hitting these field clamps could cause particle showers. These showers obviously need to be avoided in the data sample.

The vertex is the point of closest approach of the track to the beam. The vertex should be inside the target cell in the longitudinal direction, i.e., 5 cm $< z_{vertex} < 20$ cm, and in the transverse direction, i.e., $t_{vertex} < 0.75$ cm.

The detection of the scattered electron allows for the calculation of the so-called inclusive variables (Expressions 1.6 - 1.9), i.e. the variables that can be calculated with the detection of the scattered electron only. It has already been discussed in Chapter 1 that Q^2 should be large compared to the mass of the final hadronic state in order to be in the hard scattering regime where factorization is valid. Since the final hadronic state is a proton, $Q^2 \gg 1$ GeV^2 would be required to assure the factorization of the DVCS process. On the other hand, statistics are limited for large values of Q^2. The data therefore is constrained to $Q^2 > 1$ GeV^2. The squared invariant mass of the photon-nucleon system W^2 is required to be above 9 GeV^2. Although it will be shown later on in Figure 6.6 that the exclusive sample satisfies $W^2 > 9$ GeV^2

anyway, this constraint is nevertheless important since it restricts the data to the deeply-inelastic regime where the fragmentation model of the Monte Carlo is believed to work.

These constraints are applied to the data sets from 2006, for hydrogen targets. As an example, the distribution of the electron vertex z_{vertex} along the beam axis (z-axis) is shown in the upper left panel of Figure 6.3. The distribution shows the expected triangular shape, consistent with the density of the target gas in the target cell when injecting the gas at $z = 12.5$ cm. The electron vertex distribution perpendicular to the beam axis is shown in the upper right panel of Figure 6.3. The observation that the distribution do not have its maximum at the expected value of $t_{vertex} = 0$ cm, i.e. in the center of the target, is believed to be due to small misalignments of the top and bottom part of the detector.

The θ and ϕ angle distributions are shown in the middle panel of the Figure 6.3. The shape of the angular distributions reflects the acceptance of the spectrometer.

The distribution of the energy transfer ν from the incoming electron to the virtual photon is shown in the lower panel of Figure 6.3. Since different thresholds for the electron in the CALO are used, in order to avoid normalization problems, $\nu < 22$ GeV is required in the following to ensure that the electron is well above the 3.5 GeV threshold. As will be shown in Figure 6.6, this cut basically does not affect the exclusive data sample.

Distributions displayed in Figure 6.3 are extracted by a further independent analysis code, obtaining same number of DIS events as well as same mean values of the shown variables.

6.4.2 *Single Photon Events*

From the sample of DIS events, only those with exactly one charged track with the beam charge, i.e. the scattered electron, are taken into account in the following. In addition, exactly one cluster in the CALO with no track assigned to it, a so-called trackless cluster, is required. In order that this cluster is accepted as a photon in this analysis, a signal in the preshower detector $E_{pre} > 1$ MeV is required. This requirement makes the reconstructed photon energy reliable. At HERMES, the CALO is calibrated based on the

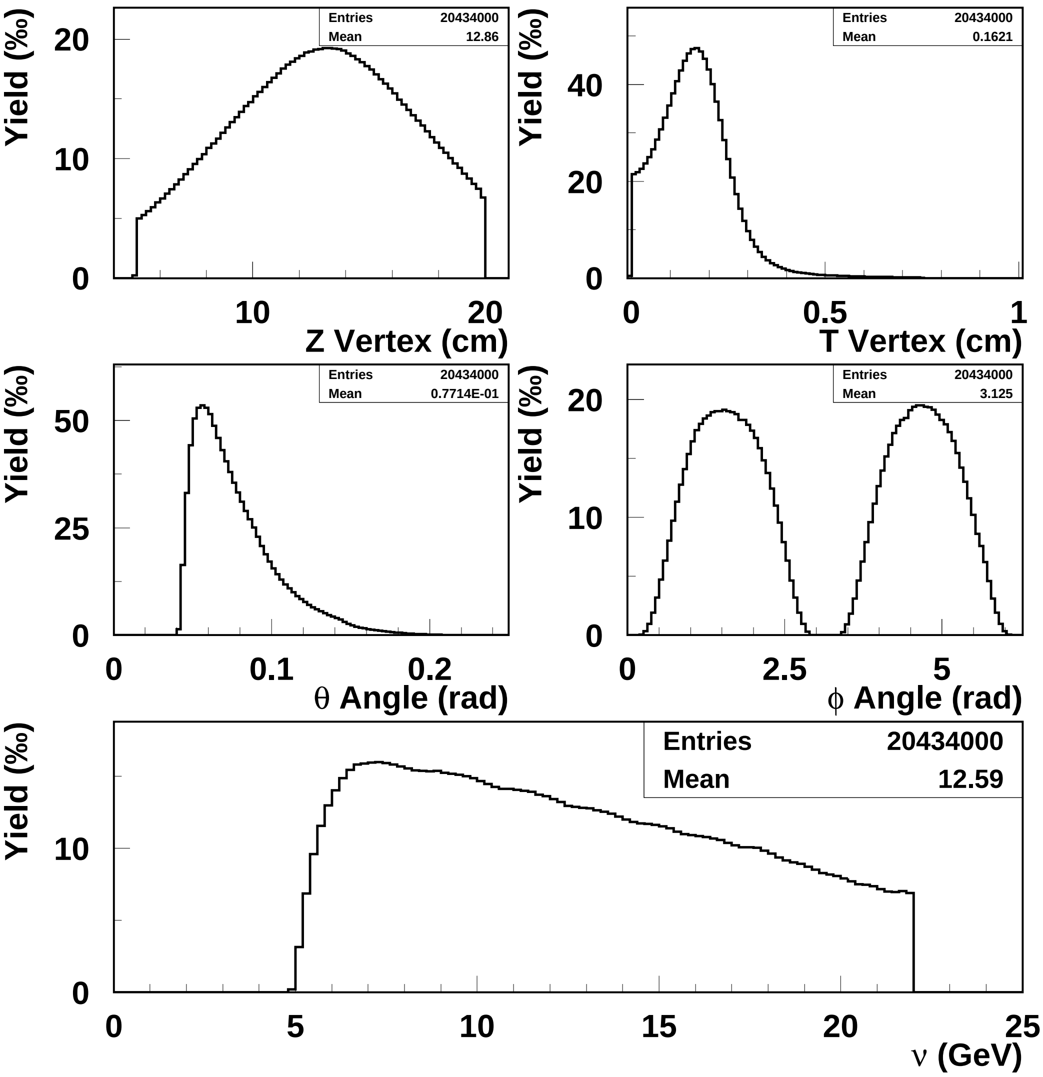

Figure 6.3: Distributions of DIS event samples from 2006 hydrogen targets for the vertex position in the longitudinal direction z_{vertex}, in the transverse direction t_{vertex}, for θ and ϕ angles and for the energy of the virtual photon ν. The data sets are normalized to 1000 DIS.

E/P ratio of a sample of electrons identified conservatively, whose energy deposition in the pre-shower detector is required to be more than that of minimum ionization particles. For photons which do not start showering in the preshower detector, the reconstructed photon energy can be wrong as much as 10% for photons of 15 GeV energy [Ely02]. Such a bias, which can lead to a poorer resolution in the missing mass and a less exclusive measurement, can be eliminated by the 1 MeV cut, although the cut will induce a 20% loss of statistics [Ely02]. However for photons a detail CALO calibration depending on the preshower signal and on the lepton charge is at the moment is being investigated and it is not yet available.

The energy of the real photon E_γ is required to be above 3 GeV. With the 3 GeV cut, the cluster cannot be due to a charged particle that escaped detection of the tracking system. It is very unlikely that such a track is not reconstructed, since the tracking efficiency is very good for tracks of momentum $>$ 3 GeV. With the missing mass cut described below, neither can the cluster be due to a neutron. Hence the cluster must have come from a photon or photons. The latter can happen when two or more photons hit the same CALO block.

The photon needs to be in the fiducial volume of the CALO for photons, $|x_{calo}| < 125$ cm and 33 cm $< |y_{calo}| < 105$ cm. The constraint in the y direction prevents photons from being incident in the outermost row of CALO blocks where the shower is not anymore fully contained in the CALO and its energy gets incorrectly reconstructed. The constraint in the x direction is given by the acceptance of the spectrometer magnet for neutral particles coming from the target.

For photons satisfying the above constraints the Mandelstam invariant t can be calculated with the virtual and real photon four-momenta q and q', respectively (Expression 1.10). The four-momentum of the real photon is q' $= (E_\gamma, \overrightarrow{q'})$ with $|\overrightarrow{q'}| = E_\gamma$ being the energy deposited by the photon in the CALO. The position of the photon cluster in the CALO (x_{calo} and y_{calo}) and the z_{vertex} of the interaction are known, thus

$$\overrightarrow{q'} = \frac{E_\gamma}{L} \cdot (x_{calo}, y_{calo}, D_{calo} - z_{vertex})$$

where $D_{calo} = 732$ cm is the distance of the CALO front to the origin $z = 0$ cm, and $L = \sqrt{x_{calo}^2 + y_{calo}^2 + (D_{calo} - z_{vertex})^2}$ is the length of the constructed vector pointing in the direction where the photon hits the CALO.

The angle between the virtual and the real photon $\theta_{\gamma^*\gamma}$ is given by Expression 1.11.

Applying all constraints, single photon samples are extracted for the 2006 hydrogen data and normalized to their respective number of DIS events.

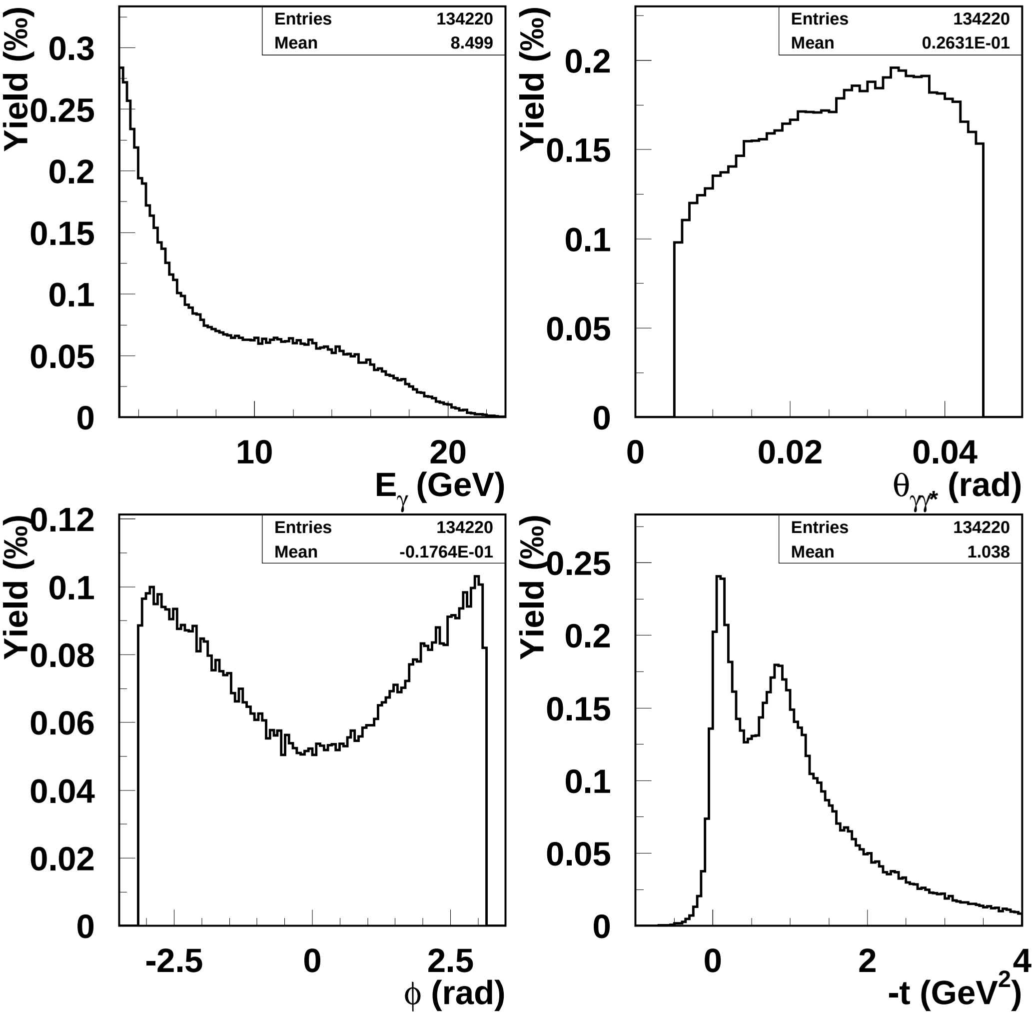

Figure 6.4: Distributions of the single photon event yields per 1000 DIS events for the hydrogen data from the year 2006 for different variables.

Samples of 134220 single photon events, corresponding to 0.66% of DIS events, taken with both beams are selected. The distributions for the variables calculated via the outgoing photon kinematics are given in Figure 6.4, with the azimuthal angle ϕ given by Expression 1.12 (Figure 1.4). A lower limit needs to be placed on the opening angle $\theta_{\gamma^*\gamma}$. Consequently, it should be calculated only in a region where the opening angle $\theta_{\gamma^*\gamma}$ is non-zero within its resolution. The latter is dominated by the position resolution of photons in the CALO which turns out to be about 0.6 mrad. Based on Monte Carlo studies the latter value is decreased to 45 mrad as indicated in the Figure, because beyond this point the exclusive event sample contains more background (semi-inclusive and Δ^+ production) than BH/DVCS events [Ell04]. Taking into account additional contributions, in particular the width of the t_{vertex} distribution in Figure 6.3, a safe lower limit of 5 mrad can be placed on the opening angle $\theta_{\gamma^*\gamma}$. The t distribution in the lower right panel of Figure 6.4 offers a possibility to distinguish exclusive and non-exclusive processes. Exclusive processes have vanishing momentum transfer, i.e. the peak at $-t \approx 0$ mostly contains exclusive events. Events with $-t > 0.5$ GeV^2 are mostly semi-inclusive. These photons predominantly originate from the decay of π^0 and η. Their largest fraction comes from the decay of the π^0 with one of the two decay photons remaining undetected, usually due to the fact that it is not within the geometrical acceptance of the HERMES spectrometer [Ell04]. In addition, photons with energies below 0.5 GeV are not detected anymore and in the case that the photons are separated by less than about 10 cm at the CALO position they are reconstructed as only one cluster. The distribution of the photon energy E_γ, shown in the upper left panel of Figure 6.4, is largely dominated by low energetic photons. It has already been claimed above that the imposed constraint $E_\gamma > 3$ GeV does not reject valuable data. Low energetic photons appear mostly at high values of t and vice versa. Hence an upper limit on t of 0.5 GeV^2 would lead to a predominantly exclusive sample with high energetic photons.

6.4.3 *Exclusive Events*

In the last step of the event selection the single photon event sample has to be reduced to a sample with predominantly exclusively produced photons. As discussed in the Section 3.1 the missing mass technique is employed to extract the sample of exclusive events. Figure 6.5 shows the squared missing mass M_x^2 distribution for the 2006 hydrogen data sample for two different E_γ threshold for single photon events. Even if 5 GeV cut is more efficient as shown in Figure since has a significant effect on the non-exclusive region, it was decided to use a 3 GeV cut since has a negligible effect on the exclusive region ($M_x^2 \sim m_p^2$). The effect on the non-exclusive region is due to the fact that the recoiling proton has a very low energy, thus energy conservation

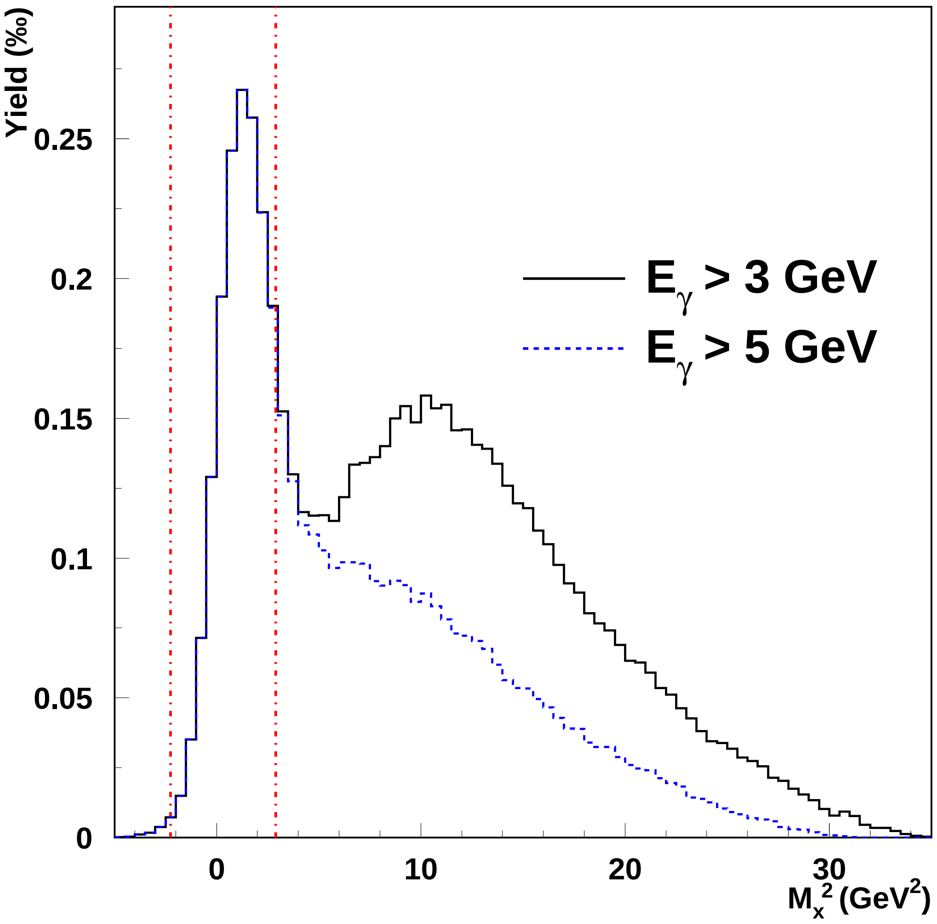

Figure 6.5: The distribution of the squared missing mass M_x^2 of the single photon event sample. The same distribution but requiring $E_\gamma > 5$ GeV (blue dashed line) instead of $E_\gamma > 3$ GeV (black solid line) is also shown. The red dashed-dotted vertical lines represent the exclusive bin (-2.25 GeV^2 $< M_x^2 <$ 2.89 GeV^2).

requires that the emitted real photon of a BH/DVCS event must carry most of the rest of the beam energy $E - E' = \nu = \frac{W^2-M^2}{2M(1-x_{Bj})}$, which is larger than $\frac{9-M^2}{2M} = 4.3$ GeV due to the requirement $W^2 > 9$ GeV^2.

In Figure 6.6 different variables are shown for exclusive events, i.e. after applying the missing mass cut described in Section 3.1 (-2.25 GeV^2 $<$ $M_x^2 <$ 2.89 GeV^2) and demonstrated in Figure 6.5. Samples of 32596 exclusive events, corresponding to 24.3% of single photon events, taken with both beams are selected. As expected, the Q^2 distribution has its maximum

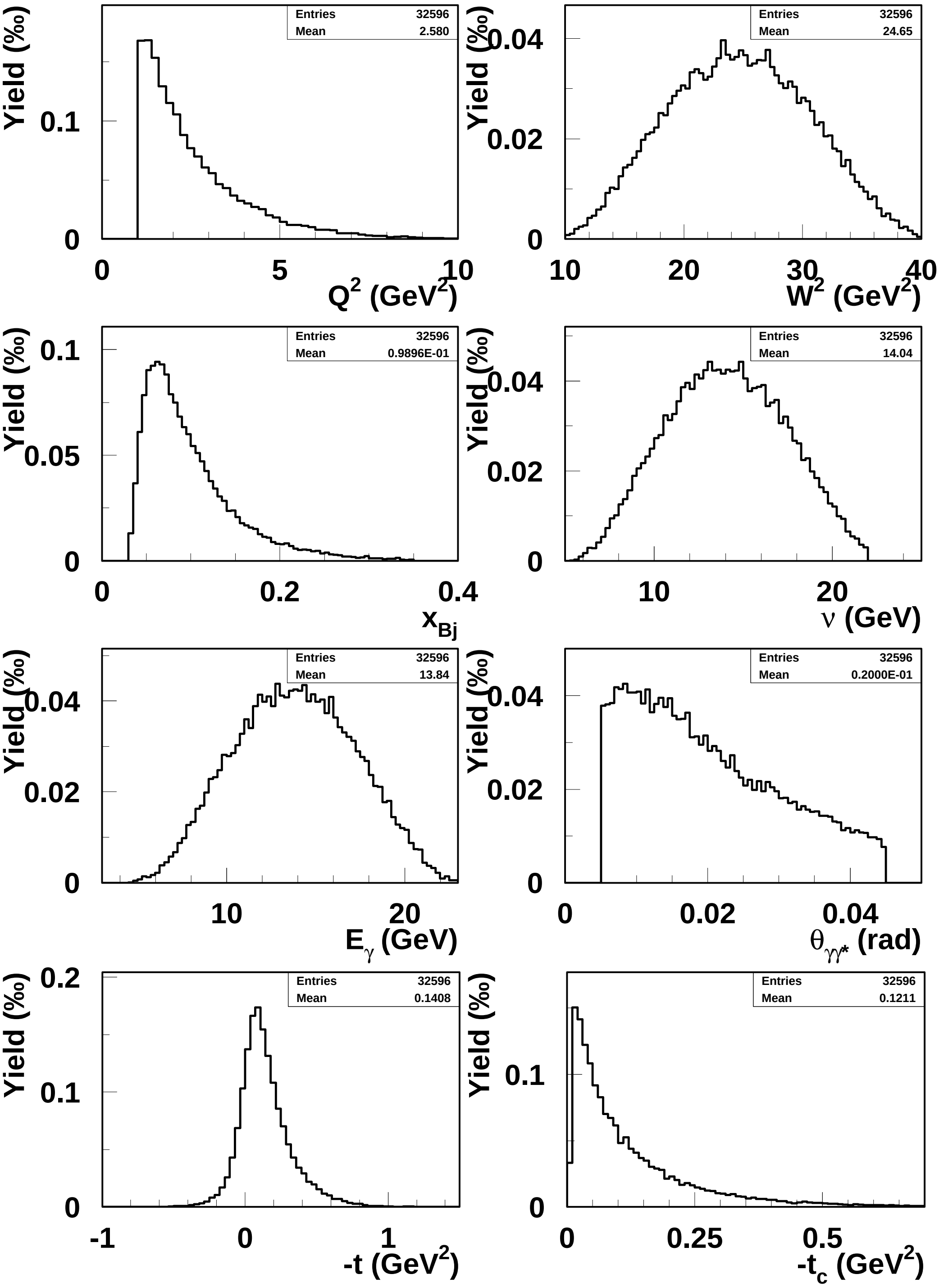

Figure 6.6: Distributions of the exclusive events for different variables. The data sets are normalized to the respective number of DIS events.

yield at $Q^2 = 1$ GeV^2 with a quick falloff towards higher values of Q^2. The x_{Bj} distribution displays the kinematic range of this variable accessible at HERMES. The W^2 and ν distributions confirm that the imposed constraints of $W^2 > 9$ GeV^2 and $\nu < 22$ GeV basically do not affect the exclusive sample. The same holds for the $E_\gamma > 3$ GeV requirement. A comparison between the E_γ and t distributions in the exclusive sample (this Figure) and in the single photon sample (Figure 6.4) shows that indeed only high energetic photons with the corresponding small values of t survive in the exclusive sample, as already discussed above. Comparing the $\theta_{\gamma^*\gamma}$ distributions from the exclusive and the single photon sample it becomes obvious that the exclusive events are peaked at small values of $\theta_{\gamma^*\gamma}$.

As already discussed in Section 3.1 t has to be calculated using the virtual and real photon kinematics (Expression 3.1) and consequently is affected by the photon energy resolution. Hence, the $-t$ distribution of exclusive events, just like the M_x^2 distribution, extends to negative values (Figure 6.6). The extraction of azimuthal asymmetries as a function of values of t implies the problem that results are shown in an unphysical region where no comparison to theoretical predictions is possible. In addition, the resolution in t determines the minimum bin width in t.

It is possible to calculate t without the knowledge of the photon energy E_γ by setting the squared missing mass in Expression 3.2 equal to the squared proton mass. The resulting expression for the photon energy can be inserted into the calculation of the squared four momentum transfer (Expression 3.1) in order to get rid of any dependence from E_γ. The result is called the squared constrained momentum transfer

$$t_c \overset{lab}{=} \frac{-Q^2 - 2\nu\left(\nu - \sqrt{\nu^2 + Q^2}\cos\theta_{\gamma^*\gamma}\right)}{1 + \frac{1}{M}\left(\nu - \sqrt{\nu^2 + Q^2}\cos\theta_{\gamma^*\gamma}\right)} \quad . \tag{6.1}$$

as it relies on the assumption $M_x = M_p$. The t_c distribution is shown in Figure 6.6 as well. Calculating t_c for the elastic BH events from the reconstructed variables in the Monte Carlo yields a resolution in t_c better than 0.1 GeV^2 (Figure 3.32), i.e., the resolution is an order of magnitude better than the measured one. Hence the constrained t method is the preferred one to use for the definition of the exclusive data set from which the azimuthal

DVCS events with positive helicity state	24783
DVCS events with negative helicity state	7813
DVCS events with negative beam charge	8821
DVCS events with positive beam charge	23775

Table 6.1: Exclusive single photon events collected for hydrogen targets, using the 2006 b2 μDST production.

asymmetries are extracted.

6.5 *Extraction of Azimuthal Asymmetries*

In the following the extractions of DVCS A_{LU} and A_C are performed with the exclusive event sample described above. DVCS A_{LU} and A_C asymmetries can be extracted from the DVCS count rate for each bin and then a fit is performed in order to extract different amplitudes.

Table 6.1 summarizes the exclusive single photon events collected for hydrogen targets, using the 2006 b2 μDST production. For the A_{LU} the exclusive single photon sample contains 24783 events in the positive helicity state and 7813 events in the negative helicity states. For the A_C samples of 8821 events taken with electron beams and 23775 events taken with positron beams are selected. The average values of the kinematic variables for the exclusive sample are (Figure 6.6):

$$\begin{aligned}
\langle Q^2 \rangle &= 2.58\ \text{GeV}^2, \\
\langle W^2 \rangle &= 24.65\ \text{GeV}^2, \\
\langle x_{Bj} \rangle &= 0.1, \\
\langle \nu \rangle &= 14.04\ \text{GeV}, \\
\langle E_\gamma \rangle &= 13.84\ \text{GeV}, \\
\langle \cos\theta_{\gamma^*\gamma} \rangle &= 1, \\
\langle -t_c \rangle &= 0.12\ \text{GeV}^2.
\end{aligned}$$

6.5.1 *Beam Spin Asymmetry* $A_{LU}(\phi)$

Using a longitudinally polarized beam and an unpolarized target, the beam spin asymmetry $A_{LU}(\phi)$, where L denotes the longitudinal polarized beam and U the unpolarized target, can be calculated via a cross section ratio as

$$A_{LU}(\phi) = \frac{1}{\langle P\rangle} \frac{\frac{\overrightarrow{N}(\phi)}{\overrightarrow{NORM}} - \frac{\overleftarrow{N}(\phi)}{\overleftarrow{NORM}}}{\frac{\overrightarrow{N}(\phi)}{\overrightarrow{NORM}} + \frac{\overleftarrow{N}(\phi)}{\overleftarrow{NORM}}} \quad ,$$

where $\overrightarrow{N}$ ($\overleftarrow{N}$) represents the exclusive yield in the helicity state parallel (antiparallel) to the beam direction. The normalization ($NORM$) for the respective helicity state can be done either to the number of DIS events or to the luminosity. The luminosity for a burst is calculated as the product of the rate in the luminosity monitor, the live time of trigger 18/26 and of the burst length. The luminosity is then given as the sum over all bursts satisfying the data quality constraints. The average value of the beam polarization $\langle P\rangle = (\langle \overrightarrow{P}\rangle + \langle|\overleftarrow{P}|\rangle)/2$ accounts for the beam not being 100% polarized.

The beam polarization measurements were carried out by both polarimeters (see Section 2.1) in parallel during most of the time in the 2006 running period. For every fill, the polarimeter group specifies the polarimeter from which the measured value should be taken (*best polarimeter*). This usually is the longitudinal polarimeter (LPOL) since it has a smaller systematic uncertainty (1.6%). Only if the LPOL shows problems during operation, the values from the transverse polarimeter (TPOL) with a systematic uncertainty of 3.4% are taken. The resulting systematic error of 1.9% for the beam polarization measurement is given by the fractional use of LPOL and TPOL in the 2006 running period. The systematic error to the A_{LU} is then 1.9% of the asymmetry in the respective bin.

The DVCS A_{LU} as a function of ϕ is shown in Figure 6.7 with the respective statistical error bars, where the normalization is done with respect to the number of DIS events. The amplitude of the $\sin\phi$ dependence can be obtained via a fit to the asymmetry. As has been explained in Section 1.2.3, $\sin 2\phi$ and $\sin 3\phi$ contributions may arise at higher twist and thus should be suppressed in comparison to the $\sin\phi$ contribution. A possible offset set can only be due to the quality of the normalization since

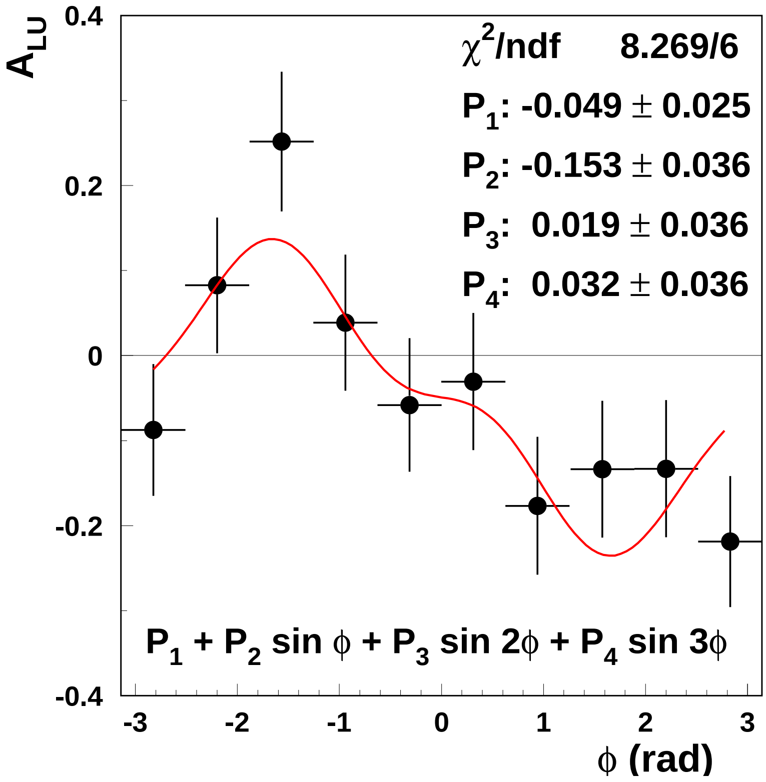

Figure 6.7: Beam spin asymmetry A_{LU} for the hard electro-production of photons off the proton as a function of the azimuthal angle ϕ for the exclusive sample (2006 preliminary hydrogen data). The solid curve shows the result of the indicated four parameter fit with the values given in the plot.

there is no helicity dependent but ϕ independent term in the photon production cross section (see Expressions 1.13 - 1.15). A fit to the function $P_1 + P_2 \sin\phi + P_3 \sin 2\phi + P_4 \sin 3\phi$ is therefore carried out. The result yields a strong $\sin\phi$ dependence of $P_2 = -0.153 \pm 0.036$ while the $\sin 2\phi$ and $\sin 3\phi$ components ($P_3 = 0.019 \pm 0.036$ and $P_4 = 0.032 \pm 0.036$) are compatible with zero. The constant term ($P_1 = -0.049 \pm 0.025$) shows a 2-sigma deviation from zero.

6.5.2 *Beam Charge Asymmetry* $A_C(\phi)$

The extraction of azimuthal dependencies of the beam charge asymmetry A_C via the fit method follows in the same way. The A_C as a function of ϕ is calculated as

$$A_C(\phi) = \frac{\frac{N^+(\phi)}{DIS^+} - \frac{N^-(\phi)}{DIS^-}}{\frac{N^+(\phi)}{DIS^+} + \frac{N^-(\phi)}{DIS^-}} \quad , \tag{6.2}$$

with the yield N^+ (N^-) and the number of DIS events DIS^+ (DIS^-) using positron (electron) beams. When both beam and target are unpolarized, the leading twist contribution should be dominated by a $\cos\phi$ behavior, possibly accompanied by a kinematically suppressed offset as discussed in section 1.2.3. However, in the analyzed data beams are not unpolarized, i.e., λ is not zero in Expression 1.15, and thus an additional $\sin\phi$ dependence is expected. In order to cancel this contribution, the *symmetrized* A_C is calculated by replacing ϕ with $|\phi|$ in Expression 6.2. The A_C as a function of $|\phi|$ is shown in Figure 6.8 with the respective statistical error bars. Using the exclusive sample, a fit to the function $P_1 + P_2\cos\phi + P_3\cos 2\phi + P_4\cos 3\phi$ yields a $\cos\phi$ dependence with an amplitude of $P_2 = 0.033 \pm 0.011$. The constant term ($P_1 = -0.056 \pm 0.008$) shows a 7-sigma deviation from zero.

It has been mentioned in Section 1.2.3 that possible higher twist contributions should exhibit a $\cos 2\phi$ and $\cos 3\phi$ behavior. From the fit both $\cos 2\phi$ and $\cos 3\phi$ components ($P_3 = 0.001 \pm 0.011$ and $P_4 = 0.007 \pm 0.011$) are compatible with zero.

6.5.3 A_{LU} and A_C in function of M_x and $-t_c$

In order to demonstrate that the azimuthal asymmetries are present in the exclusive region only, Figure 6.9 shows the $\sin\phi$ amplitude of the A_{LU} (left) and the $\cos\phi$ amplitude of the A_C (right) in several M_x bins. At higher M_x the result is compatible with zero, confirming the absence of spin and charge dependent effects.

The asymmetries are extracted also as function of the kinematic variable $-t_c$. The sin ϕ moments of the A_{LU} are shown in the left panel of Figure 6.10 as a function of $-t_c$. The $\sin\phi$ moment shows a strong $-t_c$ dependence. At small values of $-t_c$, it is compatible with zero and becomes sizeable and negative only at higher $-t_c$ values. The extracted $\cos\phi$ moments of the A_C are shown in the right panel of Figure 6.10 in dependence on $-t_c$. Also the $\cos\phi$ moment shows a strong $-t_c$-dependence. At small values of $-t_c$ it is

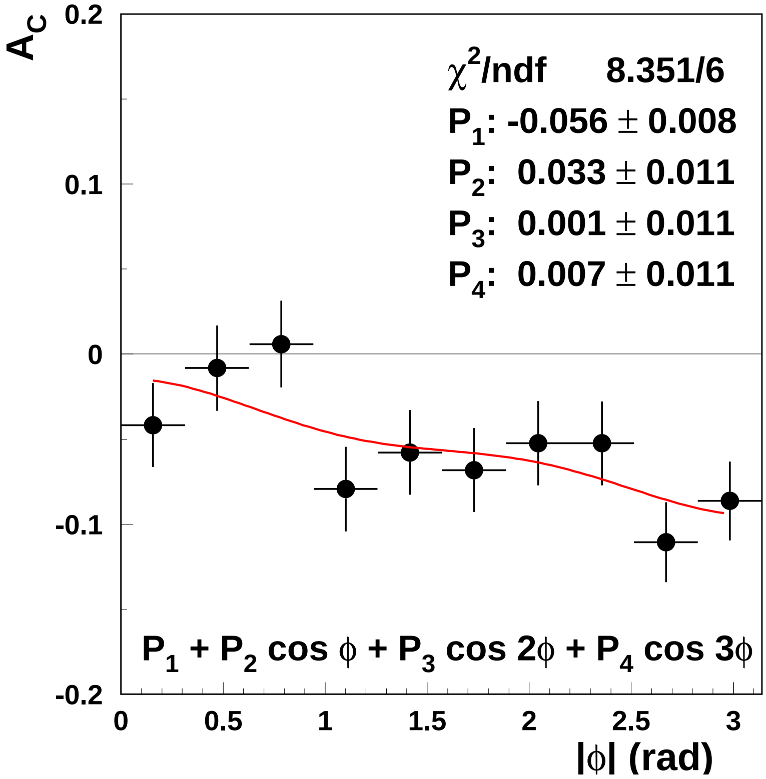

Figure 6.8: Beam charge asymmetry A_C for the hard electro-production of photons off the proton as a function of the azimuthal angle $|\phi|$ for the exclusive sample (2006 preliminary hydrogen data). The solid curve shows the result of the indicated four parameter fit with the values given in the plot.

compatible with zero and becomes sizeable and positive only at higher $-t_c$ values.

The currently available hydrogen results (Figure 1.7) are compared to the results obtained in the present study. In Table 6.2 and Table 6.3 the extracted asymmetries A_{LU} and A_C for unpolarized hydrogen targets are compared between previous published results [Air01, Air07a] and non-released results obtained from this analysis. The only difference between both data sets is due to different productions of data: the results of [Air01] and [Air07a] are extracted from the production 98d0 and 00c1, whereas the present analysis is based on the newest production 06b2. The asymmetry amplitudes are found in good agreement within the error bars. However differences in $A_{LU}^{\sin\phi}$

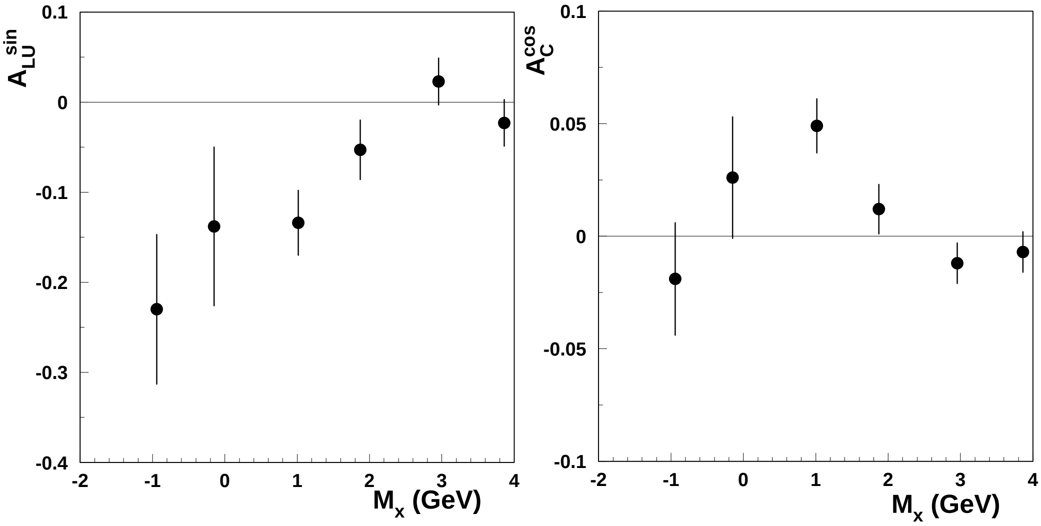

Figure 6.9: The $\sin\phi$ amplitude of the A_{LU} (left) and the $\cos\phi$ amplitude of the A_C (right) as a function of the missing mass (2006 preliminary hydrogen data). Statistical uncertainties are shown.

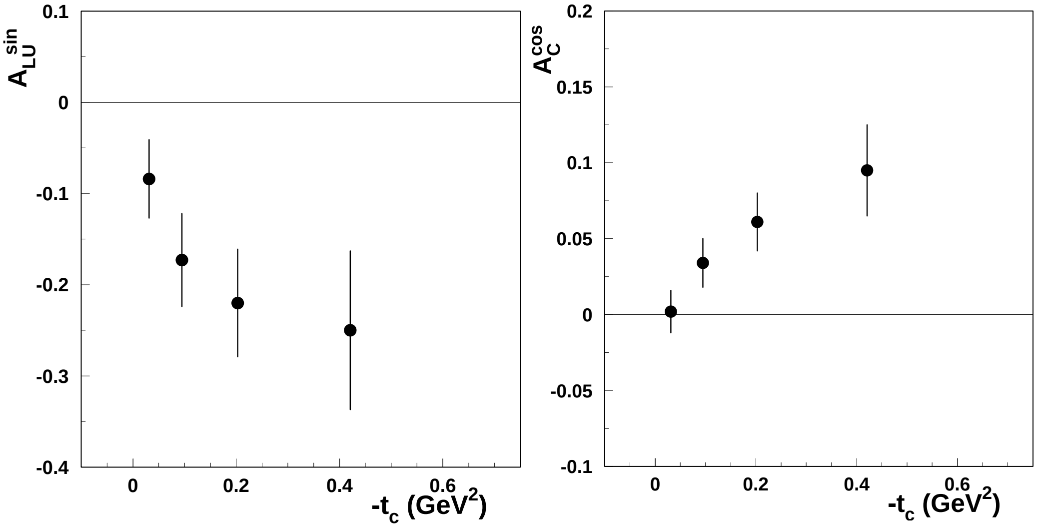

Figure 6.10: The $\sin\phi$ moment of the A_{LU} (left panel) and the $\cos\phi$ moment of the A_C (right panel) as functions of $-t_c$ (2006 preliminary hydrogen data). Statistical uncertainties are shown.

	Previous A_{LU} **Published [Air01]**	**Present A_{LU}** **Not Released**
const P_1	-0.04 ± 0.02	-0.049 ± 0.025
$A_{LU}^{\sin\phi}$ P_2	-0.18 ± 0.03	-0.153 ± 0.036
$A_{LU}^{\sin 2\phi}$ P_3	$+0.00 \pm 0.03$	$+0.032 \pm 0.036$

Table 6.2: Comparison of A_{LU} for unpolarized hydrogen targets between previous published results [Air01] and non-released results obtained from this analysis.

	Previous A_C **Published [Air07a]**	**Present A_C** **Not Released**
const P_1	-0.011 ± 0.019	-0.056 ± 0.008
$A_C^{\cos\phi}$ P_2	$+0.060 \pm 0.027$	$+0.033 \pm 0.011$
$A_C^{\cos 2\phi}$ P_3	$+0.016 \pm 0.026$	$+0.001 \pm 0.011$
$A_C^{\cos 3\phi}$ P_4	$+0.034 \pm 0.027$	$+0.007 \pm 0.011$

Table 6.3: Comparison of A_C for unpolarized hydrogen targets between previous published results [Air07a] and non-released results obtained from this analysis.

and $A_C^{\cos\phi}$ are found: the values in this study are slightly smaller than the published ones. Also the constant term of A_C is not compatible with the published result.

The published available t_c dependence for $A_C^{\cos\phi}$ [Air07a] shown in Figure 1.8 is compared to the results obtained from this study in Figure 6.11. A good agreement can be noticed in the first three t_c bins, while in the last one there is a great difference, leading the total present $A_C^{\cos\phi}$ (Figure 6.8) smaller than the published one (Table 6.3). However the difference is not critical since in the last $-t_c$ bin the contribution from associated production, which increases with $-t$[1], is large, as already mentioned, and is at present status not included in possible models [Air07a].

---

[1] The associated BH processes contribute about 5, 11, 18, and 29% to the yields in the four $-t$ bins, or 11% in the full $-t$-range, with an estimated fractional uncertainty of 10%.

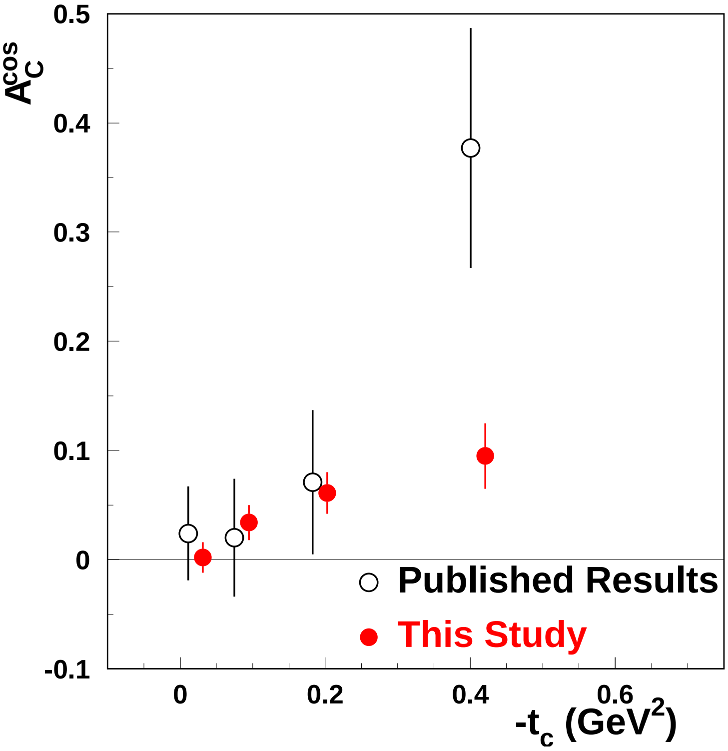

Figure 6.11: Comparison of the asymmetry amplitude $A_C^{\cos\phi}$ in dependence of $-t_c$ for hydrogen between previous results [Air07a] and non-released results obtained from this analysis.

6.6 *Miscalibration of the Calorimeter*

A negative offset, resulting in a non zero constat term P_1 (-0.056 ± 0.006) in the beam charge asymmetry A_C, is observed for the electron and positron 2006 data. The negative constant term can be caused by a significant difference in the average DVCS yield between electron and positron data. Figure 6.12 shows the missing mass distribution for both data sets. For the electron data the bottom plot shows a clear peak at about the correct position, i.e. at M_p^2. The distribution from the positron data appears to be shifted against the one from the electron data. While the shift is small for large values of M_x^2 it gets sizeable when approaching the exclusive region. This points to incorrectly reconstructed photon energies since high values of M_x^2 correspond to low photon energies and vice versa, i.e., the effect becomes visible in the

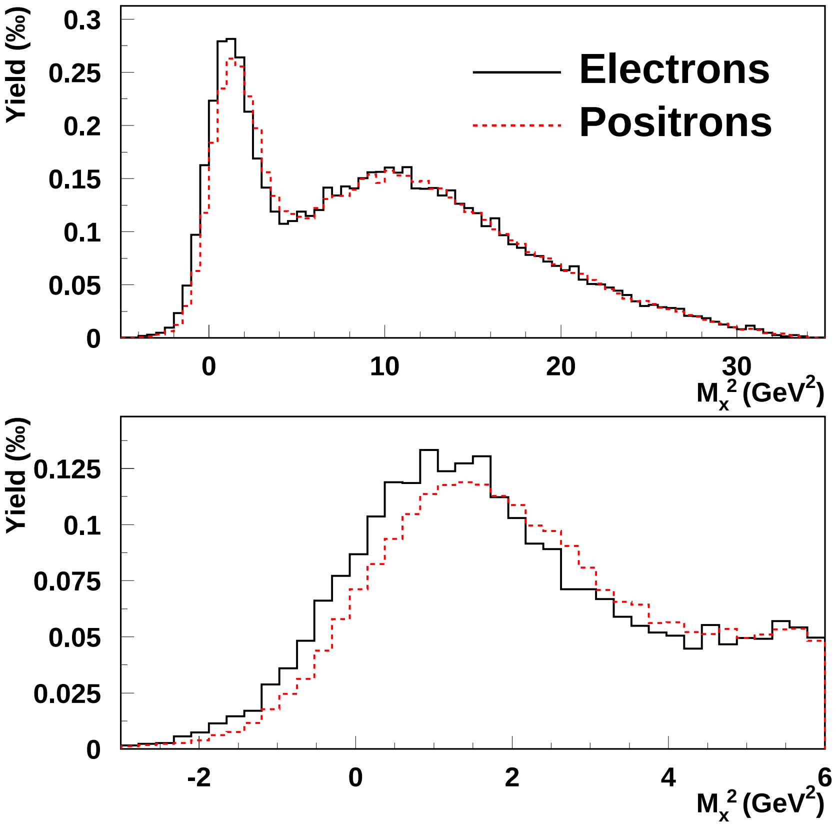

Figure 6.12: Squared missing mass distributions in the full kinematic range (upper paned) and in the small M_x^2 region (lower panel) for electron and positron data. The two distributions are normalized to the number of DIS events.

exclusive region where the photons have higher energies on average.

The squared missing mass M_x^2 is very sensitive to the photon energy E_γ (see Expression 3.2) and thus to the calorimeter calibration. Given the average kinematics of the selected BH/DVCS event sample, $\langle\nu\rangle \sim 14$ GeV, $\langle E_\gamma\rangle \sim 14$ GeV, $\langle Q^2\rangle \sim 2.6$ GeV^2, $\langle\cos\theta_{\gamma^*\gamma}\rangle \sim 1$, 1% of relative change in E_γ can result into 200 MeV^2 shift in M_x^2. The influence of a possible miscalibrated calorimeter on the present analysis is restricted because, other than M_x^2, the kinematic variables do not depend on the photon energy[2]. Hence, a miscalibrated calorimeter can only affect the present analysis in

---

[2] Note that t_c defined in Expression 6.1 is used instead of t in Expression 3.1 to calculate the invariant momentum transfer t to the target proton.

the event selection due to, e.g., the cut on M_x^2. Consequently, the extracted asymmetry amplitudes can be changed because of some events may become lost or selected in addition.

As already claimed, the CALO is calibrated based on the E/P ratio of a sample of electrons identified conservatively, whose energy deposition in the preshower detector is required to be more than that of minimum ionization particles. Measurements from the calorimeter of the deposited energy of electrons depend upon the energy (momentum) of the particle, and upon the preshower signal. The reconstructed momentum of electrons can be off by 4% in the lower and higher momentum regions. Hence by using the E/P ratios of DIS electrons, it will be rather difficult to make an absolute calibration for the calorimeter with a precision better than 1%. Therefore exists an indication of a possible 1% miscalibration of the calorimeter in the real data. Asymmetry amplitudes are extracted with 1% of relative change in the photon energy E_γ: as expected the calorimeter miscalibration has a very small influence on the extracted amplitudes. However a detail CALO calibration, using smaller calibration subperiods, is at the moment being carried out and it is not yet available.

6.7 *Recoil Information for special Single Photon Events*

Using the 2006 b2 μDST production and hydrogen targets, A_{LU} and A_C have been extracted with the missing mass technique described in Section 3.1. They have been compared to the previous published results, obtaining good agreement apart from a discrepancy likely originating from a calibration effect. DIS events have been selected with the forward spectrometer and data quality has been carried out looking only at the performance of the spectrometer. No requirements have been imposed on the Recoil Detector.

Now the next step is to include in this analysis first signals from the Recoil Detector. Since, as already claimed, the Recoil Detector was fully operational starting from September '06, only data with positron beams are taken into account. Besides data quality cuts presented in Section 6.3, runs are discarded if the SSD or the SFT do not work properly. Moreover data with Recoil Detector SC magnet off are rejected, as there is no momentum reconstruction for tracks in the Recoil Detector.

Since recoil signals will be extracted for the first time, some geometrical and kinematic cuts used for the selection of positrons and photons are opened compared to the previous analysis (see Section 6.4): ranges of some kinematic variables are chosen to be wider or even not restricted. In a first step, events with the scattered positron identified by the forward spectrometer are selected. Basically the same geometrical cuts used for the previous analysis are considered for positrons ($|x_{calo}| < 175$ cm, 30 cm $< |y_{calo}| < 108$ cm and $t_{vertex} < 0.75$ cm), except for z_{vertex}. The range in z_{vertex} is chosen to be wider than previous analysis: 0 cm $< z_{vertex} <$ 25 cm. No constraints are applied on inclusive variables (Expressions 1.6 - 1.9).

From this new sample of DIS events, only those with exactly one charged track, i.e. the scattered positron, are taken into account in the following. In addition, exactly one trackless cluster in the CALO is required. The photon needs to be in the fiducial volume of the CALO for photons, $|x_{calo}| < 125$ cm and 33 cm $< |y_{calo}| < 105$ cm, as in previous analysis. No assumption is done on the energy of the real photon E_γ as well as on the preshower signal. In the previous analysis, based on Monte Carlo studies, the upper limit on the opening angle $\theta_{\gamma^*\gamma}$ has been chosen to be 45 mrad because beyond this point the exclusive event sample contains more background (semi-inclusive and Δ^+ production) than BH/DVCS events [Ell04]. In this analysis the range of the $\theta_{\gamma^*\gamma}$ is made wider, choosing the upper limit value equal to 70 mrad. In the future the purpose would be to remove completely the $\theta_{\gamma^*\gamma}$ cut, since the Recoil Detector will be able to reject background events.

Applying these new constraints, special single photon samples are extracted for the 2006 positron-hydrogen data. The distributions for the variables calculated via the outgoing photon kinematics are given in Figure 6.13. The squared missing mass M_x^2 distribution for the special single photon sample is shown in the upper left panel of the Figure. Since no cut has been applied on the energy of the real photon E_γ, the plot is mainly dominated by events with $M_x^2 > M_p^2$. The upper right panel of the Figure shows the $\theta_{\gamma^*\gamma}$ distribution: its maximum lies at the upper limit of 70 mrad. The distribution of the photon energy E_γ, shown in the lower left panel of the Figure,

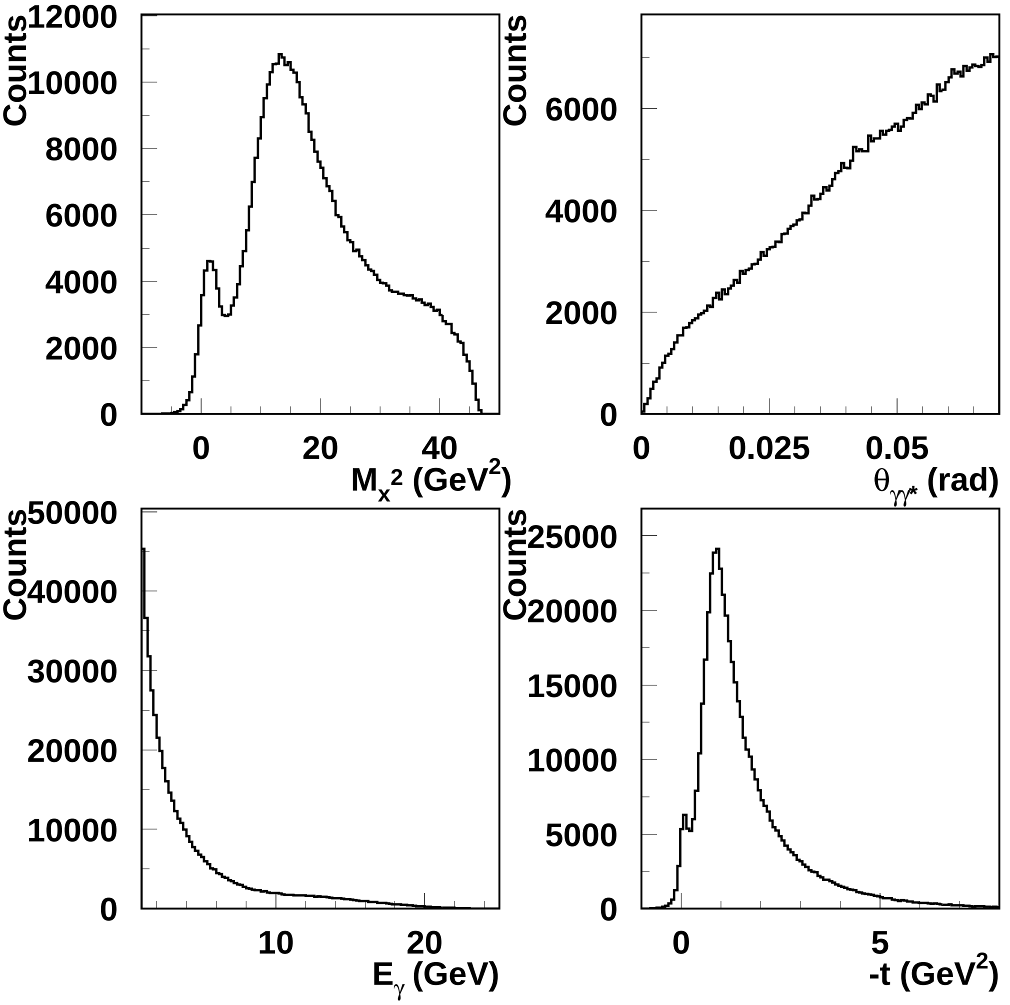

Figure 6.13: Distributions of the special single photon sample for the hydrogen data from the 2006 positron data for different variables.

is largely dominated by low energetic photons as expected. The lower right panel of the Figure shows the $-t$ distribution, dominated by large values of momentum transfer.

Recoil Detector signals are extracted for the first time in conjunction with single photon event candidates selected by the forward spectrometer by analyzing the special single photon event sample. A special production, called 06c HRC production, containing this special single photon sample is produced. In the 06c production Recoil Detector signals, missing in the

2006 b2 μDST production, are included. The tracking code XTC is then employed to extract tracks in the Recoil Detector. At present status the tracking program XTC (described in Section 5.4.2) for the Recoil Detector is under development. The code doesn't yet provide any removal of ghost tracks. Ghost tracks don't correspond to any real particle and are mainly due to the noise in the Recoil Detector. In order to get rid of ghost tracks, a strong constraint to the code is needed: for each recoil track, four space points (two for SSD and two for SFT) are required to belong to the track. In this case a recoil track found by the code is likely a good track corresponding to a particle. On the other hand such a space point cut removes a lot of statistics: particles that, due to low momentum or due to angle acceptance, don't reach the last SFT layer are not taken into account. The space point cut can be released with the tracking code becoming more efficient.

In Figure 6.14 the track multiplicity evaluated by XTC[3] for the Recoil Detector is shown. A mean multiplicity of 1.4 is obtained. The correlation between forward spectrometer and Recoil Detector is shown in Figure 6.15 where the difference between z_{vertex} extracted by the forward spectrometer for the positron track and z_{vertex} evaluated by XTC for tracks in the Recoil Detector is displayed. A clear correlation between the Recoil Detector and the forward spectrometer is observed. As in Figure 5.22, a mean difference different from zero is obtained, since the external alignment between Recoil Detector and forward spectrometer is still not in production.

Figure 6.16 and 6.17 [Vil07a, Vil07b] on the left panels show the sum of energy deposits ΔE in individual detection layers (SSD in Figure 6.16 and SFT in Figure 6.17) versus the particle momenta P reconstructed by the tracking code XTC: from the two Figures on the right part, a well defined proton/π^+ separation can be easily seen: the lower band represents π^+s and the upper band represents protons. Therefore they can be easily recognized by their energy deposition. On the left part the only displayed band represents π^-s, hence recognized from their negative charge. In the two Figures, on the right panels, same quantities, as on the left panels, are displayed after a missing mass cut ($M_X < 1.7$ GeV): it can be easily seen that only protons survive to this cut as expected, as well as a small amount

---

[3] *Method 7.*

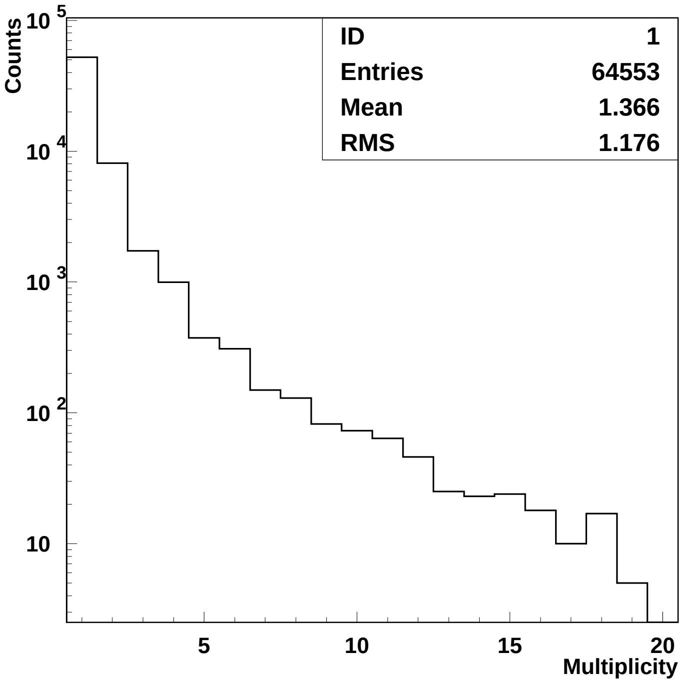

Figure 6.14: The track multiplicity for the Recoil Detector for the special single photon sample. For each track four space points (2 for SSD and 2 for SFT) are required.

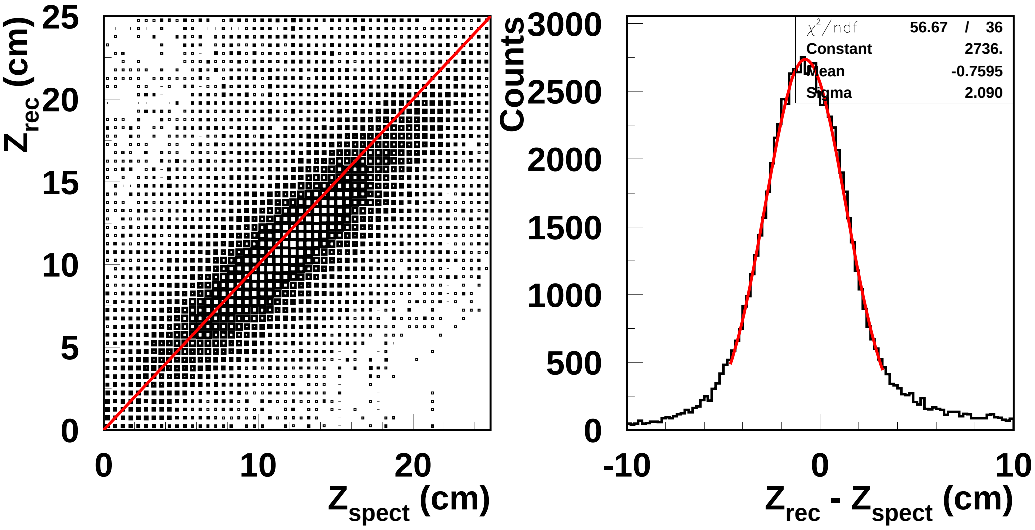

Figure 6.15: Difference between the z_{vertex} extracted by the forward spectrometer for the positron track and the z_{vertex} evaluated for the particles crossing the Recoil Detector.

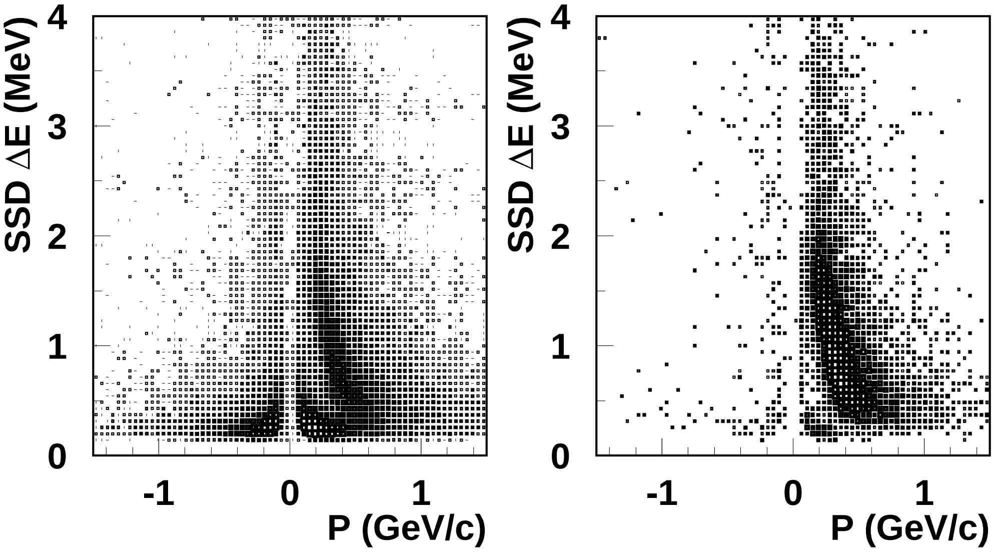

Figure 6.16: Left: sum of energy deposits ΔE in individual layers of SSD versus particle momenta P: a well defined proton/π^+ separation (on the right the lower band represents π^+) can be easily seen (π^- are recognized from their charge). Right: sum of ΔE versus P after a missing mass cut ($M_X < 1.7$ GeV). Only tracks with four space points enter these plots.

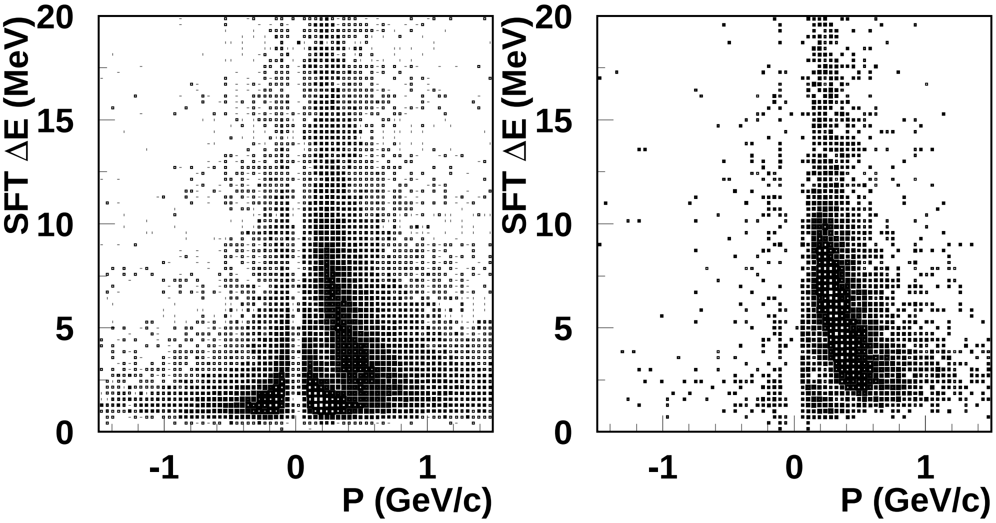

Figure 6.17: Left: sum of energy deposits ΔE in individual layers of SFT versus particle momenta P: a well defined proton/π^+ separation (on the right the lower band represents π^+) can be easily seen (π^- are recognized from their charge). Right: sum of ΔE versus P (GeV/c) after a missing mass cut ($M_X < 1.7$ GeV). Only tracks with four space points enter these plots.

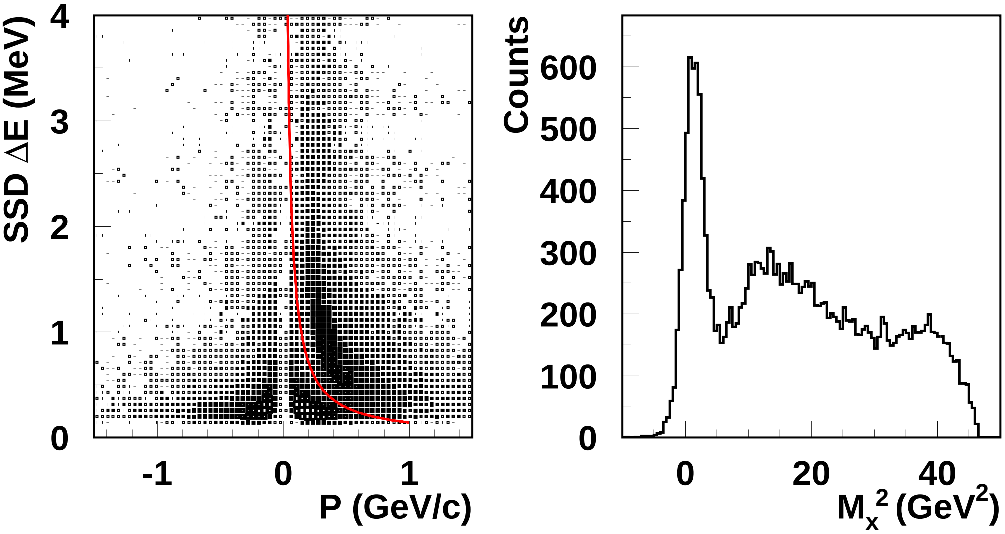

Figure 6.18: Left: sum of energy deposits ΔE in individual layers of SSD versus particle momenta P. The red line indicates a possible hyperbolic SSD PID cut ($f(x) > \frac{1}{7x}$) which removes all events from which no protons are reconstructed in the Recoil Detector. Right: the distribution of the squared missing mass M_x^2 of the special single photon sample after applying SSD PID cut.

of π^+ coming from the Δ^+ decay [Vil07a, Vil07b]. These plots reverse the logic and apply the working principle of the Recoil Detector. In this situation the Recoil Detector can also be used as a tool to measure background contribution to the previous HERMES DVCS analysis without the Recoil Detector and to eventually refine it.

Possible hyperbolic SSD and SFT PID cuts are applied on data (see Figure 6.18 and 6.19 on the left panels). An SSD PID cut $f(x) > \frac{1}{7x}$ and an SFT PID cut $f(x) > \frac{4}{5x}$ are chosen and indicated by red lines in the Figures. Requiring these two functions, events with only protons are selected in order to see the influence on the missing mass plot displayed in the upper left panel in Figure 6.13. Furthermore a cut on reconstructed momenta less than 0.6 GeV/c is required since for momenta above 650 MeV/c the pion rejection factor drops below 10 without using the PD (see Section 3.9.3). Applied these PID constraints, the obtained squared missing mass distributions for SSD and SFT are shown on the right panels in Figure 6.18 (SSD) and 6.19 (SFT) for events which have tracks with four space points in the Recoil

Detector identified as protons.

Figure 6.20 shows the ratio plot between the M_x^2 distribution (M_x^2 with recoil) shown in the right panel of Figure 6.18 and the M_x^2 distribution (M_x^2 with no recoil) shown in the upper left panel of Figure 6.13. Selecting events which have tracks with four space points in the Recoil Detector identified as protons, the semi-inclusive background is reduced successfully by more than 95%. Hopefully a more detailed PID cut as well as PD signals will increase the reduction factor, removing completely semi-inclusive background from the M_x^2 distribution on the right panel in Figure 6.18. A reduction factor of $\sim$85% can be also noticed in the exclusive peak due to the imposition of the four space point cut on the recoil track sample.

These plots (Figure 6.16 - 6.20) show for the first time for real data that the Recoil Detector can be integrated in the existing DVCS analysis framework at HERMES.

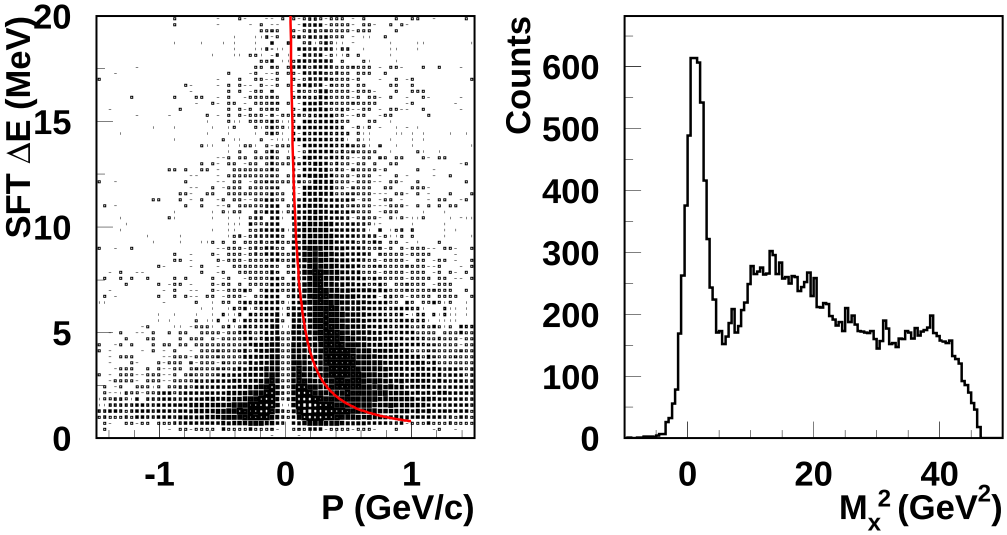

Figure 6.19: Left: sum of energy deposits ΔE in SFT layers versus particle momenta P. The red line indicates a preliminary hyperbolic SFT PID cut ($f(x) > \frac{4}{5x}$) which removes all events from which no protons are reconstructed in the Recoil Detector. Right: the distribution of the squared missing mass M_x^2 of the special single photon sample after applying SFT PID cut.

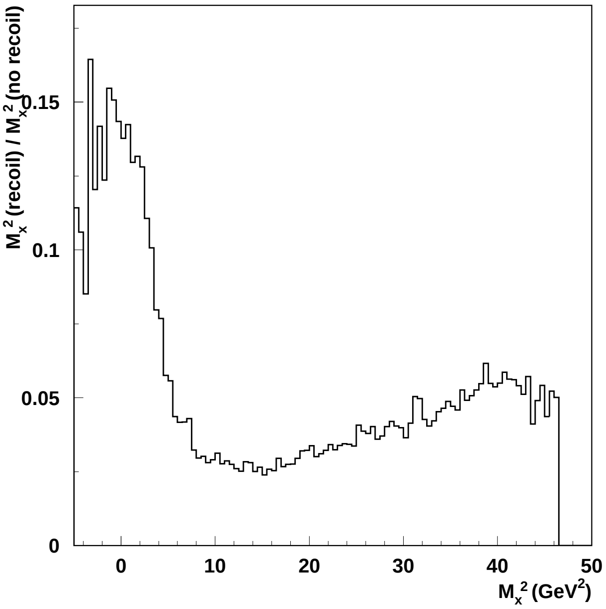

Figure 6.20: Ratio plot between the M_x^2 distribution shown in the right panel of Figure 6.18 and the M_x^2 distribution shown in the upper left panel of Figure 6.13.

Chapter 7

Conclusions and Outlook

The main goal of the HERMES experiment is the investigation of the spin structure of the nucleon. The contribution of the quark spin to the nucleon spin is known to be around 30%. Moreover, preliminary measurements favor a very small contribution from the gluon spin to the spin of the nucleon. Therefore the remaining part should be made up by unknown contributions from the orbital angular momentum of the quarks and of the gluons. The most promising way to access the size of those contributions is to determine the total angular momentum of the quarks in the framework of generalized parton distributions. This new theoretical formalism describes the quark-gluon structure of the nucleon including its spin degrees of freedom. It contains the ordinary parton distribution functions and the form factors as limiting cases and moments, respectively. Moreover, it may provide a three-dimensional description of the nucleon structure at the parton level.

Experimental access to generalized parton distributions is possible via hard exclusive reactions. Among these, the theoretically cleanest process appears to be the electro-production of real photons, i.e., Deeply Virtual Compton Scattering (DVCS). The interference term between this process and the Bethe-Heitler (BH) process provides direct access to the DVCS amplitudes. Azimuthal asymmetries with respect to the charge and the spin orientation of the incoming lepton are the tool to isolate those parts of the interference term which are directly proportional to the real and the imaginary part of the DVCS amplitudes, respectively.

In previous studies of DVCS at HERMES, only the scattered lepton and the produced real photon could be detected. The HERMES DVCS data on beam charge and beam spin asymmetries are already able to distinguish between some GPD models. Based on a certain model, the DVCS measurements on transversely polarized hydrogen lead to a first model dependent constraint for the total angular momentum of quarks in the nucleon. This method, together with increased statistics and improved models should allow for a constraint with reasonable statistical and theoretical uncertainties in the future.

In the DVCS analysis, the missing mass technique was used to determine that the target nucleon stayed intact. Due to background processes, the cut that needed to be imposed on the missing mass was severe and the data sample was greatly reduced. The main background processes that cause this are semi-inclusive deep inelastic scattering and the associated BH/DVCS process. In semi-inclusive deep inelastic scattering a lepton scatters off a nucleon (which breaks) and the scattered lepton and one photon are detected. In the associated BH/DVCS process the incoming or outgoing lepton emits a photon which is detected and the target nucleon is excited and decays into a nucleon and a pion. This was the main reason for HERMES to install a new Recoil Detector to detect the recoil particles. Therefore HERMES has dedicated its last data taking period, until middle of 2007, to the study of the DVCS process with the Recoil Detector.

The HERMES Recoil Detector consists of a target cell, a Silicon Strip Detector (SSD), a Scintillating Fiber Tracker (SFT), and a Photon Detector (PD). All are inside a superconducting magnet. The SSD uses energy deposition to determine the momentum of the particle because in its energy range the energy deposition is an unambiguous function of the momentum of the particle. The low momentum cut-off is determined by the amount of material between the interaction point and the detector. That is the reason why this detector is placed inside the beam vacuum. The SFT is located outside the beam vacuum and is surrounded by the PD. It consists of two barrels with layers of scintillating fibers. It detects particles by converting their energy deposition into light. It measures two space points of a charged particle and from the bending of the assigned track a momentum measurement can be derived. The PD is located between the SFT and the magnet. It consists (from the inside out) of three layers of tungsten showering material followed by scintillating strips. The showering material is needed to detect photons, which have a high probability to induce a particle shower in tungsten. This particle shower is detected by the scintillating strips.

With the help of the Recoil Detector, it is expected that the semi-inclusive background will be largely suppressed, and so also the associated BH/DVCS processes in which the recoiling protons were excited to a resonance state. For the data taking period with the Recoil Detector, it has been decided to use unpolarized targets instead of polarized ones by technical reasons.

A few months before installation (December 2005) in HERMES, the Recoil Detector was completely assembled in the HERMES experimental hall outside the interlock region in order to take cosmic data. This cosmic ray test experiment helped to improve the understanding of the mechanical setup of the Recoil Detector and provided HERMES the ability to anticipate some of the problems likely to arise during its installation into the spectrometer. The cosmic ray test experiment also allowed the integration of the entire detector into the HERMES data acquisition system.

The work presented in this thesis has mainly consisted of testing the Recoil Detector with cosmic rays and with the HERA lepton beam, in particular analyzing data related to the SSD. Many noise studies were carried out during the cosmic ray test experiment: it was observed for High Gain (HG) chips that noise of last several HELIX channels was always much higher than the one of the first channels, resulting in a signal to noise ratio equal or less than 2 for MIP signals. Despite of the high noise level, MIPs were detected, whose most probable signal was measured to be equal to $\sim$14 ADC Channels for an incidence angle of 90°. Residuals and efficiency were also evaluated: residuals were found to be equal to 0.27 strips after internal alignment, close to the obtained Monte Carlo value (0.22 strips), and mean efficiency was found to be $\sim$80%. Only during the dismounting of the Recoil Detector from the HERMES experimental hall, noise levels have been reduced connecting the reference potential of all silicon modules to the support structure.

The Recoil Detector was installed in January 2006 and took first data in February. The tracking in the magnetic field using the SFT was possible with the Recoil Detector superconducting magnet. In March the target cell was damaged while it was being inspected which resulted in large radiation doses to the SSD when the beam was injected. This required rebuilding the SSD in March - June. End of June 2006 HERA switched the beam charge from negative to positive. The data taking continued with the fully installed Recoil Detector in July 2006 till the 30^{th} of June 2007, last day of HERA running. Therefore unfortunately no data with electron beams are available with an operational SSD.

The same SSD noise behavior for HG chips, noticed in the cosmic ray test experiment, has been observed for positron beams. A dedicated software noise correction, by means of spline interpolation, has led the signal to noise ratio for MIPs to a value equal or better than 7.

Recoil Detector signals have been extracted for the first time for events with one single charged track identified as a positron by the forward spectrometer. Even if the reconstruction tracking code XTC for the Recoil Detector is still under development, the correlation between the Recoil Detector and the forward spectrometer for this event sample has been shown to be good.

The Recoil Detector was fully operational since September 2006 and it ran stably for 10 months without any problems. 28 millions of DIS events from hydrogen targets and 7 millions of DIS events from deuterium targets were collected for a recoil exclusive DVCS analysis. It has been shown that the Recoil Detector is able to provide particle identification, through energy deposition in the different detector layers, to positively identify recoil protons. Protons which survive applying the missing mass cut, indicating for the first time for real data that the Recoil Detector can be successfully integrated in the existing DVCS analysis framework at HERMES.

From the XTC point of view, the energy calibration for the SSD which is critical for the momentum reconstruction using the energy deposition is still in progress as well as systematic studies of the tracking software for the momentum reconstruction based on the bending in the magnetic field.

The statistics collected with the Recoil Detector will allow to extract recoil exclusive DVCS beam spin asymmetry free of background contribution as soon as XTC will be released. The recoil exclusive DVCS beam charge asymmetry will not be easily extractable with only an operational SFT: dedicated Monte Carlo studies will be needed to investigate the performance (acceptance, efficiency, tracking, PID) of the SFT with a non-operational SSD. Concerning the conventional exclusive DVCS analysis (without the Recoil Detector), the detector will be used as a tool to measure the background contribution to the previous HERMES DVCS analysis and to eventually refine it. Moreover, the Recoil Detector will provide measurements for other exclusive analysis, like hard exclusive meson or Λ-hyperon productions.

Concerning the GPDs via DVCS in the world, future studies are planned at several facilities. The collider experiments H1 and ZEUS at HERA have measured the DVCS cross sections at very small values of x_{Bj}. The newly installed spin rotators up- and downstream of their experimental areas make a longitudinal polarized beam also available to them. Together with several detector upgrades, the two experiments will be able to determine the azimuthal dependence of beam spin and beam charge asymmetries. The experiments at JLab and the COMPASS experiment at CERN have devoted a considerable part of their future physics programme to studies of GPDs. The 12 GeV upgrade of the Continuous Electron Beam Accelerator at JLab aims at accurate measurements of cross sections and single spin asymmetries with respect to beam helicity and target spin [Car01]. The COMPASS experiment at CERN is carrying out feasibility studies for DVCS measurements and the collaboration is planning to install in the future a new recoil detector [d'Ho02]. Like the experiments at HERA, the COMPASS collaboration has the advantage that lepton (muon) beams of both charges are available, allowing the extraction of the beam charge asymmetry. The high beam energies of 100 or 190 GeV would fill the gap between the low energy fixed target and the collider experiments.

Acknowledgements

Il momento di scrivere i ringraziamenti giunge alla fine della tesi, a lavoro ormai scritto. Ma la necessità di esprimerli è un sentimento che parte dall'inizio della tesi. È una necessità perché questa tesi non è solo frutto di chi la ha scritta, ma è il lavoro di un'ampia collaborazione. Ho avuto il piacere di collaborare con molti colleghi e ricercatori, che non solo mi hanno insegnato molto dal punto di vista professionale, ma soprattutto da quello umano.

Ringrazio il Prof. Raffaele De Leo e il Dott. Eugenio Nappi, i quali mi hanno offerto la possibilità di sviluppare questo lavoro di tesi, associandomi alla collaborazione HERMES.

Ho trascorso molto tempo presso il laboratorio DESY ad Amburgo, dove sono stato seguito da Ingrid Gregor e soprattutto da Jim Stewart, ai quali vanno i miei più sentiti ringraziamenti. Entrambi hanno costantemente seguito gli sviluppi del mio lavoro di tesi, e hanno avuto molta pazienza nel correggere qualche mia ingenuità e carenza.

I miei ringraziamenti vanno anche ad Elke Aschenauer per la sua disponibilità e per gli utili suggerimenti. Senza Caroline Riedl, difficilmente avrei avuto gli strumenti informatici necessari per analizzare i dati. Grazie Caro.

Desidero ringraziare Armine, mia collega di ufficio ad Amburgo, Charlotte, Fidi, Tibor, Larry, Ivana, Sergey, Alexander, Andreas. Sono loro coloro che mi hanno fornito preziosi consigli e aiuti nei miei momenti di difficoltà.

Durante il mio periodo a DESY ho incontrato moltissimi nuovi amici, italiani e non, con i quali ho condiviso momenti di relax e di divertimento. Tra questi desidero citare Peppone, Marco, Rita, Riccardo, Roberto, Yoshi, Yves, Lorenzo, Paolo.

Un caro ringraziamento va anche al mio grande amico Steffen, con il quale ho condiviso un appartamentino ad Amburgo.

Sono grato ai miei amici di università, i quali mi hanno incoraggiato per farmi giungere a questo traguardo. In particolare voglio ringraziare Edo, Bartolo, Loredana ed Alessandra che sono stati per me molto più che semplici colleghi universitari. Un ringraziamento anche a Cristina e Mimma per la cortesia dimostratami per ogni ricerca bibliografica.

Ringrazio la mia famiglia per la fiducia che ha riposto in me e nel mio lavoro, e Mariuccia che ha collaborato a questa tesi con la sofferenza per i miei lunghi periodi di lontananza e con il suo continuo incoraggiamento.

Un dolce pensiero va a mio nonno Ignazio, a cui dedico la mia tesi.

> *Te ne sei andato in silenzio, in punta di piedi, come a non voler disturbare nessuno, come era tuo solito fare, lasciando un vuoto immenso nel mio cuore incolmabile.*

The time to write the section related to acknowledgements comes to the end of my Ph.D. thesis, already written. But the necessity to express them is a feeling which starts from its beginning. It is a necessity because this thesis is not only my result, but fruit of a work of a great collaboration. I have had the pleasure of working together with many colleagues and researchers, who have not only taught me much from the professional point of view but also and, above all, from the human point of view.

To begin, I'd like to thank Prof. Raffaele De Leo and Doct. Eugenio Nappi, who offered me the possibility to develop this Ph.D. thesis, associating me to the HERMES collaboration.

Several months have been spent in the DESY laboratory, in Hamburg. In this period I have been supervised by Ingrid Gregor and, above all, by Jim Stewart, which I'd like to thank. Both have constantly followed the developments of my Ph.D. thesis, having patience in correcting some my naiveties and lacks.

I'd like to thank Elke Aschenauer for her availability and for her useful suggestions. Without Caroline Riedl, I would have difficultly had the instruments necessary to analyze data. Thanks, Caro.

I wish to thank Armine, my office colleague in Hamburg, Charlotte, Fidi, Tibor, Larry, Ivana, Sergey, Alexander, Andreas: they advised and helped me in my moments of difficulty.

During my life at DESY, I have met a lot of new friends, Italians and not. They helped me to relax and to have fun. I have greatly enjoyed my time especially with Peppone, Marco, Rita, Riccardo, Roberto, Yoshi, Yves, Lorenzo, Paolo.

I want to thank my great friend, Steffen, with whom I shared his flat in Hamburg.

I'm grateful to my friends of Bari University, with whom I reach this goal, in particular to Edo, Bartolo, Loredana and Alessandra: they have been much more than simple university colleagues. A thanks also to Cristina and Mimma for the courtesy, showed me for every bibliographical search.

A thank to my family to trust always me and to Mariuccia: she has collaborated in this thesis, suffering my long periods abroad and continuously encouraging me.

Finally a sweet thought goes to my grandfather Ignazio, to whom my Ph.D. thesis is dedicated. You will be always in my heart. Ciao.

Bibliography

[Ack98] K. Ackerstaff et al. (HERMES Collaboration), *The HERMES Spectrometer*, Nucl. Instrum. and Meth. **A417** (1998) 230

[AdaMan] ADAMO Users Manual, CERN
`http://adamo.web.cern.ch/Adamo/guide/Document.html`

[Air01] A. Airapetian et al. (HERMES Collaboration), *Measurement of the beam spin azimuthal asymmetry associated with deeply-virtual Compton scattering*, Phys. Rev. Lett. **87** (2001) 182001

[Air05] A. Airapetian et al. (HERMES Collaboration), *Quark helicity distributions in the nucleon for up, down, and strange quarks from semi-inclusive Deep Inelastic Scattering* Phys. Rev **D71** (2005) 12003

[Air07a] A. Airapetian et al. (HERMES Collaboration), *The beam charge azimuthal asymmetry and Deeply Virtual Compton Scattering*, Phys. Rev. **D75** (2007) 11103

[Air07b] A. Airapetian et al (HERMES Collaboration), *Precise determination of the spin structure function g_1 of the proton, deuteron and neutron*, Phys. Rev. **D75** (2007) 12007

[Alg76] M. J. Alguard et al., *Deep inelastic scattering of polarized electrons by polarized protons*, Phys. Rev. Lett. **37**, (1976), 1261

[Alt99] M. Altmeier et al., *A helical scintillating fiber hodoscope*, Nucl. Instrum. and Meth. **A431** (1999) 428

[Ako02] N. Akopov et al., *The HERMES dual-radiator ring imaging Cherenkov detector*, Nucl. Instrum. and Meth. **A479** (2002) 511

[And01] A. Andreev et al., *Multiwire proportional chambers in the HERMES experiment*, Nucl. Instrum. and Meth. **A465** (2001) 482

[Aot95] S. Aota et al., *Development of fiber-to-fiber connectors for scintillating tile/fiber calorimeters*, Nucl. Instrum. and Meth. **A357** (1995) 71

[Art75] X. Artru, G. B. Yodh and G. Mennessier, *Practical theory of the multilayered transition radiation detector*, Phys. Rev. **D12** (1975) 1289

[Asc97] E. Aschenauer et al., *Development of scintillating fiber detector technology for high rate particle tracking*, International Europhysics Conference on High Energy Physics, Jerusalem, August 1997, eprint arXiv:hep-ex/9710001 (1997)

[Asc00] E. Aschenauer et al., *Optical characterization of n=1.03 silica aerogel used as radiator in the RICH of HERMES*, Nucl. Instrum. and Meth. **A440** (2000) 338

[Ash88] J. Ashman et al. (European Muon Collaboration), *A measurement of the spin asymmetry and determination of the structure function g_1 in deep inelastic muon-proton scattering*, Phys. Lett. **B206** (1988) 364

[Ash89] J. Ashman et al. (European Muon Collaboration), *An investigation of the spin structure of the proton in deep inelastic scattering of polarized muons on polarized protons*, Nucl. Phys. **B328**, (1989), 1

[Ava98] H. Avakian et al., *Performance of the electromagnetic calorimeter of the HERMES experiment*, Nucl. Instr. and Meth. **A417** (1998) 69

[Bar93] D. P. Barber et al., *The HERA Polarimeter and the first observation of electron spin polarisation at HERA*, Nucl. Instrum. and Meth. **A329** (1993) 79

[Bar95] D. P. Barber et al., *The first achievement of longitudinal spin polarisation in a high energy electron storage ring*, Phys. Lett. **B343** (1995) 436

[Bau02] C. Baumgarten et al., *An Atomic beam polarimeter to measure the nuclear polarization in the HERMES gaseous polarized hydrogen and deuterium target*, Nucl. Instrum. and Meth. **A482** (2002) 606

[Bau03] C. Baumgarten et al., *A gas Analyzer for the internal polarized target of the HERMES Experiment at HERA*, Nucl. Instrum. and Meth. **A508** (2003) 265

[Bec02] M. Beckmann et al., *The longitudinal Polarimeter at HERA*, Nucl. Instrum. and Meth. **A479** (2002) 334

[Bel02] A. Belitsky et al., *Theory of Deeply Virtual Compton Scattering on the nucleon*, Nucl. Phys. **B629** (2002) 323

[Ben01] T. Benish et al., *The luminosity monitor of the HERMES experiment at DESY*, Nucl. Instrum. and Meth. **A471** (2001) 314

[Ber95] S. Bernreuther et al., *Design and performance of the large HERMES drift chambers*, Nucl. Instrum. and Meth. **A367** (1995) 96

[Ber98] S. Bernreuther et al., *The HERMES back drift chambers*, Nucl. Instrum. and Meth. **A416** (1998) 45

[Ber02] E.R. Berger, M. Diehl and B. Pire, *Timelike Compton scattering: exclusive photoproduction of lepton pairs*, Eur. Phys. J. **C23** (2002) 675

[Bic67] H. Bichsel, C. Tschalaer, *A range-energy table for heavy particles in silicon*, Nuclear Data Table **A3** (1967) 343

[Blo99] J. Blouw et al., *Design and performance of a large microstrip gas tracker for HERMES*, Nucl. Instrum. and Meth. **A434** (1999) 227

[Bra01] J. T. Brack et al., *The HERMES forward tracking chambers: construction, operation, and aging effects*, Nucl. Instrum. and Meth. **A469** (2001) 47

[Buo86] J. Buon and K. Steffen *HERA variable-energy "Mini" Spin Rotator and head-on ep collision scheme with choise of electron helicity*, Nucl. Instrum. and Meth. **A245** (1986) 248

[Car01] L. S. Cardman et al., *White Paper: The Science driving the 12 GeV Upgrade of CEBAF*, http://www.jlab.org/12GeV/collaboration.html (2001).

[CatKur] Catalogue, Kuraray

[Coo95] J. C. Cooper, *Construction and mechanical qualification of scintillating fibre doublet ribbons*, Proceedings SCIFI 93, edited by A. D. Bross, R. C. Ruchti, M. R. Wayne. River Edge, N. J., World Scientific, (1995)

[Chu96] M. Chung et al., *Development of a multichannel fiber-to-fiber optical connector for the DØ upgrade tracker*, IEEE Trans. Nucl. Sci. **43** (1996) 1153

[d'Ho02] N. d'Hose et al, *Feasibility study of deeply virtual Compton scattering using COMPASS*, Nucl. Phys. **A711** (2002) 160

[Die97] M. Diehl et al., *Testing the handbag contribution to exclusive virtual Compton scattering*, Phys. Rev. **B411** (1997) 193

[Die03] M. Diehl, *Generalized parton distributions*, Phys. Rept. **388** (2003) 41

[Ell04] F. Ellinghaus, *Beam charge and Beam spin azimuthal asymmetries in Deeply Virtual Compton Scattering*, Ph.D. thesis (2004)

[Ell06] F. Ellinghaus et al., *Can the angular momentum of u-quarks in the nucleon be accessed at HERMES?*, Eur. Phys. J. **C46** (2006) 729

[Ely02] J. Ely, *Measurement of the single spin azimuthal asymmetry in the predominantly exclusive electroproduction of photons from the proton*, Ph.D thesis (2002)

[Enk98] M. Enkelmann et al., *An optical readout for a fiber tracker*, Nucl. Instrum. and Meth. **A412** (1998) 216

[Fal99] W. Fallot-Burghardt et al., *Helix 128-3.0 User Manual*, ASIC Labor Heidelberg, HD-ASIC-33-0697 (1999)

[Fan96] A. Fantoni, *Costruzione del calorimetro a contatori di vetro al piombo dell'esperimento HERMES per la misura delle funzioni di struttura di spin dei nucleoni*, Ph.D. Thesis (1996)

[GeaMan] GEANT User manual, Detector Description and Simulation Tool, CERN
`http://wwwasdoc.web.cern.ch/wwwasdoc/geant/geantall.html`

[Göc01] M. Göckeler er al, Phys. Rev. Lett. **92** (2004) 042002

[Goe01] K. Goeke et al., *Hard exclusive reactions and the structure of hadrons*, Prog. Part. Nucl. Phys. **47** (2001) 401

[Gre02] I. Gregor et al., *Test beam results of the first prototype for the HERMES Silicon Recoil Detector*, HERMES Internal Report **02-050** (2002)

[Gru96] C. Grupen, *Particle Detectors*, Cambridge University Press (1996)

[Hen82] Henrici P., *Essential of numerical analysis*, John Wiley & Sons, New York, (1982)

[Her93] The HERMES Collaboration, *Technical Design Report*, HERMES Internal Report **93-015** (1993)

[Her01] The HERMES Collaboration, *The HERMES Recoil Detector - Technical Design Report*, HERMES Internal Report **02-003** (2001)

[Hof57] R. Hofstadter, *Nuclear and nucleon scattering of high-energy electrons*, Ann. Rev. Nucl. **7**, (1957), 231

[Hoo98] P. Hoodbhoy and X.-D. Ji, *Helicity-flip off-forward parton distributions of the nucleon*, Phys. Rev. **D58** (1998) 054006

[Hri05] I. Hristova et al., *HERMES Recoil Silicon Detector calibration to MIPs at T22 at DESY*, HERMES Internal Report **05-014** (2005)

[Ji97a] X.-D. Ji, *Gauge-invariant decomposition of nucleon spin*, Phys. Rev. Lett. **78** (1997) 610

[Ji97b] X.-D. Ji, *Deeply Virtual Compton Scattering*, Phys. Rev. **D55** (1997) 7114

[Kai97] R. Kaiser, *Measurement of the spin structure of the neutron using polarised Deep Inelastic Scattering*, Ph.D. Thesis (1997)

[Kas99] A. Kastenmüller et al., *Fast detector readout for the HADES-RICH*, Nucl. Instrum. and Meth. **A433** (1999) 438

[Kop02] M. Kopytin et al., *Decision on the readout chip for the new HERMES Silicon Recoil Detector*, HERMES Internal Report **02-020** (2002)

[Kor02] V. A. Korotkov and W.-D. Nowak, *Future measurements of Deeply Virtual Compton Scattering*, Eur. Phys. J. **C23** (2002) 455

[Kra05] B. Krauss, *Deeply Virtual Compton Scattering and the HERMES Recoil Detector*, Ph.D. Thesis (2005)

[Leo94] W. R. Leo, *Techniques for Nuclear and Particle Physics Experiments*, 2^{nd} Edition Springer-Verlag (1994)

[Lep80] G. P. Lepage and S. J. Brodsky, *Exclusive processes in perturbative Quantum Chromodynamics*, Phys. Rev. **D22** (1980) 2157

[Leu95] H. Leutz, *Scintillating fibres*, Nucl. Instrum. and Meth. **A364** (1995) 422

[Lie06] P. Liebing, *Extraction of Delta g/g from HERMES data on inclusive charged hadrons* AIP Conf. Proc. **915**, (2006), 331

[Lor97] W. Lorenzon, *Beam Polarimetry at HERA*, 7th International Workshop on Polarised Gas Targets and Polarised Beams, Urbana-Campaign (1997)

[MicUK] Micron Semiconductor LTD., Curchill Industrial Estate, Lancing, Sussex, BN15 8UN, UK

[Mul94] D. Muller et al., *Wave functions, evolution equations and evolution kernels from light-ray operators of QCD*, Fortschr. Phys. **42** (1994) 101

[Mus07] A. Mussgiller, *Pedestal drift correction*, HERMES Technical Recoil Meeting, 22^{nd} January 2007

[Pho00] Multi-anode Photomultiplier Tube Assembly H7546 data sheet, Hamamatsu, Sept. 2000

[Nas03] A. Nass et al., *The HERMES polarised Atomic Beam Source*, Nucl. Instrum. and Meth. **A505** (2003) 633

[PDG98] Particle Data Group, *The Review of Particle Physics* (1998) Eur. Phys. J. C **3**

[Pei92] A. Peisert, *Silicon Microstrip Detectors*, edited by F. Sauli, Instrumentation in High Energy Physics, World Scientific (1992), ISBN 981-02-0597-X

[Pol99] M.V. Polyakov and C. Weiss, *Skewed and double distributions in the pion and the nucleon*, Phys. Rev. **D60** (1999) 114017

[Pre95] Press W. H., Teukolsky S. A., Vetterling W. T., and Flannery, B. P., *Numerical recipes in fortran, thr art of scientific computing*, Second Edition, Cambridge University Press, Cambridge, Reprinted 1995

[Rad96] A. V. Radyushkin, *Asymmetric gluon distributions and hard diffractive electroproduction*, Phys. Lett. **B385** (1996) 333

[Rad98] A.V. Radyushkin, *Nonforward parton densities and soft mechanism for form factors and Wide-Angle Compton Scattering in QCD*, Phys. Rev. **D58** (1998) 114008

[Rei04] M. Reinecke et al., *A Silicon Strip Recoil Detector for momentum measurement and tracking at HERMES*, IEEE Trans. Nucl. Sci. **51** (2004) 1111

[Sei04] B. Seitz, *The HERMES Recoil Detector: a combined silicon strip and scintillating fibre detector for tracking and particle identification*, Nucl. Instrum. and Meth. **A535** (2004) 538

[Sok64] A. A. Sokolov and I. M. Ternov, *On polarisation and spin effects in the theory of synchrotron radiation*, Sov. Phys. Doklady **8** (1964) 1203

[Ste05] J. Stewart, *Alignment and Silicon Noise*, HERMES PRC Referee Meeting, 27^{th} September 2005

[Ste06] J. Stewart, *HERMES Report*, HERMES PRC Referee Meeting, October 2006

[Tru00] U. Trunk, *Development and characterisation of the radiation tolerant Helix128-2 readout Chip for the Hera-B Microstrip Detectors*, Ph.D. Thesis (2000)

[Tyt03] M. Tytgat, *The Recoil Photon Counter*, HERMES Internal Review Meeting, 7^{th} January 2003

[Van99a] M. Vanderhaeghen, *Deeply Virtual electroproduction of photons and mesons on the nucleon: leading order amplitudes and power corrections* Phys. Rev. **D60** (1999) 094017

[Van01b] M. Vanderhaeghen, P.A.M. Guichon and M. Guidal, *computer code for the calculatiopn of DVCS and BH processes in the reactions* $e + p \rightarrow e + p + \gamma$, Priv. Comm., (2001)

[VHa05] Y. van Haarlem, *Status of the Recoil Photon Detector*, HERMES PRC Referee Meeting, 24^{th} May 2005

[Vil07a] I. Vilardi, *Further insights into the proton spin with the new Hermes Recoil Detector*, AIP Conf. Proc. **964**, (2007), 193

[Vil07b] I. Vilardi, *First results with the Hermes Recoil Detector*, XII Research Workshop on High Energy Spin Physics (DSPIN-07) by JINR, Dubna, 2008, in press

[Wan96] W. Wander, *Reconstruction of high energy scattering events in the HERMES Experiment*, Ph.D. Thesis (1996)

[Web01] Website of the 267 WE-HERAEUS-Seminar on Generalized Parton Distributions, November 19 - 21, 2001, Scientific organizers: Peter Kroll

and Andreas Schäfer.
`http://www.theorie.physik.uni-wuppertal.de/~wwwkroll/badhonnef`

[Yas05] S. Yaschenko, *Track reconstruction accuracies and detector efficiencies for the Recoil Detector*, HERMES PRC Referee Meeting, 27^{th} September 2005

[Yas07] S. Yaschenko, *SSD-SFT alignment: first results*, HERMES Technical Recoil Meeting, 26^{th} March 2007

[Ye02] Z. Ye et al., *Radio Frequency Test for the HERMES Silicon Recoil Detector*, HERMES Internal Report **05-008** (2005)

[Ye06] Z. Ye, *Transverse target-spin asymmetry associated with Deeply Virtual Compton Scattering on the proton and a resulting model-dependent constraint on the total angular momentum of quarks in the nucleon*, Ph.D. thesis (2006)

[Yos97] Y. Yoshizawa et al., *The development and the study of R5900-00-M64 for scintillating/optical fiber read-out*, 1997 IEEE Nuclear Science Symposium Conference Record, vol.1, Albuquerque, NM, USA, 9-15 Nov. 1997. vol. 1, (1997) 877